UNIVERSITY OF SOUTHAMPTON

FACULTY OF ENGINEERING AND THE ENVIRONMENT

Civil and Environmental Engineering

Experimental investigation of static and cyclic behaviour of scaled railway ballast and the effect of stress reversal

by

Sinthuja Aingaran

Thesis for the degree of Doctor of Philosophy

February 2014

UNIVERSITY OF SOUTHAMPTON

ABSTRACT

FACULTY OF ENGINEERING AND THE ENVIRONMENT

Civil and Environmental Engineering

Doctor of Philosophy

EXPERIMENTAL INVESTIGATION OF STATIC AND CYCLIC BEHAVIOUR OF SCALED RAILWAY BALLAST AND THE EFFECT OF STRESS REVERSAL

Sinthuja Aingaran

The aim of the research was to improve the fundamental understanding of mechanical behaviour of ballast and study the effect of tamping on ballast. The experiments were carried out on scaled railway ballast to eliminate the difficulties associated with testing large particle granular materials. Consideration was given to the gradation, mineralogy and shape during scaling.

Particle characterisation work was carried out on scaled and full size ballast using imaging techniques to examine the validity of the use of scaled ballast. Detailed analysis of results is used to quantitatively measure the changes in shape with particle size. The results show measurable differences in particle shape between different particle size intervals. As the differences are small in magnitude, they do not invalidate the use of scaled ballast.

Monotonic, cyclic experiments were carried out as part of a laboratory testing programme. Scaled ballast shows generally similar stress strain behaviour to larger granular materials. The friction angle of 40° to 50° for the confining pressure range of 15 kPa to 200 kPa falls within the range of friction angle obtained for full size ballast in the literature. The effect of changing confining pressure during train loading was examined. The results show that the settlement increases and the stiffness reduces when the confining pressure cycles. The effect of principal stress reversal during tamping was examined by an extension stage after the cyclic loading. It is shown that massive settlement occurs after the extension stage during initial cycles and settlement returns back to the pre-extension stage soon under loading. The results evidence the disruption of ballast structure and loss of stiffness due to tamping. Specimens were resin stabilised within the triaxial cell after specific stress paths had been followed. The changes in structure during a specific stress path can be studied by CT examination.

List of contents

List of figures

List of tables

DECLARATION OF AUTHORSHIP

I, Sinthuja Aingaran

declare that the thesis entitled

Experimental investigation of static and cyclic behaviour of scaled railway ballast and the effect of stress reversal

and the work presented in the thesis are both my own, and have been generated by me as the result of my own original research. I confirm that:

- this work was done wholly or mainly while in candidature for a research degree at this University;
- where any part of this thesis has previously been submitted for a degree or any other qualification at this University or any other institution, this has been clearly stated;
- where I have consulted the published work of others, this is always clearly attributed;
- where I have quoted from the work of others, the source is always given. With the exception of such quotations, this thesis is entirely my own work;
- I have acknowledged all main sources of help;
- where the thesis is based on work done by myself jointly with others, I have made clear exactly what was done by others and what I have contributed myself;
- parts of this work have been published as: Le Pen, L.M., Powrie, W., Zervos, A., Ahmed, S., Aingaran, S. 2013. Dependence of shape on particle size for a crushed rock railway ballast. Granular Matter, Volume15, Issue 6, pp 849-861.

Signed: ……

Date:……

Acknowledgements

I would like to acknowledge and thank great number of people they have made possible this research.

Firstly, I am deeply indebted to my supervisors Prof. William Powrie, Dr. Antonis Zervos and Dr. Louis Le Pen for the opportunity given to me to carry out this research and for providing guidance and encouragement. In particular, my thanks go to Dr. Louis Le Pen, who worked as a visiting researcher and then Post-doctoral fellow on this project. He has shown enthusiasm towards this work and provided guidance and constructive criticisms during the research.

I'm very thankful to Harvey Skinner, Karl Scammell and Earl Peters, they worked very closely with me in the laboratory and helped greatly with technical modifications throughout various stages of testing. I'm very thankful to Dr. Athma Ram Bandari for his support and encouragement.

I would like to thank Dr. Jeff Priest for evaluating and providing critical suggestions on the 9th month and transfer reports. Dr. Louis Le Pen and Prof. William Powrie have spent time in reading through this draft and provided feedback. It has been very beneficial.

I'm very much thankful to my husband Aingaran Sellaiya who made it possible for me to carry out this research. I'm thankful to my father Sinniah Tharmalingam for inspiring and motivating me to take up a professional career and my mother Selvaraani Sinniah for all her love and patience.

1. Research Overview

1.1 Introduction

Rail transport is often preferred over other forms of transport due to some key advantages. Powrie (2013) recently presented on the advantages and challenges of rail transport at the annual James Forest lecture and some important observations from this lecture are paraphrased in the rest of this paragraph: Railway transportation is currently the only more or less universally available mode of transportation offering zero CO2 emissions at the point of use. Although electric cars have the potential to offer zero CO2 emissions, the capacity and infrastructure needs have yet to be met. Rail is energy efficient because the rolling of steel wheel on steel rail is very low friction. However, this view is increasingly challenged by road vehicles at full capacity. Rail is effective at combating congestion, as it can transport large amounts of people into city centres. Rail transportation also offers an advantage in terms of customer satisfaction due to the relatively pleasant travelling environment which also permits work to be done, whereas driving a car requires more concentration and does not allow work to be simultaneously completed. Despite these advantages rail transportation also faces challenges. For example trains are becoming faster, more frequent and heavier. As the working day is getting longer, less time is left for maintenance and the maintenance is increasingly mechanised. In 2009/10 the maintenance cost was 25% of the total operating cost in 2009/10. UK passenger miles are greater than at any time in the last 60 years. In spite of these challenges the remaining infrastructure is the same as it always was.

Further advantages of rail transportation include that, it is safer than road (ETSC, 2003) and the passenger and volume of goods carrying capacity of the railways is extremely large.

Rail transportation has some notable disadvantages over other modes of transportation, in particular road vehicles. For example train routes and timings cannot be adjusted to individual requirements and trains cannot provide door to door service. Where changes are needed to reach a passenger or freight destinations intermediate loading and unloading increases cost, wear and tear and lengthens journey times. Railway transportation is generally uneconomical for short distances. The cost of construction, maintenance and overhead expenses are very high and minimum amounts of traffic/usage are needed to keep routes open. Due to these relative disadvantages in certain key areas other modes of transport will always have a role in a comprehensive transportation infrastructure.

More recently, perhaps starting since the late 1970s, high speed trains and infrastructure have been developed that increasingly makes rail the mode of choice for passenger journeys that would previously have been covered by short haul domestic or international flights. This can be explained because where journey times are less than say 3 hours, faster train speeds mean destinations many hundreds of kilometres away can now be reached just as quickly in trains as by plane (say for example London to Paris).

There is currently a worldwide boom in the introduction of new high speed lines, with global high speed rail networks having more than doubled in length since 2000. Currently 13, 414 km of high speed railway lines are running worldwide with a further 10, 781 km under construction (Redfern, 2011). In the UK, following the success of the first high speed rail line (HS1), high speed two (HS2) was proposed between London, and the Midlands, the north of England and potentially at a later stage the central belt of Scotland. The proposed HS2 network will be 649 km by 2025 (Redfern, 2011). Thus a fundamental scientific understanding of railway foundation is essential to face a growing demand in the railway sector in a sustainable manner.

The track bed is constructed of layers above the natural ground. It reduces the stresses induced by train passage to acceptable levels and prevents excessive settlement. Careful consideration should be given to efficient and effective methods of track bed construction and maintenance procedures.

Railway systems are generally constructed using either ballast or slabs. Conventional ballasted tracks are usually preferred over slab tracks due to their lower construction costs and simplicity in design and construction (Indraratna and Salim, 2005). However ballast specifications still remain largely empirically based. In ballasted track the main considerations are the thickness of the ballast layer, the durability of the ballast, and the ease of ballast renewal. Scientifically developed methodologies have the potential to enhance the performance of ballasted rail track and save money spent on maintenance, renewal and disposal of ballast.

Despite the importance of ballast in track, it has received relatively little attention compared with superstructure components. Although a considerable amount of research has been carried out on strength, settlement and breakage of ballast, there is a knowledge gap in the area of track maintenance. Rail track starts to settle and loses its geometry with repetitive loading. Maintenance is therefore required to restore geometry. Although maintenance tamping initially corrects track line and level, it disturbs the structure of compacted ballast causing the principal effective stress to rotate by 90° from the vertical to the horizontal. This leads to a temporary loss of strength and stiffness (Selig and Waters, 1994).

In the past, a number of researchers have carried out monotonic and cyclic loading triaxial tests to study the strength and deformation properties of ballast. In this research, triaxial tests will be carried out on scaled ballast. The use of scaled ballast eliminates the requirement for large triaxial apparatus. The triaxial tests will be carried out to investigate the mechanical behaviour of ballast (strength, friction, settlement of ballast) and the effect of stress path reversal (tamping) on ballast structure. This research will contribute to better and more economical ballast layer design leading to reduced maintenance and renewal requirements.

1.2 Aim and Objectives

The aim of the project is to improve the fundamental understanding of mechanical behaviour of ballast and study the effect of tamping on ballast by carrying out experimental studies on model ballast material.

Several objectives are set to achieve this aim.

- Development of a scaled ballast that is representative of full size railway ballast for triaxial testing
- Investigation of the mechanical behaviour of the scaled ballast by carrying out monotonic and cyclic laboratory triaxial tests on scaled ballast
- Simulation of the effect of tamping and study its influence on the structure of ballast developed by repetitive loading

1.3 Organisation of the thesis

This remainder of this thesis is organised into 6 further chapters:

Chapter 2 provides the background to this research in detail.

Chapter 3 describes the development of scaled ballast using the parallel gradation method and presents the characterisation work carried out to examine the effect on particle shape of scaling.

Chapter 4 describes the triaxial apparatus, test preparation and procedure, test parameters and justification for loading. It also investigates factors potentially influencing the test results such as membrane penetration, creep and Young's modulus of the membrane.

Chapter 5 examines the stress, strain and strength of scaled ballast in monotonic triaxial test at effective cell pressures from 15 kPa to 200 kPa. It considers both the dry and

saturated behaviour of ballast. The difficulty associated with presenting stress dilatancy plots for scaled ballast by relying on the volume behaviour of the controller is highlighted. The chapter compares the friction angles obtained for scaled ballast with the friction angle values obtained for various full size ballast materials in the literature.

Chapter 6 examines the cyclic behaviour of ballast material and the effect of stress reversal on its structure. The first section of this chapter describes and compares the cyclic behaviour of ballast at constant and cyclic confining stresses in terms of settlement, volumetric strain, stiffness and Poisson's ratio. The second section of this chapter examines the effect of tamping on the ballast by imposing a stress reversal on the triaxial specimen.

Chapter 7 presents the conclusions and recommendations for the future research.

2. Literature Review

2.1 Overview

A considerable amount of research has been carried out on railway ballast throughout the world. However, there are still gaps in our understanding of its geomechanical behaviour. Improvement of the current state of understanding of ballast geomechanics is a prerequisite for the development of more cost effective construction methods and reducing maintenance.

This chapter includes sections on:

- The rail track system; introducing the ballasted track and track maintenance.

- Ballast; detailing the selection of ballast material, the expected functions of ballast, factors affecting the mechanical response of ballast and current ballast specifications.

- Characterisation of particle shape; focusing on the elements used to characterise particle shape, particularly measurements of form and roundness. It briefly introduces how form and roundness parameters have evolved during the 20th century and identifies the advantages and draw backs of different measurements.

- Structure in granular material; describing the formation of fabric structure within aggregates, types of particle contacts and influence of structure on the mechanical behaviour of aggregates.

- Strength of ballast; describing the strength of ballast obtained in triaxial testing in terms of peak stress ratio, shear strength, friction angle, critical strength and tensile strength.

- Stresses during the train loading; presenting the field, experimental, numerical model results regarding the stresses developed in the substructure due to train loading.

- Granular material behaviour under cyclic loading; describing the results of tests on ballast like aggregates available from the literature. In this section two aspects of ballast performance are considered; (1) resilient behaviour due to cyclic loading (2) plastic strain due to cyclic loading. The shakedown concept is reviewed.

- Testing on scaled material; introducing the parallel gradation technique and presenting works on rockfill and railway ballast model material.

2.2 Railway track

Rail track systems are made up of two parts, the superstructure and the substructure. The superstructure includes the steel rails, fastening system, rail pads, and timber or concrete sleepers/ ties. The substructure consists of ballast, sub ballast and sub grade. Figure 2.1 shows the layout of a typical ballasted track.

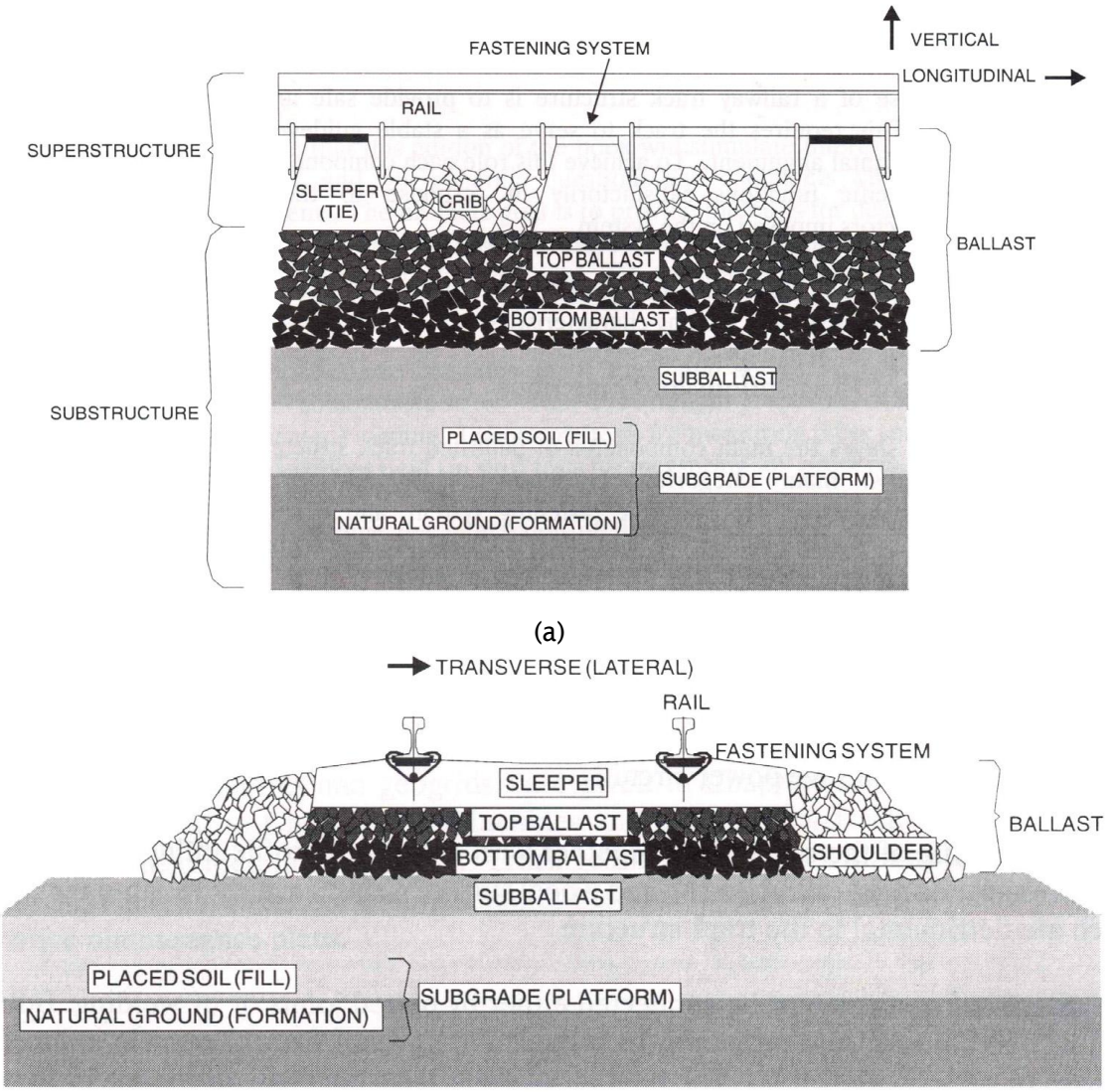

Figure 2.1: Layout of a typical ballasted track (a) Longitudinal view; (b) Transverse view (Selig and Waters, 1994)

Periodically, maintenance is required to restore the track design geometry which is lost as a result of repeated traffic loading (Selig and Waters, 1994). There are two types of maintenance generally in use, tamping and stone blowing. It has been said that tamping and stone blowing are used to correct respectively long wavelength faults and short

wavelength faults (Selig and Waters, 1994). However, there is still some uncertainty as to the optimal maintenance method to use and in what circumstances.

During tamping the ballast is compacted below the sleepers using vibrating tines. The process consists of lifting the sleeper to a desired level and inserting vibrating tines into the ballast. The tamping tines then squeeze ballast to fill the void underneath the lifted sleeper. Additional ballast is also placed into the cribs and onto the ballast shoulders so that after lifting the sleepers remain fully embedded within the ballast to the regulation profile. Thus the correct line and level of rail and sleeper is recovered. Afterwards, the tines are lifted and moved to the next sleeper. This procedure is shown on Figure 2.2. The main objective of the operation is to fill the void space under the sleeper by compacting the ballast (Saussine et al., 2008).

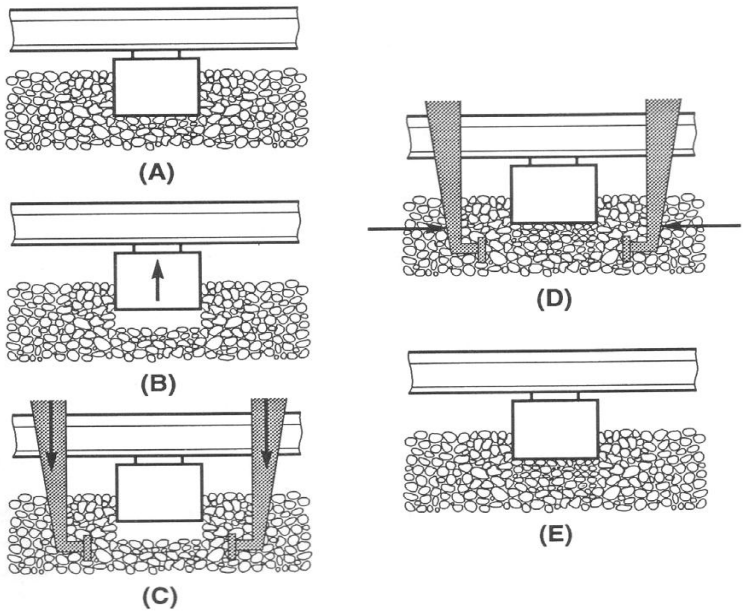

Figure 2.2: Tamping sequence (Selig and Waters, 1994)

Although the ballast is pushed into the void under the sleepers to support the sleepers at required profile, the ballast will soon return to its pre-maintenance profile. This phenomenon is called “ballast memory” and is shown in Figure 2.3. The tamping process disturbs and dilates the compacted ballast. Therefore, the ballast that fills the space under the sleeper is loose and hence under trafficking, the settlement increases at a faster rate and the ballast will soon return to its previous compacted profile.

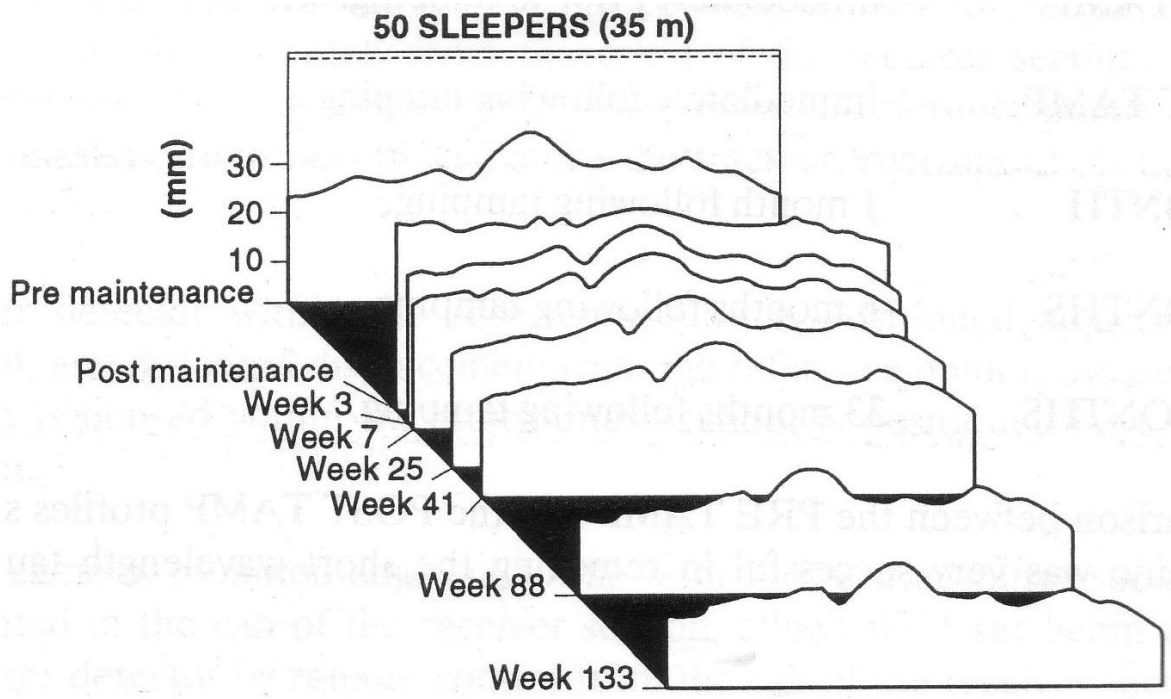

Figure 2.3: Effect of ballast memory (Selig and Waters, 1994)

The ballast memory effect depends on the amount of sleeper lift (Selig and Waters, 1994). Figure 2.4 shows the sleeper settlement in the subsequent 66 weeks of trafficking as a function of tamping lift. It shows that for relatively low lifts, the settlement is approximately equal to the lift. This indicates no lasting change in the inherent track shape. Also for the high lifts (a lift which exceeds the D50 size of the ballast), the settlements are not as large as the lift. This indicates more lasting improvement in the inherent track shape.

During low lifts, squeezed ballast is pushed upwards to fill the void. During higher lifts, squeezed ballast is pushed upwards and additional ballast particles are added to the ballast skeleton underneath the sleeper as there is sufficient room for them. The new ballast skeleton is then compacted by the subsequent traffic loading and a new geometry is achieved Selig and Waters (1994).

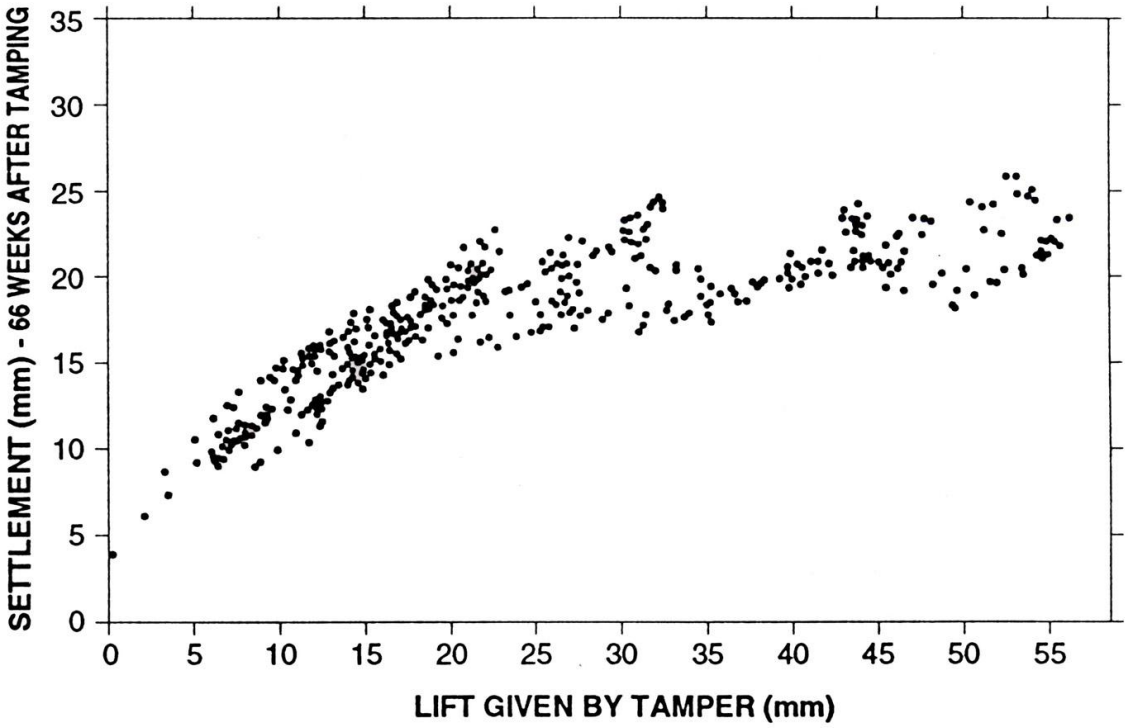

Figure 2.4: Sleeper settlement as a function of tamping lifts (Selig and Waters, 1994)

After the tamping process, Track geometry quality, defined by the deviation of the geometrical position of the rails against their theoretical position resulting from the statistical quality of the line and level of the intended track layout is measured using track recording vehicles and compared with the limiting values agreed in the contract with the asset owner (Luber et al., 2010). The track geometry quality measurement is carried out according to European Standards EN 13848-5 (2008) and EN14363 (2005).

During stone blowing the rails and sleepers are raised by the stone blowing machine to the target level, creating an empty space under the sleeper. Then the stone blowing tubes are inserted into the ballast layer and a measured quantity of stone is blown by compressed air into the space. Afterwards, the tubes are withdrawn from the ballast layer and the sleeper is lowered onto the top of the blown stone. This procedure is shown on Figure 2.5.

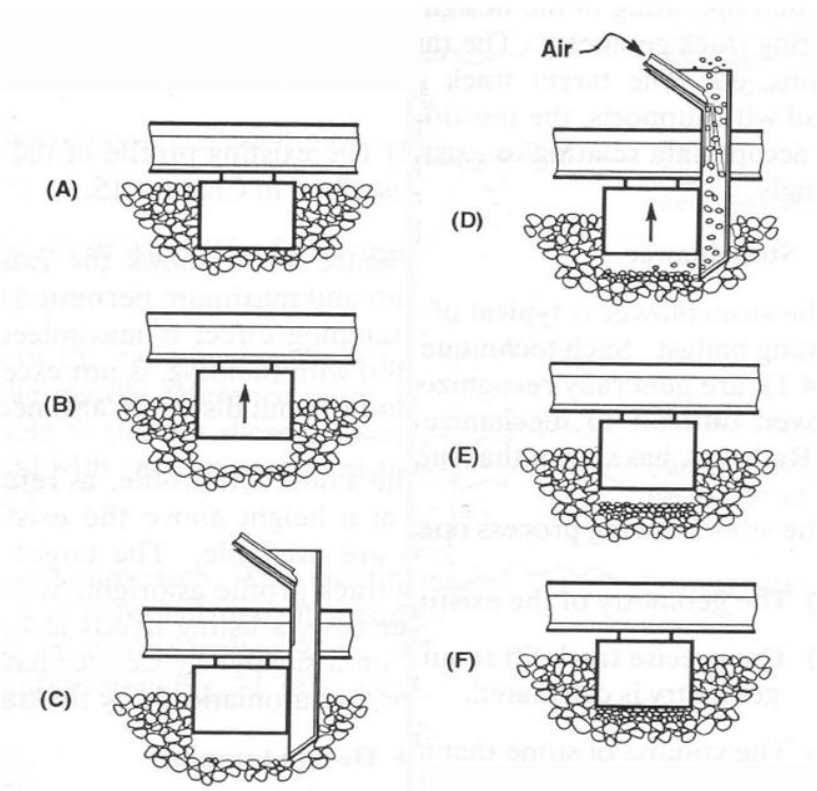

Figure 2.5: Stone blowing process (Selig and Waters, 1994)

Selig and Waters (1994) concluded that tamping leads to ballast degradation. One field investigation by British Railways measured the breakage of ballast after 20 tamps (Burks, 1975). This showed that the proportion of larger particles (38-51 mm) was significantly reduced by 15-45 % of the initial proportion. Whereas the smaller particle size range (less than 13 mm) was increased from 1% before tamping to 5% of the total specimen after tamping. A further British Railway laboratory study confirmed this behaviour (Wright, 1983) where it was found that 2 to 4 kg of material less than 14 mm size was generated per tamp for a single sleeper. A further factor influencing breakage during tamping is the strength of the parent rock material, field tests by AAR (Association of American Railroads) showed that fine material generated from tamping was higher for limestone ballast than granite ballast (Chrismer, 1989).

2.3 Ballast

Ballast is an unbound coarse aggregate which is laid above the sub ballast, between the sleepers (crib), and beyond the sleeper ends (shoulder). The ballast layer is typically a minimum of 250 mm to 300 mm thick. Ballast materials are selected throughout the world based on local availability, environmental regulations, and economic considerations. Various rock materials are used including granite, basalt, limestone, slag,

quartzite, and rheolite. Suitable ballast materials are likely to be crushed angular hard stones, uniformly graded, free of dust and dirt and not prone to cementing action (Indraratna and Salim, 2005).

Ballast is expected to perform many functions as a substructure component. It reduces the stress transmitted to the sub grade layer to prevent failure. It provides resilience and energy absorption for the entire track. Large voids are required in ballast to provide permeability for drainage. It should suffer minimal plastic deformation during maintenance cycles. Ballast should have resistance against crushing, attrition, mechanical degradation and weathering (Indraratna and Salim, 2005).

Indraratna and Salim (2005) noted that the mechanical response of ballast is governed by four main factors;

1. Characteristics of the constituent particles (size, shape, surface roughness, particle crushing strength, resistance to attrition)
2. Bulk properties of the granular assembly including particle size distribution, void ratio, degree of saturation
3. Loading parameters including current state of stress, previous stress history and applied stress path
4. Particle degradation

Ballast materials in the UK must comply with the specifications provided by Network Railway (RT/CE/S/006 Issue 3, 2000). The new (2005) specification follows the European railway ballast specification (BS EN 13450:2002), and focuses on five ballast properties to ensure the quality of track ballast. These are ballast grading, Los Angeles Abrasion Value (LAAV), Micro-Deval Attrition Value (MDA), flakiness index, and particle length index. The specification requires ballast to conform to the particle size distribution shown in Table 2.1.

Square Mesh Sieve (mm)	Cumulative % by mass passing BS sieve
63	100%
50	70-100%
40	30-65%
31.5	0-25%
22.4	0-3%
32-50	≥50%

Table 2.1: The new (2005) specification for ballast particle size distributions

(RT/CE/S/006 Issue 3, 2000)

2.4 Characterisation of particle shape

Particle shape is considered to have a major influence on the mechanical behaviour of a granular material, e.g. its undrained strength, volumetric compressibility and internal stress distribution (Clayton et al., 2007). Particle shape can be described by three elements which are form, roundness, and roughness (Barrett, 1980). Figure 2.6 shows these elements.

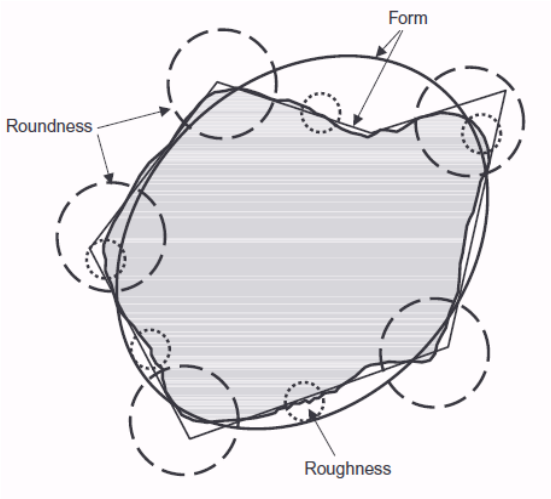

Figure 2.6: Elements of particle shape (after Barrett, 1980)

Form measures the overall shape of a particle. Roundness (inverse angularity) accounts for major surface irregularities which emphasize the corners and edges of a particle. Roughness is a measure of small scale irregularities. Roughness describes particle surfaces between corners. In this research to characterise scaled ballast particles, only form and roundness parameters are used. Roughness is not reviewed in this report. Roughness of scaled ballast can be considered equivalent to full size ballast if a similar parent rock is used for the scaled ballast. Shape parameters are expressed as dimensionless ratios, as they should be independent of size (Barrett, 1980)

2.4.1 Form

Although form is a three dimensional concept, many researchers have proposed two dimensional estimates because of its relative simplicity (Clayton et al., 2007). However, the two dimensional estimates often do not differentiate between bulky and platy nature of particles having similar outlines in one plan view.

In the past, various researchers have proposed three dimensional estimates of form. Table 2.2 shows some of the three dimensional form parameters. These parameters are generally derived from three orthogonal particle lengths. It is difficult and time consuming to obtain three orthogonal lengths. Thus three dimensional estimates of form

cannot easily be applied to small particles or large numbers of variable particles (Clayton et al., 2007).

Author	Formula	Name	Reference form	Notes
Zingg,1935	$\frac{I}{L}, S/I$	Zingg diagram		three dimensional estimate of form based on two independent ratios
Wadell,1932	$\sqrt[3]{\frac{vol\ of\ particle}{vol\ of\ circumscribing\ spher}}$	Wadell's sphericity	Sphere	ratio of particle volume to the volume of the circumscribing sphere
Krumbein,1941	$\sqrt[3]{\frac{I.S}{L^2}}$	Krumbein intercept sphericity	Ellipsoid	function of volume ratio of the ellipsoid defined by the three axes to the circumscribing sphere
Aschenbrenner, 1956		Working sphericity	Tetrakaide -kahedron	ratio of surface area of rock particles to the surface area of the reference form
Sneed and Folk, 1958	$\sqrt[3]{\frac{S^2}{L.I}}$	maximum projection sphericity	Sphere	ratio of sphere equal to the volume of particle, to the sphere with the same maximum projection area

Table 2.2: Three dimensional estimates of form parameter; where L, I, S are major, intermediate, minor particle dimensions (after Barrett, 1980)

From three orthogonal axes only two independent ratios can be obtained, and this is the limit for the number of independent parameters of form. Zingg's (1935) diagram is an early and clear expression of this (Barrett, 1980). Zingg (1935) calculated two independent ratios I/L and S/I which were plotted on a diagram known as Zingg plot (Figure 2.7). He split the diagram into four areas to classify the shape as 'flat', 'spherical', 'flat and columnar' and 'columnar'. I/L and S/I are termed as elongation ratio and flatness ratio respectively. These ratios I/L and S/I have long been used as a measure of elongation and flatness respectively (Blott and Pye, 2008). Another commonly used ratio S/L is the product of the coordinates in the Zingg plot which is termed as degree of equancy (Blott and Pye, 2008).

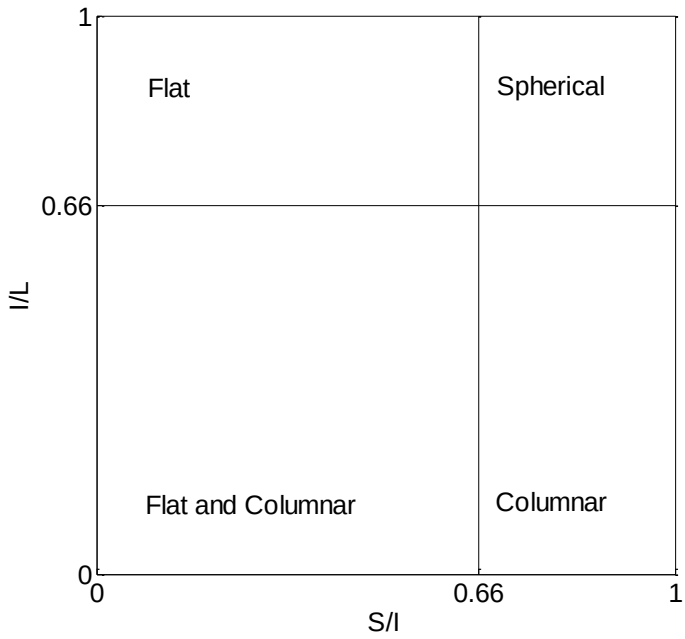

Figure 2.7: Zingg diagram (redrawn from Zingg,1935)

Clayton et al.(2007) proposed a practical method to measure the three dimensional form of a coarse particle, known as 'scalene ellipsoid equivalent sphericity'. The scalene ellipsoid was selected as the reference particle shape for the development of this form parameter. A scalene ellipsoid is an ellipsoid in which the lengths of all three semi-principal axes are different. Their working hypothesis was that the platy or bulky nature of soils can be expressed through the minimum and maximum particle dimensions (S/L). They stated that when non-spherical particles are dispersed onto a horizontal surface, they settle into their most mechanically stable position and present their largest projection area in the plan view.

Their method was developed for use with large numbers of similarly shaped particles. A known mass and number of particles can be photographed lying flat and processed using image analysis software to determine average measurements.

Figure 2.8 shows the measurement of individual particle dimensions assuming it is a scalene ellipsoid. Major (L) and intermediate (I) dimensions are taken as the diameters of a circumscribed (D_{cc}) and inscribed circles (D_{ic}) in plan view, while S is the minimum value D_{ic} in the side and end elevations. The dimension (S) is obtained by measuring L and I using imaging and then determining the average volume of the particles (equation 2.1 and 2.2).

Smallest dimension of scalene ellipsoid;

$$S = \frac{6V}{\pi LI} \tag{2.1}$$

where V- volume of scalene ellipsoid and

L, I and S - major, intermediate and minor particle dimensions.

Average volume of particles, V;

$$V = \frac{W}{nG_s\rho_w} \tag{2.2}$$

where W- mass of specimen,

G_s- Specific gravity and

n- number of particles.

The scalene ellipsoid equivalent sphericity (SEES) is calculated using equation 2.3. For SEES measurements, Diameter(max) and Diameter(min) parameters in Image Pro Plus are considered in close approximation to diameter of circumscribed circle (D_{cc}) and inscribed circle (D_{ic}) respectively. Diameter(max) and Diameter(min) are the lengths of the longest and shortest lines joining two points on the particle perimeter and passing through its centroid. Thus Major (L) and intermediate (I) dimensions are determined from Diameter(max) and Diameter(min) parameters from plan view image of the particle. (Clayton et al., 2007).

$$SEES = \frac{S}{L} = \frac{\left(\frac{W}{\mathrm{nG_s}\rho_\mathrm{w}}\right)\left(\frac{6}{\pi LI}\right)}{L} \tag{2.3}$$

where W - mass of specimen,

G_s - specific gravity,

n - number of particles and

L, I and S - average major, intermediate and minor particle dimensions.

SEES can differentiate bulky particles having the same major, intermediate and minor dimensions but different volumes because of their shape. Also, it differentiates between bulky and platy particles having the same major and intermediate dimensions. The limitation is that it cannot differentiate between rod-like and plate-like particles having the same major and minor dimensions, because SEES does not adequately account of the intermediate dimension. As the population of rod-like particles is insignificant in igneous crushed rocks used for railway ballast, this drawback can be ignored.

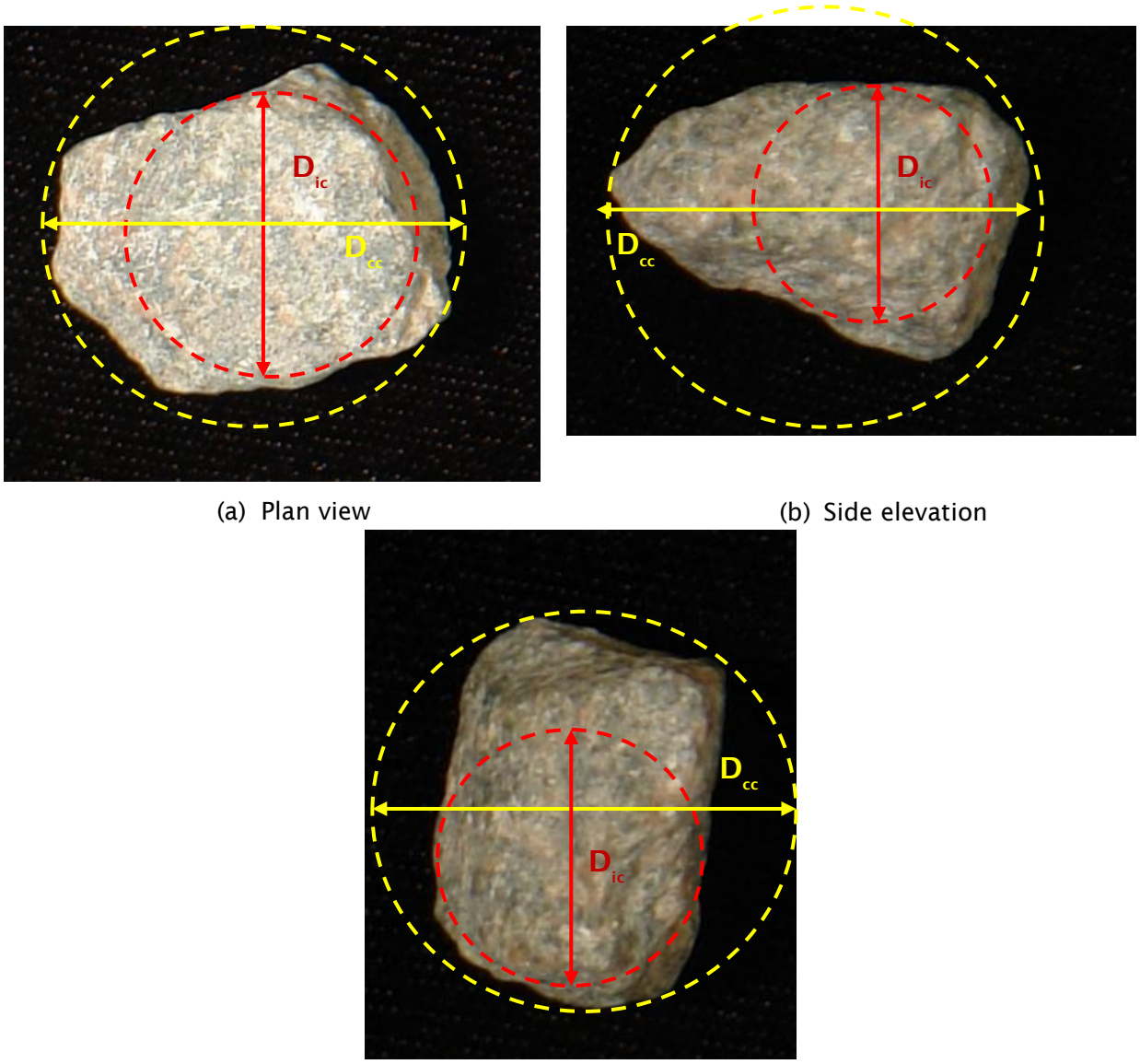

(a) Plan view (b) Side elevation

(c) End elevation

Figure 2.8: Measurement of individual particle dimensions: (a) plan view; (b) side elevation; (c) end elevation

2.4.2 Roundness

Roundness measures the relative sharpness of the corners and edges of particles. It is quantified using 2D views of particles. Early studies had proposed measures of roundness using visual comparison scales, for example Mackie (1897). Wentworth (1919) introduced the first quantitative roundness measurement technique. He defined roundness as, "the ratio of the radius of curvature of the most convex part of surface to half of the longest diameter through the point". He considered that roundness was dependent on the curvature of the corners of a particle. Table 2.3 shows some roundness measurements

proposed by other researchers based on Wentworth's concept. In all these measurements, the curvature of the corners is divided by the particle size. They differ in whether the sharpest corner or all corners are considered and what measure of particle size is used. Figure 2.9 shows how the particle size and curvature are measured to calculate roundness parameters. The roundness measurements shown in Table 2.3 are extremely time consuming and not readily amendable to automation.

Reference	Formula	Name	Range
Wentworth (1919)	D_k/L	Shape index	0-1
Wentworth (1923)	$\frac{D_k}{(L+I)/2}$	Roundness ratio	0-1
Wadell (1932)	$\frac{\Sigma(D_k, D_c)/n}{D_i}$	Wadell roundness	0-1
Cailleux (1947)	$(D_k/L)x\ 1000$	Cailleux roundness index	0-1000
Kuenen (1956)	D_k/I	Kuenen roundness index	0-1
Dobkins & Folk (1970)	D_k/D_i	Modified wentworth roundness	0-1
Swan (1974)	$\frac{(D_{k1}+D_{k2})/2}{D_i}$	Swan roundness index	0-1

Table 2.3: Roundness parameters (I); where L= Longest axis of the grain; I= Intermediate axis of the grain; D_i, diameter of largest inscribed circle; D_c diameter of curvature of corners other than the sharpest corner; D_k diameter of curvature of sharpest corner

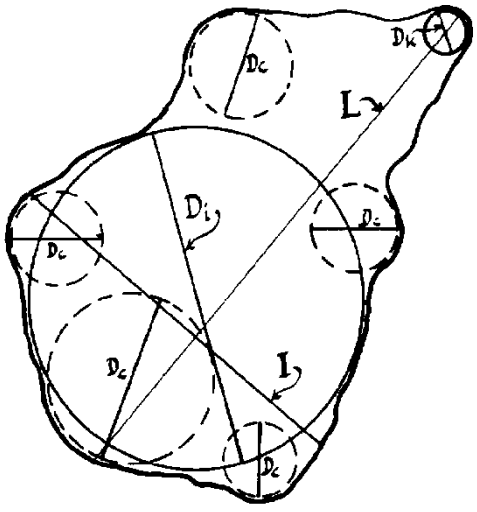

Figure 2.9: Measuring the roundness parameter. Particle lying on the plane of maximum projected area with the shortest axis vertical to the paper. (Dobkins and Folk, 1970)

Some of the roundness parameters were termed circularity by Blott and Pye (2008). The concept "circularity" for particle shape analysis as distinct from form and roundness does not have widespread acceptance. These parameters are referred to here as roundness to be consistent with previous work. They use a circle as a reference shape and in this way these measures are distinct from other form and roundness methods. Cox (1927) developed the 'percentage roundness' as the ratio of the area of the grain to the area of a circle with the same perimeter, which later became known as the 'form factor'. Many of the roundness parameters others have proposed are related to the form factor (Table 2.4). Also some of these measures are known not to be independent of form (e.g. form factor).

Image pro plus provides automatic measurement of roundness which is the inverse of Cox's roundness 'form factor', $4\pi A/p^2$.

$$Roundness = \frac{P^2}{4\pi A} \tag{2.4}$$

where P - Perimeter of the shape

A - Area of the object

It has a range between 0 to ∞ and uses a circle as a reference form. It is same as: (perimeter of shape) ^{2} / (perimeter of circle of equivalent area) ^{2}

A new measurement of roundness termed as 'ellipseness' is going to be introduced in this project and the roundness measurement will not rely on the existing roundness measures.

Reference	Formula	Range	Name	Notes
Pentland (1927)	$\frac{4A}{\pi L^2}$	0-1		Ratio of the area of the grain to the area of a circle with diameter equal to the longest diameter of the grain. Pentland called this 'roundness'
Cox (1927)	$\frac{4\pi A}{P^2}$	0-1	Form factor	Ratio of the area of grain to the area of a circle with the same perimeter. Cox called this 'roundness'. (Image Pro Plus software uses the inverse of Cox's roundness $P^2/4\pi A$ as a roundness measurement)
Tickell (1931)	$\frac{4A}{\pi(D_c)^2}$	0-1		Ratio of the area of grain to the area of the smallest circumscribing circle. Tickell called this 'roundness'
Wadell (1933)	$\frac{c}{C} = \sqrt{\frac{4\pi A}{P^2}}$	0-1		Ratio of the perimeter of a circle with the same area as the grain to the actual perimeter of the grain. Square root of Cox's (1927) formula
Wadell (1935)	$\frac{d_c}{D_c} = \sqrt{\frac{4A}{\pi(D_c)^2}}$	0-1		Ratio of the diameter of a circle with the same area as the grain to the diameter of the smallest circumscribing circle. Formula also given in Wadell (1933) but in a different form
Riley (1941)	$\sqrt{\frac{D_i}{D_c}}$	0-1	Inscribed circle sphericity	Square root of the ratio of the diameter of the largest inscribed circle to the diameter of the smallest circumscribing circle.
Janoo (1998)	$\frac{P^2}{A}$	4π to α		General ratio of perimeter to area
Foresto et al (2000)	$\frac{A}{P^2}$	0 to 4π	aggregate shape factor	Non-normalised version of the form factor
Hausner (1966)	$\frac{P^2}{4\pi A}$		Surface factor	Inverse of the form factor
Diamond et al (1982)	$NRF = \frac{r_p}{r_a}$		Nuclear roundness factor	Ratio of radius of a circle with the same perimeter as the object, to the radius of circle with same area

Table 2.4: Roundness parameters (II) (Blott and Pye, 2008, Ritter and Cooper, 2009)

2.5 Structure in granular material

Structure in granular material can be characterized as bonded structure or fabric structure. Bonded structure forms due to the bonds between particles and fabric structure is the result of particle interlocking. Studies of fabric structure in the absence of bonding are rare in the literature, because of the difficulty of obtaining or preparing representative samples. Recent technical developments facilitate the recovery of undisturbed block samples, examination of its intact fabric in sections, and direct shear and triaxial testing (Cresswell and Barton, 2003).

2.5.1 Development of fabric structure

Fabric structure (particle interlocking) is developed through diagenetic processes such as compaction, pressure solution of detrital grains, and crystal overgrowth (Barton, 1993, Dusseault and Morgenstern, 1979). When naturally deposited sands undergo compaction, grain rotation takes place leading to interlocking. Pressure solution is a process by which grains dissolve at intergranular contacts. It consists of dissolution of stressed material at grain contact, aided by a seepage flux (Barton, 1993). Pressure solution increases the grain contact area, so the types of interparticle contacts change from tangential to mainly straight or concavo/convex (Siever, 1959, Taylor, 1950). Pressure solution causes porosity reduction (Dusseault, 1977), and leads to interlocking. Crystal overgrowth occurs due to excess silica in the solution. On the areas of grains not in contact with other grains, overgrowth contributes to interlocking, but not to cementing until the texture develops to a very high degree (Dusseault and Morgenstern, 1979).

Barton (1993) stated that changes during the initial stage of diagenesis (referred to as aging) lead to increased stiffness in sand. Micro-interlocking of grain asperities during aging attributes to stiffness (Mesri, 1990). The increased stiffness is considered to result from frictional rather than cohesive effects (Schmertmann, 1991).

The descriptive fabric classification is shown in Figure 2.10 (Siever, 1959). Particle interlocking can be measured by the tangential index, which is the percentage of tangential contact to all grain contact observed in a thin section (Barton, 1993).

Ballast may develop a fabric structure due to compaction during traffic loading. When traffic loading takes place, grain rotation may take place and this will lead to interlocking of particles. In general ballast in rail track foundations is angular in nature and have flat surfaces and concave or convex particles, this will help to form interlocking of particles. In triaxial tests on ballast, a non-linear failure envelope and a peak friction angle of greater than 45° at lower confining pressure were observed (Raymond and Davies, 1978, Indraratna et al., 1998). In a railway, the confining pressure in the ballast is expected to be low. According to Selig and Alva-Hurtado (1982) the in-situ lateral stress in a typical

ballast bed was approximately 5-40 kPa. The high values of peak friction angle observed during the tests on ballast at low cell pressure are expected to be related to interlocking and the ability of ballast to dilate under low stress levels (Indraratna et al., 1998). In accordance with this, Raymond and Davies (1978) reported that the intercept of Mohr-coulomb's failure envelope must be due to dilatancy, changing friction angle, or particle interlock due to compaction, or all three, as there cannot be any cohesion in dolomite ballast. They reported the interlock is probably the major factor. After the maintenance period temporary loss of strength and stiffness is observed in rail track (Selig and Waters, 1994). This can be attributed to the destruction of the fabric structure developed within the ballast during trafficking.

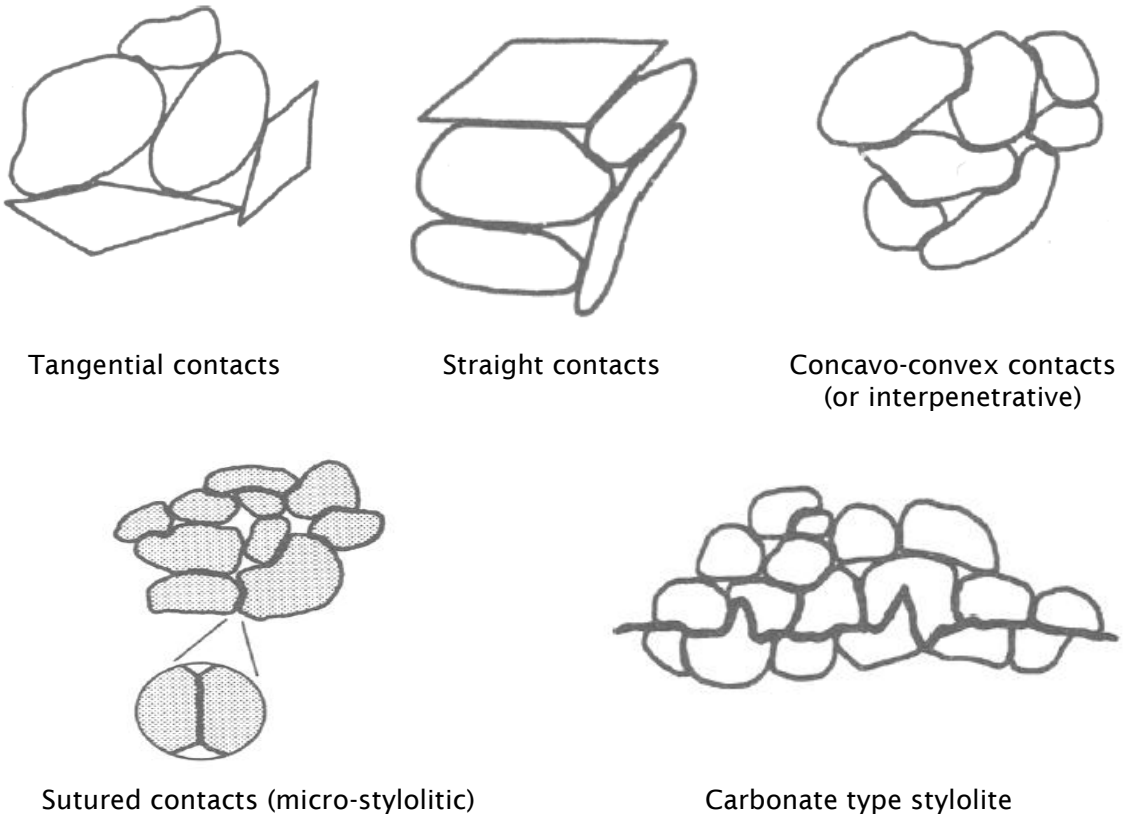

Figure 2.10: Intergranular fabric classification (Siever, 1959)

2.5.2 Influence of fabric structure

In the literature, a locked sand is an example of an interlocked fabric structure. Locked sands have been found to have relative densities greater than 100 %, without a cemented structure. The minimum porosity achieved by compacting the disaggregated locked sand is higher than the in-situ porosity of the locked sand. This is attributed to the peculiar fabric that develops as a result of diagenetic processes which, while reducing porosity, do not create a cemented structure (Dusseault and Morgenstern, 1979). Figure 2.11(a) shows

a purely locked sand with no trace of cementing material. Figure 2.11(b) shows the intergranular contacts typical of a locked sand. Locked sands develop structural resistance with fabric due to interlocking.

Dusseault and Morgenstern (1979) carried out shear tests on locked sands and reported small strains to failure, high rates of dilation, and a curved Mohr-coulomb envelope. Thus locked sands are capable of supporting large loads with only small deformations.

When compared to dense pluviated sand, locked sands have high angles of effective shearing resistance (Dusseault and Morgenstern, 1979). Cresswell and Powrie (2004) also reported that locked sands exhibit high dilation rates and stress ratios compared with pluviated specimens.

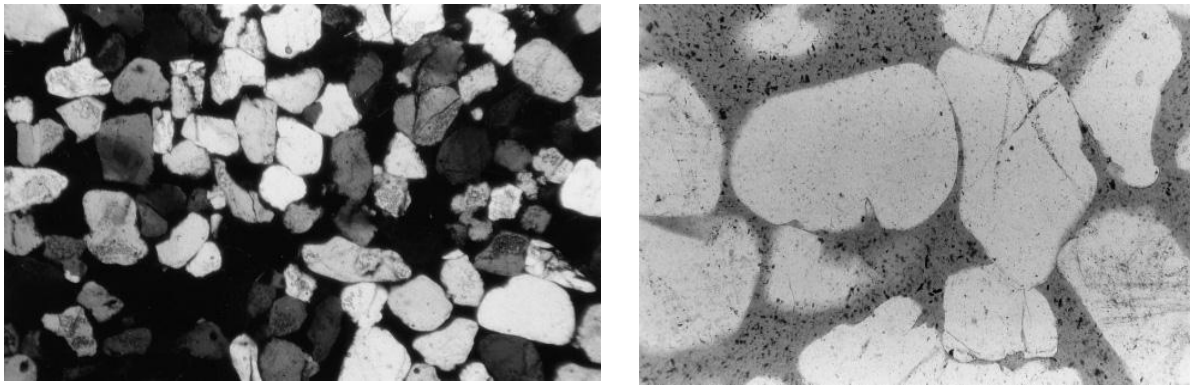

(a) (b)

Figure 2.11: (a) Purely locked sand in absence of cement; (b) Intergranular contact of locked sand (Cresswell and Barton, 2003)

Dusseault and Morgenstern (1979) reported that the disruption of a fabric structure returns the shear strength behaviour of material to that of ordinary sand. In accordance with this Cresswell and Powrie (2004) also reported that when the structure is disturbed locked sands lose their additional strength. The high effective shear strength of locked sands is purely due to their fabric structure.

Cresswell and Powrie (2004) carried out a series of triaxial tests to investigate the influence of fabric structure on the yield and failure behaviour of locked sands. In tests on unbonded locked sands (at effective cell pressures 50 kPa to 800 kPa), stress ratios in excess of critical were mobilised without the need for dilation (Cresswell and Powrie, 2004). This is in contrast to tests on unstructured sands, in which any mobilised stress ratio in excess of critical state is associated with dilation. In the past, mobilisation of stress ratios in excess of critical without dilation was considered as a characteristic of cemented sand. Even for sandstone with both bonding and fabric structure, it was

considered to be an effect of bonding (Cuccovillo and Coop, 1999). Cresswell and Powrie (2004) concluded that since the tests were carried on purely locked sand (zero cement content) the behaviour could be a result of fabric structure alone.

There is no evidence in the literature that fabric structure has been investigated in larger granular materials such as railway ballast. A lack of knowledge of the fabric structure of ballast and its development over different stages of the ballast life cycle due to traffic load and track maintenance is apparent. Maintenance tamping rearranges the particles and destroys any fabric structure developed within the ballast during train loading. Thus a better understanding of how the fabric structure develops within the ballast and how it influences the deformation characteristics of ballast will help to identify the lifespan of ballast and plan the maintenance period appropriately.

2.6 Strength of ballast

The static peak strength of ballast material can be considered as the peak stress ratio $(q/p')_{max}$. The static peak strength of ballast is determined by carrying out monotonic loading on specimen. In general, the static peak strength of ballast reduces with increasing confining pressure (Figure 2.12) (Indraratna and Salim, 2005, Suiker et al., 2005). Also, the strain corresponding to the peak strength increases with increasing confining pressure. This can be attributed to the interlocking of particles reducing with increasing confining pressure. The post peak behaviour of ballast is often characterized by a strain – softening behaviour (Indraratna et al., 1998).

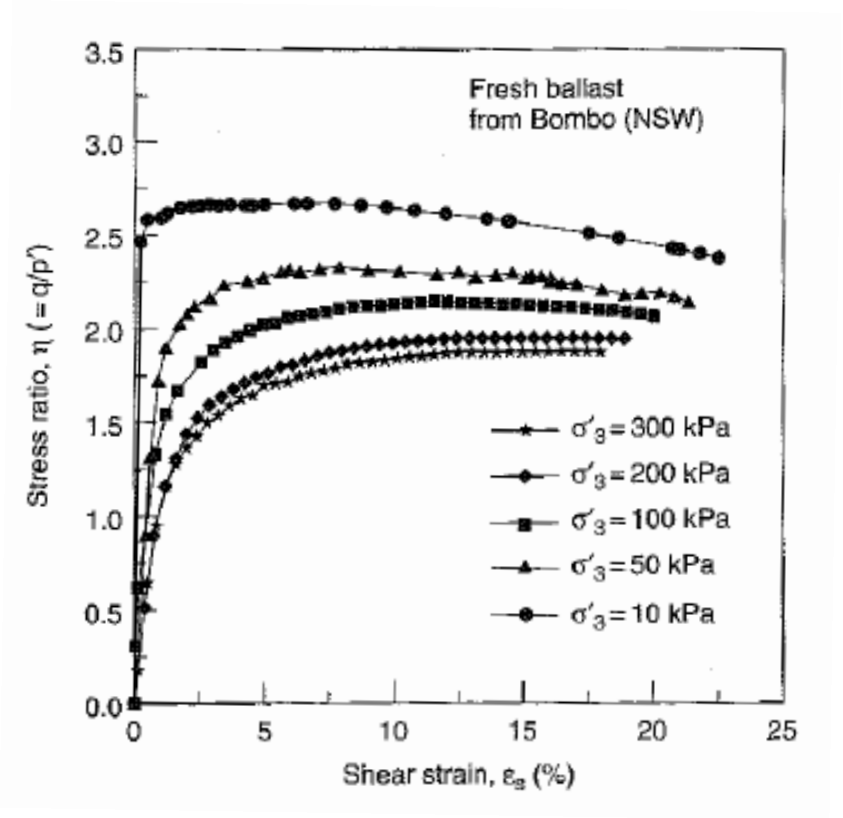

Figure 2.12: Stress strain behaviour during Triaxial drained compressions tests (Indraratna et al., 1998)

In contrast to sand, a large granular material like ballast does not show a clear visible failure plane. The peak deviator stress $(\sigma_1'-\sigma_3')_p$ can be considered as a failure point of ballast (Indraratna et al., 1998).

The shear strength of ballast can be expressed in terms of the principal stress ratio at failure (at peak deviator stress) (Indraratna and Salim, 2005). The principal stress ratio at failure reduces with increasing confining pressure (Figure 2.13). It can be attributed to greater interlocking of particle at low confining pressure. Also dilatancy diminishes at higher confining pressure.

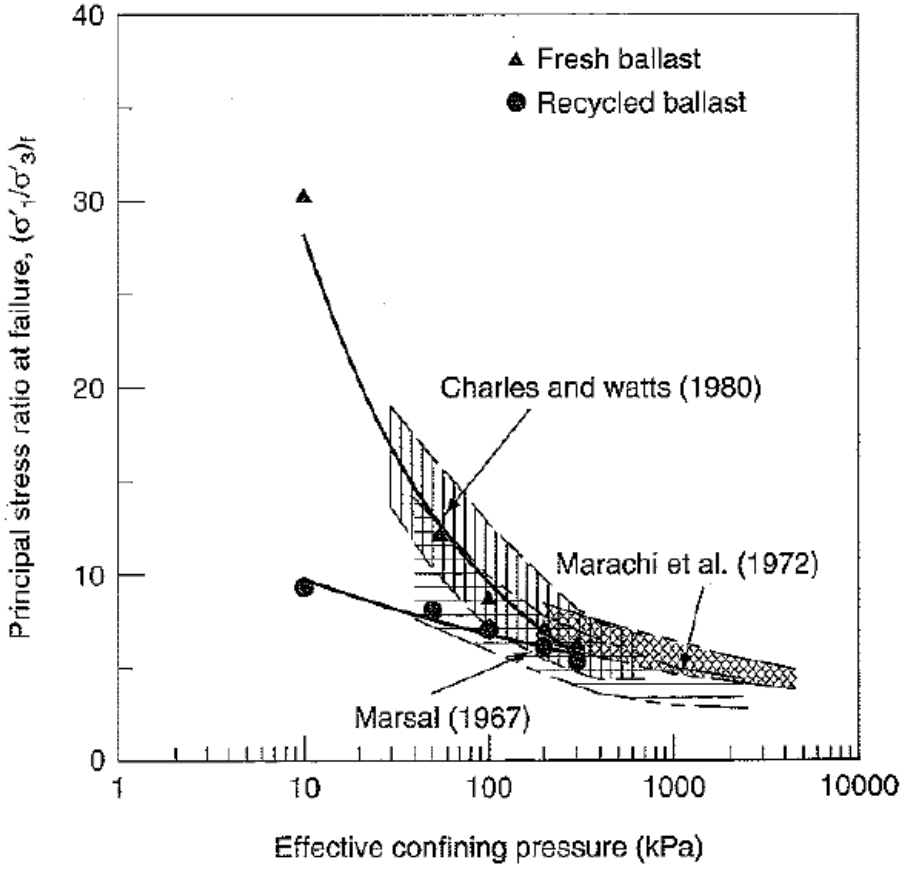

Figure 2.13: Shear strength of fresh and recycled ballast (modified by Salim (2004) and inspired by Indraratna et al. (1998))

The variation of shear strength of ballast with normal stress can be represented by a series of Mohr circles (Figure 2.14). At lower normal stresses the shear strength envelope is curved and passes through the origin (zero cohesion). The non-linear failure envelope at low normal stresses (normal stresses below 400 kPa are representative of railway ballasted foundations (Jeffs and Tew, 1991)) is due to dilatant behaviour of the material. Although at higher confining pressure the shear strength envelope tends to become linear, the conventional (linear) Mohr-Coulomb equation cannot be used to describe the shear strength. If a linear envelope is fixed to these circles, it will contain an intercept which means the material has cohesion, but this would not be correct for a granular material.

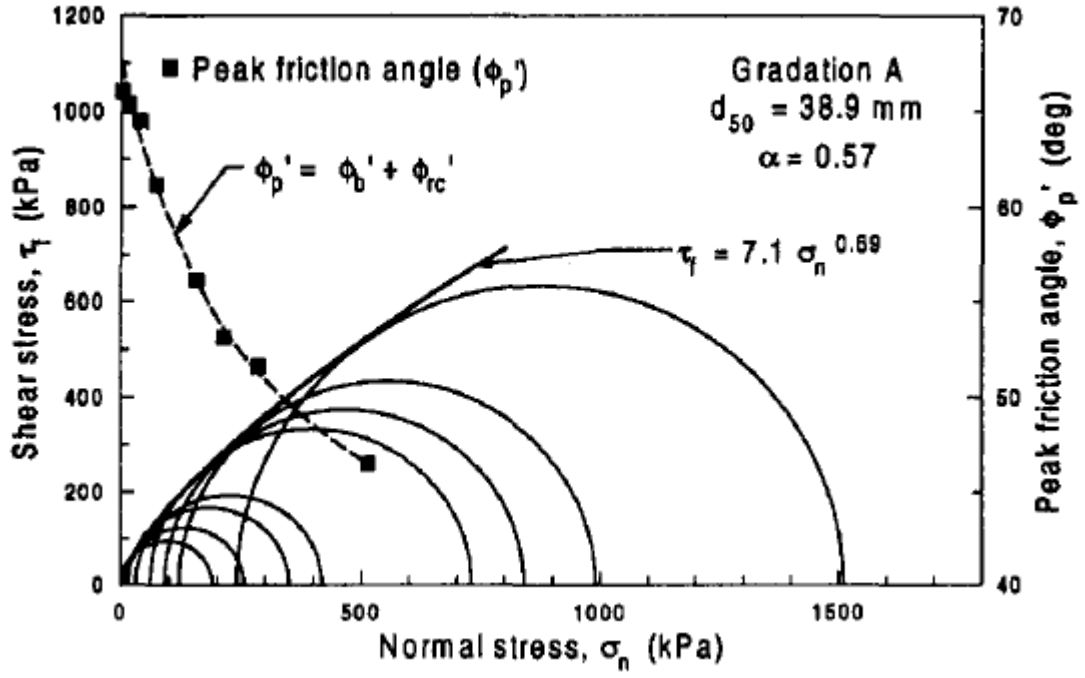

Figure 2.14: Mohr-Coulomb failure envelope for Latite Basalt (Indraratna et al., 1998)

The variation of shear strength with normal stress for ballast and other rockfill materials has been summarized by Indraratna et al.(1998). It confirmed that all shear strength envelopes are non-linear as shown in Figure 2.15. Indraratna et al.(1993) proposed a non-linear strength criterion for graywacke rockfill. It was extended to express the shear strength of ballast at low confining pressures as follows:

$$\frac{\tau_f}{\sigma_c} = m\left[\frac{\sigma_n}{\sigma_c}\right]^n \tag{2.5}$$

where τ_f - shear stress at failure,

σ_n -normal stress on the failure plane,

σ_c - uniaxial compression strength of parent rock, and

m,n - dimensionless constants.

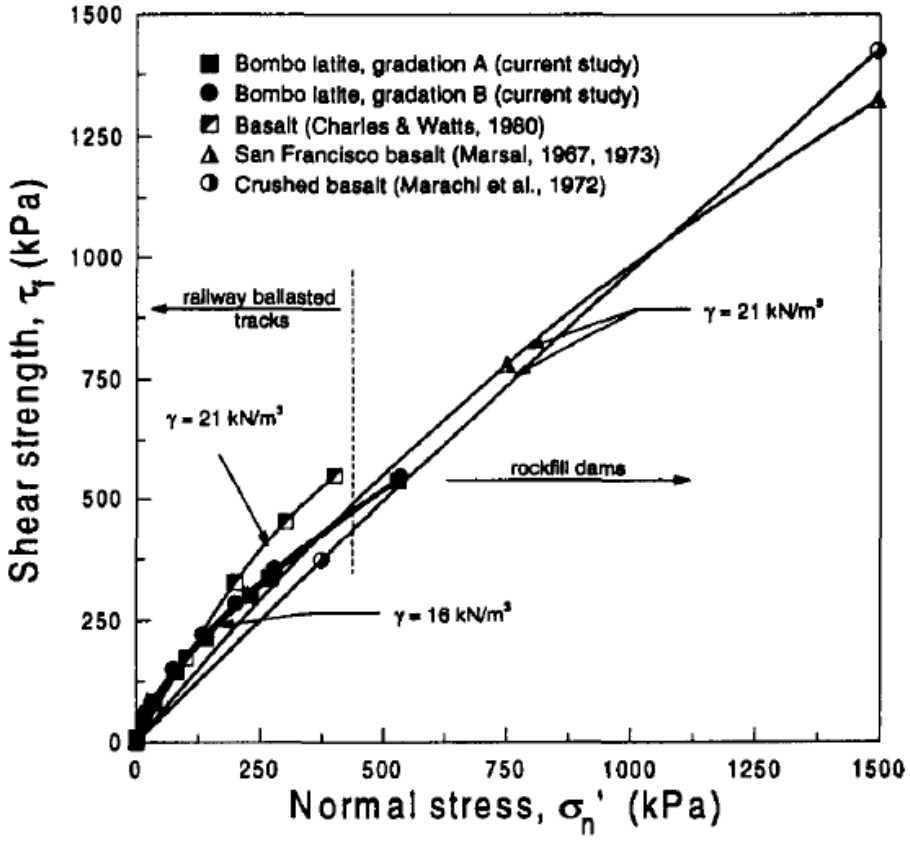

Figure 2.15: Shear strength of ballast and other rochfill aggregates (Basalt) at low to medium range of confining pressures (Indraratna et al., 1998)

The friction angle corresponding to the peak deviator stress of ballast can be estimated by drawing a tangent to each Mohr circle. The peak friction angle of ballast is conventionally calculated from triaxial test results by rearranging the Mohr-Coulomb failure criterion as follows;

$$\left(\frac{\sigma_1'}{\sigma_3'}\right)_p = \frac{1 + sin\phi'_p}{1 - sin\phi'_p} \quad (2.6)$$

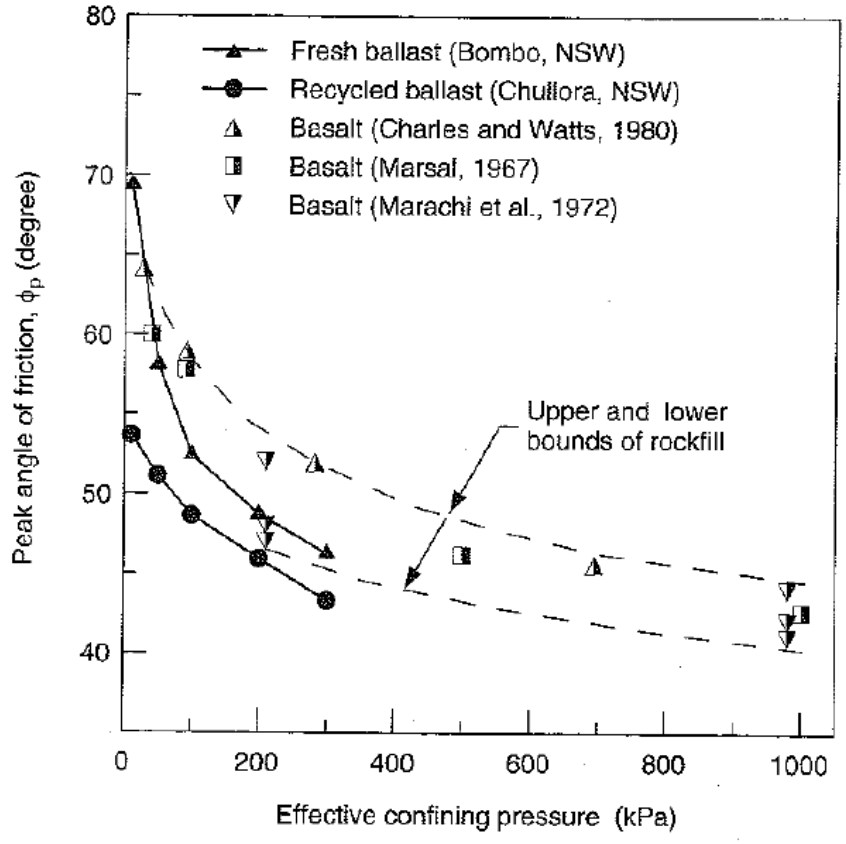

Figure 2.16: Variation of peak friction angle with effective confining pressure ballast (modified by Salim (2004) and inspired by Indraratna et al. (1998))

Figure 2.16 shows that the friction angle of ballast and other rockfill materials decreases with increasing confining pressure. For example, the peak friction angle of fresh and recycled ballast decreases from 69° to 46° and 54° to 43° respectively as the confining pressure increases from 10 kPa to 300 kPa. The friction angle of ballast at a particular confining pressure may also depend on the mineralogy of the parent rock.

The end points of shear tests represent the critical states of material, where the material continues to deform at constant stress ratio q/p' and constant specific volume. The line joining critical states is often referred to as the critical state line, which can be represented by the equation q=Mp'. Indraratna and Salim (2001) reported the critical state line for ballast (Figure 2.17). The results showed that, at the end of drained shearing, states of stress (p',q) of all ballast specimens lie on a critical state line. They show that the deviator stress at the critical state of ballast material increases with confining pressure. Critical state parameters (M) of approximately 1.90 and 1.67 were determined for fresh and recycled ballast respectively.

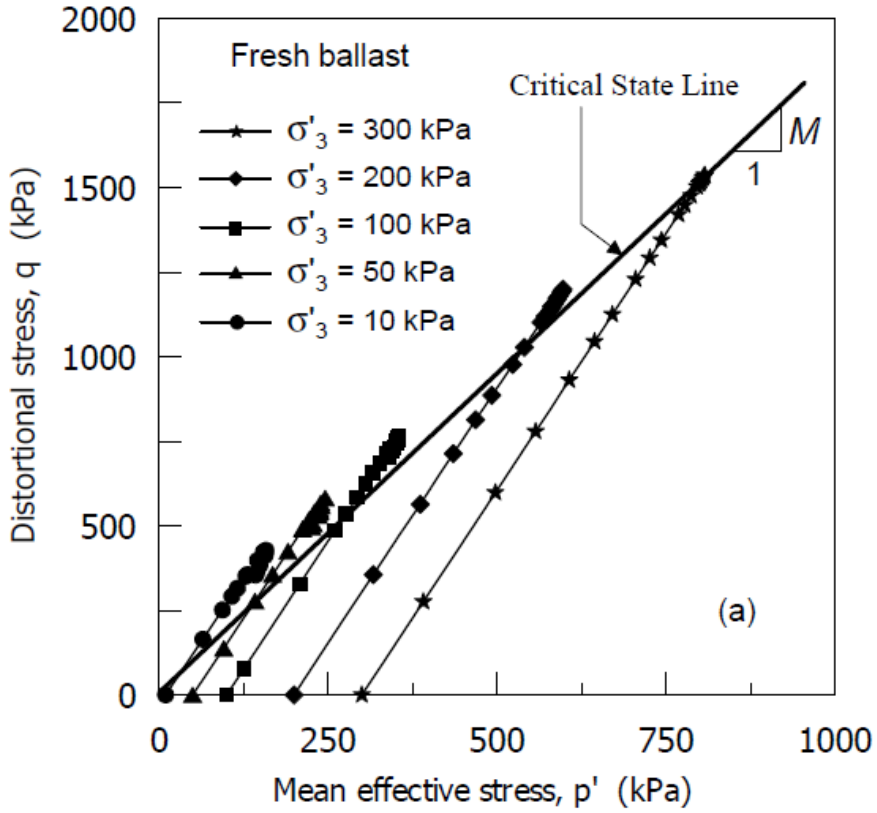

Figure 2.17: Variation of p' and q in drained Triaxial shearing (Indraratna and Salim, 2001)

Crushing strength (resistance of grains to fracture) is a key parameter governing ballast degradation. Fracture in a particle is initiated by tensile failure and the tensile strength of individual ballast particles can be measured using a series of single particle crushing tests. The maximum load at which a particle fractured (F_f) can be recorded and the corresponding tensile strength (σ_f) can be calculated by equation $\sigma_f = F_f/d^2$ where d is the initial particle diameter. Tensile strengths of various sized fresh and recycled ballast particles were studied (Indraratna and Salim, 2003). The results showed that fresh ballast has a higher tensile strength than recycled ballast (Figure 2.18). This can be attributed to the greater number of micro-cracks in recycled ballast than in fresh ballast, as recycled ballast has undergone millions of cycles in the past.

The tensile strength also decreases linearly with increasing grain size. Larger grains are more vulnerable to breakage, as they contain more flaws and have a higher probability of defects (Lade et al., 1996).

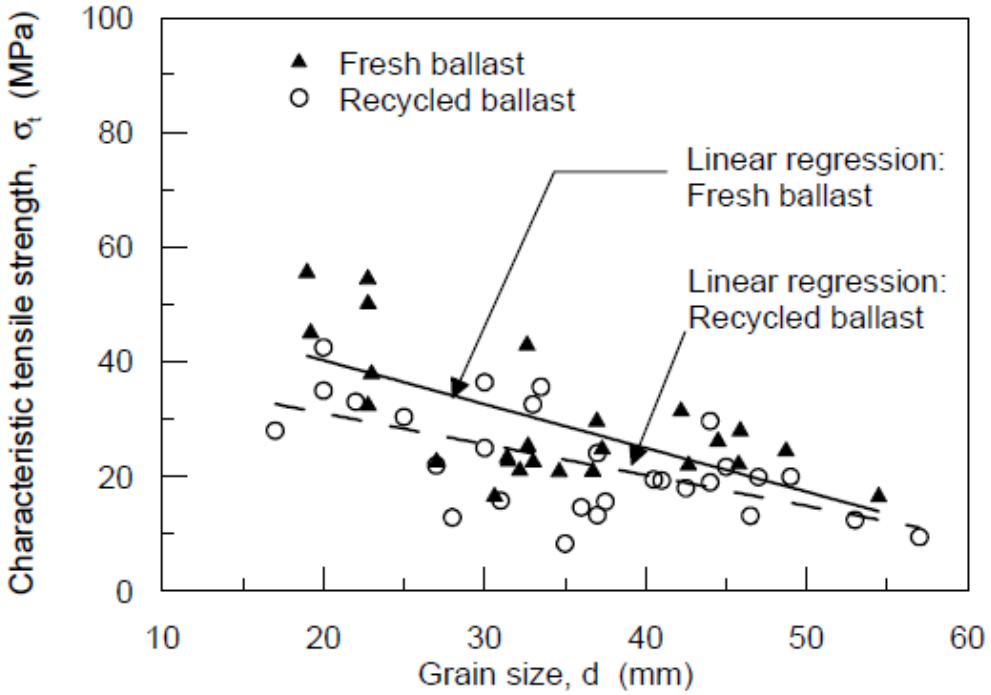

Figure 2.18: Single grain crushing strength of ballast (Indraratna and Salim, 2003)

2.7 Stresses during train loading

The vertical and horizontal stresses experienced by the sub structure components in rail track at different depths below the sleeper have been investigated by Shenton (1975), Stewart et al. (1985), Powrie et al. (2007), and Le Pen (2008) based on field measurements, experimental observations and numerical models (Table 2.5) .

Shenton (1975) reported a maximum sleeper base contact pressure distribution which varied between 200 kPa to 250 kPa under an estimated 200 kN axle load with 50% transfer to a sleeper immediately beneath an axle. The measurements were made using pressure cells mounted along the base of a sleeper. Figure 2.19 shows the uneven distribution of pressure below a sleeper, which results from the discrete nature of ballast. The sleeper base contact pressure below the rail is greatest with the average value for the whole sleeper approximately 100 kPa. The measurements also show that the vertical stresses below the sleeper reduce with increasing depth (Table 2.5).

The lateral confining pressure in rail track ballast is expected to be relatively low. Stewart et al. (1985) carried out a box test to study residual horizontal stresses (horizontal stresses at unloaded state) in the ballast with repeated loading. A cyclic vertical load ranging up to 4000 lbf (~18 kN) was applied through a tie segment (22.86 cm wide and 29.21 cm long). This led to a vertical stress of 270 kPa ($18kN/(9x11.5x0.0254^2)$) on the ballast. They reported that the horizontal stress in the ballast in the loaded and unloaded states (at maximum and minimum loads of cyclic loading respectively) fluctuated between 20 kPa and 60 kPa and eventually reached approximately 30 kPa (Figure 2.20). The measurements shown are from the instrumented side panel of the box at sensor bar 5, which is on the top of the ballast layer compared to the other sensor bars in the side panel.

Powrie et al. (2007) carried out numerical studies using finite element analysis to study the stress changes in the ground below the ballasted railway track. An axle load of 250 kN was considered for the study. The results were reported in terms of normalized lengths and stresses. These values can be expressed in the standard units by multiplying 2.42 m and 426.88 kPa respectively. Figure 2.21 shows the variation of vertical stresses with depth results from the 2D FEA Analysis. It shows a vertical stress of about 65 kPa at the depth < 2.42 m from the sleeper soffit.

For the 3D analysis the length of mesh in the longitudinal direction (x) was taken as that of an MBA box wagon. The dimensions of the mesh were 60 m x 60 m in the vertical and transverse directions. Figure 2.22 shows the vertical stresses below the sleeper and the influence of the wheel load location based on the 3D FEA. These values do not consider

the effect of heterogeneity (stiffness increasing linearly with depth). The calculated vertical stress at the ballast surface below the centreline of the sleeper was 107 kPa.

Figure 2.23 shows the variation of vertical stress with depth considering effect of heterogeneity. It clearly shows the transition with depth from axle loading (at 314.6 mm) to bogie loading (at 1185.8 mm) to wagon loading (at 4041.4 mm). Figure 2.24 shows the changes in stress components at different depths on central longitudinal plane. The horizontal stress is represented by σ_{xx} in the figure. The K_o values resulted from the reported vertical and horizontal stresses are also included.

Le Pen (2008) studied the impact on confining stress within the ballast of cyclic loading using a full scale testing apparatus consisting of a G44 sleeper overlying a 300 mm depth of ballast within a rigidly confined bay. This apparatus is 5 m long, 0.65 m high and 0.65 m wide. Four pressure plates were placed at the side of the rig (i.e. 325 mm from the sleeper). A cyclic vertical load of 10 kN to 80 kN was applied for 100 cycles. The confining pressure was measured at the minimum and maximum points of each load cycle. Figure 2.25 shows the box plot of all tests where load was centrally applied for the mean measured confining stress across all pressure plates for the initial and final load cycles. At the minimum point of load cycle, confining stress increased from a median of 4.8 kPa to 6.4 kPa. Also at the maximum point of load cycle, confining stress reduces from a median of 13 kPa to 11.7 kPa.

<table>
<tr><th>Source</th><th>Axle load</th><th>Note</th><th>σ_v'</th><th>σ_h'</th></tr>
<tr><td>Shenton (1975)</td><td>200 kN</td><td>Field measurement

Boundary stress were defined by means of pressure cells mounted along the base of a sleeper and cells buried just below the bottom of the ballast layer, these measurements being made for a range of different ballast depths</td><td>50 – 250 kPa at sleeper ballast interface

<table><tr><th>Depth (mm)</th><th>Vertical stress (kPa)</th></tr><tr><td>200</td><td>75</td></tr><tr><td>400</td><td>45</td></tr><tr><td>600</td><td>35</td></tr><tr><td>800</td><td>25</td></tr></table></td><td>No information available for horizontal stresses</td></tr>
<tr><td>Stewart (1985)</td><td></td><td>Experimental measurement~ Box test

Max cyclic load of 4000 lb ~ 18 kN was applied, producing a tie contact pressure equivalent to that of a 32 kip ~ 142.34 kN wheel load from a train.</td><td>Average pressure beneath the tie segment was around 270 kPa

(A load was applied through a tie segment 9 in. wide by 11.5 in. long: 18 kN/(9x11.5x0.0254^2) = 269.56 kPa)</td><td>Horizontal stress fluctuate between 20 – 60 kPa

Horizontal stress in the loaded state decreases with increasing number of cycles. On the other hand horizontal stresses in the unloaded state increases with number of cycles and becomes approximates</td></tr>
<tr><td>Powrie et al. (2007)</td><td>25.4 tonnes = 250 kN</td><td>2D model:
On a cross-section of the track using 8-node biquadratic elements with reduced integration

Intermediate mesh used (mesh size 60 m x 60 m, comprised of 1634 elements)

$Length = \frac{x}{S = 2420\,mm}$

$Stress = \frac{x}{\frac{axle\ load}{plan\ areas\ of\ sleeper}}$</td><td>64 kPa at the depth <2.42 m from the sleeper soffit

<table><tr><th>Depth (m)</th><th>Vertical Stress (kPa)</th></tr><tr><td>< 2.42</td><td>64.03</td></tr><tr><td>12.1</td><td>13.66</td></tr><tr><td>24.2</td><td>7.68</td></tr><tr><td>36.3</td><td>4.70</td></tr><tr><td>48.4</td><td>3.42</td></tr><tr><td>60.5</td><td>2.56</td></tr></table></td><td>Horizontal stresses were not predicted from 2D modeling</td></tr>
</table>

<table>
<tr>
<td></td>
<td></td>
<td>3D FEA:
20-noded quadratic brick elements with reduced integration

Dimension of mess 60 m x 60 m in vertical and transverse direction, mess in longitudinal (x) direction was taken as that of an MBA box wagon.</td>
<td>106.72 kPa at ballast surface below the center line of sleeper

<table><tr><td>Depth (mm)</td><td>Vertical stress (kPa)</td></tr><tr><td>Ballast surface</td><td>106.72</td></tr><tr><td>242</td><td>42.70</td></tr><tr><td>726</td><td>21.34</td></tr></table>
The above values related only to the incremental stresses due to the wheel load applied and did not include the in-situ stresses

<table><tr><td>Depth (mm)</td><td>Vertical stress (kPa)</td></tr><tr><td>314.6</td><td>42.70</td></tr><tr><td>1185.8</td><td>25.61</td></tr><tr><td>4041.4</td><td>12.81</td></tr></table>
The above values considered the effect of heterogeneity and Poisson ratio</td>
<td><table><tr><td>Depth (mm)</td><td>Horizontal stress (kPa)</td></tr><tr><td>314.6</td><td>-34.15</td></tr><tr><td>1185.8</td><td>12.81</td></tr><tr><td>4041.4</td><td>4.27</td></tr></table>
The above values considered the effect of heterogeneity and Poisson ratio

<table><tr><td>Depth (mm)</td><td>σ_v (kPa)</td><td>σ_h (kPa)</td><td>σ_v/σ_h</td></tr><tr><td>314.6</td><td>42.7</td><td>-34.15</td><td>-1.25</td></tr><tr><td>1185.8</td><td>25.61</td><td>12.81</td><td>1.99</td></tr><tr><td>4041.4</td><td>12.81</td><td>4.27</td><td>3</td></tr></table></td>
</tr>
<tr>
<td>Le Pen (2008)</td>
<td>150 kN</td>
<td>Normal load at sleeper ballast interface – 80 kN

Experimental:
Cyclic vertical load: 10- 80 kN

Confining pressure was measured at min & max points of each load cycle.</td>
<td>Average pressure beneath the sleeper was around 14 kPa to 112 kPa

(A load was applied through a sleeper 0.285 m wide and 2.5 m long)</td>
<td>Confining stress increases from its initial value at 10 kN of load from a median of 4.8 kPa to 6.4 kPa after 100 cycles

Max confining stress when 80 kN of load is present reduces from a median of 13 kPa to 11.7 kPa after 100 cycles</td>
</tr>
</table>

Table 2.5: Stresses experienced by the sub structure components in rail track

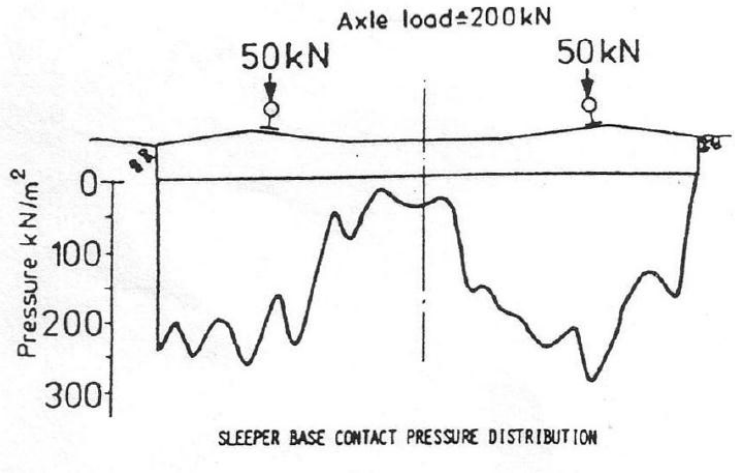

Figure 2.19: Uneven pressure distribution below sleeper (Shenton, 1975)

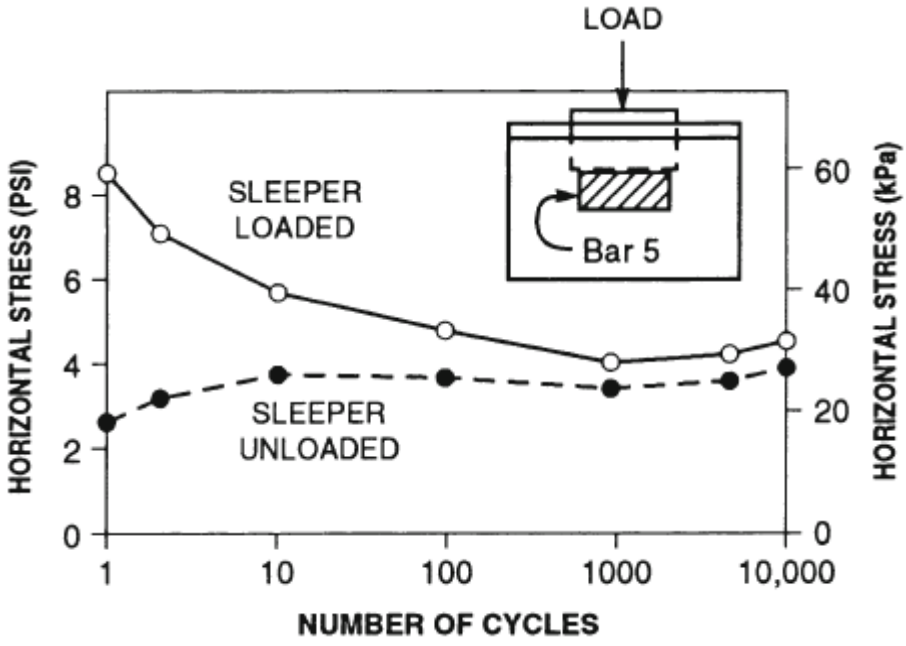

Figure 2.20: Effect of repeated load on horizontal stress in box test (Stewart et al., 1985)

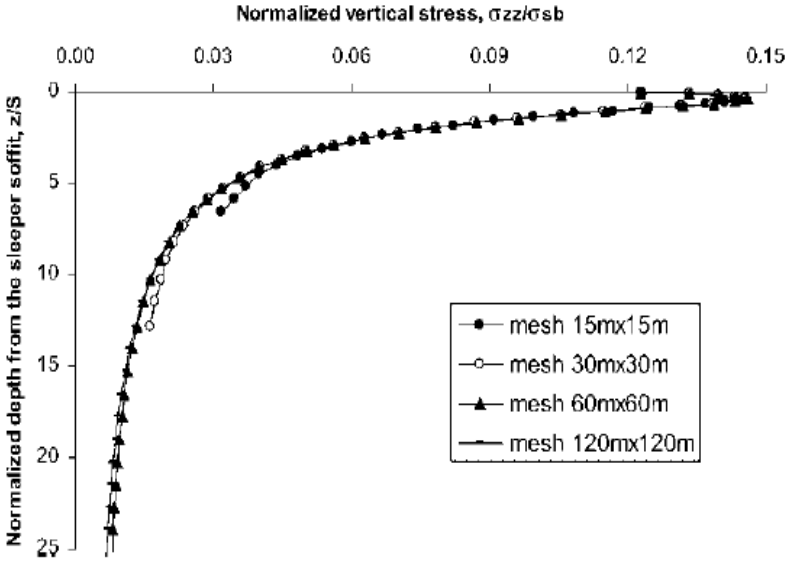

Depth		Vertical stress	
z/S	m	σ_{zz}/σ_{sb}	kPa
< 1	< 2.42	0.15	64.03
5	12.1	0.032	13.66
10	24.2	0.018	7.68
15	36.3	0.011	4.70
20	48.4	0.008	3.42
25	60.5	0.006	2.56

Figure 2.21: Vertical stress with depth on the centre-line for different mesh sizes for Gibson soil (Powrie et al., 2007)

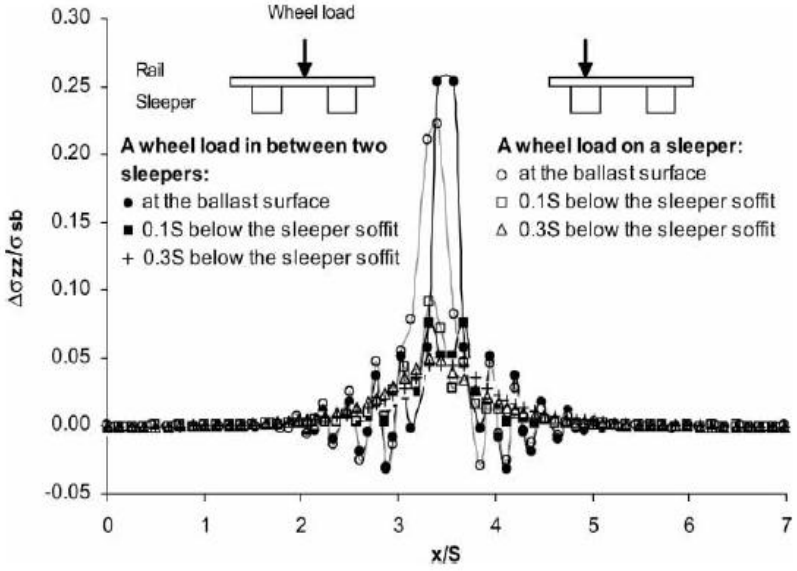

Depth		Vertical stress	
S	mm	σ_{zz}/σ_{sb}	kPa
ballast surface		0.25	106.72
0.1	242	0.10	42.70
0.3	726	0.05	21.34

Figure 2.22: The influence of wheel load location on vertical stress at different depths (incremental stresses due to the wheel loads applied and didn't include the in-situ stresses) (Powrie et al., 2007)

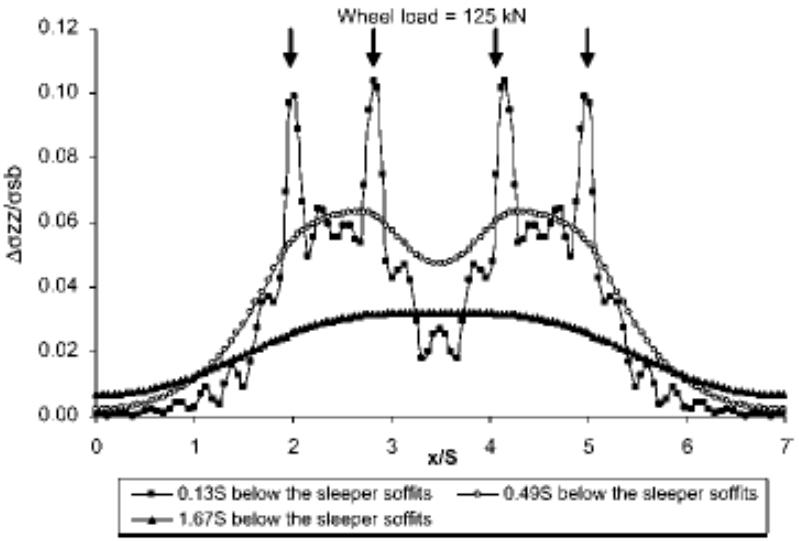

Depth		Vertical stress	
S	mm	$б_{zz}$/ $б_{sb}$	kPa
0.13	314.6	0.10	42.70
0.49	1185.8	0.06	25.61
1.67	4041.4	0.03	12.81

Figure 2.23: Variation in vertical stress increment on the centre plane with longitudinal distance, for different depths (3D FEA, with E=30+10.89 (z/S) and υ=0.49 for the natural ground, without initial stresses)

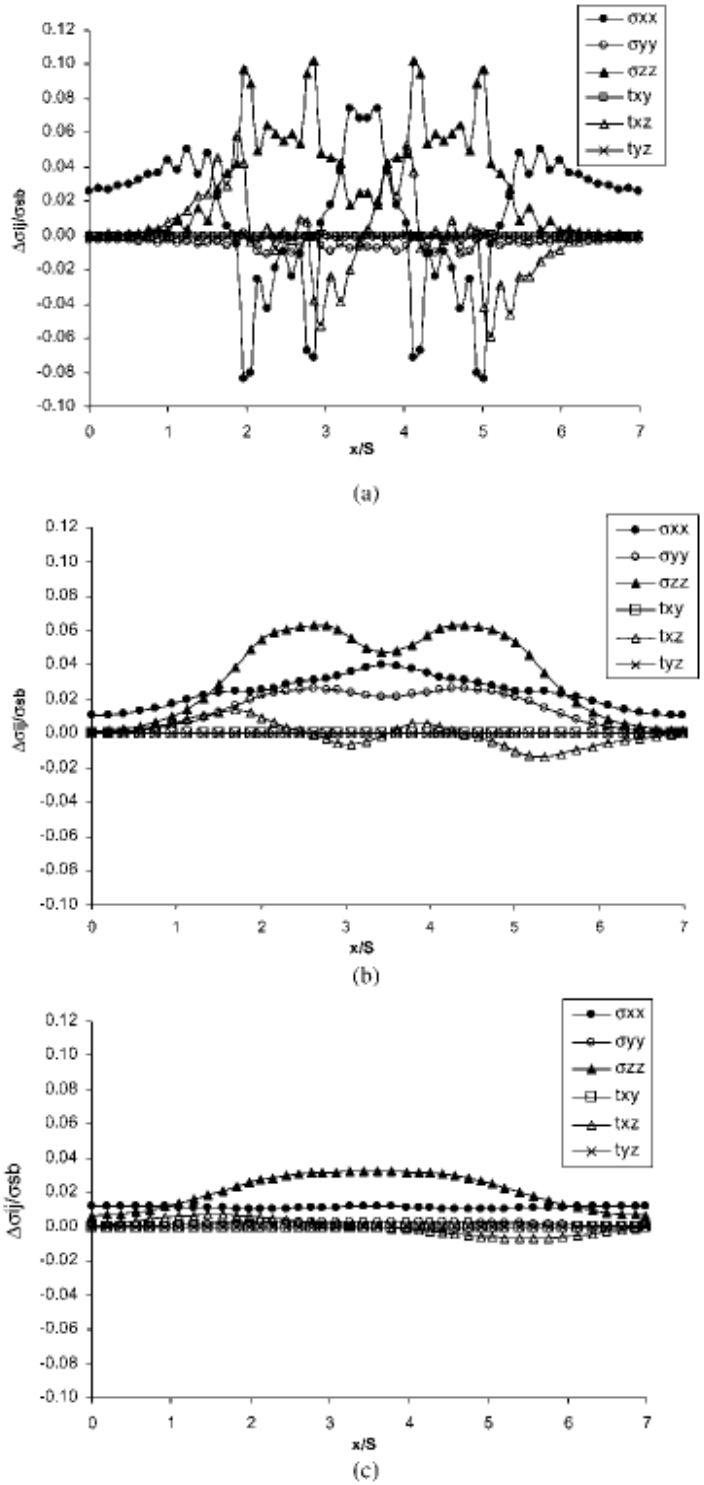

Depth		Horizontal stress	
S	mm	$б_{xx}$	kPa
0.13	314.6	-0.08	-34.15
0.49	1185.8	0.03	12.81
1.67	4041.4	0.01	4.27

depth	$б_v$	$б_h$	$б_v / б_h$
(mm)	(kPa)	(kPa)	
314.6	42.7	-34.15	-1.25
1185.8	25.61	12.81	1.99
4041.4	12.81	4.27	3

Figure 2.24: Variation in components of stress increment on the centre plane with longitudinal distance: (a) at a depth of 0.13S; (b) 0.49S; (c) 1.67S (Powrie et al., 2007)

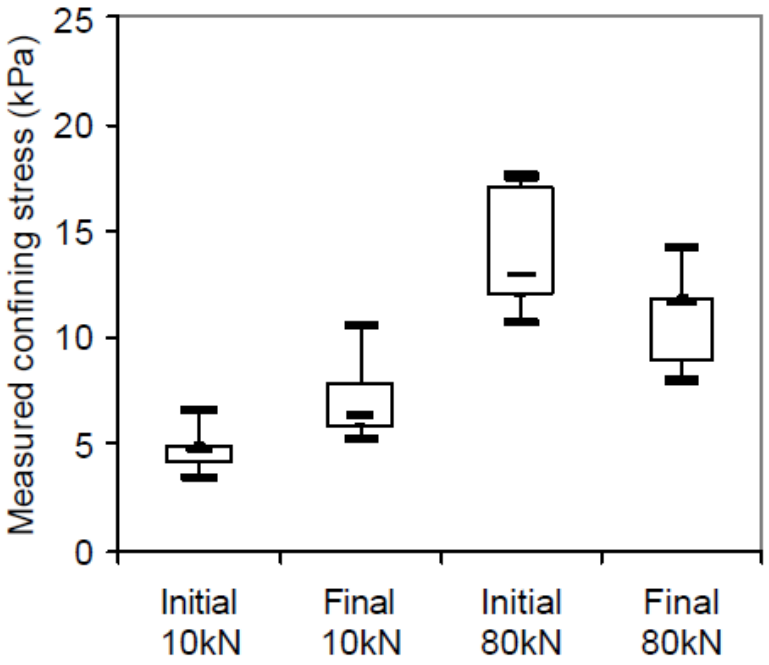

Figure 2.25: Plot of measured confining stress at cycle 1 and cycle 100 for centrally loaded tests (Le Pen, 2008)

2.8 Behaviour of granular material under cyclic loading

Cyclic loading may be used to simulate real rail track conditions during traffic loading and maintenance in a controlled manner in a laboratory. The important issue in cyclic loading is what vertical stress, confining pressure, and loading frequency in the laboratory should be applied to the specimen.

The typical maximum loading frequency of traffic loading on a railway track is 8-10 Hz for a normal train and 30 Hz for a high speed train (assuming an axle spacing of 2.6 m and train speed of 75-94 km/h) (Aursudkij et al., 2009). In the past, researchers have applied very low frequencies for the first few cycles of triaxial cyclic loading experiments. The low frequencies were applied to prevent impact loading, and to allow for larger deformation occurs during the initial cycles. Researchers also tend to select different frequencies for initial loading, as a result of testing facility limitations (Table 2.6).

Source	Commencement Frequency	Frequency loading	Reason
(Shenton, 1975)	0.1 Hz for 8 cycles	0.1 Hz to30 Hz (0.1 Hz, 1 Hz, 10 Hz, 20 Hz, and 30 Hz)	During the first few loading cycles, the permanent deformations were very large and the hydraulic supply was not sufficient to maintain the high frequencies
(Lackenby et al., 2007)	Less than 5 Hz	20 Hz	To prevent impact loading and loss of actuator contact with the specimen
(Anderson and Fair, 2008)	0.16 Hz for first 50 cycles	0.5 Hz	To allow for the larger deformations at the start of the test
(Aursudkij et al., 2009)	5 minutes period for 1-5 cycles 1 minutes period for 6-30 cycles	4 Hz	Deformations during the first few cycles were large. The capacity of the testing machine was not sufficient in terms of the hydraulic oil flow required to give the required deformation rate.

Table 2.6: Frequencies during the cyclic loading of ballast

During cyclic loading, granular materials undergo resilient and permanent deformation as illustrated in Figure 2.26. Resilient and permanent strains are respectively the recoverable and irrecoverable portions of strain during unloading.

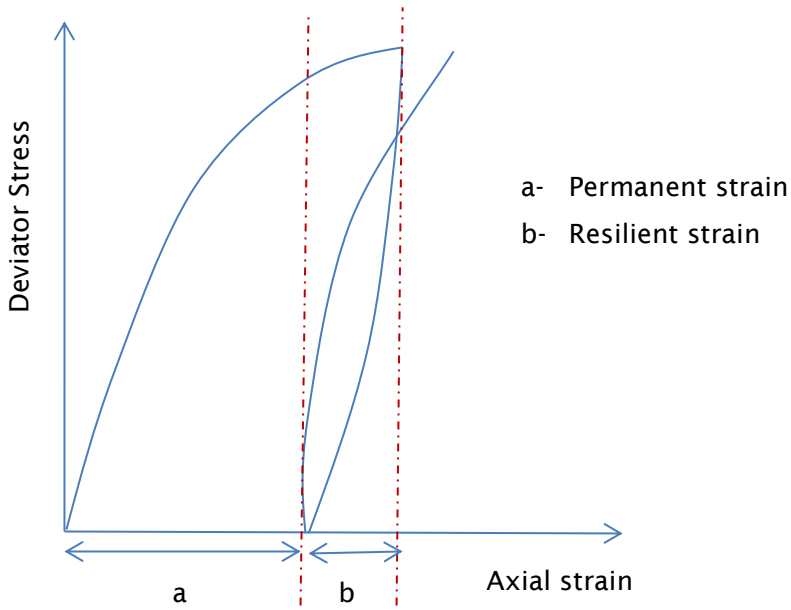

Figure 2.26: Resilient and Permanent strain during cyclic loading

Section 2.8.1 discusses the influence of different factors on the resilient behaviour of granular materials and section 2.8.2 discusses the influence of those same factors on plastic behaviour.

2.8.1 Resilient behaviour of granular material

In the past, researchers have described the resilient behaviour of granular material by means of the Resilient modulus (E_r) and Poisson's ratio (υ) (equations 2.7 and 2.8). The resilient modulus describes the long-term elastic behaviour of materials under repetitive traffic loading. The resilient modulus is defined as the repeated deviator stress change divided by the recoverable (resilient) axial strain during unloading in a triaxial test (Seed et al., 1962).

$$Resilient\ modulus\ (E_r) = \frac{\Delta(q_{max,cyc} - q_{min,cyc})}{\varepsilon_{1,r}} \tag{2.7}$$

$$Resilient\ Poisson's\ ratio\ (\upsilon) = -\frac{\varepsilon_{3,r}}{\varepsilon_{1,r}} \tag{2.8}$$

where; $q_{max,cyc}$, $q_{min,cyc}$ = maximum, and minimum deviator stress

$\varepsilon_{1,r}$= Resilient axial strain

$\varepsilon_{3,r}$= Resilient horizontal strain

The resilient behaviour of ballast is mostly described by resilient modulus (E_r). The material response (strain) to stress for an isotropic elastic material can also be described by the Bulk modulus (K_r) and Shear modulus (G_r). The bulk modulus (K) measures the material's resistance to uniform volumetric compression. It is defined as the pressure increase needed to cause a given relative decrease in volume. The shear modulus (G) is defined as the ratio of shear stress to the shear strain. In literature, less consideration is given to the ballast response to stress in terms of bulk modulus and shear modulus. The bulk modulus and shear modulus can also be used to describe the ballast response to stress during cyclic loading (equation 2.9, 2.10).

$$Bulk\ modulus\ (K_r) = \frac{\Delta\ Average\ effective\ stress\ (p')}{\Delta\ Volumetric\ strain} \tag{2.9}$$

$$Shear\ modulus\ (G_r) = \frac{\Delta\ Deviator\ stress/_2}{\Delta\ Shear\ strain} \tag{2.10}$$

An increasing resilient modulus implies increasing stiffness. The resilient behaviour of ballast contributes to the deflection of track bed during train passage. The resilient behaviour of the subgrade also has a significant impact on the degradation and rate of settlement of track (Raymond and Bathurst, 1987). The resilient behaviour of granular material is affected by many factors (Lekarp et al., 2000a). In the past, researchers have often drawn contradictory conclusions on the nature of the impact of these factors.

2.8.1.1 Aggregate type and shape

Resilient modulus values for aggregates such as limestone, sandstone, granite and rhyolite can differ by 20-50% (Zaman et al., 1994). In the past, many researchers reported that the resilient modulus increases when the particle shape becomes more angular and the texture rougher (Hicks, 1970, Hicks and Monismith, 1971, Allen, 1973, Allen and Thompson, 1974, Thom, 1988, Barksdale and Itani, 1989, Thom and Brown, 1989). Also, increasing surface roughness results in a higher resilient modulus (Hicks, 1970, Hicks and Monismith, 1971, Allen, 1973). Most ballast specifications stipulate crushed rock particles, assuming that freshly exposed surfaces have a higher

roughness (Indraratna and Salim, 2005). However it is not good practice to rely on assumptions. Ballast specifications should be based on quantitative methods for the roughness of the ballast.

2.8.1.2 Aggregate grading, fine content and size

Thom and Brown (1988) conducted cyclic loading triaxial tests on crushed dolomites with different particle size distributions but similar maximum particle sizes. They reported that uniformly graded aggregates showed higher stiffness than well graded aggregates. In contrast other researchers have reported higher stiffness for well graded aggregates (Raymond and Diyaljee, 1979, Van Niekerk et al., 1998). This can be attributed to the higher effective internal friction angle of well graded aggregates. On the other hand, uniformly graded aggregates may have a larger void volume and provide better drainage. As ballast is expected to provide both high stiffness and good drainage, it should have an optimum grading considering both stiffness and drainage potential.

Thom and Brown (1987)reported that resilient modulus increases when the amount of fine increases. Hicks and Monismith (1971)reported reduction in resilient modulus with increasing fine content for partially crushed aggregates, whereas the effect was opposite when the aggregates were fully crushed. Jorenby and Hicks (1986) observed initial increment in resilient modulus followed by reduction as clayey fines were added to a crushed aggregate.

Janardhanam and Desai (1983) carried out cyclic triaxial tests to study the effects of particle size on ballast behaviour. They observed increasing resilient modulus with increasing mean grain size (7, 16 and 30 mm) at all confining pressures (10, 15, 20 and 30 psi). Thom (1988) and Kolisoja (1997) also reported increasing resilient modulus with increasing maximum particle size for aggregates with the same amount of fine and similar shape of particle size distribution.

2.8.1.3 Placement Density

Many researchers indicate that the resilient modulus increases with increasing density (Hicks, 1970, Hicks and Monismith, 1971, Allen and Thompson, 1974, Kolisoja, 1997). In contrast, Thom and Brown (1988) and Brown and Selig (1991) stated that the effect of density is relatively insignificant. In general it is accepted that increases in ballast density enhance the track strength and stability. Thus, a critical stage of ballast life is immediately after track construction or maintenance where the ballast is in its loosest

state (Indraratna et al., 1998). After the track construction and maintenance period, ballast is further compacted and settles down with train loading. Thus in the long term, the resilient modulus does not depend on initial ballast density.

2.8.1.4 Degree of Saturation

Previous studies of granular materials at high degree of saturation have reported a resilient modulus decreasing with increasing saturation (Haynes and Yoder, 1963, Hicks and Monismith, 1971, Barksdale and Itani, 1989, Dawson et al., 1996, Heydinger et al., 1996). Haynes and Yoder (1963) observed a 50% decrease in the resilient modulus in gravel as the degree of saturation increased from 70% to 97%. Hicks and Monismith (1971) and Dawson et al. (1996) reported that the resilient modulus decreases steadily as the degree of saturation increases above its optimum value. It can be argued that saturated materials develop excess pore-water pressures under repeated loading, which reduces the effective stress with a subsequent decrease in both strength and stiffness.

A granular material like ballast with larger voids can dissipate excess pore pressure through drainage unless there is a flooding event. In any case in saturated conditions, the subgrade mix with water to form a slurry and with cyclic loading pumps to the ballast layer (termed as clay pumping) contaminating the ballast layer, and this may stop the drainage. In unsaturated conditions, wetting of ballast contacts may reduce the interparticle friction angle due to some complex mechanisms like surface tension.

2.8.1.5 Effect of stress

Stress has the most significant impact on the resilient properties of granular materials. The resilient modulus increases considerably with increasing confining pressure (Monismith et al., 1967, Uzan, 1985, Lackenby et al., 2007, Anderson and Fair, 2008). Also, the resilient modulus increases with an increasing sum of principal stresses (= $\sigma_1'+\sigma_2'+\sigma_3'$) (Smith and Nair, 1973).

Lackenby et al.(2007) reported that the resilient modulus increases with maximum deviator stress ($q_{max,cyc}$) applied during the cyclic loading. Aursudkij et al.(2009) reported that the final resilient modulus increases with the sum of principal stresses and follows the k-θ model ($M_r = k_1\theta^{k2}$ where θ is the sum of principal stresses and k_1 and k_2 are empirical constants). The resilient Poisson's ratio increases with increasing deviator stress and decreasing confining pressure (Hicks, 1970, Brown and Hyde, 1975, Kolisoja, 1997). Brown and Hyde (1975) reported that similar values of both

resilient modulus and plastic strain were found from cycling of the confining pressure and maintaining a constant cell pressure at the mean of the cycled confining values. In the past, most tests have not cycled the confining pressure which may be closer to what happens in reality.

2.8.1.6 Stress history and number of load cycles

Stress history may have an influence on the resilient behaviour of a material as a consequence of progressive densification, particle rearrangement, and the development and dissipation of excess pore water pressure (Dehlen, 1969). Boyce et al. (1976) carried out cyclic loading triaxial tests on well-graded crushed limestone compacted to the same density and reported that excessive permanent deformation can influence the resilient strain.

Studies have reported that the resilient modulus becomes steady and stable after a small number of load cycles, often less than 1000 cycles (Hicks, 1970, Allen, 1973, Shenton, 1975). Recent studies show different conclusions. Aursudkij et al. (2009) observed that the resilient modulus became approximately constant after 50, 000 load cycles. In contrast, Lackenby et al. (2007) reported that continuing increase in resilient modulus with load cycles, with a little change in resilient modulus beyond 100, 000 cycles (Figure 2.27). Anderson and Fair (2008) carried out cyclic loading of ballast with a deviator stress range from 15 kPa to 250 kPa. They observed an increasing resilient modulus with number of load cycles for all tests up to 100,000 cycles. Also, they carried out 1 million and 1.8 million load repetition tests to study breakage due to cyclic loading. They observed increasing resilient modulus with increasing load cycles up to 100, 000 cycles, and then a drop in resilient modulus above 100,000 cycles.

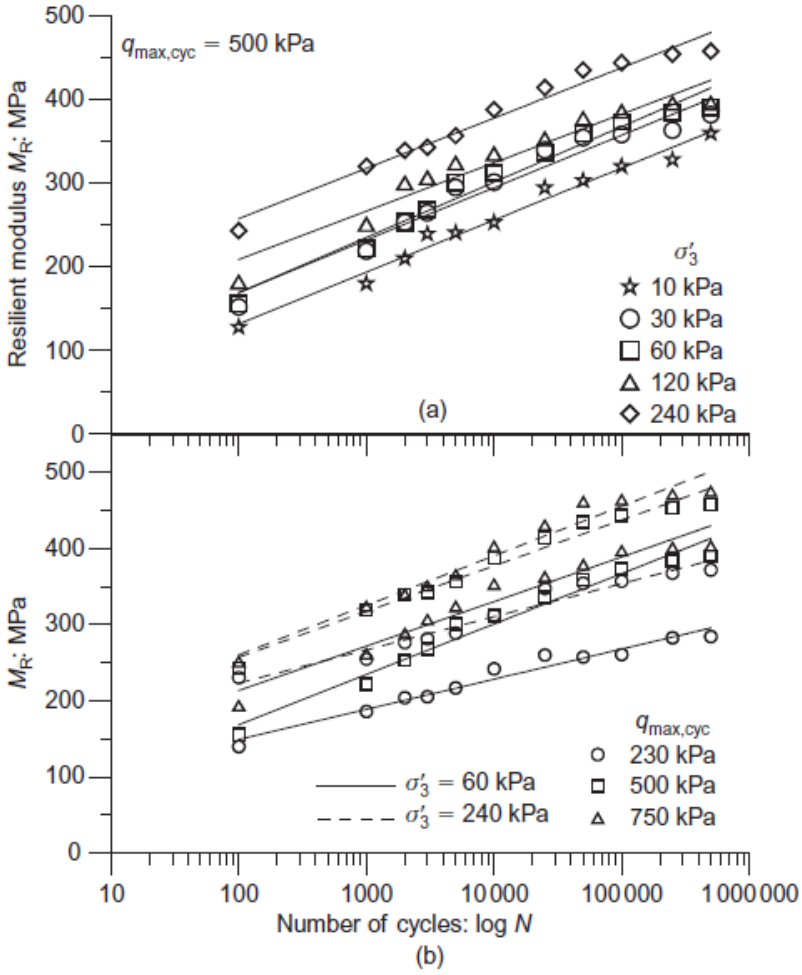

Figure 2.27: Resilient modulus of ballast under various stress states: (a) effect of confining pressure; (b) effect of deviator stress (Lackenby et al., 2007)

2.8.1.7 Effect of load duration and load sequence

Load duration or frequency has little or no significant impact on the resilient behaviour of granular materials provided the rate is such that the response is drained (Seed et al., 1965, Morgan, 1966, Hicks, 1970, Boyce et al., 1976, Thom and Brown, 1987). Seed et al. (1965) reported very small increases of resilient modulus (from 160 MPa to 190 MPa) as the load duration decreased from 20 min to 0.3 s on sand material. Hicks (1970) reported no change in the resilient modulus or Poisson's ratio for load durations of 0.1 s, 0.15 s and 0.25 s. Hicks (1970) and Allen (1973) reported that the stress sequence or order in which the vertical stresses were applied to a specimen had almost no impact on the resilient properties of granular materials.

2.8.2 Permanent deformation of granular material

Permanent strain accumulates due to particle rearrangement and particle breakage. Few studies have been carried out on the plastic response and permanent deformation of granular track materials compared with resilient behaviour, as quantifying the build-up of permanent deformation is very time consuming. However, the literature reveals that permanent deformation of granular material is affected by several other factors in addition to the number of cycles.

2.8.2.1 Aggregate shape, Grading, Fines Content, and Size

Angular aggregates give less permanent settlement than rounded aggregates (Allen, 1973, Jeffs and Marich, 1987, Jeffs, 1989). This may be due to angular materials having higher angles of effective shearing resistance due to better particle interlocking. Raymond and Diyaljee (1979) reported that well graded ballast gave lower settlement than uniform ballast. This can be attributed to the higher effective angle of friction and lower void ratio of well graded ballast compared with uniform ballast. When the amount of fines in granular material increased, permanent deformation increases (Thom and Brown, 1988, Barksdale, 1972). Raymond and Diyaljee (1979) studied ballast sizing. They reported that smaller aggregates showed less deformation under smaller cyclic loads, but when the load amplitude was increased from 140 kPa to 210 kPa, they failed immediately. Larger aggregates resisted cyclic loading without a sign of failure when the load amplitude was increased from 140 kPa to 210 kPa, but had higher deformation at smaller loads. This can be attributed to bedding errors and more void spaces with larger aggregates.

2.8.2.2 Placement Density

Barksdale (1972) reported an average of 185% more permanent axial strain when granular materials were compacted at 95% instead of 100% of relative density. Allen (1973) observed an 80% reduction in total plastic strain in crushed limestone as the specimen density was increased from Proctor to modified Proctor density. Selig and Water (1994) reported that low density ballast leads to high plastic strains. Although track stability can be increased by increasing density by compaction, high compaction can lead to particle breakage (Indraratna and Salim, 2005).

2.8.2.3 Degree of Saturation

Haynes and Yoder (1963) observed more than 100 % increase in total permanent axial strain when the degree of saturation increased from 60% to 80%. Barksdale (1972)

reported that soaked samples showed up to 68% greater permanent axial strain than those tested in an unsaturated condition.

Indraratna et al. (1997) carried out one-dimensional compression to study the effect of sudden wetting on deformation and degradation of ballast. One of the specimens was flooded, after it was kept for up to 24 hours at maximum axial stress of 950 kPa. It settled up to 2.6 mm during the flooding. The wet and dry ballast settled by 10.1 mm and 6.2 mm respectively during the test. Flooding increased the settlement of wet ballast by 40% (2.6/6.2 x100%) of the total settlement of dry ballast. The permanent deformation resistance of granular materials can be improved significantly by providing drainage.

2.8.2.4 Effect of Stress

Stress is one of the important factors influencing the permanent deformation of granular materials. Morgan (1966) carried out repeated loading triaxial tests and reported that permanent axial strain is directly related to deviator stress and inversely related to confining pressure. Lashine et al. (1971) and Brown and Hyde (1975) carried out cyclic triaxial tests on crushed stone and stated that the measured permanent axial strain was directly related to the ratio of deviator stress to confining pressure. In contrast, Knutson (1976) reported that a stress ratio of 60/15 (60 kPa deviator stress to 15 kPa confining pressure) causes larger permanent strain than 20/5 although both correspond to a ratio of 4.

2.8.2.5 Stress History

The current stress state of a material is a result of the loading history. Brown and Hyde (1975) reported that granular material undergoes the largest permanent deformation when the highest stress level is applied immediately. In other words when the stress level is increased gradually, the permanent deformation is considerably smaller.

Diyaljee (1987) conducted cyclic tests to investigate the effects of stress history on ballast behaviour. He carried out experiments on identical ballast specimens with the same grading, density and confinement. The ballast specimens were subjected to single-stage, variable, and progressively increasing loadings.

Figure 2.28(a) shows the results from variable sequence loading. It shows that specimens T3 and T4 in stage 2 loading (140 kPa) deformed similarly to the specimens

T5 and T6 in stage 1 loading (140 kPa), although T3 and T4 were subjected to 50 % of stage 2 loading at stage 1 (70 kPa).

Figure 2.28(b) shows the results from progressively increasing loading, where the specimens were subjected to stresses larger than critical stress of 210 kPa. The specimens T4 and T9 with a maximum loading history of 210 kPa showed less deformation at 245 kPa cyclic stress compared to specimen T13 at the same stress without previous load history. This reduction in deformation is due to internal resistance caused by previous stress application.

Thus he concluded that if the previous stress history was less than 50 % of the currently applied cyclic deviator stress, it will not increase the plastic strain accumulation. On the other hand, if the previous stress history was more than 50 % of currently applied cyclic deviator stress, it will significantly decrease the plastic strain accumulation in ballast.

If a new specimen is used for each cyclic experiment in the laboratory, the effect of stress history on permanent deformation can be eliminated for each stress path applied.

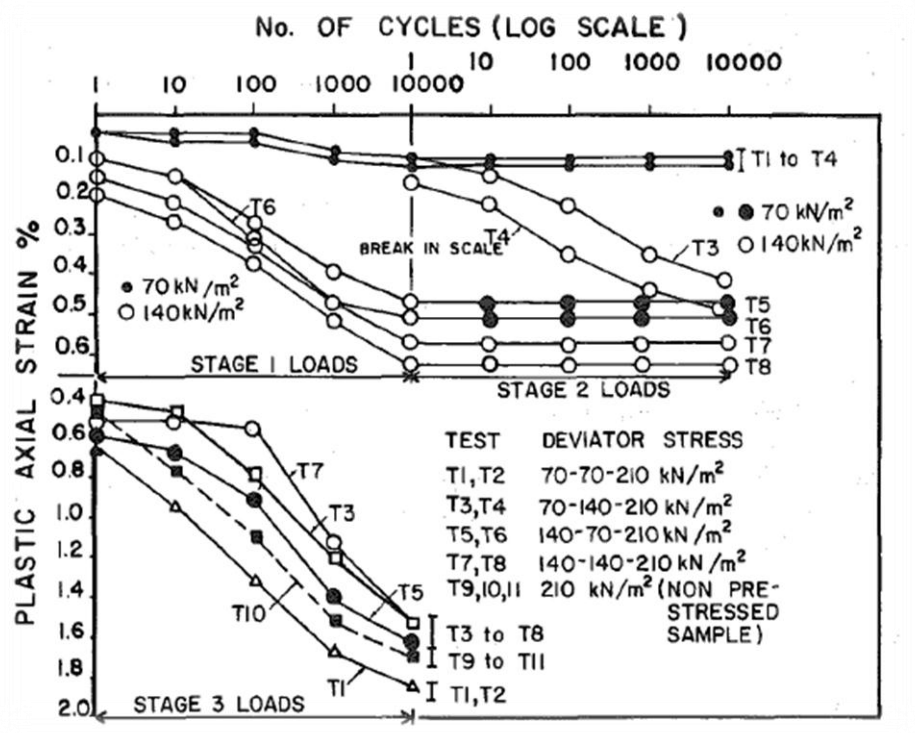

(a)

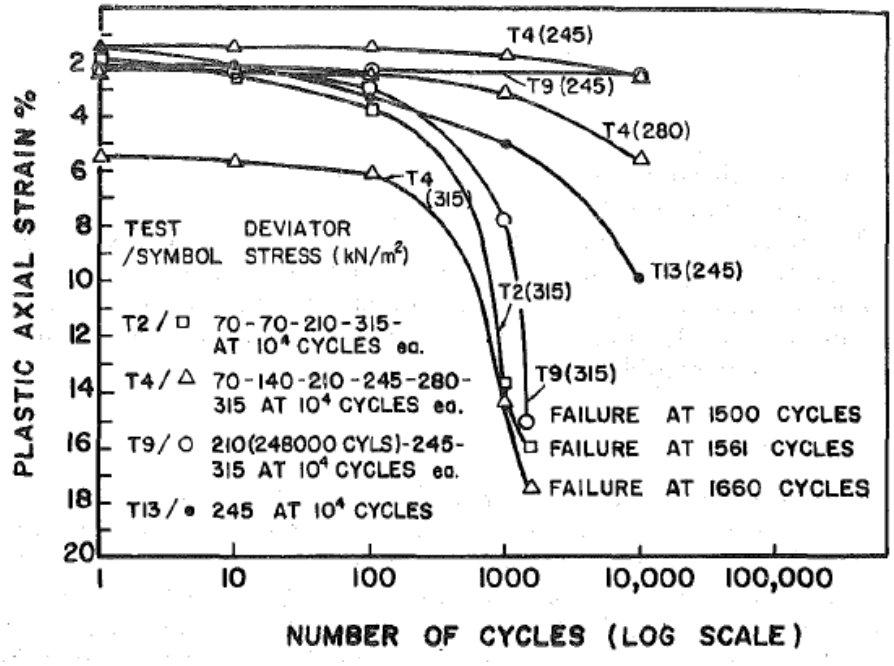

(b)

Figure 2.28: Effect of stress history on permanent deformation (a) Cyclic stress up to 210 kPa (Variable sequence stress differences), (b) Cyclic stress above 210 kPa (Progressively increasing stress differences) (Diyaljee, 1987)

2.8.2.6 Principal Stress Rotation

In-situ granular materials undergo principal stress rotation during vehicular passage. According to the literature review of Lekarp et al. (2000b), the effect of principal stress rotation on permanent strain is not yet clearly understood. It is extremely difficult to reproduce real traffic conditions involving a continuous change of principal stress direction in laboratory experiments. The literature suggests that principal stress rotation results in larger permanent strains than those predicted by controlled laboratory triaxial tests (Lekarp et al., 2000b).

Lim (2004) reported that there is no principal stress rotation for ballast near the sleeper. When the traffic load is transferred through the sleeper onto the ballast, the load is concentrated near the sleeper. The major principal stress directly beneath the sleeper suddenly increases as the wheels approach and rapidly decreases as the wheels move away. However only the deeper ballast or subgrade is expected to experience the principal stress rotation depending on the load spreading capacity or stiffness of the ballast and the lower layers (Lim, 2004).

2.8.3 Shakedown

The permanent axial strain becomes "stable" after a certain number of cycles, a process termed 'shakedown'. In the literature, there are confusions over the limit of shakedown. In general, researchers define shakedown as when there is an insignificant rate of increase of permanent axial strain with number of cycles.

Collins and Boulbibane (2000) reported that pavements which operate at loads less than critical load (or less than failure load) will eventually shake down to a steady state. However there is no consistent definition of this critical load. If the structure's response is purely elastic so that no further permanent strain occurs, it is said to have undergone 'shakedown'. However at higher load levels, permanent cyclic strain is significant leading to structural failure.

Collins and Boulbibane (2000) stated that the structure is assumed to behave like a rate-independent elastic/plastic material in the shakedown theory and this concept is appropriate for unbound or sealed gravel pavements. They classified the response of elastic/plastic structure to cyclic loading into four zones based on load level as shown in Figure 2.29.

In the 'Elastic' zone, the load level is sufficiently small to cause permanent strain from the first load application. All deformation is fully recovered and the response is purely elastic. In the all other zones, the load level exceeds the elastic limit load and permanent strain accumulates. In the 'Elastic Shakedown' zone, after a certain number of cycles the structure's response is elastic, so that no further permanent strain occurs. This means the structure's response changes after certain number of cycles due to the buildup of residual stresses, changing material properties, and changes to the structure geometry. At this stage the structure is said to have shaken down.

In the 'Plastic Shakedown' zone, after a certain number of cycles, permanent strains settle into a closed cycle called cyclic plasticity. In the 'Ratchetting' zone, the load level is very high which causes the permanent strain to go on increasing indefinitely. If cyclic plasticity or ratchetting occurs the structure will fail. The critical load below which the structure shakes down and above which it fails is called the shakedown load. The critical shakedown load is a key design parameter in pavements and is defined by upper and lower bound limits.

The shakedown concept is widely viewed from a pavement perspective, where the plastic strain over many load cycles will eventually cause failure. In pavements the failure occurs in the form of a sub-surface slip, rut formation or surface cracking. The shakedown concept has been applied to railway tracks. In railway, failure is due to non-uniform settlement of sleepers into the ballast, similar to rutting failure in pavements (Fair, 2003).

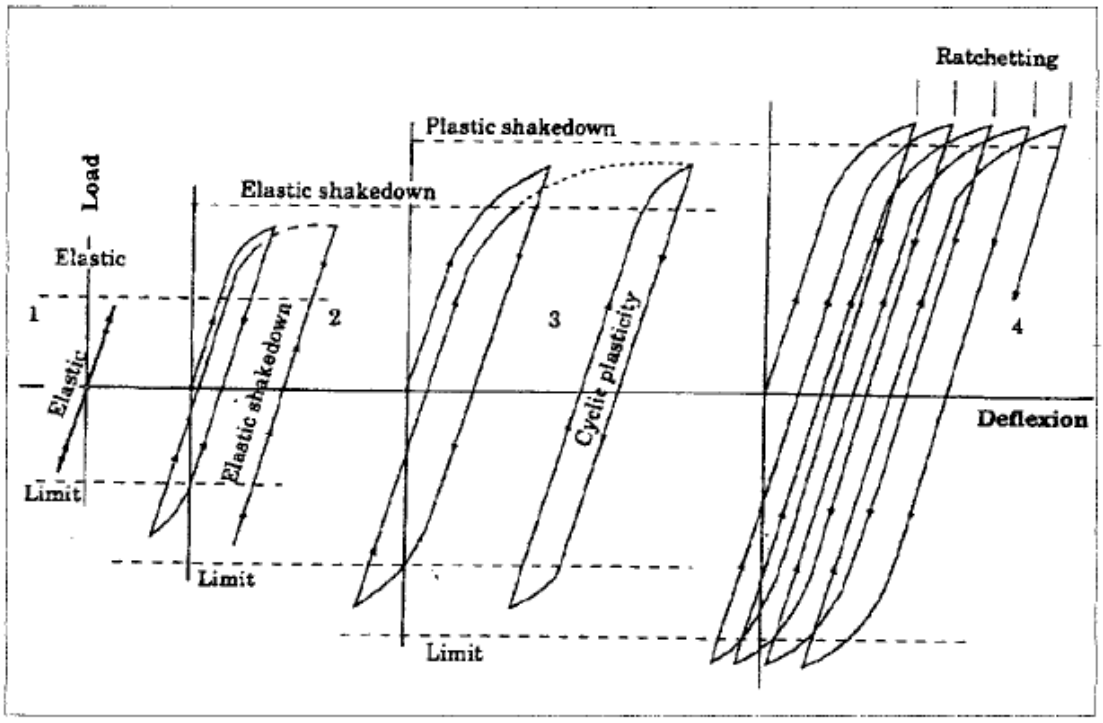

Figure 2.29: Response of elastic/plastic structure to repeated loading cycles(Collins and Boulbibane, 2000)

Suiker (2002) showed the shakedown region in the p′-q plane during cyclic loading (Figure 2.30). The cyclic response of a granular material is substantially elastic in the shakedown region. Suiker (2002) defined the boundary between shakedown and cyclic densification in terms of a ratio n (where n is the ratio of (q/p′) cyclic divided by (q/p′) static max.). Figure 2.31 shows the deviator strain against load cycles for different n ratios, where the solid line represents the total deformation and the dashed line represents the permanent deformation. He reported that at lower cyclic stress levels, n<0.82 permanent deformation rate at 1 million load cycles has become negligibly small. He identified the cyclic response has been almost elastic and called this phenomenon as shakedown.

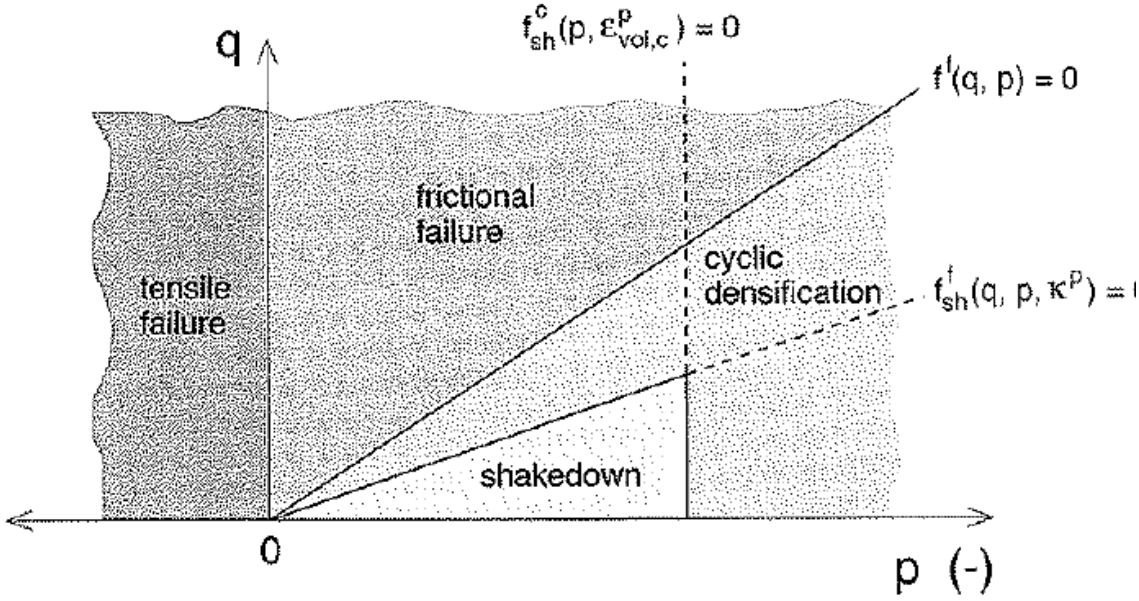

Figure 2.30: Map of various response regimes in p′-q plane during cyclic loading (Suiker, 2002)

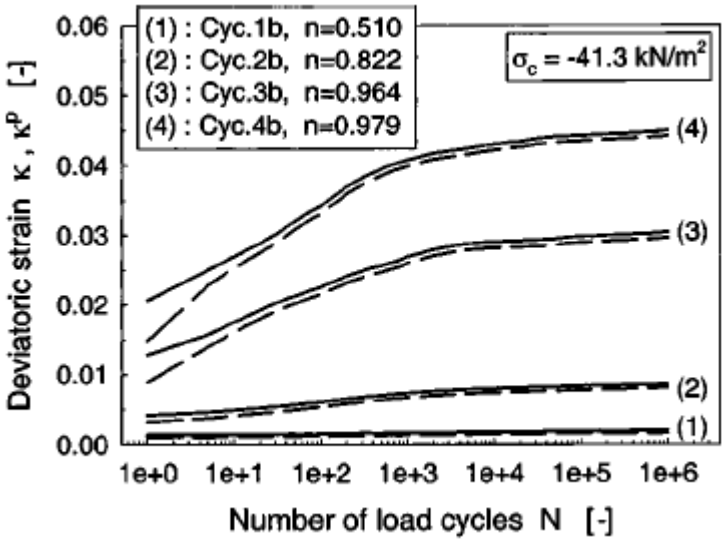

Figure 2.31: Cyclic response of ballast for various stress levels (Suiker, 2002)

Some researchers have observed that the shakedown normally occurs after 10,000 cycles as shown in Figure 2.32 (Lackenby et al., 2007, Aursudkij et al., 2009). In contrast, Anderson and Fair (2008) reported increasing axial strain with number of

cycles over 100,000 cycles. Some researchers reported that a ballast specimen stabilises within about 100,000 load cycles, beyond which the rate of settlement is negligibly small (Jeffs and Marich, 1987, Ionescu et al., 1998, Indraratna and Salim, 2005).

Jeffs and Marich (1987) conducted cyclic load tests on ballast up to 2.5 million cycles. The results showed a rapid increase in initial settlement during the first 100,000 cycles, followed by a region in which the rate of settlement is low (Figure 2.33). Also a sudden increase in settlement rate in the region was observed. This can be attributed to 're-compaction', following failure of particle contact points (Jeffs and Marich, 1987).

Ionescu et al. (1998) reported a rapid increase in initial settlement during the first 20,000 cycles, followed by a stabilisation up to 100,000 load cycles, after which settlement increases in decreasing rate (Figure 2.34).

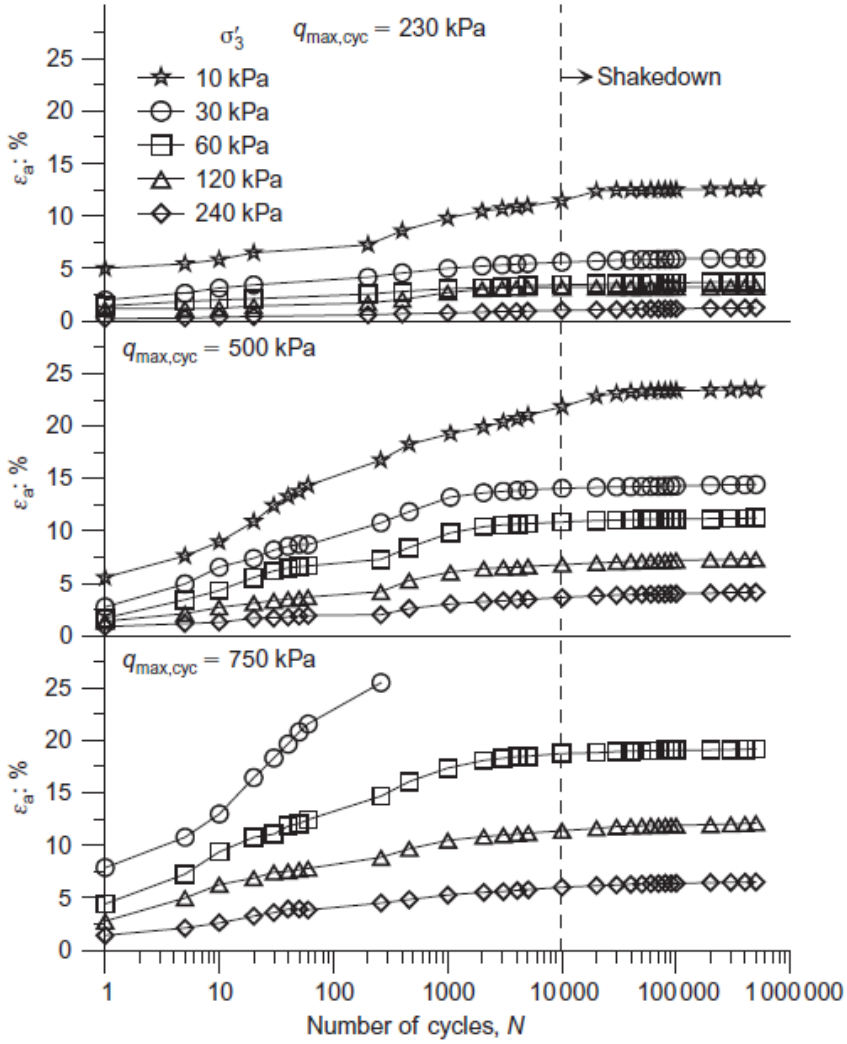

Figure 2.32: Axial strain against logarithmic number of cycles

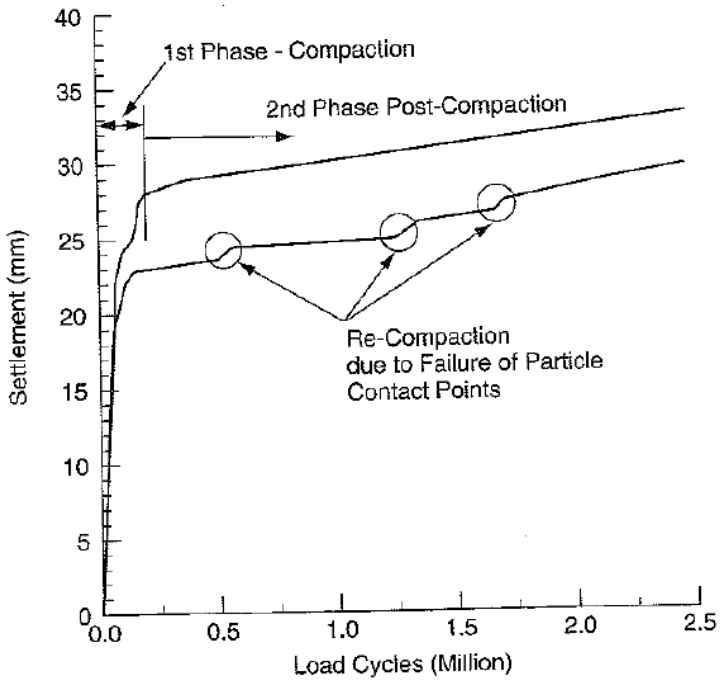

Figure 2.33: Settlement of ballast under cyclic loading (Jeffs and Marich, 1987)

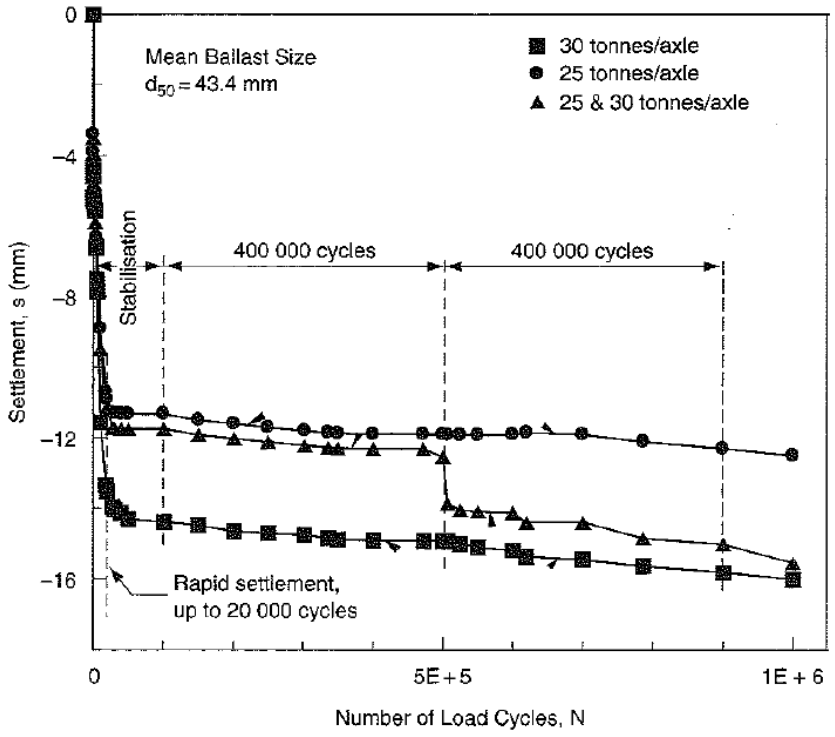

Figure 2.34: Settlement of ballast under cyclic loading (Ionescu et al., 1998)

Raymond and Diyaljee (1979) reported that the plastic strain of ballast may not be linearly related to the logarithm of the number of load cycles for all ballast types, grading and load magnitudes. Diyaljee (1987) reported that plastic strain of ballast may be increased non-linearly with increasing logarithm of load cycles at a higher cyclic deviator stress.

Shenton (1975) reported that track settlement increases linearly with the logarithm of load cycles. Later in 1984, he examined track settlement data from different parts of world. He concluded that a linear relationship of track settlement with logarithm of load cycles is only true over a short period of time as shown in Figure 2.35. It shows the settlement increases very rapidly after 100,000 cycles. This may be due to the attrition and fracture of ballast particles with repeated loading. A rapid increase in settlement indicates that the ballast is approaching life expiry and needs replacement.

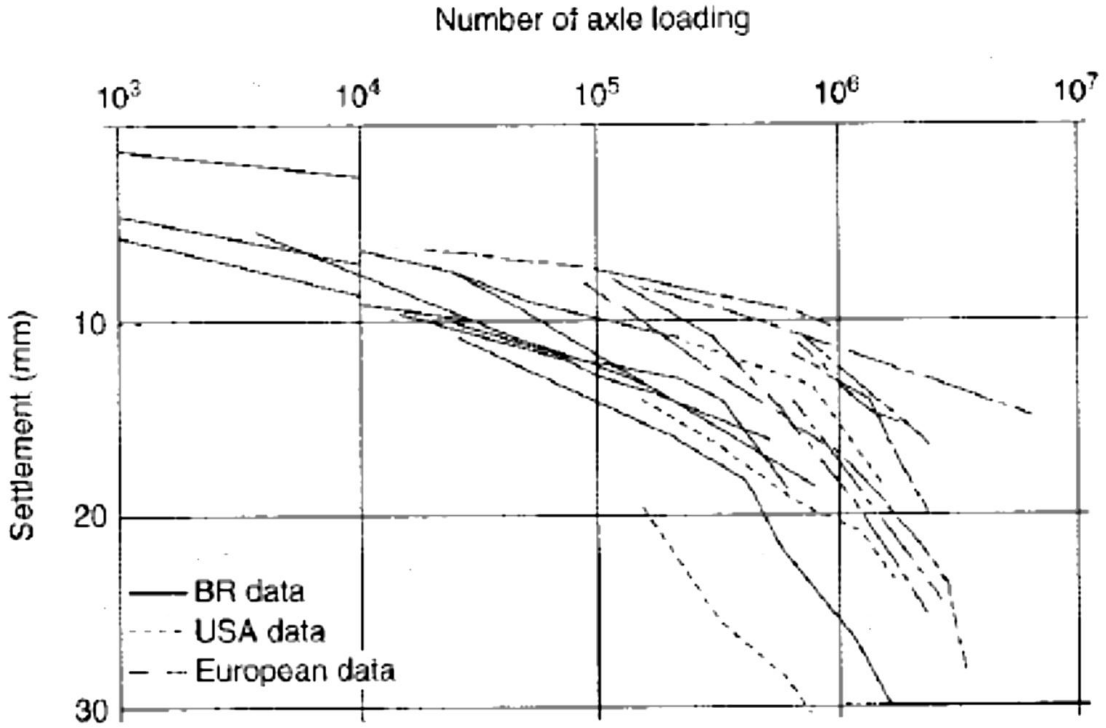

Figure 2.35: Track settlement at different parts of the world (Shenton, 1984)

Katzenbach and Festag (2004) carried out cyclic loading on angular gabbro sand up to 4.4 million cycles. They observed regions in which the plastic strain increments become smaller with increasing number of loading and called it cyclic shakedown

(Figure 2.36). They found specimen would reach cyclic shakedown after a period, but with further cycling the specimen may undergo further plastic strain. They attributed this behaviour to local failure. They could not observe final shakedown, in which no further plastic strain accumulated under continued cyclic loading. This cyclic shakedown region did not appear for the experiments carried out on quartz sand up to 3 million cycles.

Interestingly the test on gabbro sand and the test on ballast carried out by Ionescu et al. (1998) suggests that shakedown can be followed by further plastic strain accumulation. At the same time, failure of ballast is difficult to observe during cyclic loading due to the absence of peak strength or a location of material weakening or clear shakedown limit. The failure of ballast can be defined by arbitrary level of strain accumulation (Indraratna et al., 1998). Thus the experiments are normally carried out up to certain number of cycles or an arbitrary level of strain accumulation.

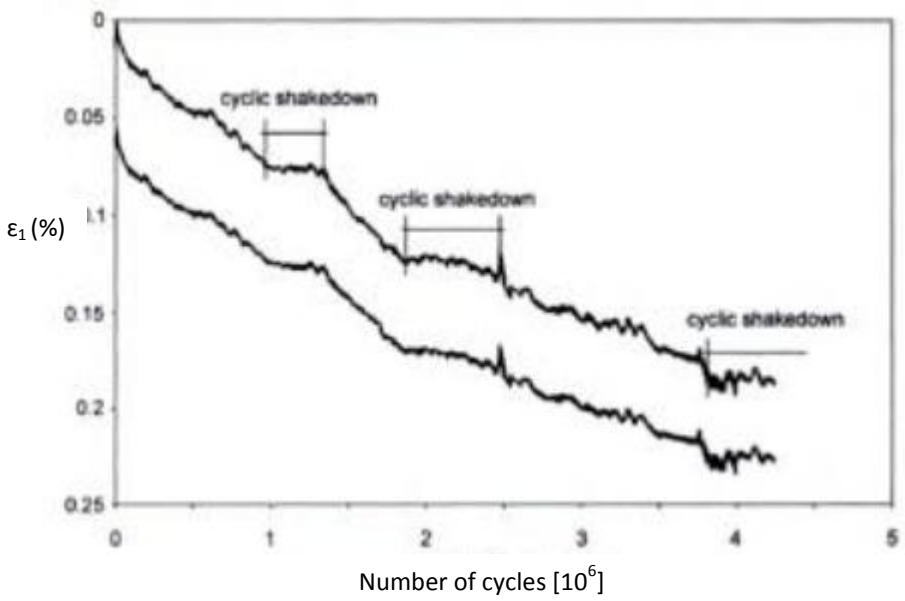

Figure 2.36: Development of vertical strain on Gabbro sand (Katzenbach and Festag (2004))

2.9 Testing on scaled material

Laboratory triaxial testing of larger granular materials like railway ballast or rockfill (rockfill dams) faces difficulties because of their particle size. A representative specimen needs to be accommodated in the apparatus without size effect influencing the results; literature suggests ratio of specimen size to maximum particle dimension of 6 needs to be achieved to obtain reliable results (Marachi,1972).

Two methods have been followed to test the larger granular materials.

i. Testing the material in large scale apparatus
   For example some large scale apparatus were developed to test the railway ballast (e.g.: Indraratna et al,1998; Anderson and Fair,2008; Aursudkij et al,2009), but they are expensive to build
ii. Testing a model material which has similar characteristics as the prototype/ original material which can be accommodated in standard laboratory apparatus

The challenge with a model material is preserving the particle properties such as shape, stiffness and strength with scaling.

Scalping and parallel gradation techniques can be used to create a model material at smaller size. In scalping, the model material is created by removing the particles larger than a certain size from original material. In parallel gradation, model material is created using smaller size particles having a particle size distribution parallel to the original material. For a uniformly graded material like railway ballast, scalping will result in the removal of much of the specimen; thus the parallel gradation technique is more appropriate. The validity of model material relies on whether it behaves in similar way as original material.

Lowe (1964) used the parallel gradation approach to model shell dam material for testing in a triaxial apparatus which accommodates specimens of 6 in (150 mm) in diameter. As the shell dam material composed River Cobble Gravel and Terrace Cobble Gravel, both of these materials were modeled at one-eighth scale having maximum size particles of 1.5 in (38 mm) giving a specimen size to maximum particle size of 4.

He reviewed the behaviour of a pack of spheres under loading to assess the validity of the model material as shown in Figure 2.37. The maximum contact pressure depends only on the pressure applied to the outside faces of the pack and the modulus of elasticity of the material of the spheres. The contact pressure is independent of the size of the spheres. Void ratio effects are primarily functions of particle size distribution and particle shape. Thus the model material of coarse fractions where the

difference between the prototype and model is only the particle size should closely duplicate the contact stresses and void ratio. The model material is expected to behave in a similar way to the prototype material, if the shape and mineralogical composition of both are similar.

Lowe (1964) determined consolidated drained and undrained shear strength of coarse cobble gravel using these one-eighth scaled model materials. He concluded that the tests on model specimens gave valuable information regarding the shear strength of the prototype material.

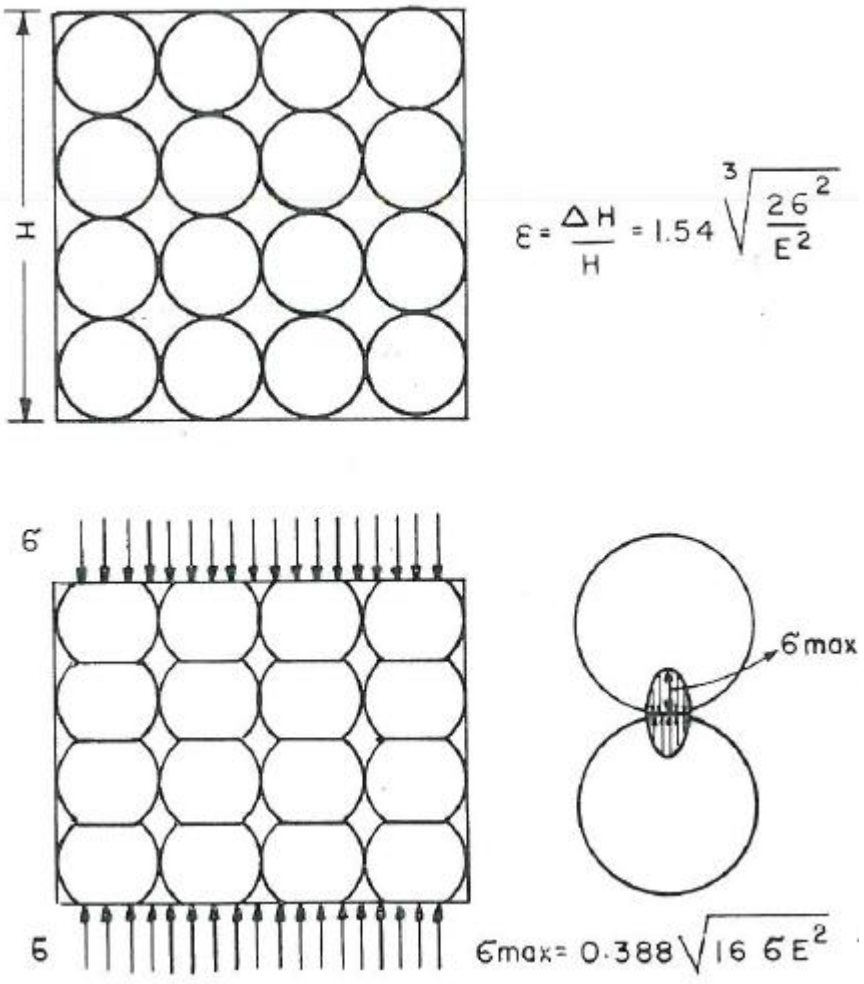

Figure 2.37: Contact pressures for a pack of spheres under compression

Researchers have attributed the theoretical basis of the parallel gradation modeling scheme to the Hertizian theory of elastic deformation relates to the circular contact area of two spheres (Sevi,2009; Marachi,1972).

Contact between two spheres:

For contact between two spheres of radius 'R_1' and 'R_2', the area of contact is a circle of radius 'a'. The applied load is 'L'. The ellipsoidal distribution of pressure in the contact area as a function of distance from the centre of the circle;

$$p(r) = p_o \left(1 - {r^2}/{a^2}\right)^{1/2}$$

The equilibrium load, L

$$L = \int_0^a p_o \sqrt{1 - {r^2}/{a^2}}\ 2\pi r\, dr = {2}/{3}\, p_o \pi a^2$$

The Hertz equation for elastic contact:

Maximum contact stress, p_o

$$p_o = {3L}/{2\pi a} = \left[{6LE^2}/{\pi^3 R^2}\right]^{1/3}$$

Radius of the contact area, a

$$a = {3LR}/{4E}$$

where; $${1}/{R} = {1}/{R_1} + {1}/{R_2}$$

$${1}/{E} = {(1 - {\nu_1}^2)}/{E_1} + {(1 - {\nu_2}^2)}/{E_2}$$

E_1 and E_2 are the modulus of elasticity

ν_1 and ν_2 are the Poisson's ratios associated with each body

For a given externally applied stress, the maximum contact pressure does not depend on the particle size. The average stress the particle carries as seen from the outside,

$s=P/(\pi R^2)$ depends on p_o and some constants but not on R, where P is the externally applied force on the particle and R is the particle radius. Therefore for a given applied stress p_o is independent of particle size.

Hertz's equation assumes both objects are perfectly elastic and no friction between surfaces, which in reality may not be the case.

Marachi et al. (1972) reported that the Hertz equation and its application to particles having perfect geometric similarity shows that the values of contact stresses and strains are independent of particle size. Their review indicated that the coefficient of friction for quartz, which is a highly elastic material, is constant and independent of area and normal load. They concluded that the frictional and deformational characteristic of assemblage of particles should not be size dependent provided that the contacts are not stressed beyond their elastic limit.

Marachi et al. (1972) carried out consolidated drained triaxial compression tests on model rockfill materials. Three test series incorporated experiments on Pyramid dam material (very angular particles), Crushed basalt (angular particles) and Orville dam material (well-rounded to rounded particles). Three gradation model materials were created using the parallel gradation technique with largest grain sizes of 6 in (152 mm), 2 in (51 mm) and 1/2 in (13 mm), accommodated in triaxial specimens having diameters of 36 in (914 mm), 12 in (305 mm) and 2.8 in (71 mm) respectively.

Reducing the particle size of the rock fill materials did not significantly affect the isotropic consolidation characteristics of specimens. Although the axial strain at failure increased with particle size, the trend was not pronounced. Principal stress ratio at failure was greatest for the small specimens and least for the large specimens, somewhere in between for the intermediate size specimens. The difference between the values of principal stress ratios at failure for the large and intermediate size specimens varied. For some of the tests this difference was almost negligible, while for others it was notable. They reported that some of the variations in results could be due to the minor differences in the initial void ratios of the specimens.

The angle of effective shearing resistance was affected to some extend by the particle size. The angle of effective shearing resistance at a given confining pressure was greatest for the small specimens and lowest for the large specimens. The angles of effective shearing resistance of small specimens were 3° to 4° more than the large specimens. This trend was not affected by the confining pressure or the material type.

The volumetric strains during shear were least compressive for the small specimens. The strength and volume change characteristics of the Pyramid dam and Crushed basalt materials were very similar, although these two materials were significantly different in their properties and state of weathering. It can be due to particle shapes were closer, as both materials were angular in shape and had same particle size distribution. They concluded that particle shape has a much greater effect than mineralogy on the volume change characteristics under similar testing conditions. The particle shapes for the three gradations of each rock fill material were not quantified and compared. Thus it is not clear whether the changes in some mechanical properties observed with particle size is due to particle shape or other characteristics related to scale.

They had confidence that the modeling technique seemed to provide a useful method for predicting strength and deformation characteristics of field rockfill materials.

Varadarajan et al. (2003) carried out consolidated triaxial tests on three gradation model materials representative of alluvial (rounded particles) and blasted (angular) rockfill materials obtained from two dams. Both materials showed an increase in deviator stress, axial strain and volumetric strain at failure with increasing particle size. The breakage factor increased with the size of the particles and confining pressure. The angle of shearing resistance increased with the size of the particles for the alluvial material which contained rounded/ subrounded particles, but the opposite trend was observed for the blasted material which contained angular to sub angular particles. The difference was attributed to interlocking and breakage varied between the material due to the variation in particle shape and particle strength. Again, the particle shape between different model gradations with scaling was not examined.

Sevi (2008) carried out monotonic and cyclic experiments on prototype and model materials of Iron Mountain Trap Rock ballast material. Three gradations of railroad ballast were tested, prototype ballast material with a maximum grain size of 2.5 in (63.5 mm) and two model materials with maximum grain size of 1.5 in (38 mm) and 3/4 in (19 mm). All these gradations were tested in triaxial specimens of 16.5 in (419 mm) diameter and 34 in (850 mm) height.

Monotonic testing on parallel gradations of railroad ballast indicated a trend towards higher capacities for the smaller grain size specimens. Specimen gradations 2.5, 1.5 and 3/4 showed average peak load of 16.2 kN, 16.83 kN and 18.55 kN and average deviator stress of 119 kPa, 121 kPa and 134 kPa respectively at 20.7 kPa confining

pressure. The variations of average deviator stress between gradations were not significant.

Cyclic tests were performed on the three railroad ballast gradations at three different stress ratios up to 10,000 cycles. Figure 2.38 shows the plots of permanent axial strain, permanent volumetric strain and resilient modulus for the gradations. Although differences between gradations are observed the variations are not dramatic.

Permanent axial strain increased as the particle size reduced at the two higher cyclic stress ratios. This trend was not evident at the lower stress ratio where permanent axial strain was lower for the smaller gradation.

Although the resilient modulus data are not entirely clear, parallel gradations of larger particles show a higher resilient modulus. This was attributed to the fewer particle contacts of larger particles within the specimen compared to smaller particles. A general trend of lower angle of repose for decreasing particle diameter was observed.

There is no clear trend in permanent volumetric strain data. At the lowest stress level, the smallest gradation exhibited the largest volumetric contraction. At medium stress level, there was no trend regarding the grain size. At the highest stress level, the prototype material contracted and the two model gradation materials dilated throughout the cycles. These different trends challenge the parallel gradation model.

Particle shape analysis indicated that smaller particles exhibit a larger average length to width ratio than larger particles. Lower length to width ratio of larger particles indicated more block particles at the larger grain sizes. Particle corners were observed to be rounder for the larger particles and sharper for the smaller particles.

Sevi (2008) concluded scaled down material did not consistently model the prototype material as assessed by permanent axial strain, permanent volumetric strain and resilient modulus. They attributed the poor modeling to different particle shape between particle sizes as evidenced by particle shape and relative density analysis. Despite the construction of all specimens to same initial density, the relative densities of the different gradations were different (0.66 for 3/4 gradation, 0.31 for 1.5 gradation and 0.09 for 2.5 gradation) as the minimum and maximum densities of different gradations vary between 1442-1554 kg/m3 and 1634-1730 kg/m3. Overall, particle shape may prove to be a prominent indicator of the similarity in behaviour expected between gradations of different sizes within a cyclical loading framework.

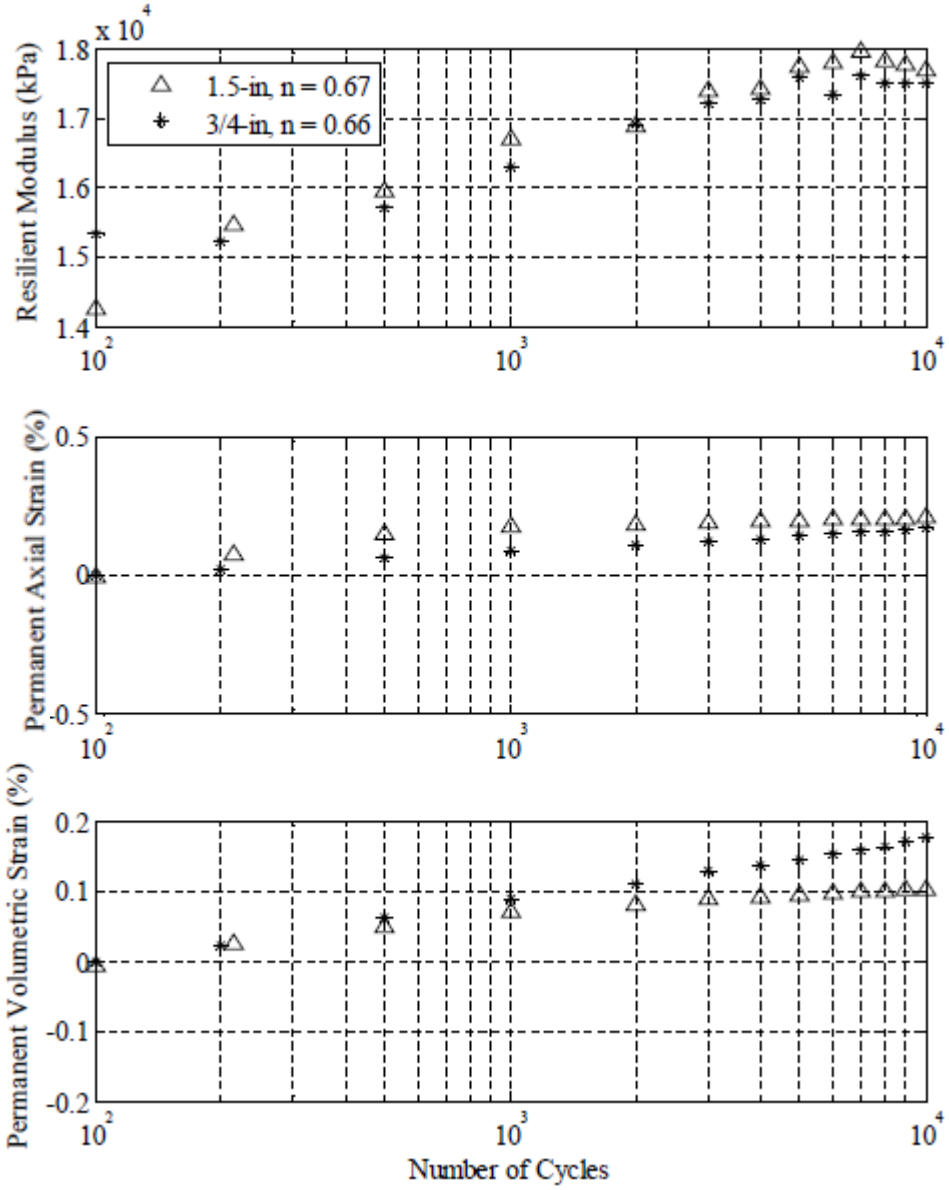

(a) Stress ratio, n=0.67

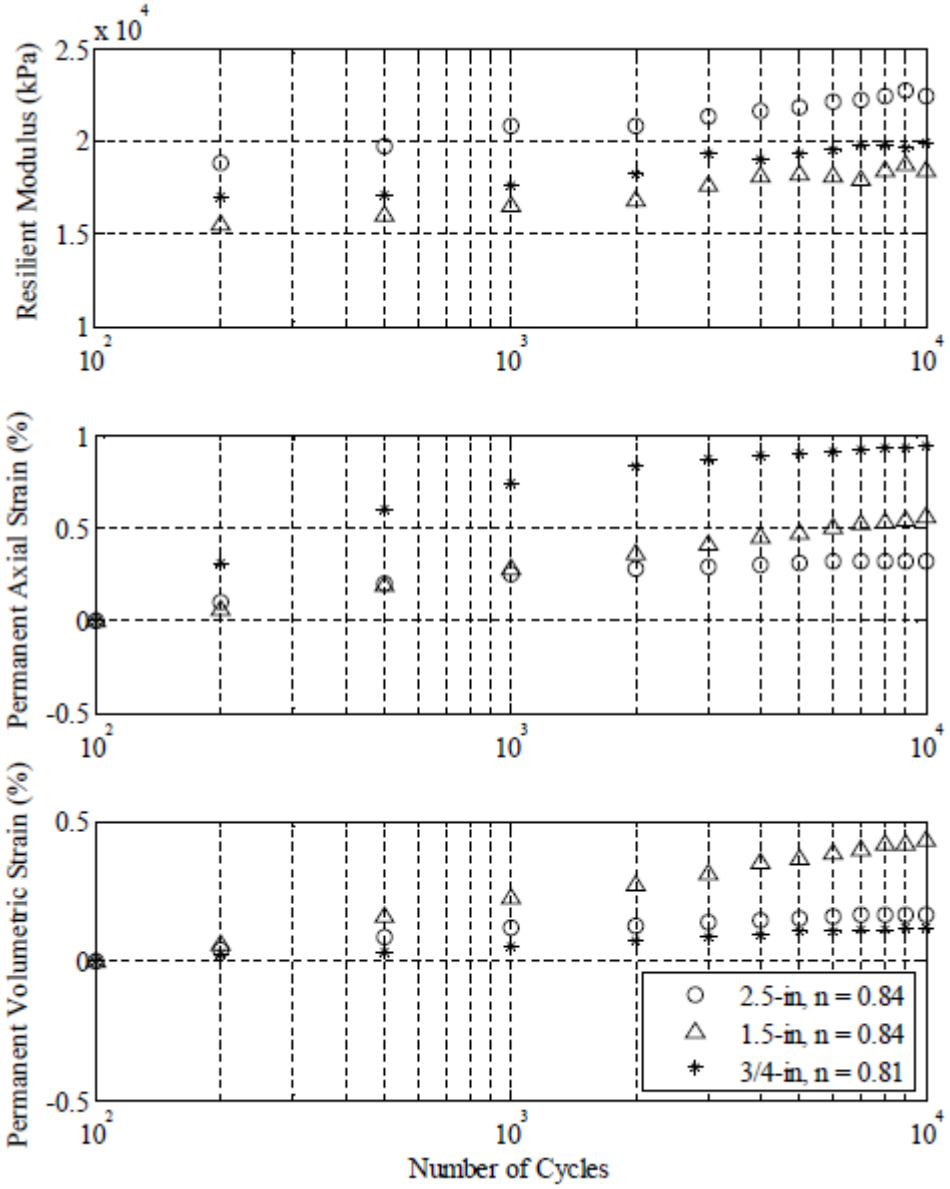

(b) Stress ratio, n=0.84

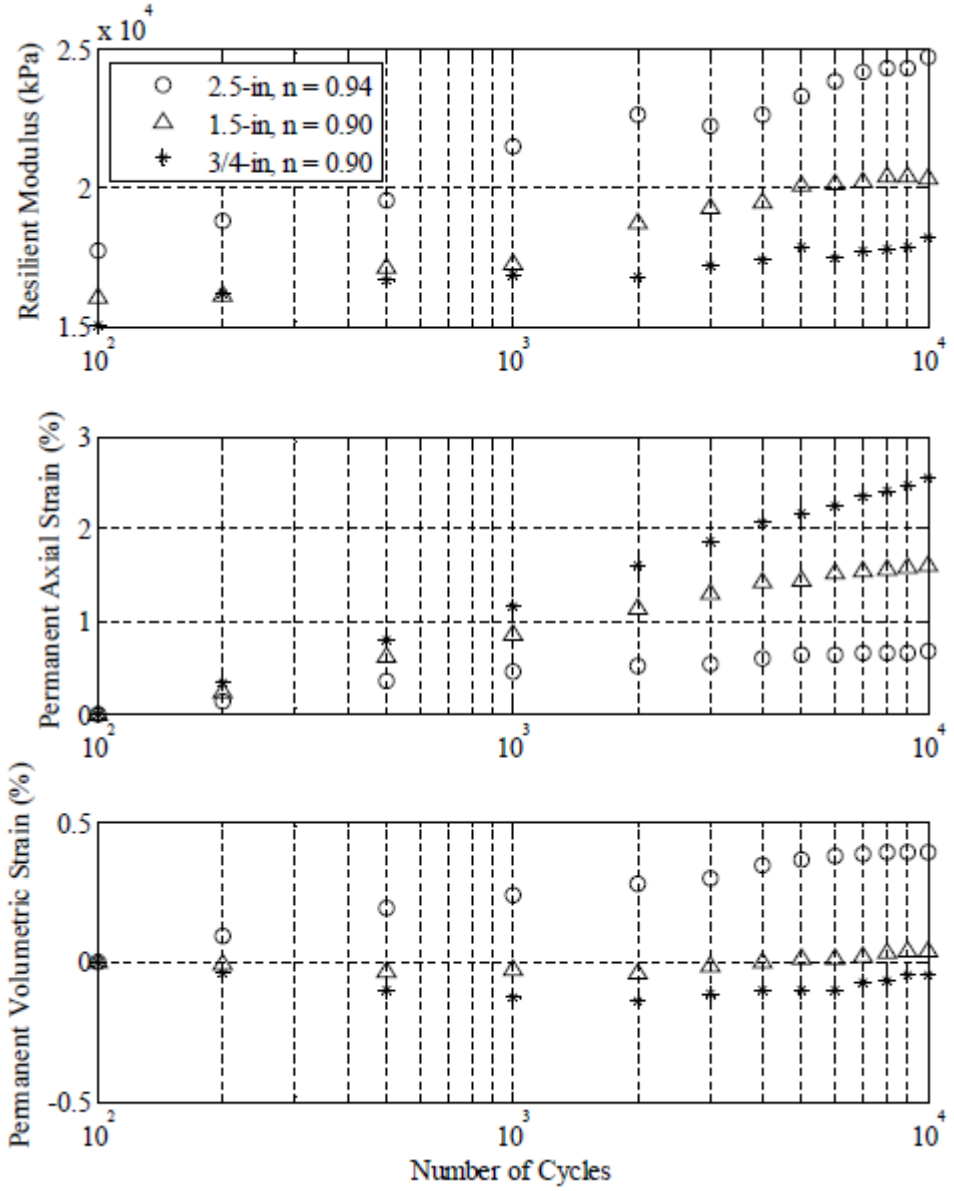

(c) Stress ratio, n=0.90

Figure 2.38: Resilient modulus, permanent axial strain, and permanent volumetric strain comparison between gradations (Sevi, 2008).

2.10 Summary

Ballast is an important component in rail track and the ballast material should comply with rail track specification. SEES is a practicable way to measure form and only requires plan view images of particles. Quantification of other form parameters (Table 2.2) is time consuming as three dimensional measurements are required. Measurements of roundness parameters that require measurements of the curvature of corners described in Table 2.3 are time consuming. Most of the roundness parameters included in Table 2.4 are less time consuming using recent imaging technique developments (for example; image pro plus software). Image pro plus 6.1 (MediaCybernetics, 2006) automatically quantifies the roundness of particles, using the inverse of Cox's roundness ($p^2/4\pi A$) as the roundness measurement.

In the literature, the influence of fabric structure on its mechanical properties has been studied on small granular materials like locked sand. The fabric structure of locked sands is the reason for its high angle of shearing resistance and high rates of dilation compared to dense pluviated sand or ordinary sand. Also, this review identifies the development of fabric structure in larger granular materials like ballast has not been studied in the past. Thus there is a knowledge gap on fabric structure of larger granular materials such as railway ballast.

Strength of granular material is defined by the angle of effective shearing resistance. Failure of ballast cannot be observed visually due to absence of failure plane. The critical strength increases with increasing confining pressure. Static peak strength decreases with increasing confining pressure (Figure 2.12). Higher static peak strength at low confining pressure is potentially due to greater friction and interlocking. Tensile strength of ballast reduces with increasing grain size (Figure 2.18).

The ballast and sub ballast layers experience vertical and horizontal stress increases during train loading. Few works exist regarding the vertical stress at the sleeper ballast interface. Box test results showed that the horizontal stress became stable after certain number of cycles. Le Pen (2008) studied the horizontal stress at minimum and maximum points of each load cycles for 100 cycles. The variation of horizontal stress with load cycles is less studied and understood in literature.

The literature has revealed that the resilient and permanent deformation of ballast can be influenced by many factors. However, researchers have not expressed the same view in the way some of these factors contribute to the resilient and permanent deformation of materials.

There are discrepancies in the way aggregate grading, particle size, placement density, and number of cycles have been perceived to contribute to the resilient deformation of the material. The key discrepancies are as follows.

- *Aggregate grading:* Researchers are varied in their views as to whether well-graded or uniformly graded aggregates contribute to higher stiffness.
- *Particle size:* Researchers are varied in their views as to whether the resilient modulus increases or reduces with increasing particle size.
- *Placement density:* While some researchers concluded that the resilient modulus increases with increasing density, others concluded its effect on resilient modulus was insignificant.
- *Number of cycles:* Researchers have three different views regarding how the number of cycles influences the resilient modulus as follows.
    i. The resilient modulus becomes stable after certain number of cycles. They have not expressed the same view on how many cycles need to reach stabilisation
    ii. The resilient modulus increases with the number of cycles
    iii. The resilient modulus increases up to 100,000 cycles, then reduces

Also there is a contradiction in the way permanent deformation is thought to be influenced by the number of cycles. Researchers were varied in their views on whether the settlement becomes stable after certain number of cycles or increases continuously. These differences may be explained by test being carried out on different types of ballast and also cyclic stress levels differing.

Further research into these factors will improve the understanding of how they influence the resilient and permanent deformation of ballast. The knowledge gained will help to select suitable ballast sources to the track bed construction.

Triaxial testing on larger granular materials have been carried out using either large scale apparatus or scaled down materials. Scalping and parallel gradation techniques can be used to model the material at smaller size. Researchers have carried out experiments on rockfill model material using parallel gradation technique due to its larger particle size. Recently testing on railway ballast model material using parallel gradation technique has been introduced (Sevi, 2008).

3. Characterisation of scaled ballast

3.1 Introduction

In this project, laboratory experiments were carried out using a 1/3 parallel gradation of full size ballast. Characterising both the scaled and full size ballast was carried out to evaluate how similar the scaled particle shapes were to the full size material. Particle shape was quantified using measures of form and roundness (see section 2.4). Roughness was not quantified for the characterisation work but it was expected to be similar. This is because both the scaled and full size ballast are formed by the same production process from the same newly quarried virgin parent rock as follows: larger boulders quarried are sent through a series of crushers (up to 7) rendering the rock progressively smaller. After an appropriate number of crushers depending on the target size, particles are sent to screens. The screens are used to sieve the particles into the desired size range.

It is therefore reasonable to conclude that the full size and scaled ballast particle surfaces are freshly exposed surfaces (have not undergone "polishing") and are expected to have a reasonably homogeneous surface roughness.

The chapter includes sections on;

- Scaled ballast preparation using the parallel gradation method
- Photographing the particles
- Image analysis methods
- Analysis and results of particle characterisation for form and roundness

The chapter section 3.5 was done in close collaboration with Dr. Louis le pen, Sharif Ahmed, Dr. Antonis Zervos and Prof. William Powrie and has formed the basis of a paper submitted to Granular Matter (Appendix A).

3.2 Scaled ballast preparation

Railway ballast particles range between 22.4 mm to 63 mm in size (RT/CE/S/006 Issue 3, 2000). This is too large for most triaxial apparatuses and although tailor made larger apparatus are available (Indraratna et al., 1998, Aursudkij et al., 2009), they are expensive, difficult to operate and the benefits are uncertain. The triaxial apparatus used in this project can accommodate specimens of 150 mm diameter and 300 mm height. This is not large enough to accommodate full size ballast particles but this size of apparatus is much more economical and is more commonly available.

Scaled ballast was mapped to a parallel gradation at 1/3 of the full size ballast. Table 3.1 shows the Network Rail standard for the railway ballast particle size distribution together with the 1/3 scale.

Network Rail standard		1/3 scale
% passing by weight	sieve size(mm)	
100.0	62.5	20.83
85.0	50	16.67
47.5	40	13.33
12.5	31.5	10.50
1.5	22.4	7.47

Table 3.1: Ballast particle size distribution

It is generally accepted that when the sample size ratio approaches 6, the influence of the sample to particle size ratio on results becomes negligible (Marachi et al., 1972, Indraratna et al., 1993). The sample to particle size ratio is defined as the diameter of the triaxial specimen divided by the maximum particle dimension. The scaled ballast particles can be accommodated within the 150 mm diameter triaxial cell without influencing the results as the sample size ratio is more than 6 (150/20.83).

Scaled and full size ballast particles were obtained from Cliffe Hill quarry, Leicestershire, a major supplier to Network Rail organization. To comply with the Network Rail standard ballast particle size specification, these procured aggregate particles were sieved and properly blended.

Dry sieving was carried out to BS 1377-2 (1990) using a mechanical sieve shaker and the ASTM sieves which most closely mapped to the 1/3 scale of full size ballast as shown in Table 3.2. The sieved particles were blended by weight to the 1/3 scale particle size distribution (Figure 3.1).

Sieve size	% passing by weight
22.4	100
16	80
13.2	45
11.2	20
9.5	7

Table 3.2: Scaled ballast particle size distribution

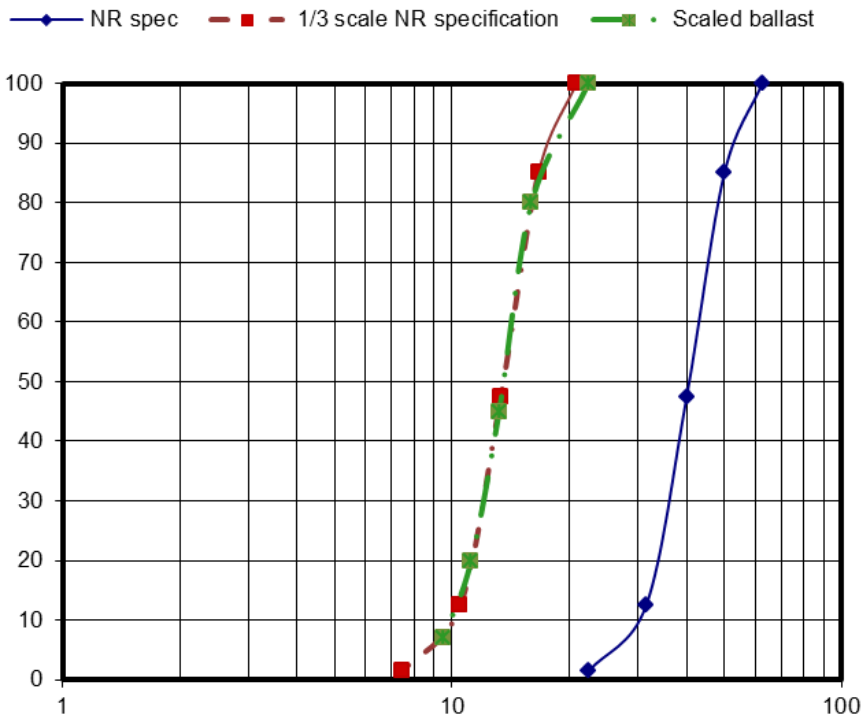

Figure 3.1: Particle size distribution of full size and 1/3 scale ballast particles mapped onto available sieve sizes

3.3 Photographing the particles

Images of ballast particles were captured to characterise the particle shapes. Captured images were processed using image analysis software and analysed for selected measurements to calculate estimates of form and roundness.

A digital camera was held in place on a bench top using a tripod as shown in Figure 3.2. External lighting was used to provide consistent illumination to the ballast particles. The particles were placed on top of a black velvet cloth and the camera was

positioned approximately 1.2 m above the particles with the focal length set to 120 mm.

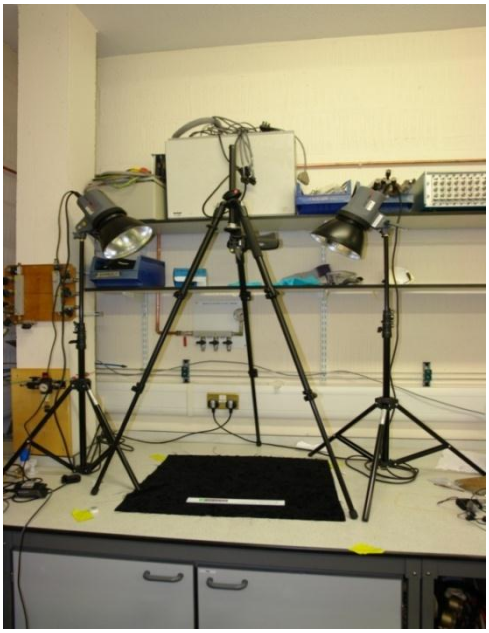

Figure 3.2: Photographic arrangement

A group of particles (15 particles) were randomly taken from each sieve sizes. Each particle was weighed. The particles were laid on their mechanically most stable faces in the plan view presenting longest and intermediate dimensions to the camera as shown in Figure 3.3 and photographed. To capture the images of the side and end elevations, particles were rotated by 90 degrees about the appropriate axes (Figure 3.4). Particles were balanced with their side and end elevations to the camera with the support of Blu-tack.

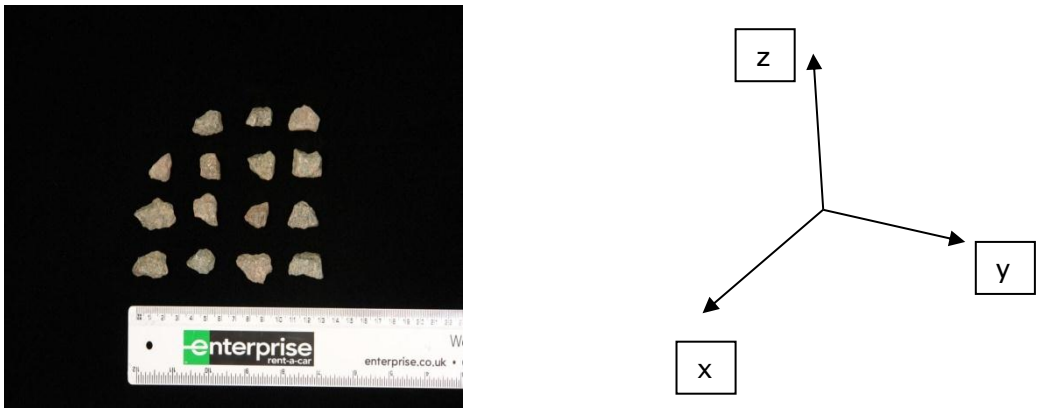

Figure 3.3: Particles are placed on plan view; Z indicate vertical direction, X and Y represent side elevation and end elevation of particles in plan view

Plan view 16mm Elevation side Elevation end

Figure 3.4: Images captured in three orthogonal direction; from the 16mm sieve (15 particles)

The three orthogonal images of each particle were used to evaluate the accuracy of SEES to quantify form. Further particles were photographed in plan view only. Another set of particles from each sieve size was photographed without weight measurement for roundness measurements only.

3.4 Image analysis

Images of ballast particles were processed using Image pro plus (IPP) version 6.1 (MediaCybernetics, 2006), this is a convenient commercial image analysis software, although others are available and software such as Matlab may also be used with bespoke code. Initially the images were segmented to isolate the region of the particle from the background (Figure 3.5). This was done by a consistent method of histogram

based thresholding. Measurements of area, diameter and perimeter to use for quantifying form and roundness were determined as follows:

- The area by a counting the squares method.
- The lengths of the longest (D_{max}) and shortest (D_{min}) diametrical lines are found by joining two points on the particle perimeter and passing through its centroid.
- The perimeter was determined using 8 point connect, i.e. by joining lines through the centroids of the perimeter pixels.

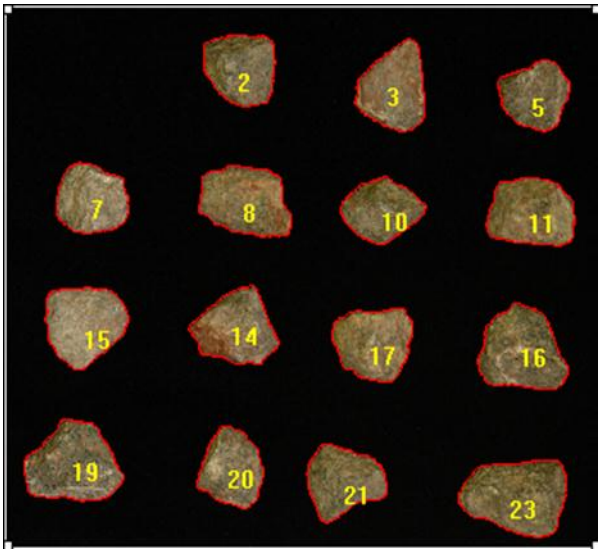

Figure 3.5: Boundary identification, one of the outputs from IPP

3.5 Results of particle characterization

3.5.1 Form

The longest (L), intermediate (I), and smallest (S) dimensions of particles used to determine the parameters of form were measured by two different methods. In the first method, images of particles were taken in three different orthogonal projection planes capturing longest, intermediate and shortest dimensions. In the second method, images of particles were taken in plan view capturing the longest and intermediate dimensions, and S was calculated using the SEES method (Equation 2.3).

The actual S/L ratios determined from the three orthogonal views were compared with SEES values to evaluate the applicability of the SEES approach. Comparison of S/L found using SEES and by taking three orthogonal views are shown in Figure 3.6 and

Figure 3.7. In general, SEES provide comparable values to the actual S/L. Figure 3.8 shows the boxplot of S/L ratio for both scaled and full size ballast. On each box, the central mark is the median, the edges of the box are the 25th and 75th percentiles, the whiskers extend to the most extreme data points not considered outliers, and outliers are plotted individually.

Scaled ballast shows similar median S/L ratios from both methods with an error of 1.8 %. Full size ballast shows slightly different median S/L ratios from both methods, with an error of 5.3 % (Figure 3.8).

Mean S/L ratios determined using both methods for particles retained on each sieve interval are given in Table 3.3. The values obtained from both methods are similar. The SEES approach underestimates S/L compared with the other method by 2% for most particle sizes except 31.5 mm and 40 mm, where errors are -7.7% and -10.2% respectively. Overall, the differences are relatively small.

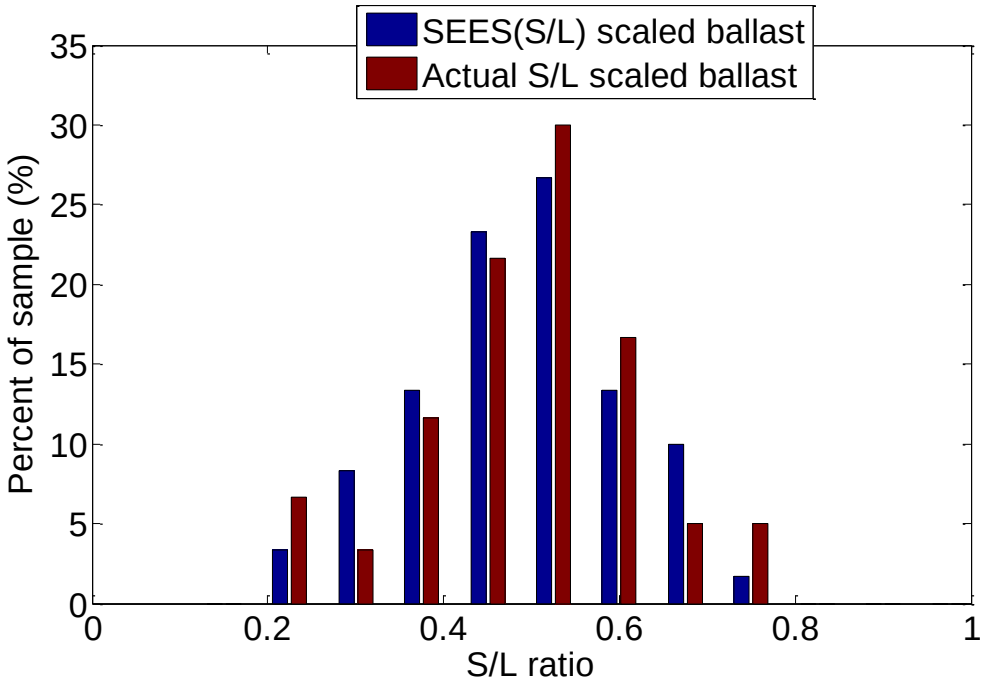

Figure 3.6: SEES and actual S/L values of scaled ballast (60 particles)

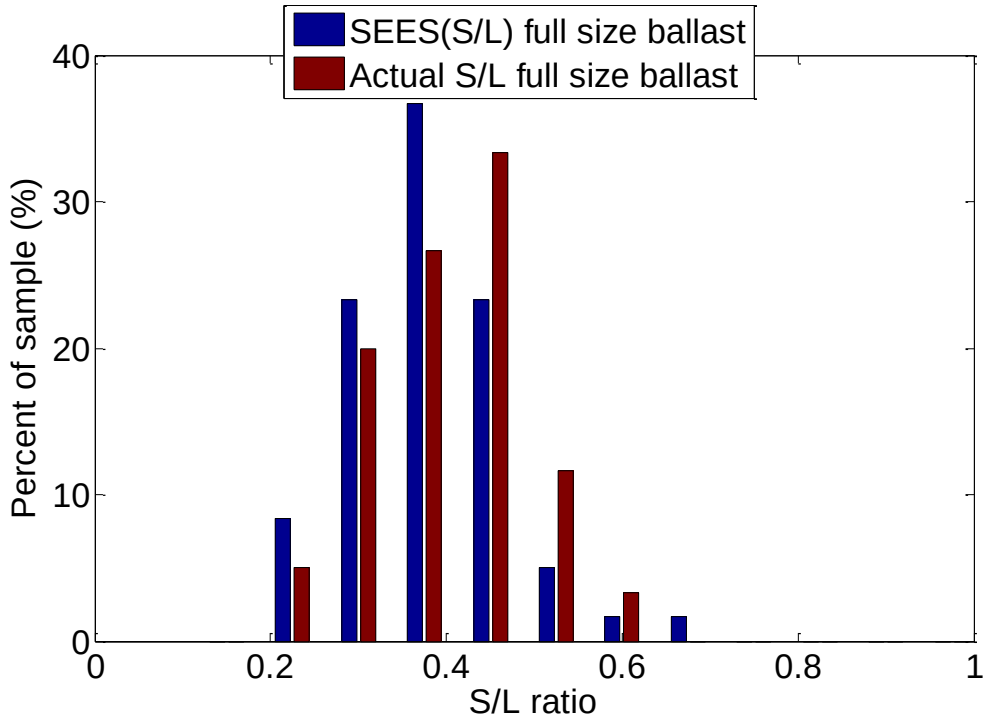

Figure 3.7: SEES and actual S/L values of full size ballast (60 particles)

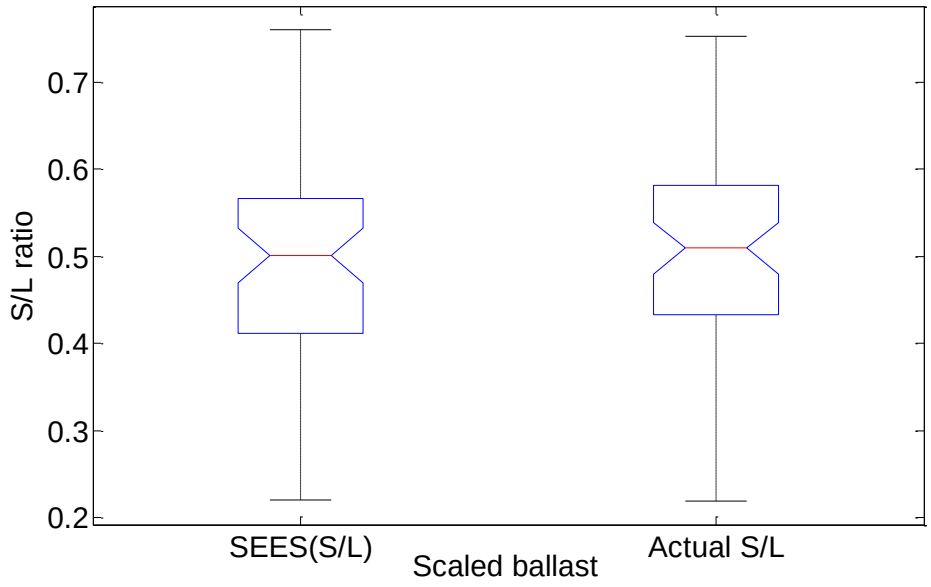

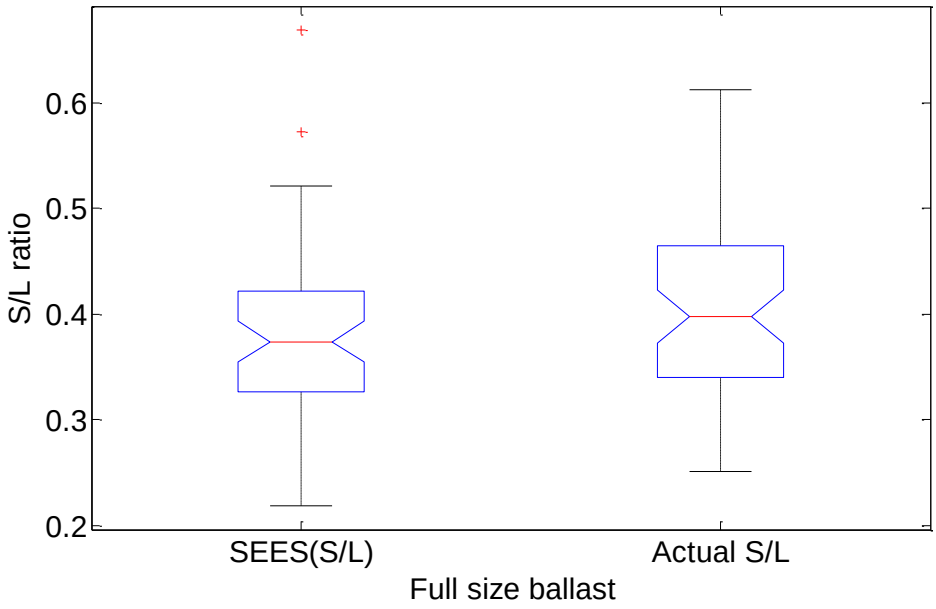

Figure 3.8: Boxplot of S/L ratio

Catching sieve size (mm)	SEES S/L	Actual S/L	Difference
9.5 mm	0.456497	0.466799	-2.2%
11.2 mm	0.439975	0.446969	-1.6%
13.2 mm	0.532818	0.542271	-1.7%
16 mm	0.53264	0.54185	-1.7%
22.4 mm	0.410818	0.417279	-1.5%
31.5 mm	0.364161	0.394332	-7.7%
40 mm	0.355414	0.395671	-10.2%
50 mm	0.389904	0.397703	-2.0%

Table 3.3: Mean S/L ratio of each sieve interval

The S/L ratios for both scaled and full size ballast fall within a positively skewed probability distribution (Figure 3.9 and Figure 3.10). In a positively skewed distribution the right tail is longer and the mass of distribution is concentrated on the left of the figure. Full size ballast shows lower S/L ratios than scaled ballast (Figure 3.10). The cumulative distribution of the S/L ratio shows the relative differences in S/L within the sieve interval (Figure 3.11). Full size particles fall in the left band. Scaled ballast particles fall on the right band except for the 9.5 mm sieve interval curve, which falls

in between the two bands. Although there is no consistent trend of reducing S/L ratio with increasing particle size, there are differences in S/L ratio with particle size.

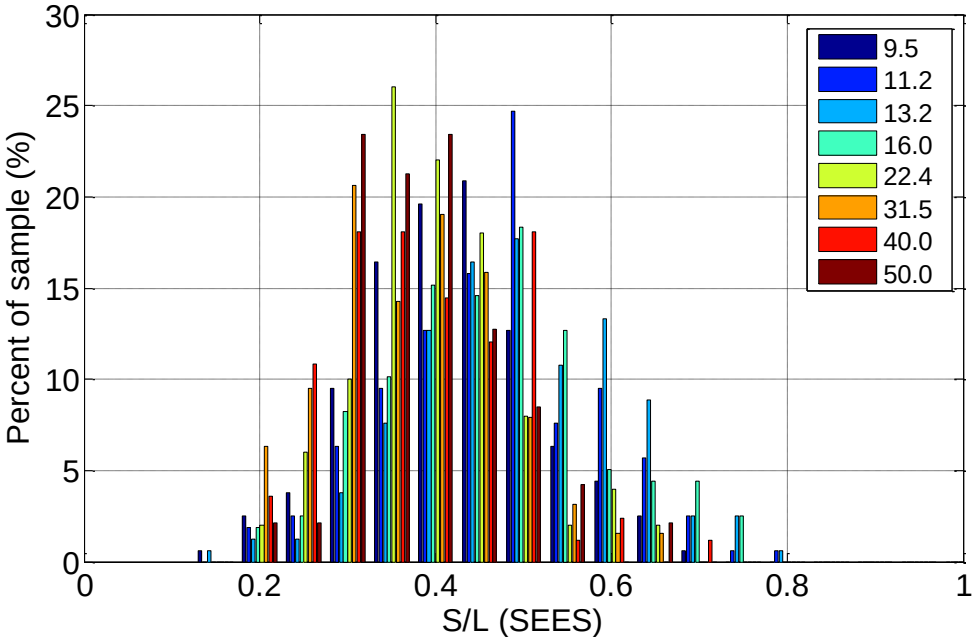

Figure 3.9: SEES values for each catching sieve size of ballast

(158 particles in each sieve intervals of 9.5 mm, 11.2 mm,13.2 mm, and 16.0 mm; 50 particles in 22.4 mm sieve; 63 particles in 31.5 mm sieve; 83 particles in 40 mm sieve; and 47 particles in 50 mm sieve)

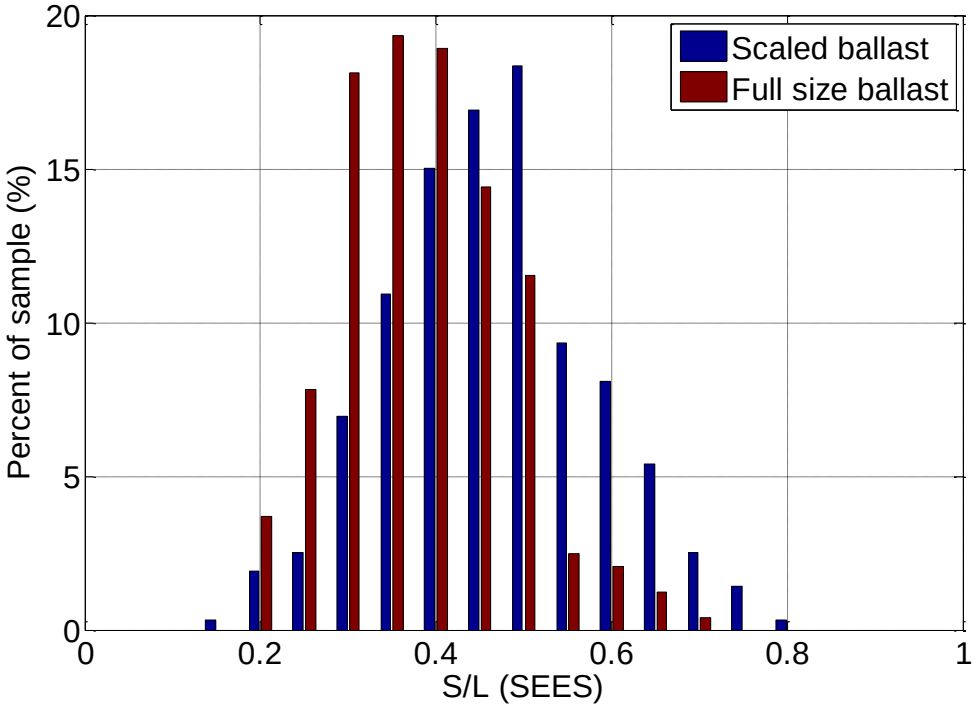

Figure 3.10: Comparison of SEES values of both scaled and full size ballast (632 scaled and 243 full size particles)

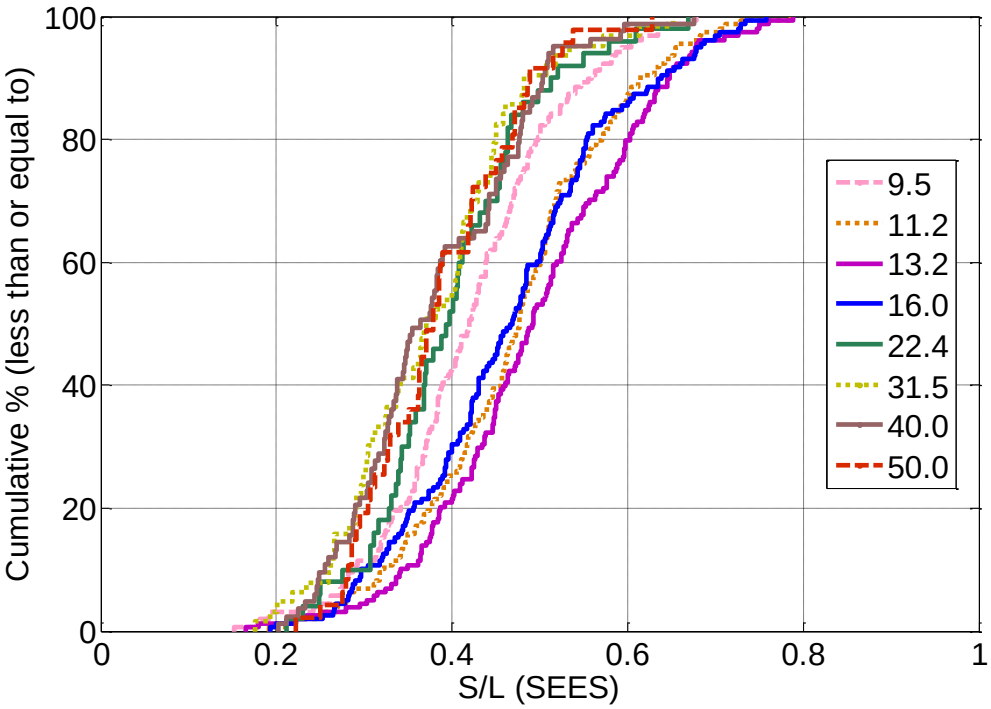

Figure 3.11: Cumulative distribution curves for S/L by catching sieve size

The I/L ratio of each sieve interval are shown in Figure 3.12. Ballast particles fall within a negative skewed probability distribution. Scaled and full size ballast particles are closer in term of their elongation ratio, I/L (Figure 3.13). Figure 3.14 shows the S/I ratio of each sieve interval particles. Full size ballast shows generally lower S/I ratios than scaled ballast (Figure 3.15).

Boxplots of S/L, I/L, and S/I ratios are shown in Figure 3.16. Full size ballast shows lower ratios than scaled ballast, although the ratios are reasonably close. Differences in the median values of S/L, I/L, and S/I between scaled and full size ballast are 18%, 5%, and 13% respectively.

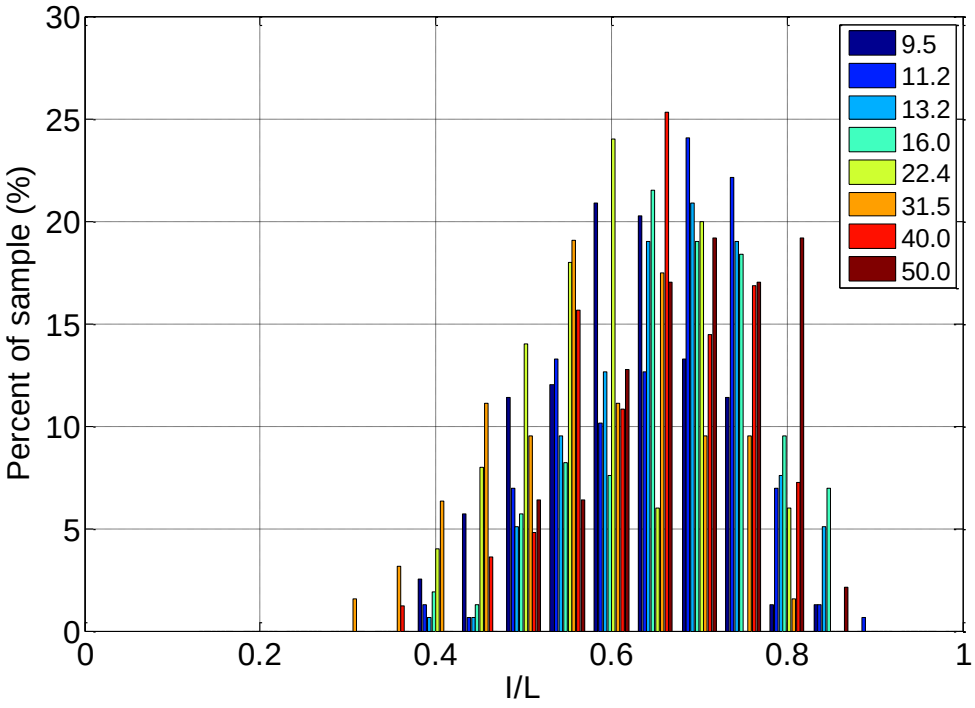

Figure 3.12: I/L values for each catching sieve size of ballast

(158 particles in each sieve intervals of 9.5 mm, 11.2 mm,13.2 mm, and 16.0 mm; 50 particles in 22.4 mm sieve; 63 particles in 31.5 mm sieve; 83 particles in 40 mm sieve; and 47 particles in 50 mm sieve)

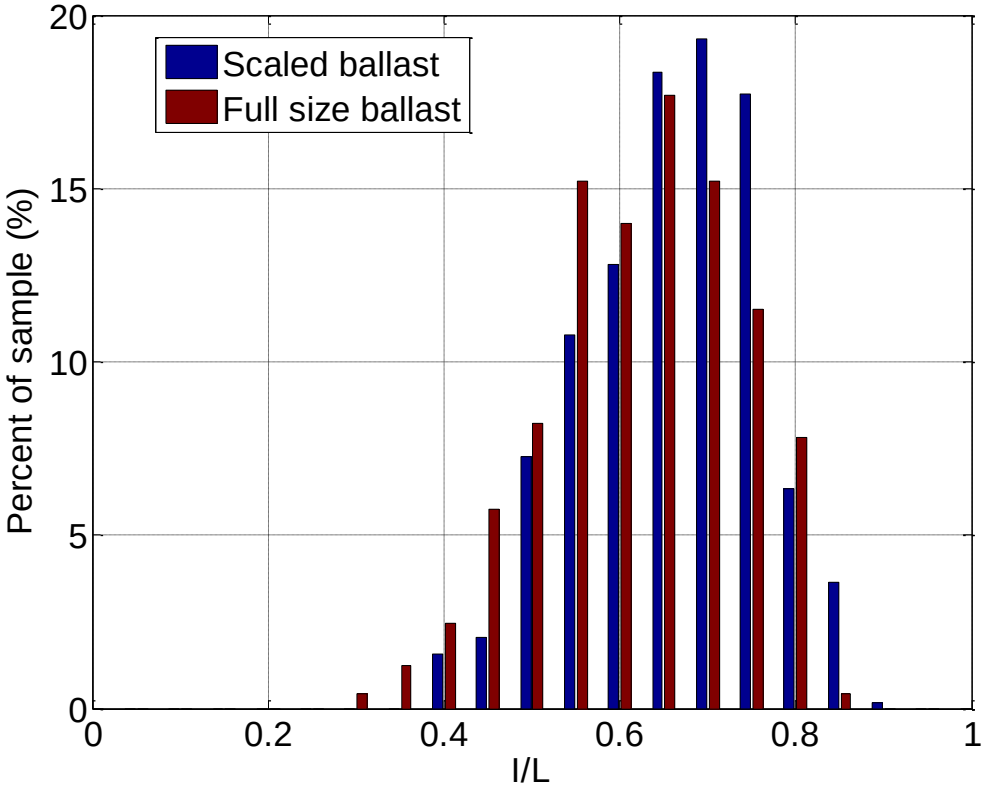

Figure 3.13: Comparison of I/L values of both scaled and full size ballast (632 scaled and 243 full size particles)

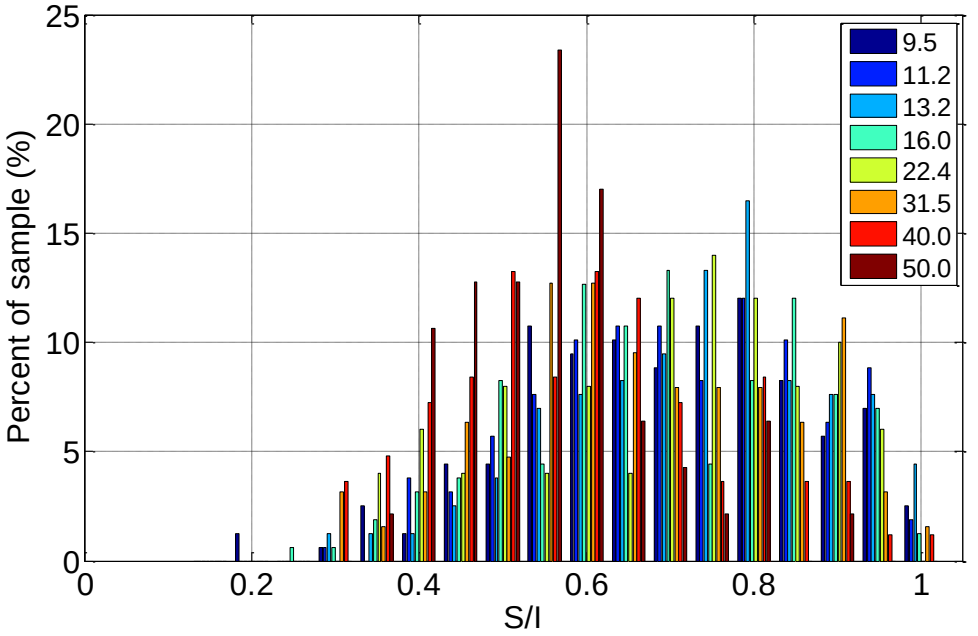

Figure 3.14: S/I values for each catching sieve size of ballast

(158 particles in each sieve intervals of 9.5 mm, 11.2 mm,13.2 mm, and 16.0 mm; 50 particles in 22.4 mm sieve; 63 particles in 31.5 mm sieve; 83 particles in 40 mm sieve; and 47 particles in 50 mm sieve)

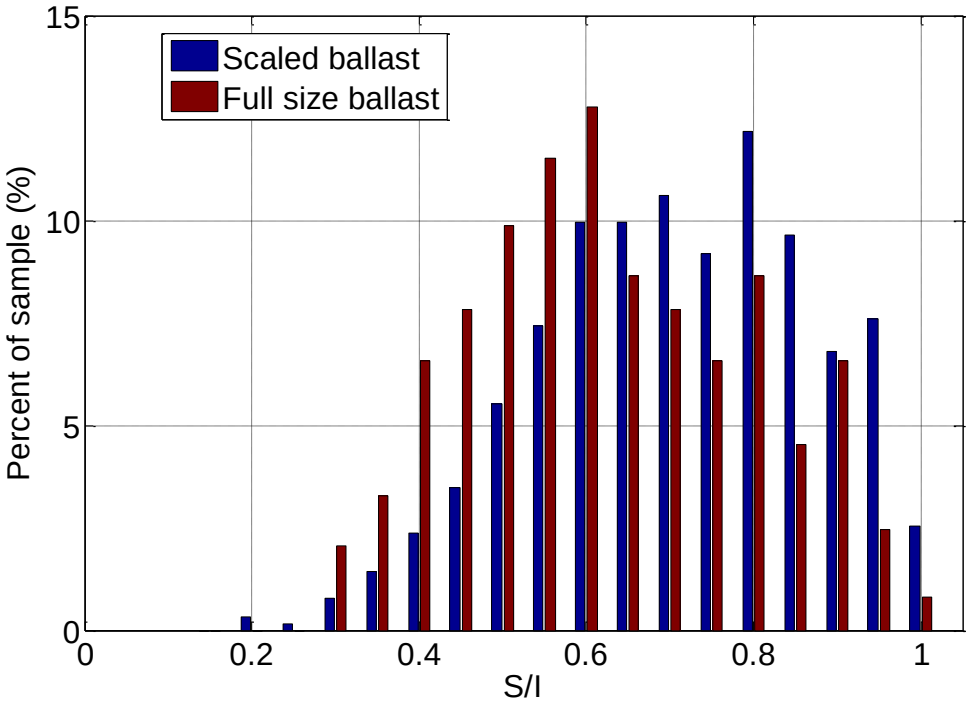

Figure 3.15: Comparison of S/I values of both scaled and full size ballast (632 scaled and 243 full size particles)

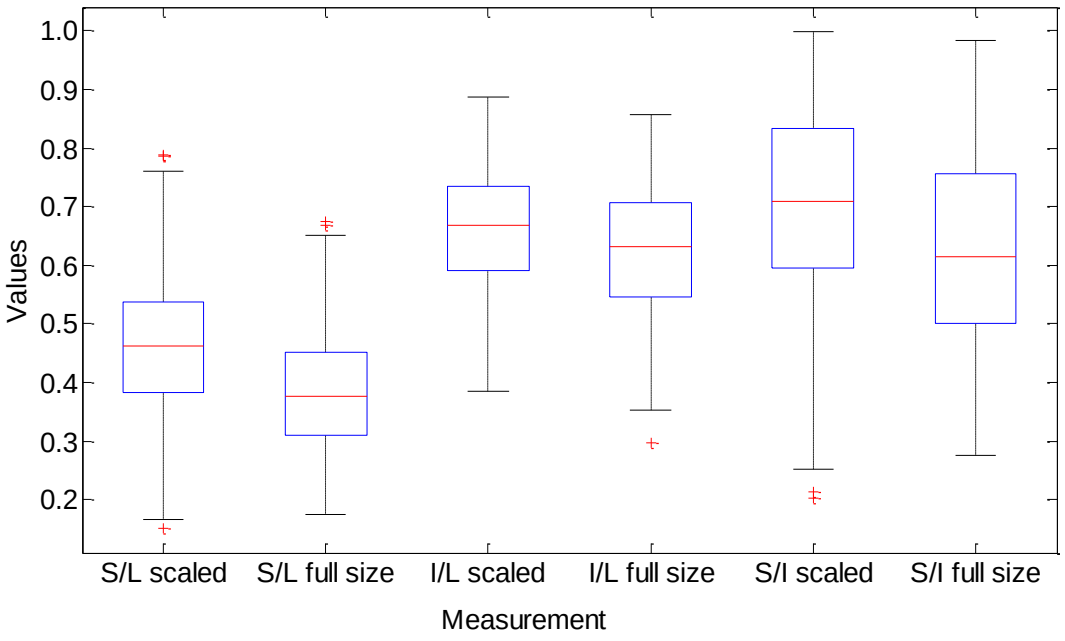

Figure 3.16: Boxplot of S/L, I/L, and S/I ratio of scaled and full size ballast

Figure 3.17 shows the Zingg plot for the individual particles in each sieve interval. Although the particles from each sieve interval spread in to all four regions, they are spread around the crossover region. Figure 3.18 shows the Zingg plot for average values of each sieve intervals. According to the Zingg plot, 11.2 mm, 13.2 mm, and 16 mm catching sieve particles are 'spherical', 9.5 mm, 22.4 mm, and 31.5 mm sieve interval particles are 'columnar', 40 mm particles are 'flat and columnar', and 50 mm particles are 'flat'. Although the differences in form between different sieve interval ballast particles are measurable, they are not dramatic because of their closeness in location on the Zingg plot.

Table 3.4 shows summary of key statistics from the S/L, I/L, and S/I data, where 'S' is measured using SEES approach.

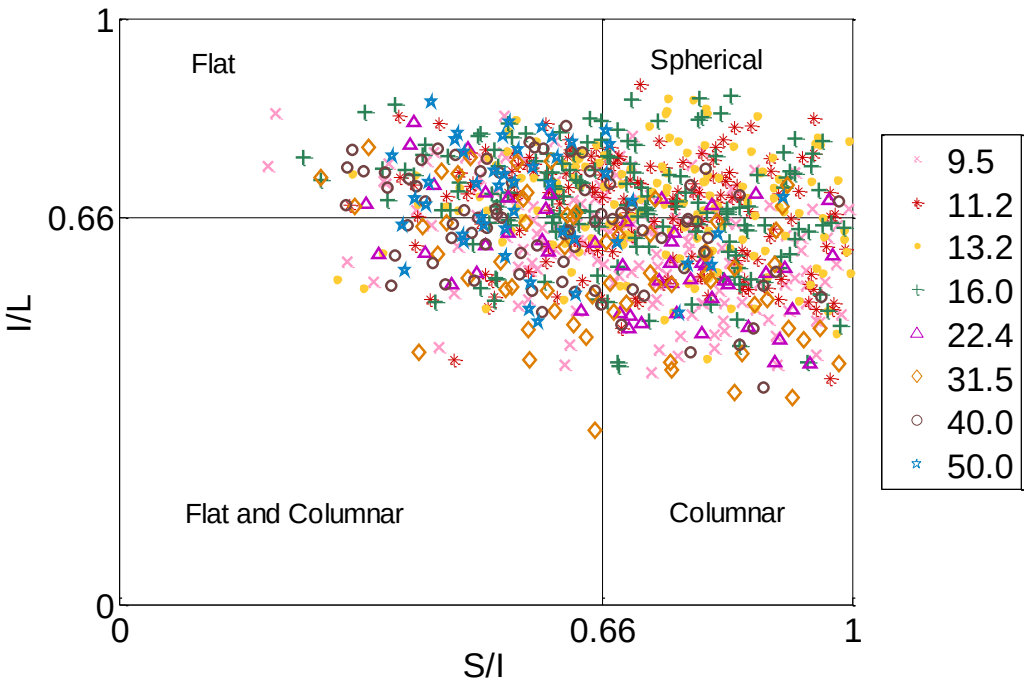

Figure 3.17: Zingg plot all data for each catching sieve size

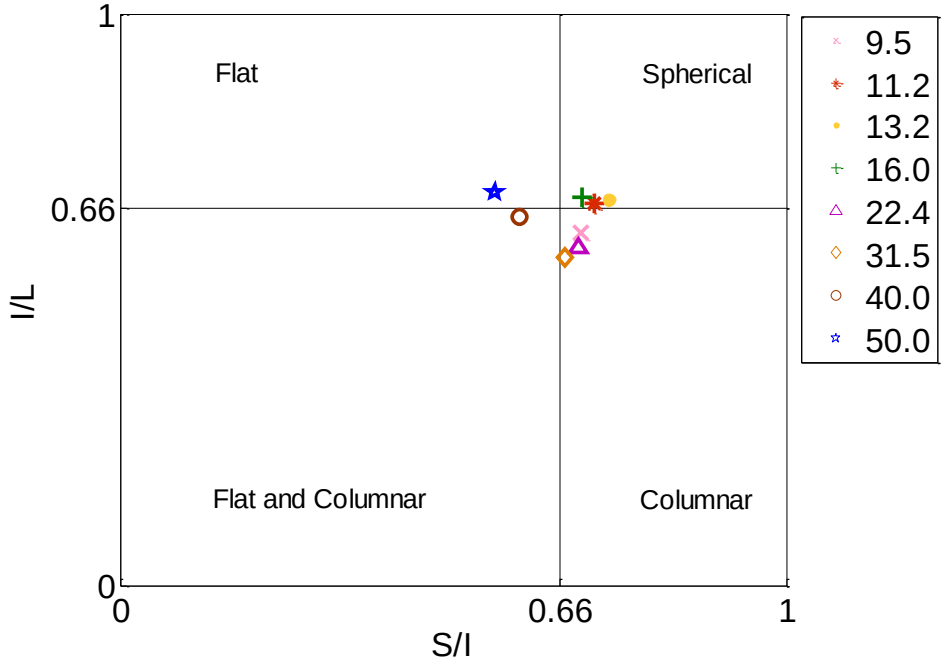

Figure 3.18: Zingg plot average for each catching sieve size

Ratio	Statistics	Catching sieve (mm)							
		9.5	11.2	13.2	16	22.5	31.5	40	50
S/L	Mean	0.420	0.472	0.494	0.466	0.399	0.375	0.380	0.385
	Median	0.420	0.476	0.492	0.468	0.395	0.371	0.364	0.379
	Maximum	0.679	0.786	0.788	0.758	0.669	0.652	0.675	0.628
	Minimum	0.152	0.191	0.166	0.192	0.212	0.176	0.202	0.223
	quartile 1	0.360	0.399	0.422	0.390	0.340	0.300	0.308	0.318
	quartile 3	0.482	0.539	0.586	0.543	0.456	0.445	0.457	0.445
	+/-	0.101	0.112	0.119	0.120	0.093	0.099	0.098	0.085
I/L	Mean	0.616	0.668	0.676	0.680	0.592	0.575	0.645	0.688
	Median	0.621	0.693	0.681	0.680	0.583	0.574	0.654	0.693
	Maximum	0.838	0.888	0.864	0.869	0.822	0.781	0.818	0.857
	Minimum	0.395	0.386	0.420	0.407	0.411	0.296	0.370	0.481
	quartile 1	0.550	0.594	0.618	0.636	0.529	0.500	0.579	0.627
	quartile 3	0.683	0.739	0.737	0.748	0.670	0.658	0.719	0.768
	+/-	0.096	0.094	0.090	0.099	0.094	0.113	0.094	0.095
S/I	Mean	0.692	0.712	0.733	0.693	0.688	0.667	0.599	0.563
	Median	0.698	0.708	0.750	0.693	0.725	0.665	0.607	0.540
	Maximum	0.996	0.991	0.998	0.989	0.973	0.982	0.983	0.906
	Minimum	0.203	0.315	0.298	0.252	0.337	0.275	0.310	0.373
	quartile 1	0.573	0.598	0.627	0.585	0.543	0.553	0.483	0.480
	quartile 3	0.818	0.839	0.848	0.830	0.809	0.804	0.699	0.619
	+/-	0.167	0.158	0.156	0.167	0.173	0.172	0.160	0.119

Table 3.4: Summary data for S/L, I/L and S/I

The distribution of particle shape is unknown, however a Weibull distribution is commonly used to model material strength. The Weibull distribution is a continuous probability distribution able to model a variety of probability distribution types.

The Weibull cumulative distribution function (CDF) and Weibull probability density function (PDF) are given by following equations.

$$CDF = f(x \mid a, b) = 1 - e^{-\left(\frac{x}{a}\right)^b} \tag{3.1}$$

$$PDF = f(x \mid a, b) = ba^{-b}x^{b-1}e^{-\left(\frac{x}{a}\right)^b} \tag{3.2}$$

Where ‘a’ and ‘b’ are scale and shape parameters. The Weibull shape parameter ‘b’ is also known as the Weibull slope because ‘b’ is equal to the slope of the line in a Weibull probability plot. The Weibull probability plot is used to assess graphically whether the data could come from a Weibull distribution. If the data can be matched by a Weibull function, the plot will be linear. The shape parameter of a Weibull distribution of strength is known as Weibull modulus in the field of material science. Different values of shape parameter ‘b’ have effects on the behaviour of the distribution. When b=1 the Weibull distribution is identical to the exponential distribution and when b=2 to the Rayleigh distribution. The Weibull distribution approximates to the normal distribution when ‘b’ is between 3 and 4. The Weibull scale parameter ‘a’ determines the range of the distribution. When ‘a’ is increased while b remains constant, the distribution gets stretched to the right and the height decreases.

A Weibull distribution can be used to model the probability distribution of S/L and ellipseness. Because the S/L and ellipseness data fall in a nearly linear line on the Weibull probability plot (Figure 3.19), the function will provide a reasonable approximation to the sample distribution. The Weibull parameters ‘a’ and ‘b’ are shown in Table 3.5. Figure 3.20 shows the Weibull cumulative distribution function for the S/L data from each sieve interval. The similarity between the Weibull cumulative distribution plot (Figure 3.20) and the measured cumulative distribution plot

(Figure 3.11) demonstrates that the Weibull function closely approximates the measured data. Figure 3.21 shows the Weibull probability distribution function for S/L for each sieve interval. The figure shows that there are slight differences in S/L between different sieve interval particles, but the differences are not dramatic. As the shape parameter is between 4 and 5, the distributions look like normal distributions although they are skewed slightly to the right (Table 3.5). Although larger particles tend to have a lower S/L ratio, the trend is not clear from the plot when comparing different sieve size intervals (Figure 3.21).

Catching sieve (mm)	95 % confident intervals				best fit	
	lower		upper			
	a	b	a	b	a	b
9.5	0.4431	4.042	0.4764	5.1166	0.4594	4.5477
11.2	0.4979	4.1261	0.5345	5.2298	0.5159	4.6453
13.2	0.5213	4.1258	0.5595	5.245	0.5401	4.6519
16	0.493	3.7872	0.5326	4.8047	0.5124	4.2657
22.4	0.408	3.6368	0.4656	5.4363	0.4358	4.4464
31.5	0.3874	3.3777	0.4406	4.8778	0.4131	4.0591
40	0.3956	3.5155	0.4418	4.8426	0.418	4.126
50	0.3932	3.8556	0.4467	5.8656	0.4191	4.7555

Table 3.5: Weibull parameters for S/L

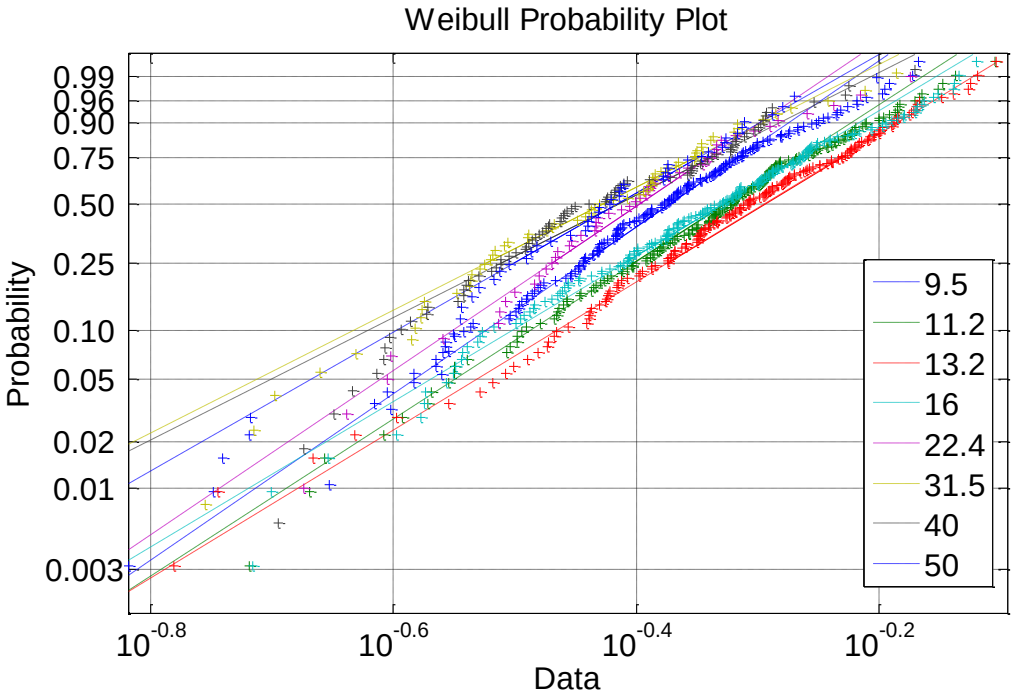

(a) S/L (SEES) data

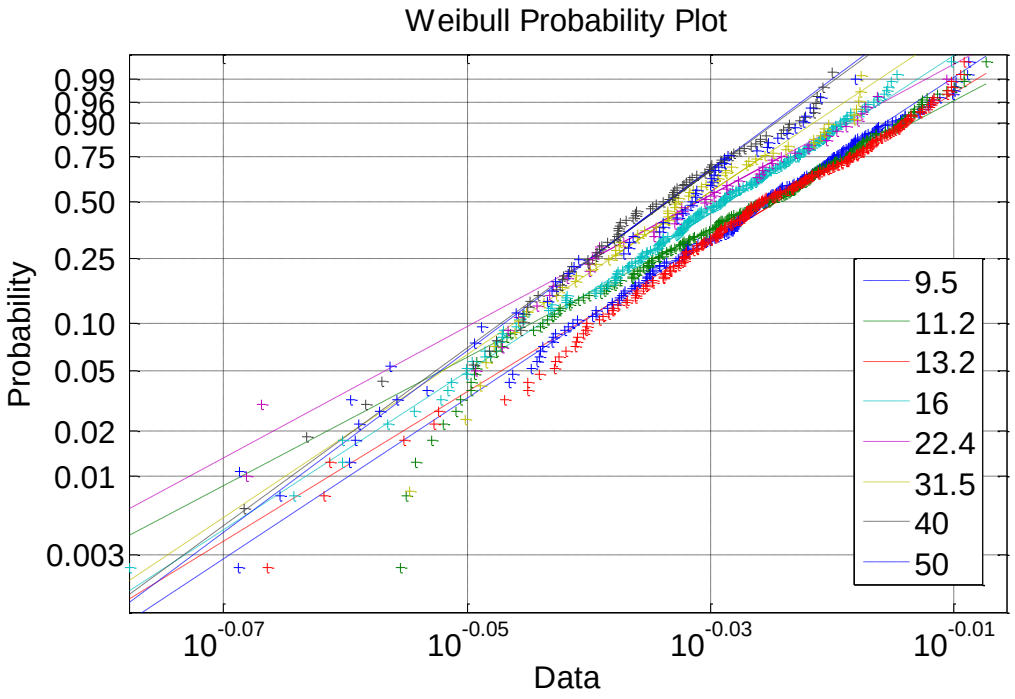

(b) Ellipseness data

Figure 3.19: Weibull probability plot of S/L and ellipseness data by catching sieve size

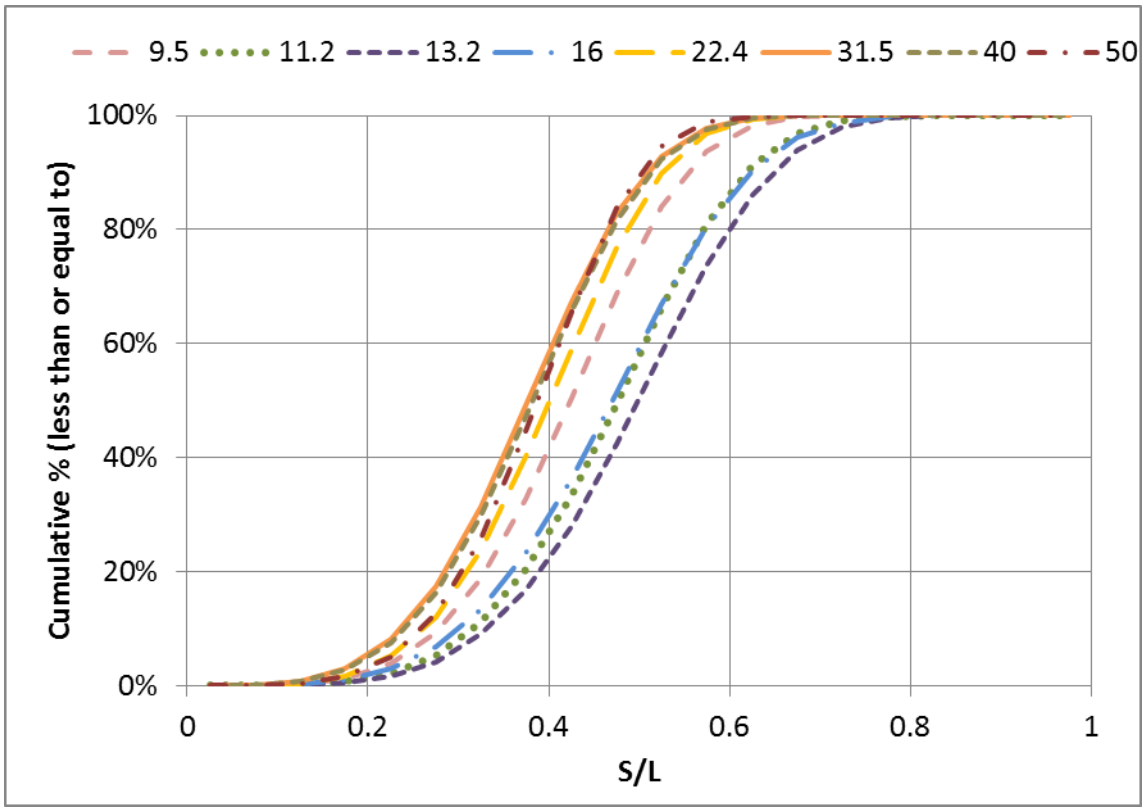

Figure 3.20: Weibull cumulative distribution function for S/L by catching sieve size

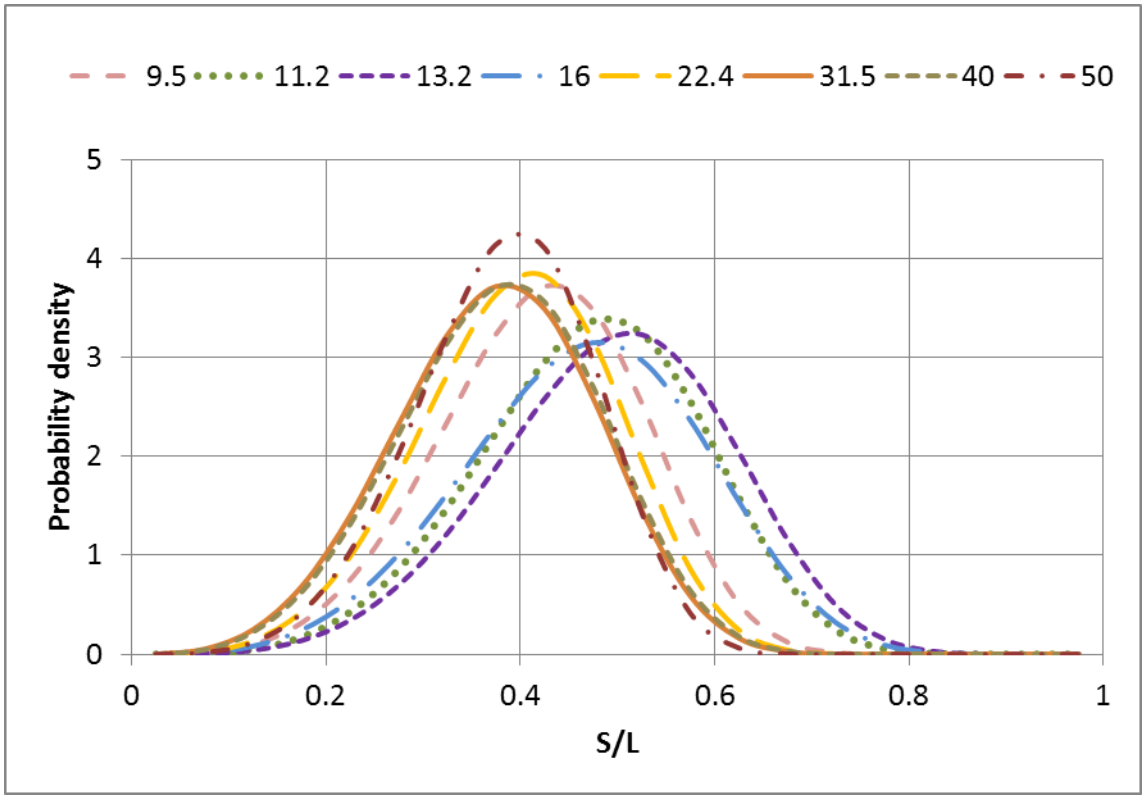

Figure 3.21: Weibull probability distribution function for S/L by catching sieve size

3.5.2 Roundness

Roundness can be measured by quantifying the ratio of the perimeter (P) of the 2D projection of a particle to the perimeter of a reference shape of the same area (i.e. $A_o = A_e$), but different perimeters (i.e. $P_o \neq P_e$) using automatic image analysis (where subscripts o and e denote the particle (object) and reference shape).

In this project, a new measure of roundness termed as 'ellipseness', E was used. To be consistent with the reference shape adopted in the form analysis (SEES), an ellipse was selected. Also an ellipse will better represent the shape of ballast particles in plan view than a circle.

$$E = \frac{Perimeter\ of\ equivalent\ area\ ellipse}{Perimeter\ of\ particle} = \frac{P_e}{P_o} \tag{3.3}$$

E has a range between 0 and 1. When the ellipseness approaches 1, the particle becomes more ellipse like i.e. rounder. E was calculated using Equation 3.3 from parameters estimated from image pro plus, which are L (D_{max}), perimeter (P_o) and area (A_o) for each particle. The perimeter of the equivalent area ellipse, P_e is calculated using Equation 3.4.

$$P_e \approx \pi(a+b)\left(1 + \frac{3\left(\frac{a-b}{a+b}\right)^2}{10 + \sqrt{4 - 3\left(\frac{a-b}{a+b}\right)^2}}\right) \tag{3.4}$$

where a is the major radius of the ellipse, $a = L/2 = D_{max}/2$.

b is the minor radius of the ellipse, $b = A_o/\pi a$.

Figure 3.22 shows the ellipseness of ballast particles in each sieve interval. Ellipseness of ballast particles fall in a negative skewed distribution (Figure 3.22 and Figure 3.23). Figure 3.24 shows the cumulative distribution graph of ellipseness for each sieve interval. It shows that larger size particles have lower ellipseness values. Median values of full size and scaled ballast are similar, with a difference of 1.3 % (Figure 3.25).

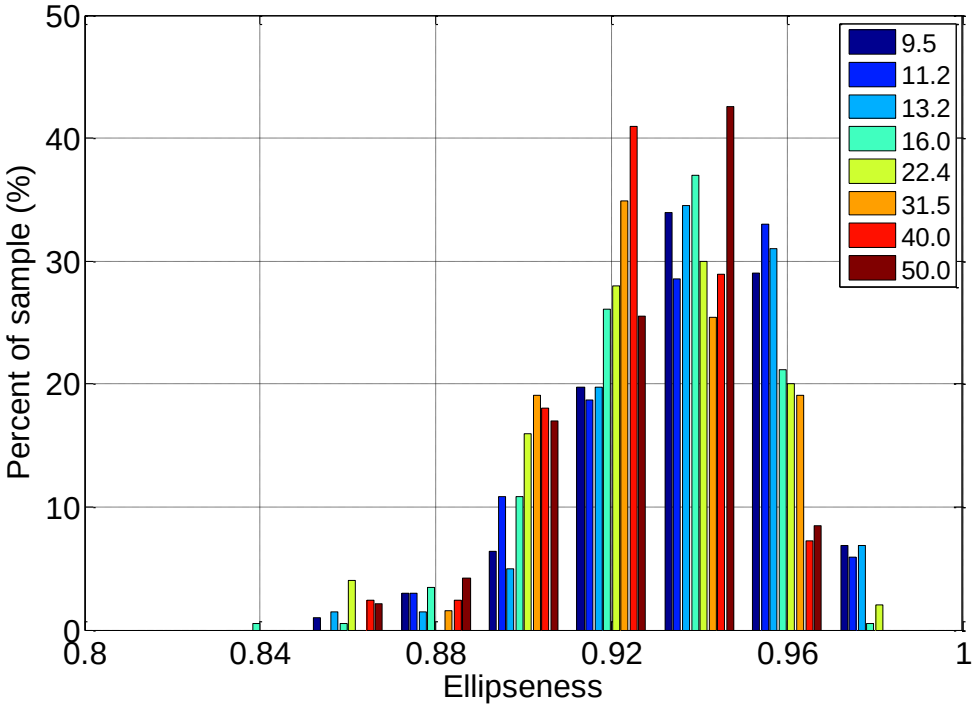

Figure 3.22: Ellipseness for each catching sieve interval ballast particles

(203 particles in each sieve intervals of 9.5 mm, 11.2 mm,13.2 mm, and 16.0 mm; 50 particles in 22.4 mm sieve; 63 particles in 31.5 mm sieve; 83 particles in 40 mm sieve; and 47 particles in 50 mm sieve)

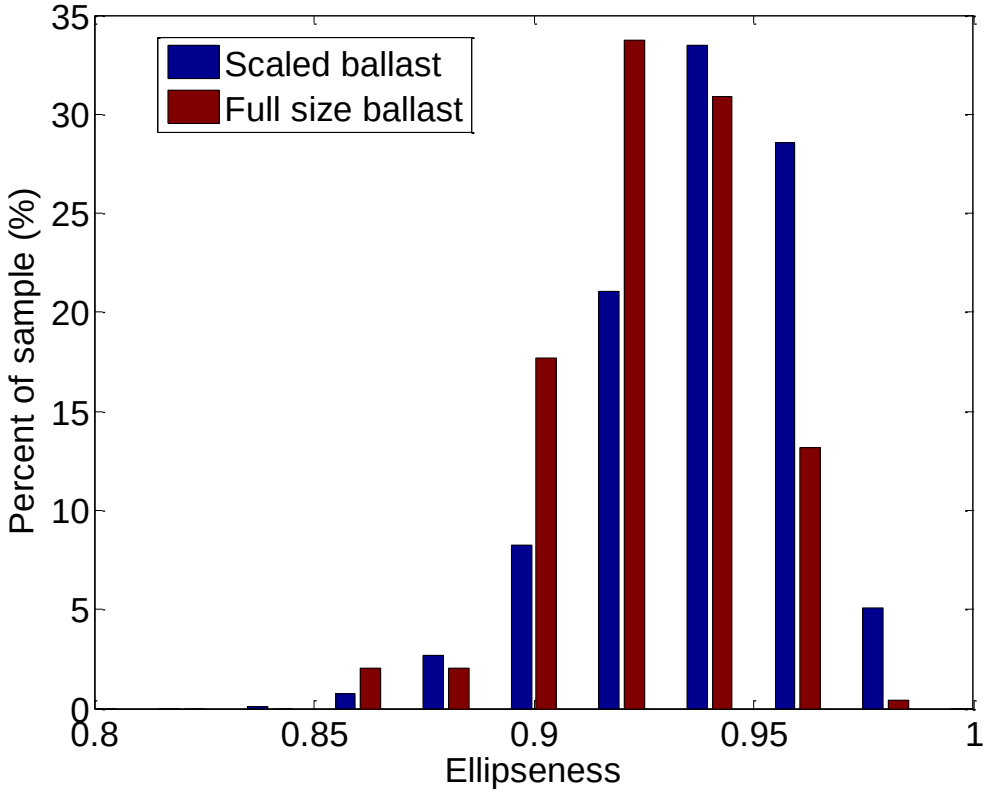

Figure 3.23: Comparison of ellipseness of both scaled and full size ballast (812 scaled and 243 full size particles)

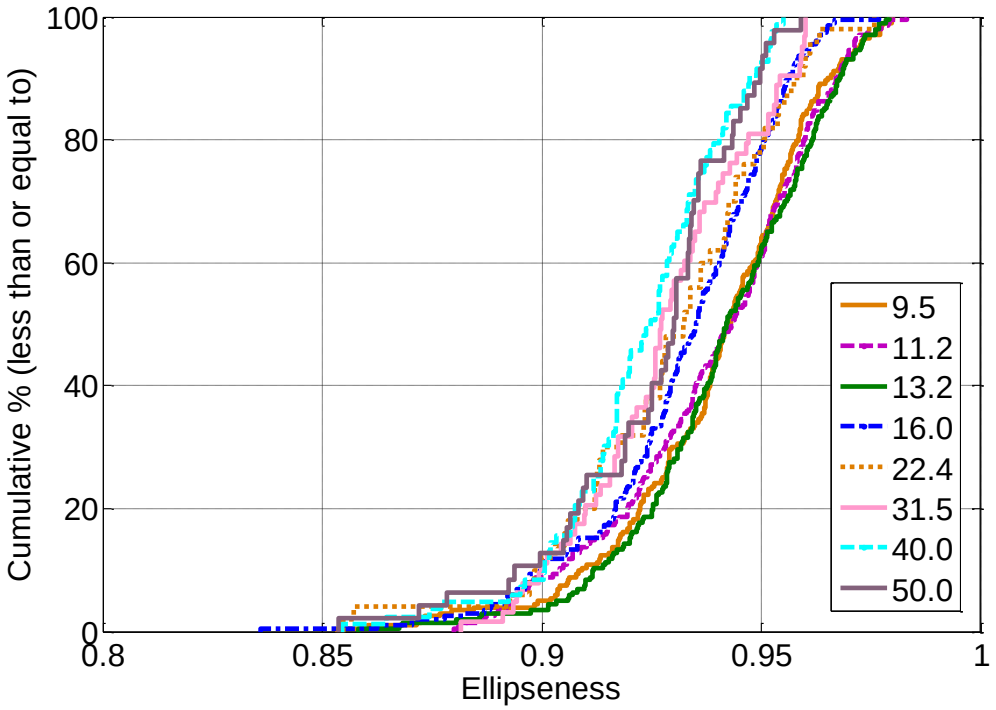

Figure 3.24: Cumulative distribution curves for ellipseness by catching sieve size

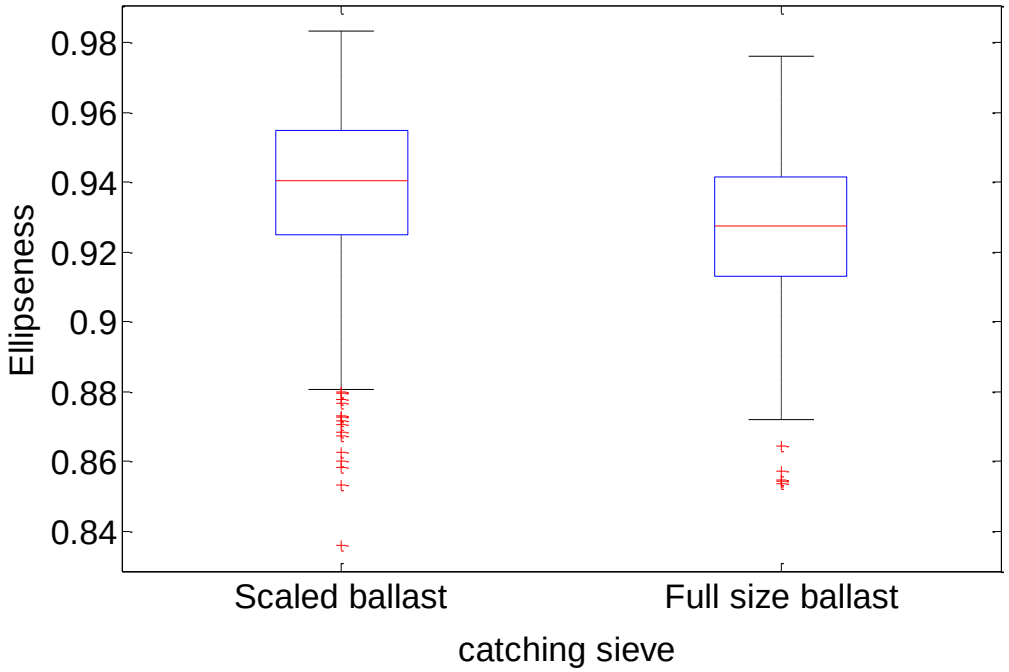

Figure 3.25: Boxplot of ellipseness of scaled and full size ballast

Weibull parameters for ellipseness are shown in Table 3.6. Figure 3.26 shows the Weibull cumulative distribution function. Figure 3.27 shows the Weibull probability distribution function which is negatively skewed by high shape factor. Smaller particles are rounder than larger particles, with slightly higher ellipseness values. In other word, larger particles are more angular than smaller particles as they show slightly lower ellipseness values compared to smaller particles.

Catching sieve (mm)	95 % confident intervals				best fit	
	lower		upper			
	a	b	a	b	a	b
9.5	0.9472	46.1511	0.9526	57.1724	0.9499	51.367
11.2	0.947	43.8331	0.9527	54.4517	0.9498	48.8548
13.2	0.9488	47.0855	0.9541	58.4028	0.9514	52.4397
16	0.9392	48.2265	0.9443	59.814	0.9417	53.7086
22.4	0.9342	37.0975	0.9462	56.9157	0.9402	45.9503
31.5	0.9329	43.7752	0.9422	64.0007	0.9375	52.9305
40	0.9281	48.0098	0.9355	67.1111	0.9318	56.7626
50	0.9293	45.4772	0.9391	71.6689	0.9342	57.0903

Table 3.6: Weibull parameters for ellipseness

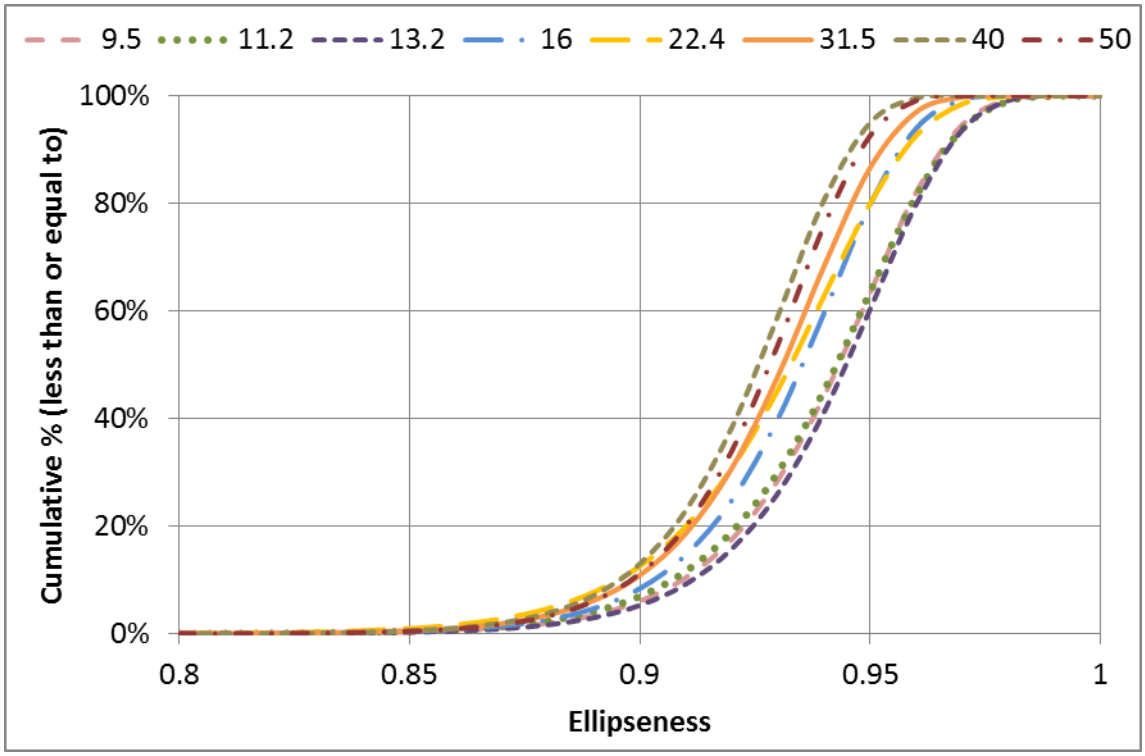

Figure 3.26: Weibull cumulative distribution function for ellipseness by catching sieve size

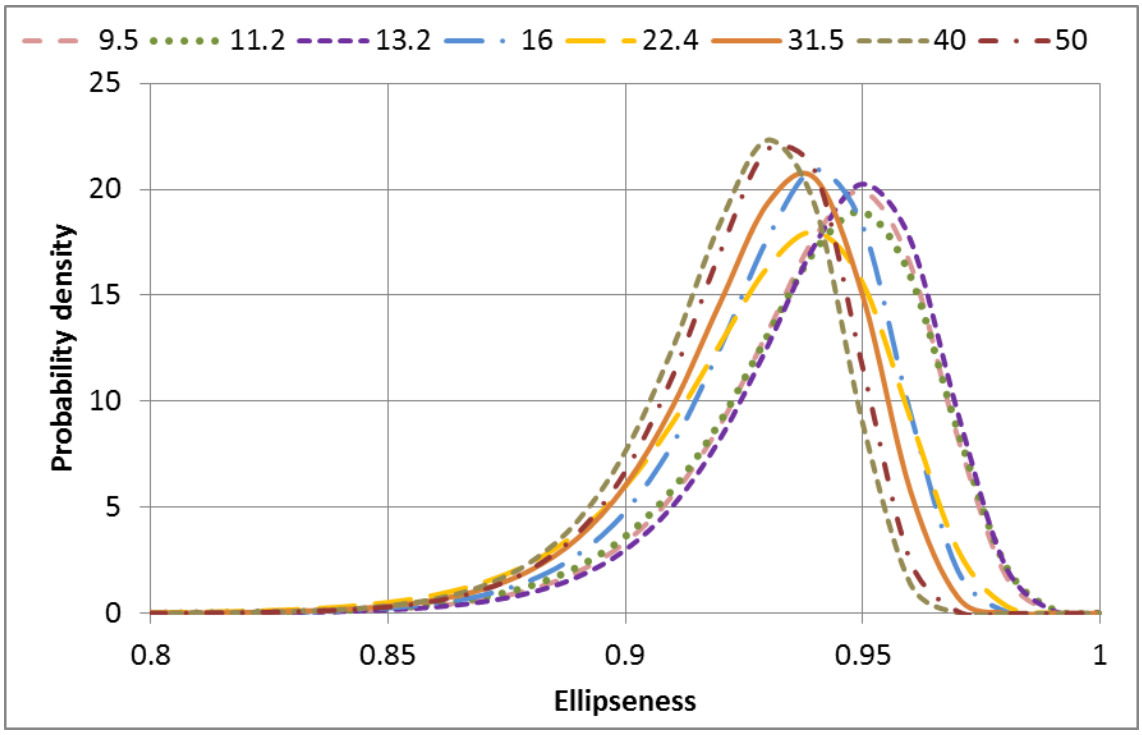

Figure 3.27: Weibull probability distribution function for ellipseness by catching sieve size

3.6 summary

SEES has been demonstrated as an appropriate measurement to estimate S, I and L from the comparison of actual S/L ratios determined from the three orthogonal views with the SEES S/L ratios.

A new measure of roundness termed ellipseness has been introduced, which is a less time consuming measurement using automatic image analysis.

The distributions of form and roundness of ballast particles can be well matched using a Weibull distribution. Although there is a weak trend for larger particles to have lower S/L and ellipseness, the trend may not be clear when comparing any two sieve size intervals.

There are measurable differences in S/L and ellipseness between different sieve size interval particles. However the differences are small in magnitude and do not necessarily invalidate the use of scaled material for lab testing.

4. Triaxial apparatus and test procedure

4.1 Triaxial Apparatus

The triaxial apparatus used in this project is shown in Figure 4.1, it was manufactured by GDS Instruments Ltd and comprises a computer controlled load frame based static triaxial testing system. The fundamental hardware elements are shown in Figure 4.2. The apparatus is computer controlled using GDSLAB software.

Figure 4.1: Triaxial apparatus

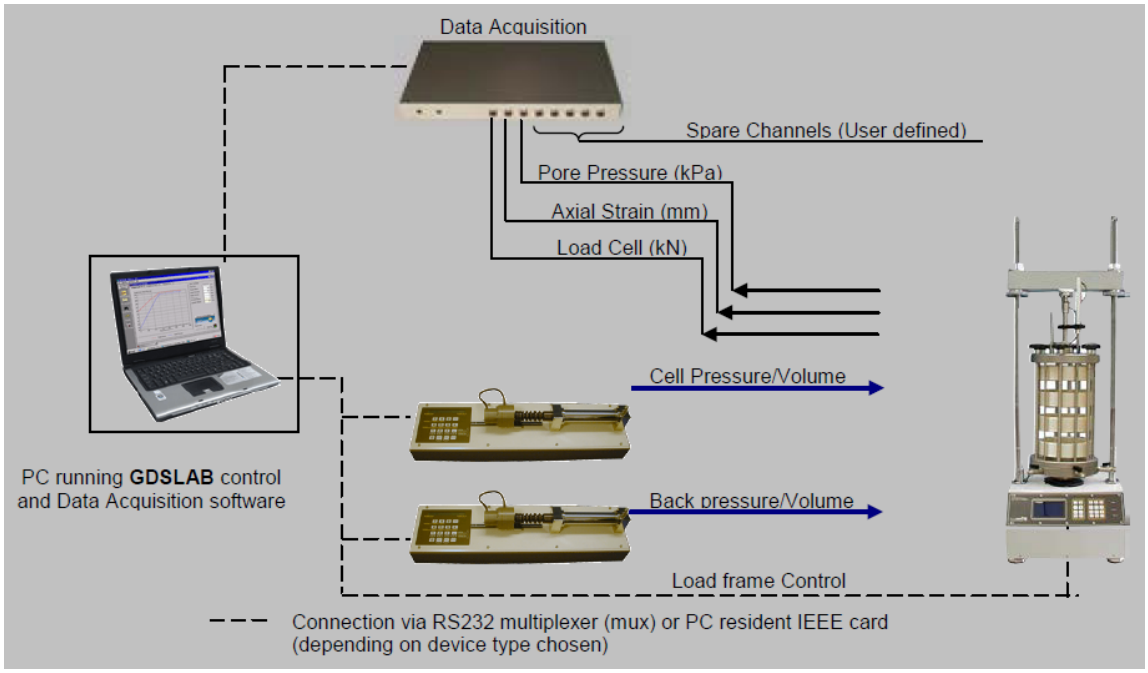

Figure 4.2: Diagram of the GDS Triaxial Automated System hardware elements (www.gdsinstruments.com)

A triaxial cell with a maximum safe pressure of 1700 kPa was used. The cell has an internal diameter of 220 mm and a height of 487 mm, and accommodates specimens of 300 mm height and 150 mm diameter. The triaxial cell was mounted in a 50 kN reaction frame. A bottom up mechanical drive unit was used to apply axial load.

The pressure controllers were used to apply cell and back pressure and measure volume change of the specimen. Axial displacement, axial load, cell pressure, back pressure, and pore pressure were logged by computer. The axial displacement was measured using a 50 mm range Linear Variable Displacement Transducer. The axial load was measured by an internal load cell with a normal working load range of 32 kN and a maximum range of 47 kN. Cell pressure and pore pressure were measured by 1000 kPa rated pressure transducers.

Scaled railway ballast was used in this apparatus with the parallel gradation designed to achieve a ratio of specimen diameter to maximum particle size (D/d_{max}) of more than 6, which is sufficient for relative particle to specimen size effects to be ignored (Marachi et al., 1972). The specimen height to diameter ratio was 2. If the height to diameter ratio is equal or greater than 2, friction between the specimen and end platens will not affect the overall specimen strength (Bishop and Green, 1965).

4.2 Calibration

Pressure transducers

A DH.Budenberg 580 series hydraulic dead-weight tester was used to calibrate the pressure transducers and load cell (Figure 4.3). The pressure or load was increased in steps over the range of the transducer, and then decreased incrementally. The voltage was measured at each step.

The sensitivities of the cell pressure and pore pressure transducers during the calibration shown in Figure 4.4 were 12.51745 kPa/mV and 12.46224 kPa/mV respectively. The loading and unloading points are in a straight line with coefficient of conformity value (R^2) of 1 and errors smaller than 1 kPa.

Figure 4.3: Calibration frame- Budenberg S/No 26494/500

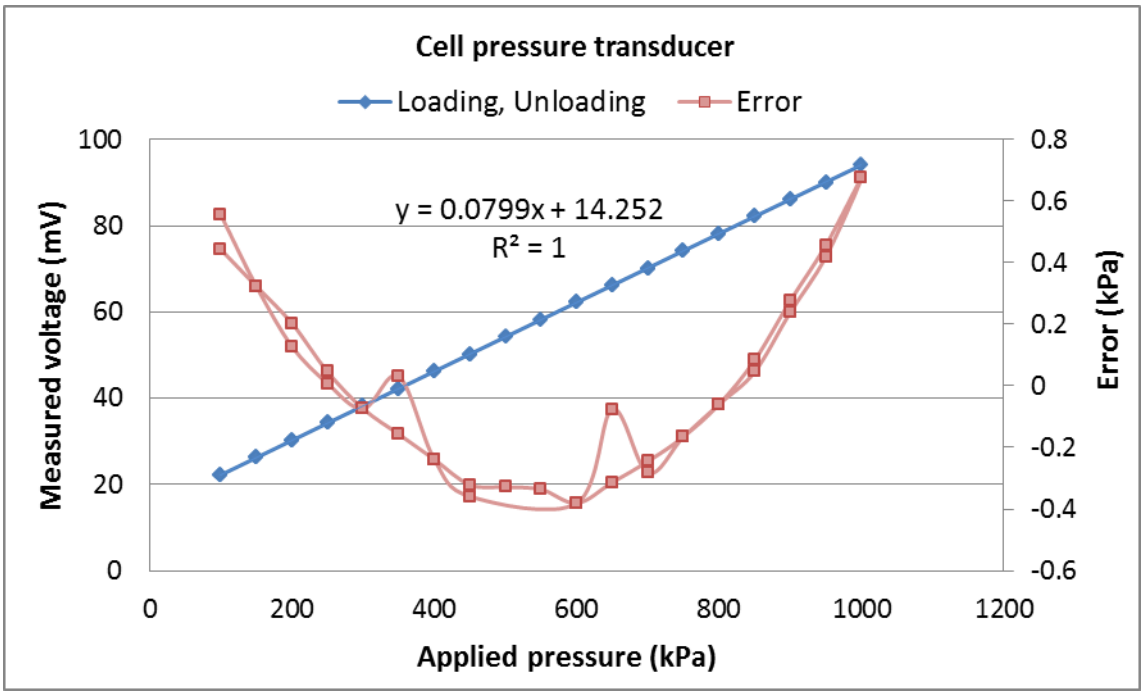

(a) Cell pressure transducer

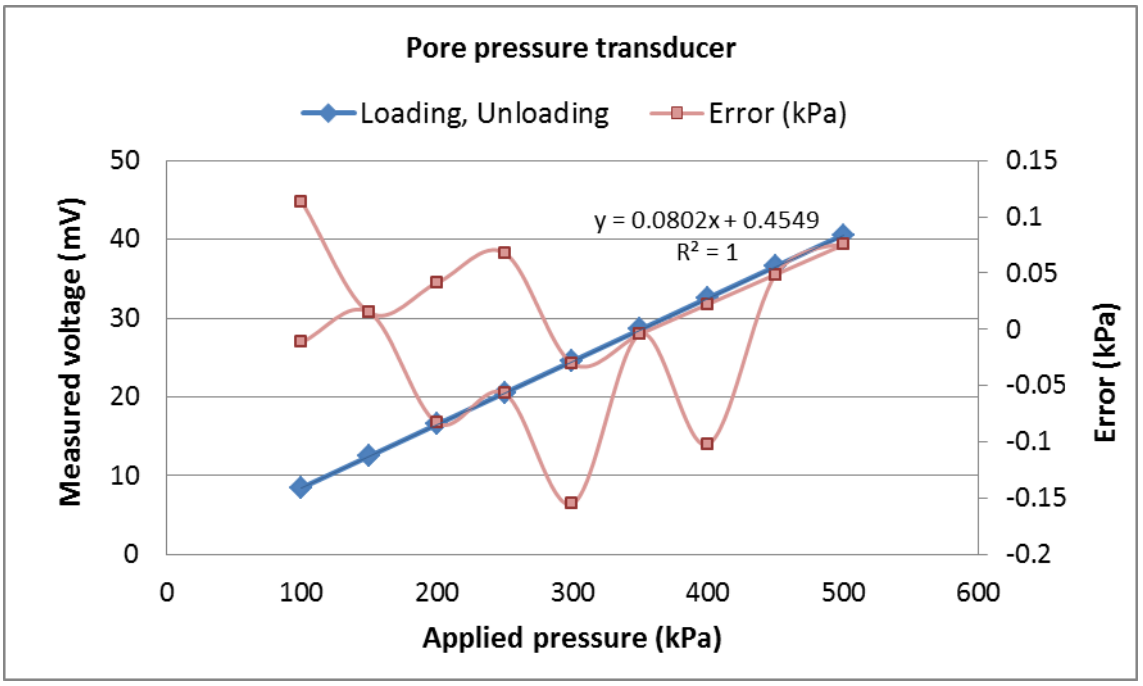

(b) Pore pressure transducer

Figure 4.4: Calibration of pressure transducer

Load cell

The load cell was calibrated against a 50 kN proving ring in a calibration frame. Although the full range of the load cell is 32 kN, the load was only increased up to 24 kN due to the limitation of weights. The sensitivity was 1.48248 kN/mV during the calibration shown in Figure 4.5. The calibration points are linear with a coefficient of conformity of 1, and the errors are acceptably small.

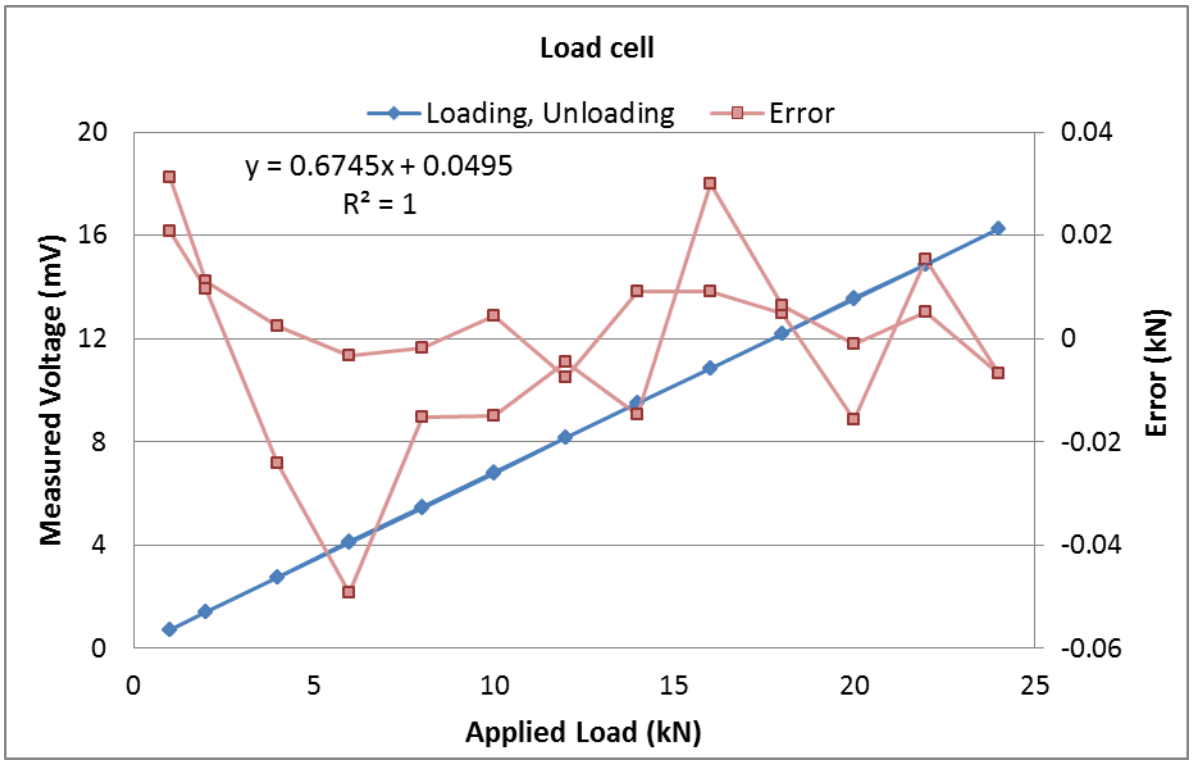

Figure 4.5: Calibration of load cell

Linear Variable Displacement Transducer (LVDT)

The 50 mm range LVDT was calibrated using a micrometer. The sensitivity of the LVDT during calibration shown in Figure 4.6 was 0.005009 mm/mV.

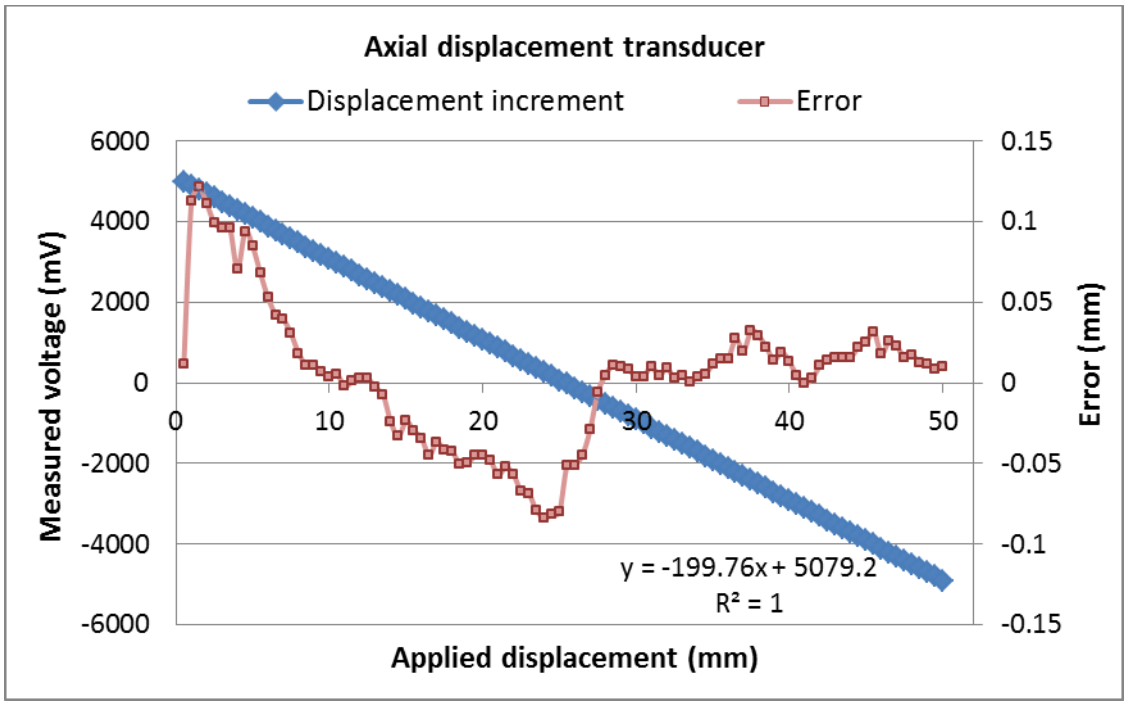

Figure 4.6: Calibration of the axial displacement transducer

4.3 Creep test

To determine whether the Perspex Triaxial cell exhibited significant creep, a creep test was carried out. A constant cell pressure was applied for 24 hours and the volume of water going into and out of the cell was measured using the cell pressure controller. The volume change with time did not exhibit typical creep behaviour or follow any particular pattern during creep tests (Figure 4.7). The volume change in positive direction implies water get into the cell, thus expansion of the cell.

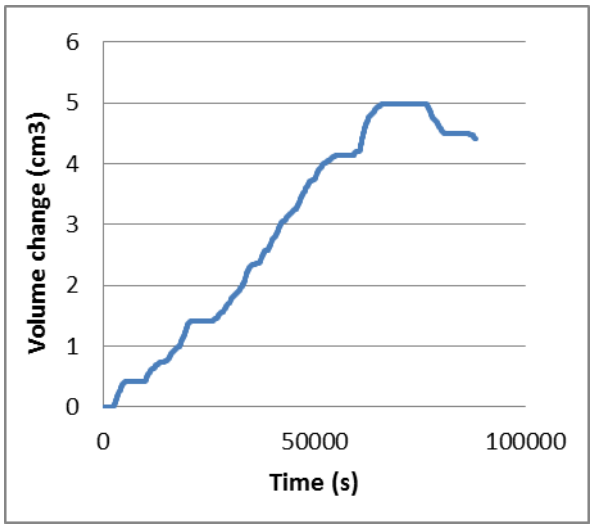

(a) 60 kPa

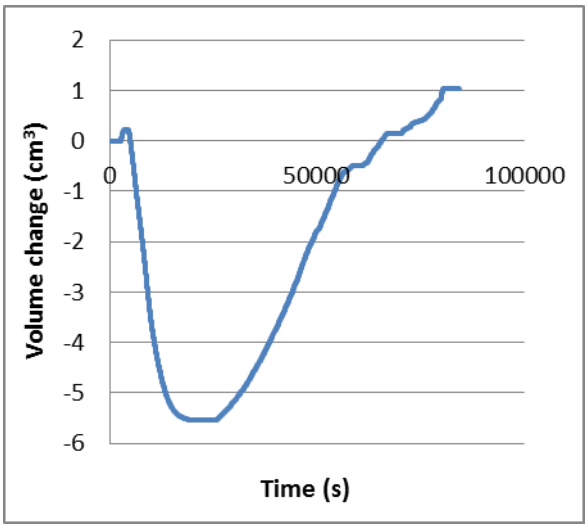

(b) 160 kPa

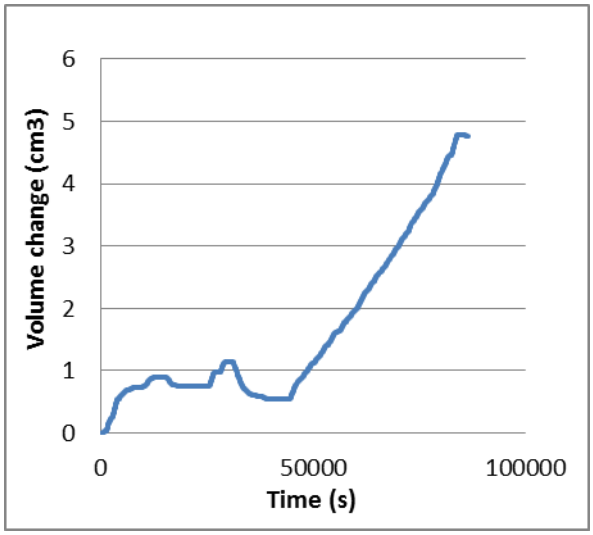

(c) 160 kPa

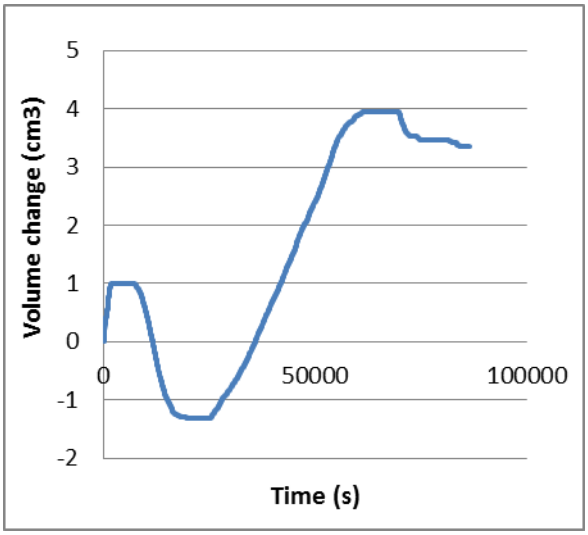

(d) 160 kPa

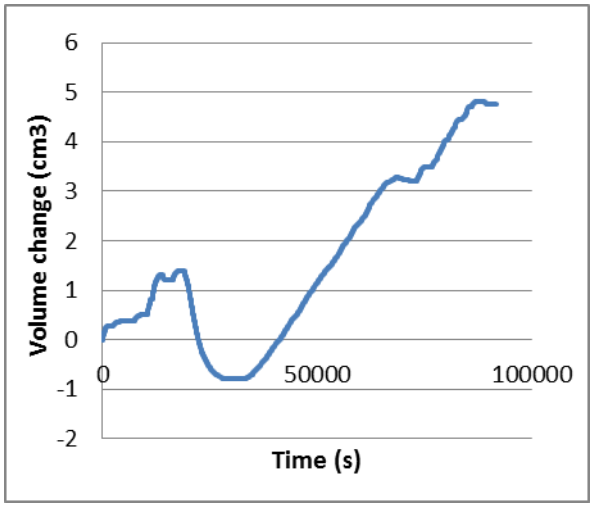

(e) 300 kPa

Figure 4.7: Volume change of cell against time for creep test

The cell temperature was measured using a thermistor for the 60 kPa and 160 kPa creep tests (Figure 4.8). The volume change pattern seemed to be repeatable over 24 hours from the 160 kPa cell pressure creep test which was carried out over 48 hours (Figure 4.8 b). If the volume change is purely due to temperature, the graph of volume change against temperature change would be expected to follow a straight line (Equation 4.1). The measured volume change of the cell cannot be entirely attributed to the temperature change as the relationship is not linear (Figure 4.9).

$$\Delta v = \frac{3\pi {d_0}^2 h_0}{4} \left(\alpha_p - \alpha_w\right) \Delta T \tag{4.1}$$

where; $\Delta v = volume\ of\ water\ into\ the\ cell$

$d_0 = internal\ cell\ diameter$

$h_0 = cell\ height$

$\Delta T = temperature\ change$

$\alpha_p = coefficient\ of\ linear\ thermal\ expansion\ of\ perspex$

$\alpha_w = coefficient\ of\ linear\ thermal\ expansion\ of\ water$

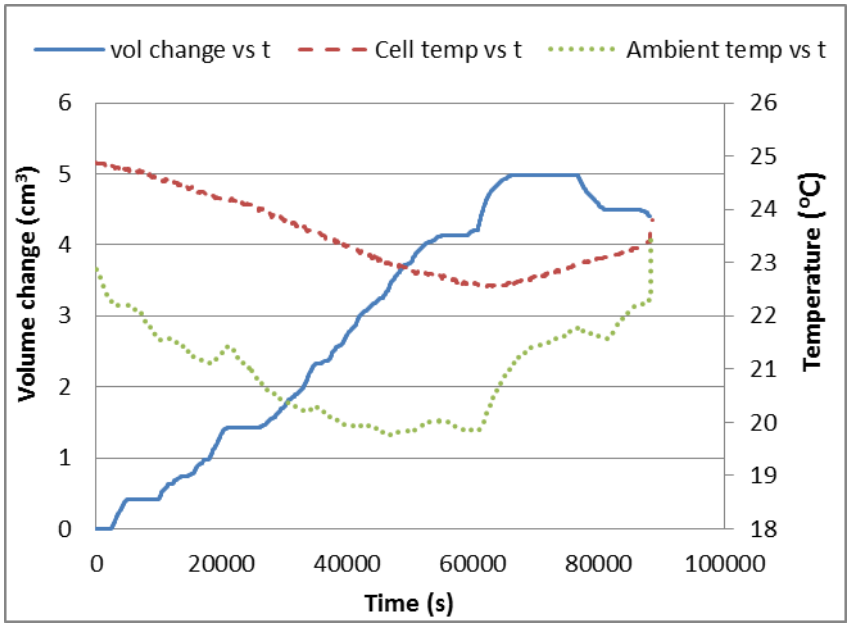

(a) 60 kPa

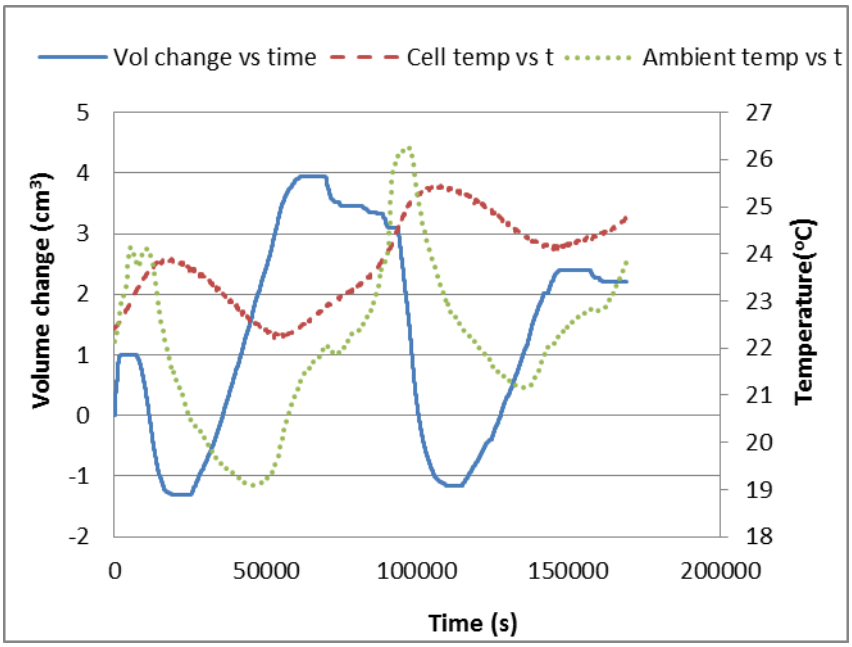

(b) 160 kPa

Figure 4.8: Cell volume and temperature against time

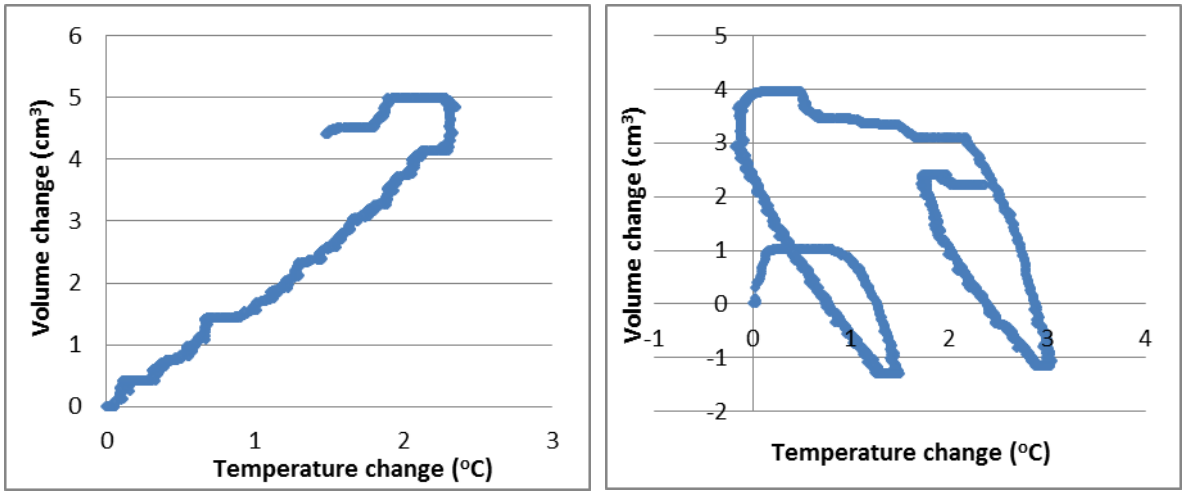

(a) 60 kPa (b) 160 kPa

Figure 4.9: Volume changes against cell temperature changes

When the volume change due to a change in temperature (Equation 4.1) is deducted from the total volume change, the resulting volume change does not follow the usual creep curve (Figure 4.10).

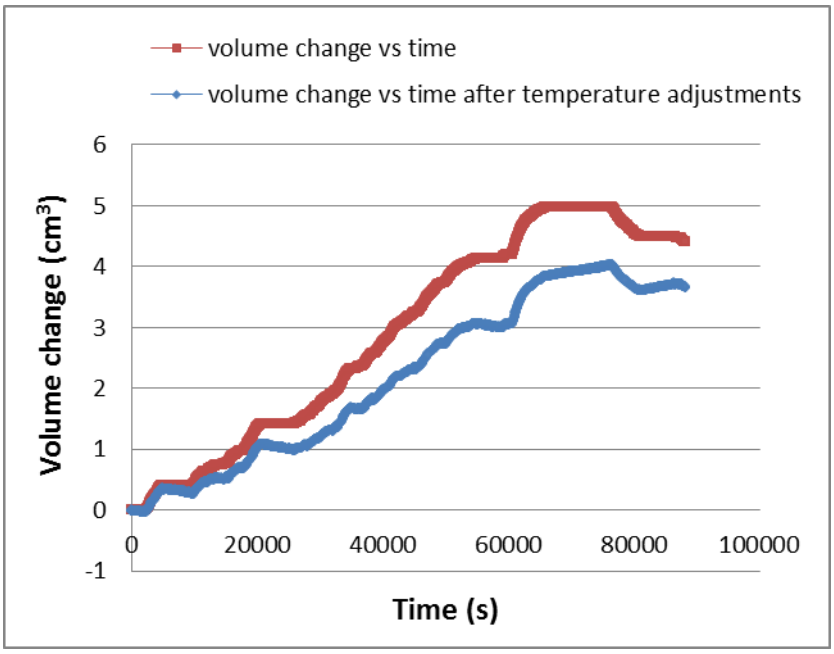

(a) 60 kPa

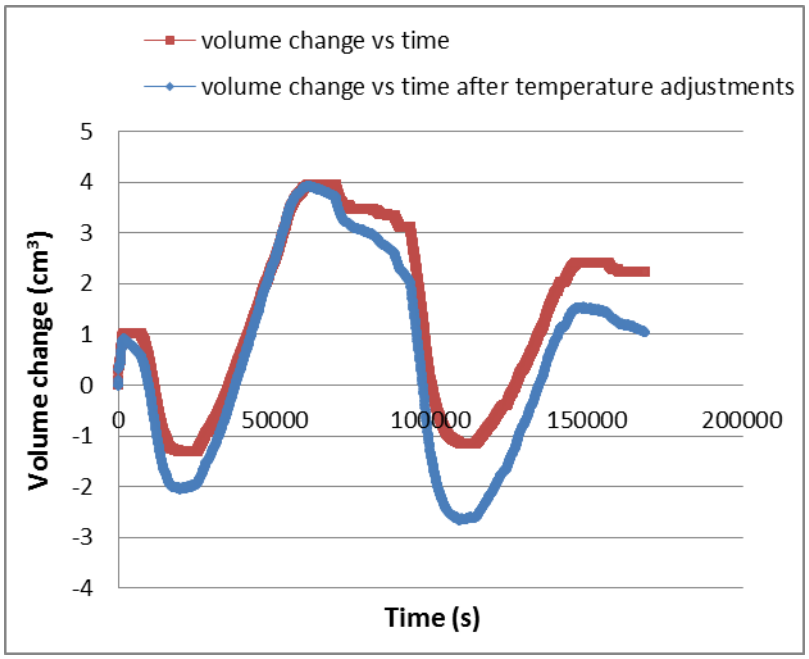

(b) 160 kPa

Figure 4.10: Volume change against time before and after expected temperature volume change adjustments

Although the cell pressure applied by the controller only varies by +/- 1 kPa, the cell pressure measured by the transducer at the bottom of the cell varies during the test (Figure 4.11). Thus the volume change pattern could be partly due to the cell pressure fluctuations within the cell. The room was not temperature controlled, thus the

pressure variations recorded by the transducer might also be due to temperature effects.

The cell pressure transducer connected to the water inlet valve of the cell base was used to process the triaxial test data. As this transducer is very close to the cell, the water pressure variations that occur within the cell during the test can be measured more accurately than the pressure sensor within the controller. Also this transducer was calibrated manually.

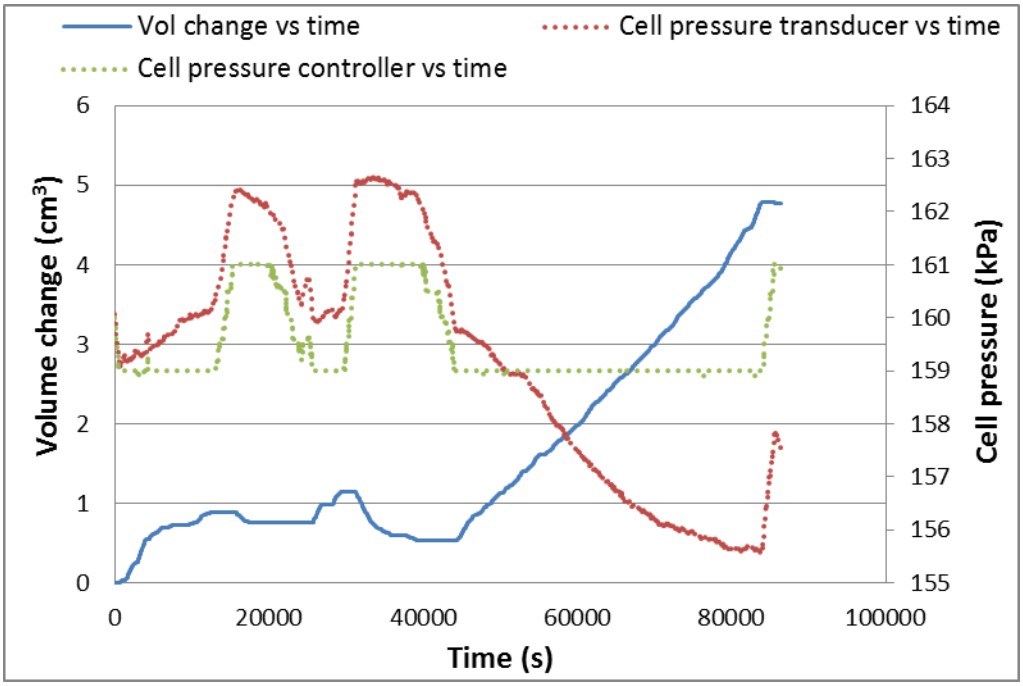

(a) 160 kPa

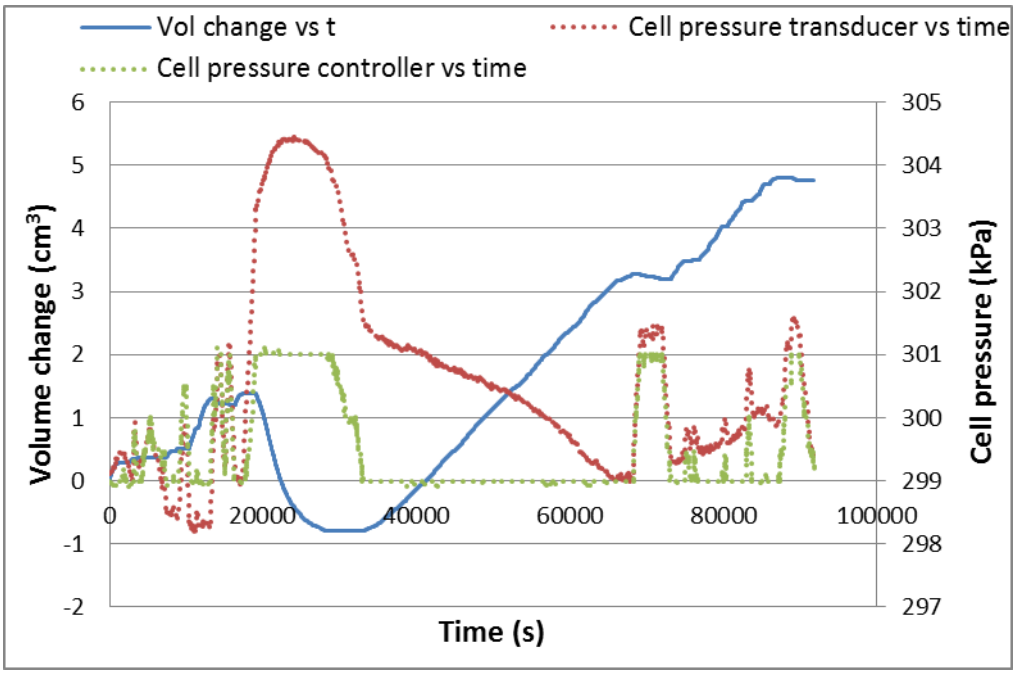

(b) 300 kPa

Figure 4.11: Volume change of cell and cell pressure monitored during creep test

In summary, no clear relationship was determined between volume change, temperature change, pressure change and time. Many factors including the creep of cell, temperature effects in lines and cell pressure variation within the cell may be attributed to this volume change behaviour at constant cell pressure applied by pressure controller with +/-1 kPa pressure variation. The volume change over 24 hours would give rise to a maximum error of 0.1 % of the initial sample volume. Therefore any creep effect is considered negligible.

4.4 Membrane penetration test

In triaxial tests on larger granular material like ballast, membrane penetration is significant due to the relatively large particle sizes in relation to membrane thickness and the flexibility of the membrane. Membrane penetration introduces difficulties in quantifying the volumetric deformation of specimens during triaxial tests from the amount of water movement within the cell. In monotonic tests the effect is small and can be ignored. However when the cell pressure cycles the membrane pushes into and out of the particle voids. This action renders accurate measurements of volume change impractical by the direct measurement of water volume change.

Membrane tests were carried out to assess the effect of membrane penetration when the cell pressure changes. Two types of test were carried out.

i. The cell pressure was increased in steps and brought back to datum following every increment. Cell pressure was increased from 15 kPa to 60 kPa in 5 kPa increments. This test was done on an unglued specimen
ii. The cell pressure was cycled between 30 kPa and 60 kPa for 100 cycles. This test was carried out on both unglued and glued specimens.

Membrane test where cell pressure was increased in steps:

A scaled ballast specimen with an initial density of 1529.3 kg/m^3 was tested. The cell pressure was brought to an initial 15 kPa and left overnight. The cell pressure was increased in steps from 15 kPa to 60 kPa and reduced back to 15 kPa (Figure 4.12). The loading ram was fixed to the reaction frame. Otherwise, water movement would result partly from the ram movement. A small space was left between the ram and the top cap of the specimen and the axial displacement was targeted at 0 mm.

Figure 4.12 shows there are both resilient and permanent components of volume change when the cell pressure is increased and reduced. When the cell pressure increment is higher, membrane penetration is higher with a larger volume of water pushed into the cell from the controller. Although the major portion of volume change is due to membrane penetration, as the specimen is unglued (particles are free to move) a small portion of volume change is due to particle movement.

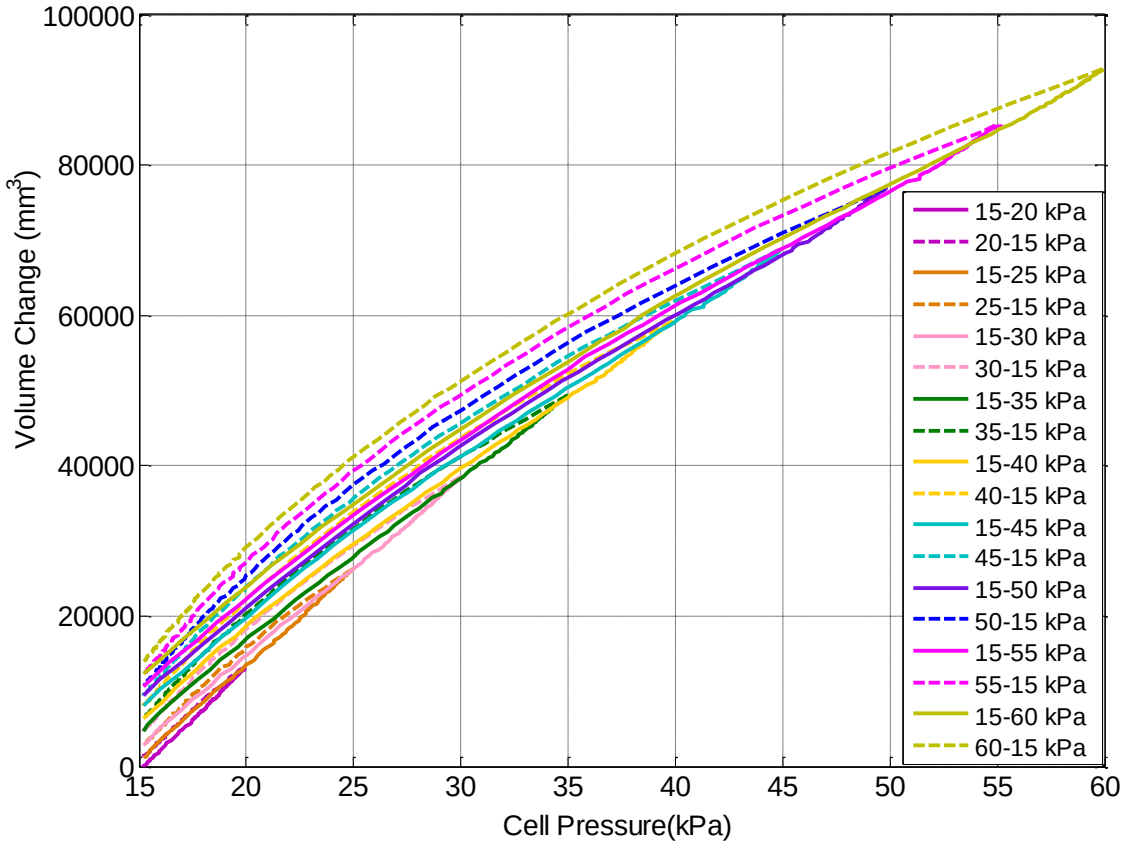

Figure 4.12: Volume change of controller when the cell pressure was increased in steps

Membrane test where cell pressure was cycled:

The cell pressure was cycled between 30 kPa and 60 kPa for approximately 100 cycles with a period of 40 minutes/cycle. The test was carried out on an unglued specimen with an initial density of 1529.3 kg/m^3. From this test, linear and polynomial correlations were obtained between cell pressure change and volume change from a portion of data having a reasonable coefficient of correlation (Figure 4.13). The membrane penetration correlation with time was not unique. This polynomial correlation was assumed as a volume change due to membrane penetration when the cell pressure cycle between 30 kPa and 60 kPa. Based on this, an attempt was taken to find out the specimen volume change during a cyclic test where the cell pressure cycles.

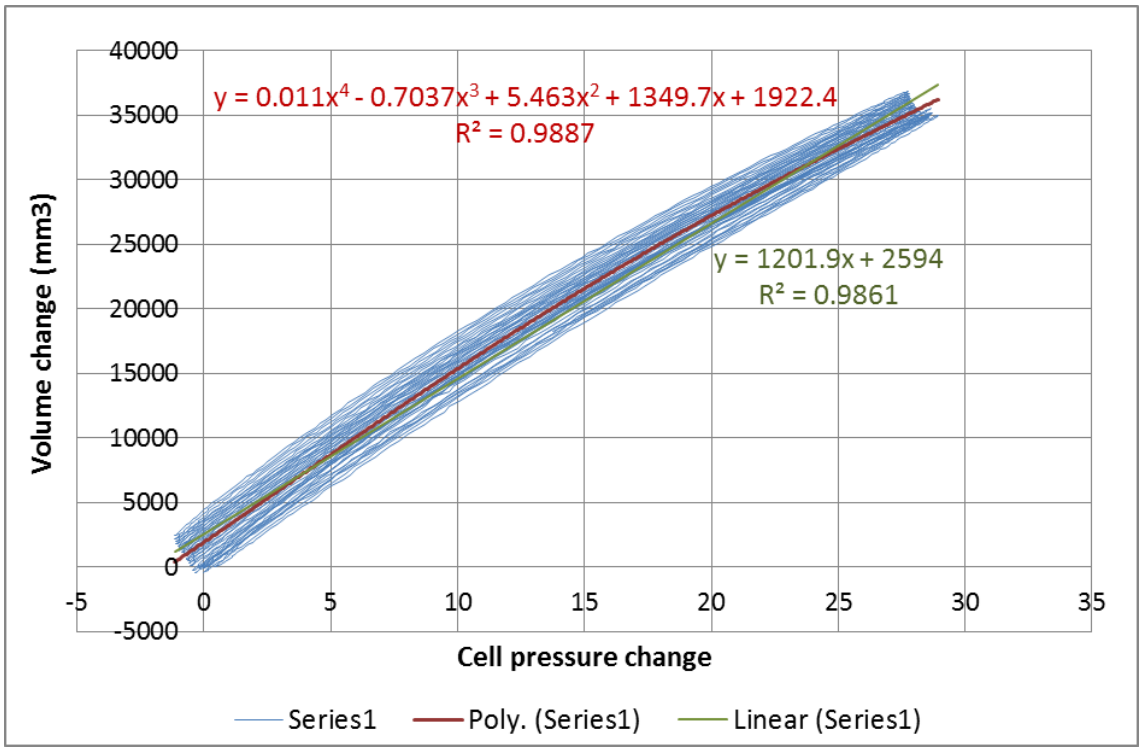

Figure 4.13: Linear and polynomial correlations between volume change and cell pressure change for unglued specimen

Figure 4.14 shows the volume change measurement from the cell pressure controller for one of the cell pressure cyclic tests where the deviator stress, q= 5 kPa to140 kPa and cell pressure = 30 kPa to 60 kPa with a period of 40 minutes per cycle. The membrane penetration volume correction based on a polynomial function derived from Figure 4.13 and the volume change after the correction are also shown.

Although this polynomial correlation improves the amplitude of volumetric strain within a cycle, it does not correct the permanent volumetric strain accumulation during the test. The permanent volumetric strain obtained in this test was many times (8 times) greater than the permanent axial strain, which could be due to membrane creep (accumulation of permanent volume change due to membrane penetration). This method of correction provided plausible values for bulk modulus, shear modulus, and Poisson's ratio, more consistent with values reported in the literature. For example, Figure 4.15 shows the Poisson's ratio before and after the correction.

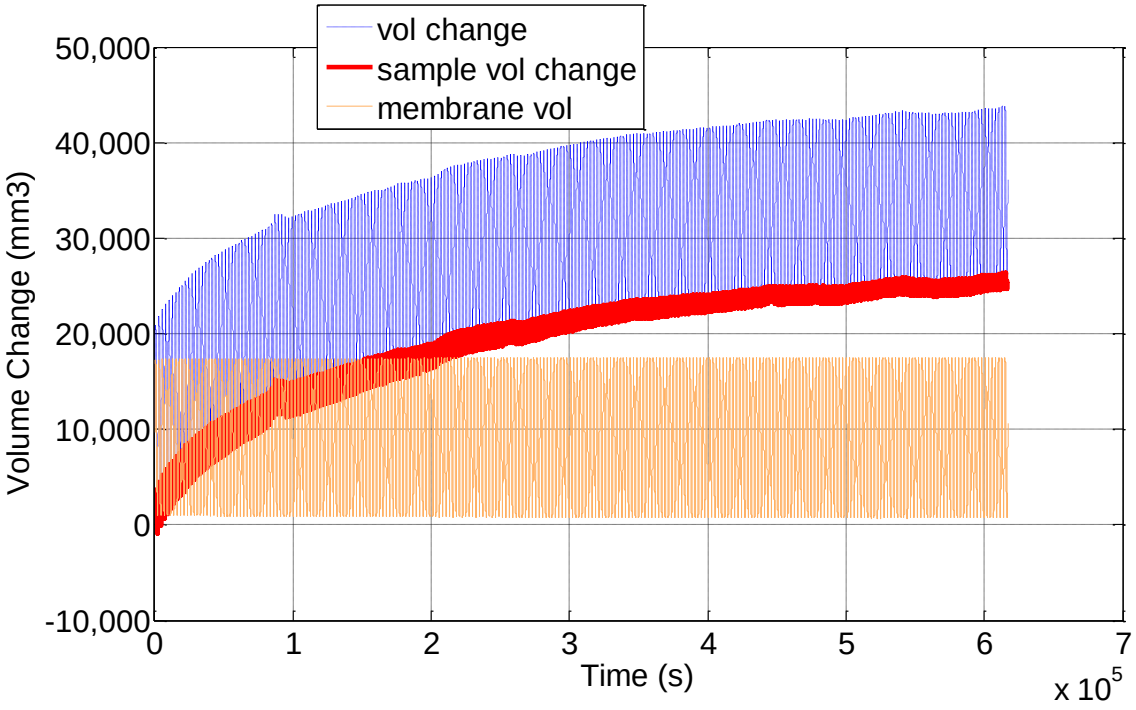

Figure 4.14: Volume change from controller for the cell pressure cyclic test

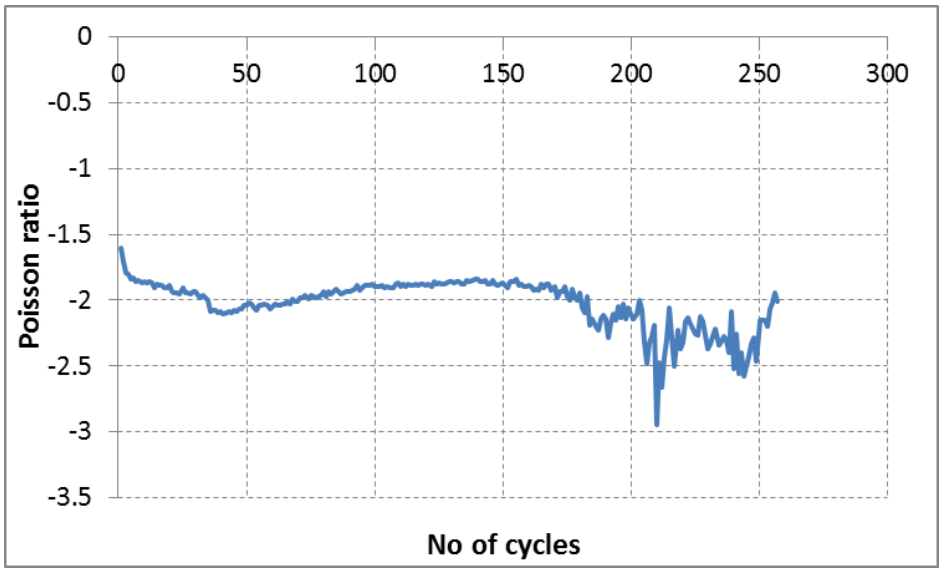

(a)

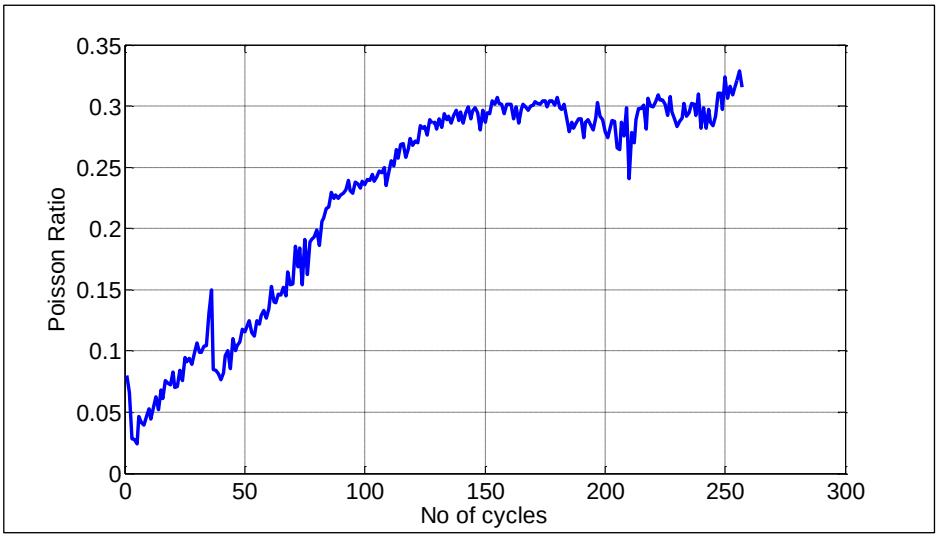

(b)

Figure 4.15 :Poisson's ratio of cell pressure cyclic test (a) before the correction (b) after the correction- polynomial function correction from unglued specimen membrane test

A glued specimen was prepared using epoxy resin to eliminate free movement of particles. Figure 4.16 shows the volume change against cell pressure change for glued and unglued specimens when the cell pressure cycles. Like the unglued specimen, applying a polynomial correlation between cell pressure change and volume change derived for the glued specimen reduces the amplitude of volumetric strain and improves the bulk modulus, shear modulus, and Poisson's ratio in line with other reported values.

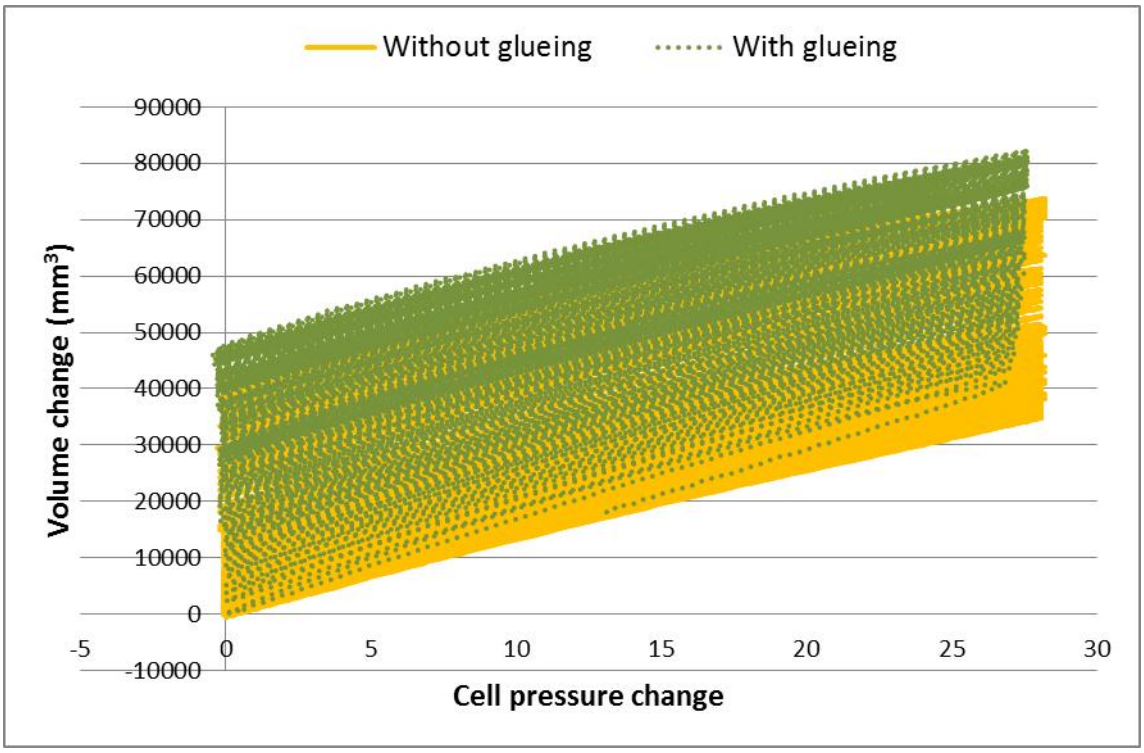

Figure 4.16: Volume change against cell pressure change for glued and unglued specimens

Figure 4.17 shows the volume change against number of cycles during a membrane test on the glued specimen where the cell pressure was cycled between 30 kPa and 60 kPa. As the specimen was glued, particle rearrangement was absent. The test shows that volume change from the controller seems to have both repetitive and creep membrane penetration elements. Thus the volume change during the glued specimen membrane test can be presented by a combination of sinusoidal waveform and creep polynomial functions (Figure 4.18).

The basic form of sine wave function of time (t) is given by:

$$y(t) = A.\sin(2\pi ft + \varphi) = A.\sin(\omega t + \varphi) \tag{4.2}$$

where;

A = the amplitude, which is the peak deviation of the function from zero.

f = the ordinary frequency, which is the number of oscillations (cycles) that occur each second of time.

ω = 2πf- the angular frequency, which is the rate of change of the function argument in units of radians per second

φ = the phase, which specifies (in radians) where in its cycle the oscillation is at t= 0.

Repetitive membrane penetration was calculated from the sine wave function as follows;

$$Cyclic\ sinusoidal\ membrane\ penetration = Amplitude\ of\ volume\ change\ * sin(2\pi Cycle + starting\ phase) + Intercept\ of\ volume\ change \quad (4.3)$$

Where;

Amplitude and Intercept of volume change = 1800 mm^3

Starting phase= 0. These values are taken from Figure 4.17.

The creep function was calculated by extracting the minimum volume change from Figure 4.17 (when the cell pressure = 30 kPa) during each cycle and fitting a polynomial through these points as shown in Figure 4.19.

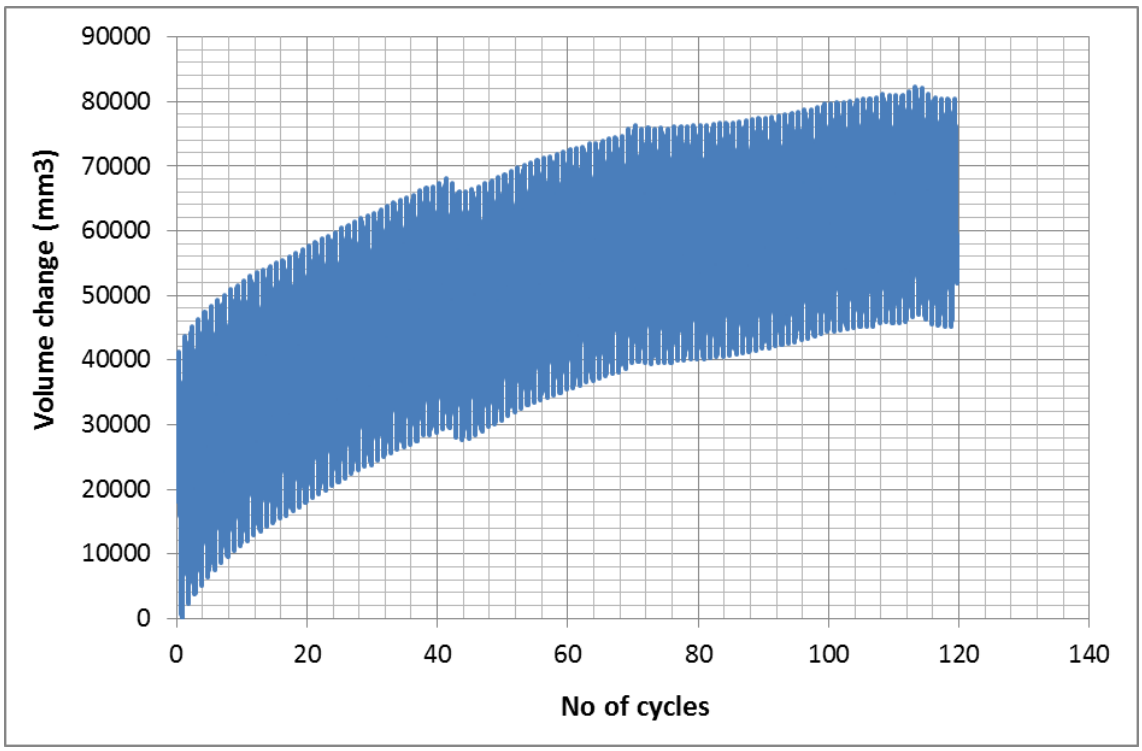

Figure 4.17: Volume change of controller during the membrane test on glued specimen

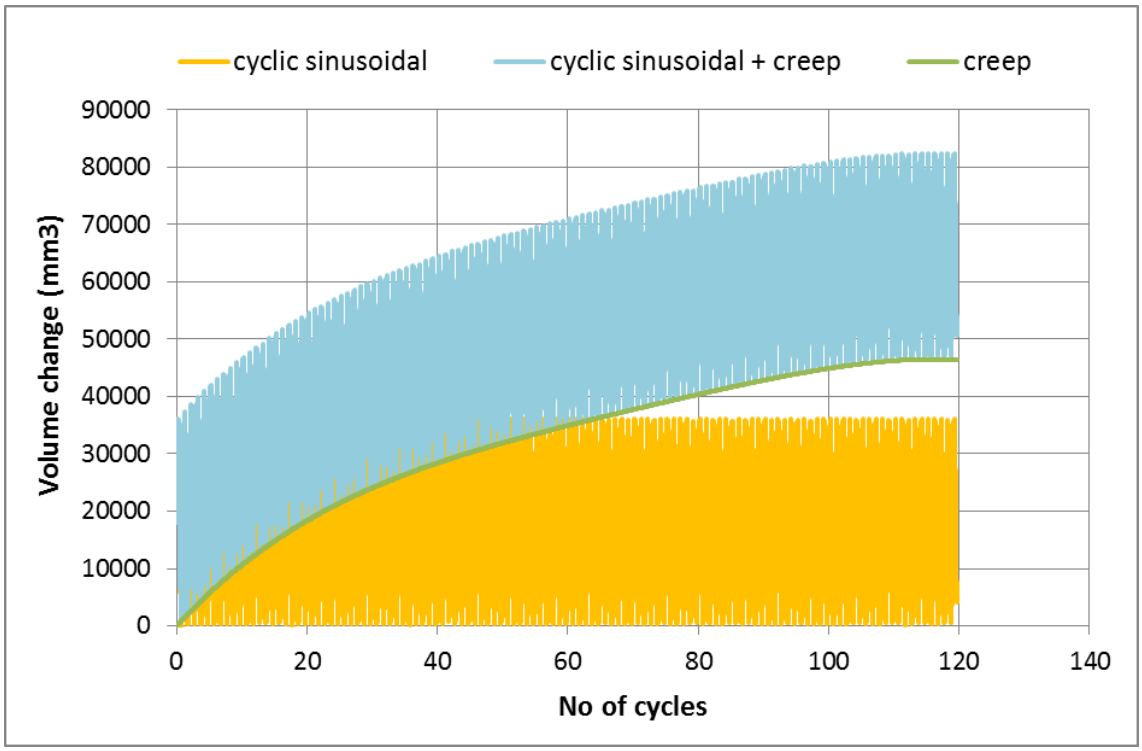

Figure 4.18: Sinusoidal wave and creep membrane penetration elements

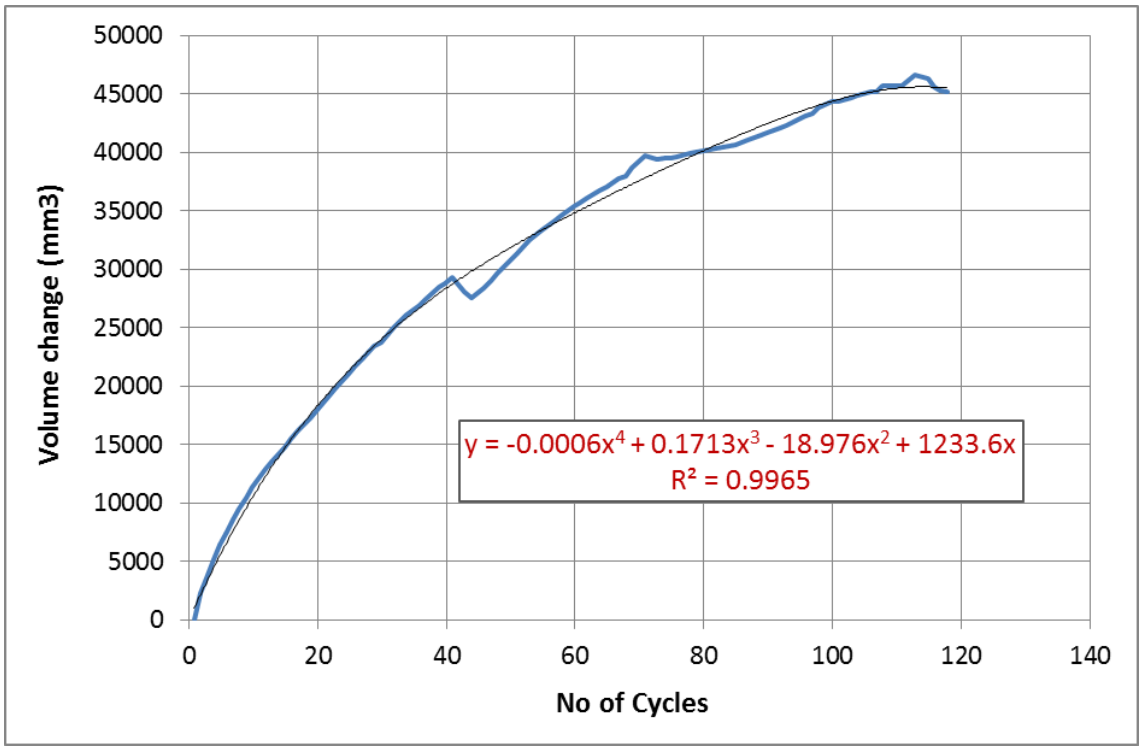

Figure 4.19: Fitting polynomial correlation for the membrane creep element during the membrane test on glued specimen

Figure 4.20 shows a comparison of the membrane test volume change and the sinusoidal wave and creep functions. These show that a reasonable match is achieved despite some unusual discontinuities in the creep component of movement (e.g. at 40 cycles). These sudden movements may be attributed to membrane slippage on the platens.

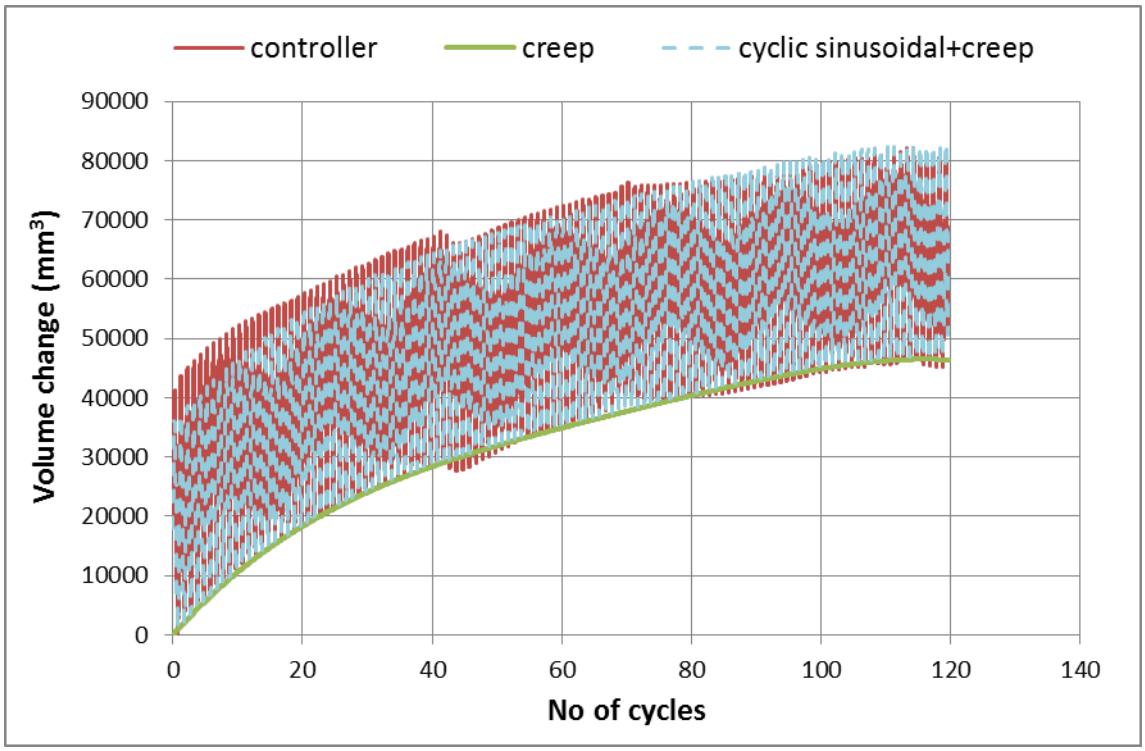

Figure 4.20: Volume change of controller during the membrane test on glued specimen is matched by Sinusoidal wave and creep membrane penetration elements

The sine wave and creep membrane correction functions were applied to a cell pressure cyclic test where q= 5kPa to 140 kPa, cell pressure= 30 kPa to 60 kPa, and period= 40 minutes/cycle (Figure 4.21).

Figure 4.21 shows that initially the corrections appear to perform well and the small band of difference between the corrected values and the measured values represents the volume change due to particle rearrangement. However, after about 18 cycles the correction over predicts the creep component of movement and overtakes the measured maximum controller water volume change.

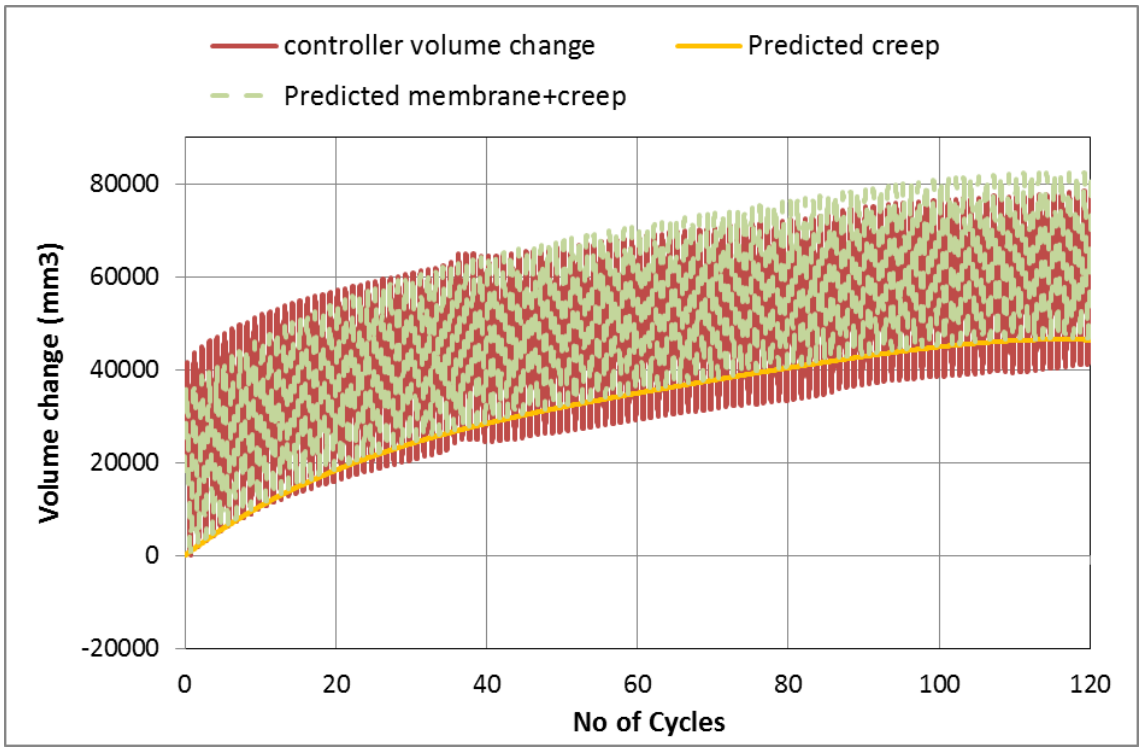

Figure 4.21: membrane correction applied to the cell pressure cyclic test

The differences may be due to:

- Axial stress suppressing membrane creep
- An inherent variability between specimens

In conclusion, it wasn't possible to reliably correlate membrane penetration with cycles. This is mainly due to creep effects. Slippage of membrane on platen may also have contributed.

From the membrane test observations, an alternative volume change measurement technique using radial Hall Effect strain gauges was introduced for cycled cell pressure tests.

4.5 Membrane Young's modulus test

The Young's modulus of the membrane is needed to correct for membrane stress that may be applied to the specimen but which is not directly measured.

Young's modulus tests need to cover the expected range of stress within the membrane during a triaxial test. To determine test parameters the stress range was estimated based on the typical Young's modulus of a latex membrane (1400 kPa according to ASTM D4767-02) and the measured radial strain. These calculations estimate the maximum stress as 4.4 kPa.

Based on the expected stress ranges, tensile/extension tests were carried out on strips of membrane material.

Three membrane extension tests were carried out to determine the Young's modulus of the 2 mm thick Latex membranes used (Table 4.1 and Table 4.2).

- Test 1 was carried out using a 15 mm wide and 250 mm long membrane strip and the deflection was measured by micrometer (Figure 4.22).
- Test 2 was carried out using a 25 mm wide and 260 mm long membrane strip and the deflection was measured by micrometer.
- Test 3 was carried out using a 25 mm wide and 260 mm long membrane strip and the deflection was measured by height gauge (Figure 4.23).

Test 1	length = 250 mm width= 15 mm		Test 2	length = 260 mm width= 25 mm	
Weight (g)	Deformation t=0	Reading	Weight (g)	Deformation t=0	Reading
0	0	micrometer	0	0	micrometer
20	0.9	micrometer	10	0.61	micrometer
50	2.656	micrometer	20	0.84	micrometer
100	5.328	micrometer	50	1.676	micrometer
150	8.318	micrometer	100	3.764	micrometer
200	12.88	micrometer	50	2.38	micrometer
250	16.422	micrometer	150	5.588	micrometer
300	20.214	micrometer	50	1.892	micrometer
400	24.78	micrometer	200	7.71	micrometer
450	39	manual	50	1.984	micrometer
550	45.5	manual	250	10.062	micrometer
0	11	manual	50	2.432	micrometer
750	73.5	manual	300	12.58	micrometer
0	11	manual	50	2.438	micrometer
1000	113	manual	400	17.282	micrometer
0	12	manual	50	2.4	micrometer
			450	20.444	manual
			50	2.873	micrometer
			550	25.07	manual
			50	2.502	micrometer
			750	38	manual
			50	4.328	micrometer
			1000	57	manual

Table 4.1: Deflection measurement using micrometer during extension test

Test 3	length = 260 mm width= 25 mm	
Weight (g)	Deformation t=0 min	Reading
0	0	height gauge
10	0.44	height gauge
20	0.57	height gauge
50	1.63	height gauge
100	3.51	height gauge
50	2.14	height gauge
150	5.46	height gauge
50	1.96	height gauge
200	7.46	height gauge
50	2.62	height gauge
250	9.65	height gauge
50	3.08	height gauge
450	18.78	height gauge
50	3.32	height gauge
750	36.29	height gauge
50	5.42	height gauge
1000	53.13	height gauge
50	7.06	height gauge

Table 4.2: Deflection measurement using height gauge during extension test

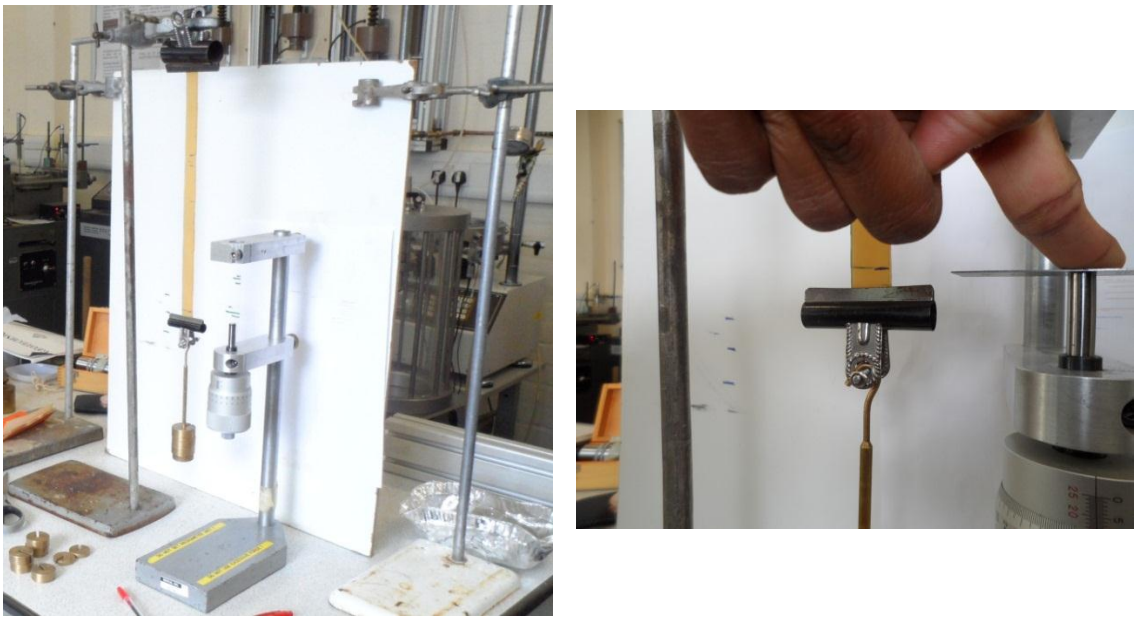

Figure 4.22: Membrane deflection measured by micrometer

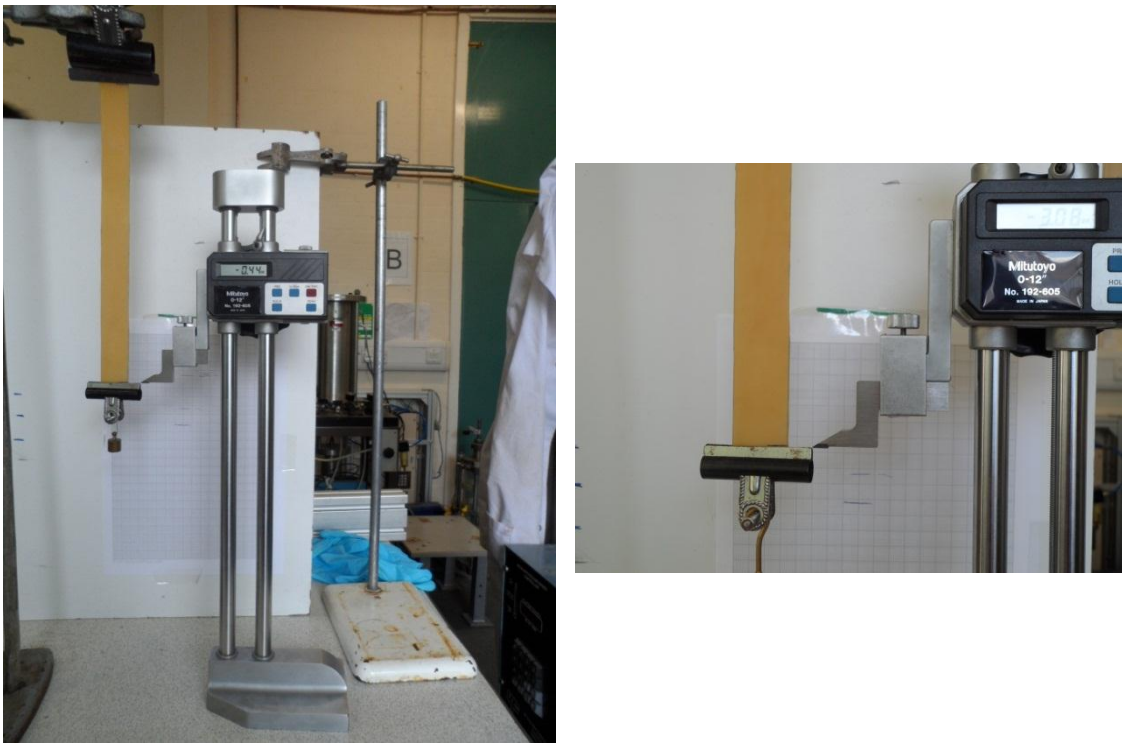

Figure 4.23: Membrane deflection measured by height gauge

The stress-strain behaviour of the membrane during the extension tests is shown in Figure 4.24. Young's modulus values obtained from the initial stress loading points up to 50 kPa during the extension tests are shown in Figure 4.25. Young's modulus from Test 1, Test 2, and Test 3 are 1526.4 kPa, 1332.1 kPa, and 1385.7 kPa respectively, giving an average value of 1414.73 kPa.

Test 3 was more reliable as readings were taken using a height gauge where less human error has been introduced. For comparison, during Test 1 and Test 2 readings were taken using micrometer where the readings depend on eye level to judge the extension of the membrane.

The Young's modulus of the latex membranes obtained from these tests are close to the typical Young's modulus of latex of 1400 kPa according to ASTM D4767-02. Thus Young's modulus of latex membrane was taken as 1400 kPa for calculating the additional radial stress due to membrane deformation (membrane correction) during the monotonic shear tests.

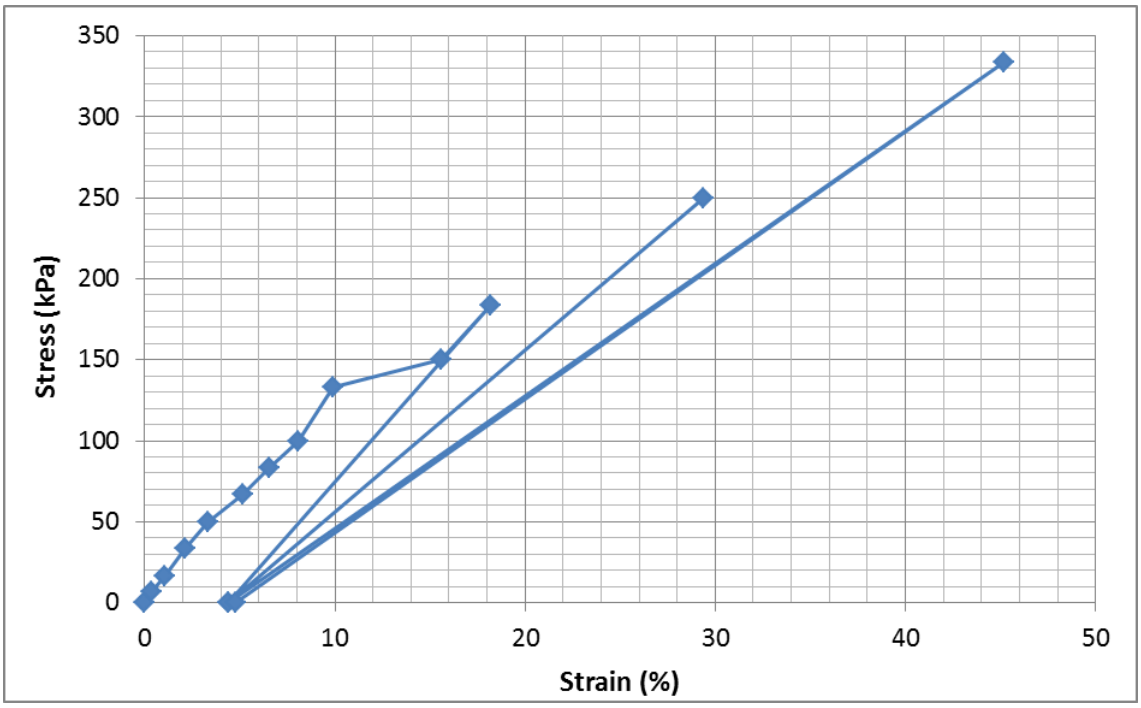

(a) Test 1: 15 mm width and 250 mm length , deflection measured by micrometer

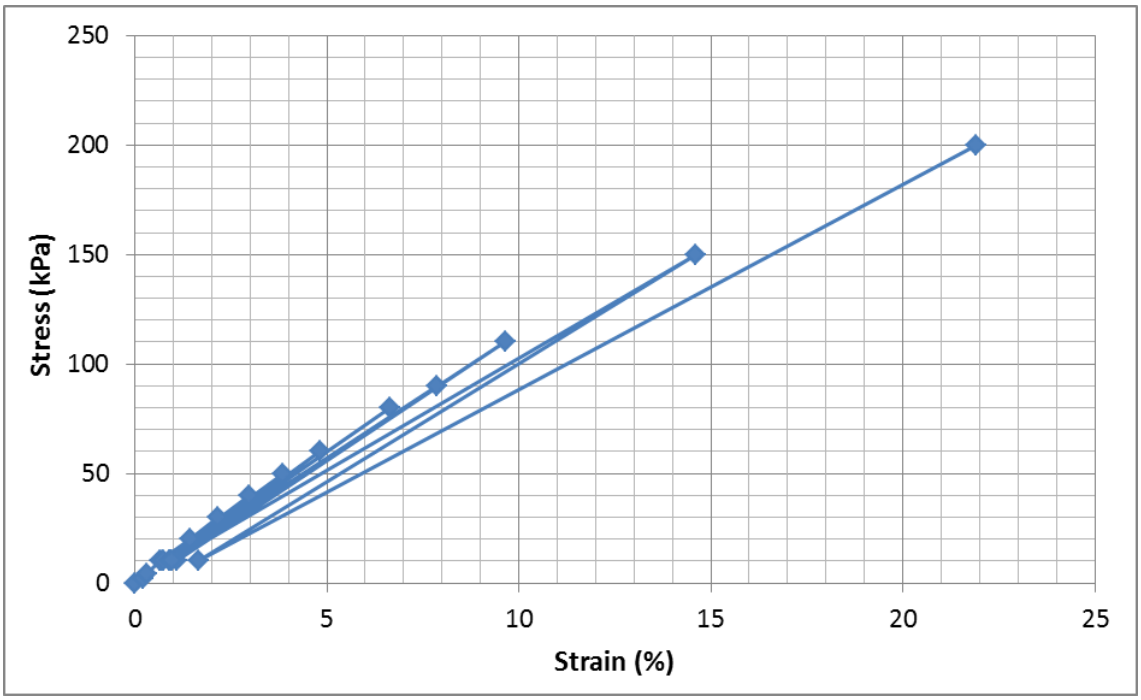

(b) Test 2 : 25 mm width and 260 mm length, deflection measured by micrometer

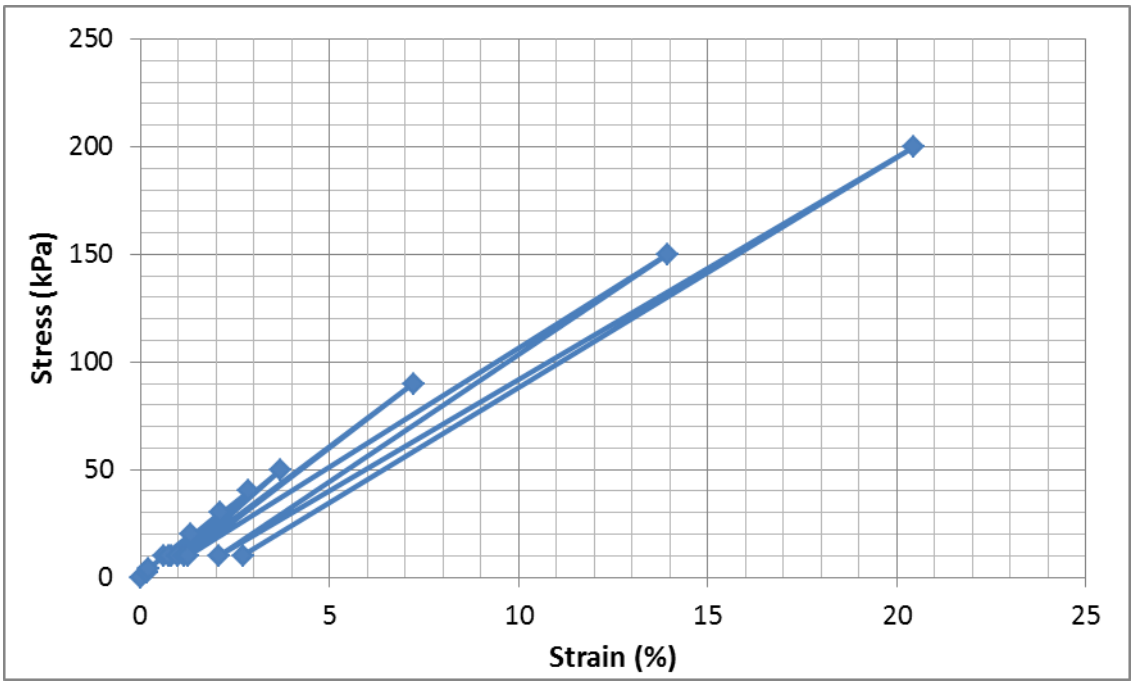

(c) Test 3: 25 mm width and 260 mm length, deflection measured by height gauge

Figure 4.24: Stress-strain behaviour of membrane during extension test

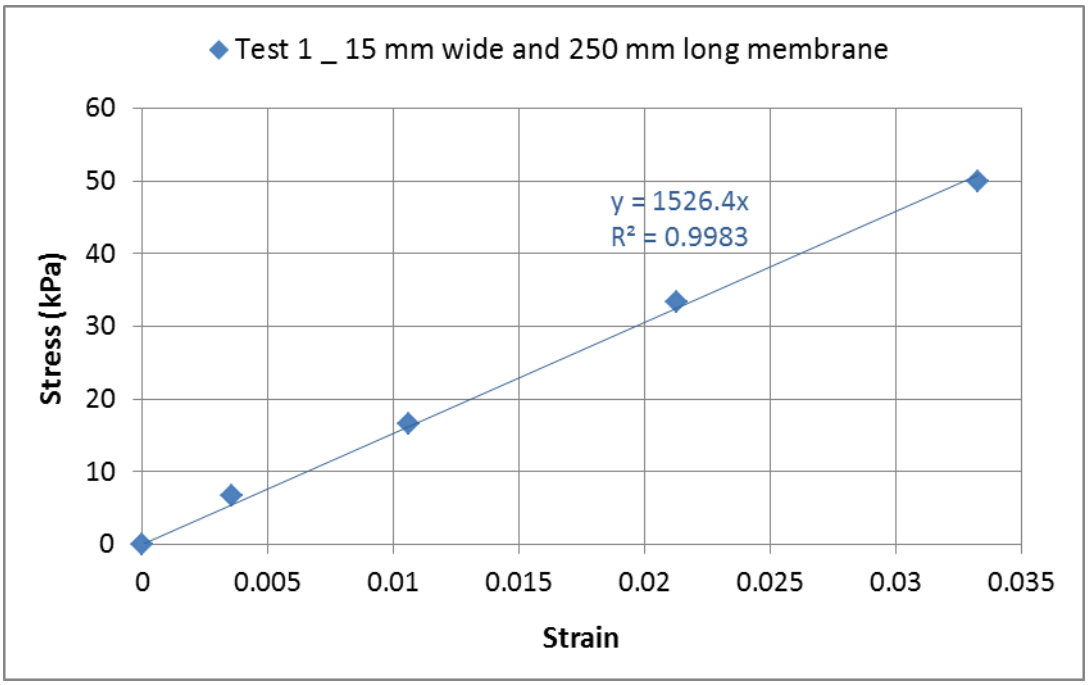

(a) Test 1: deflection measured by micrometer

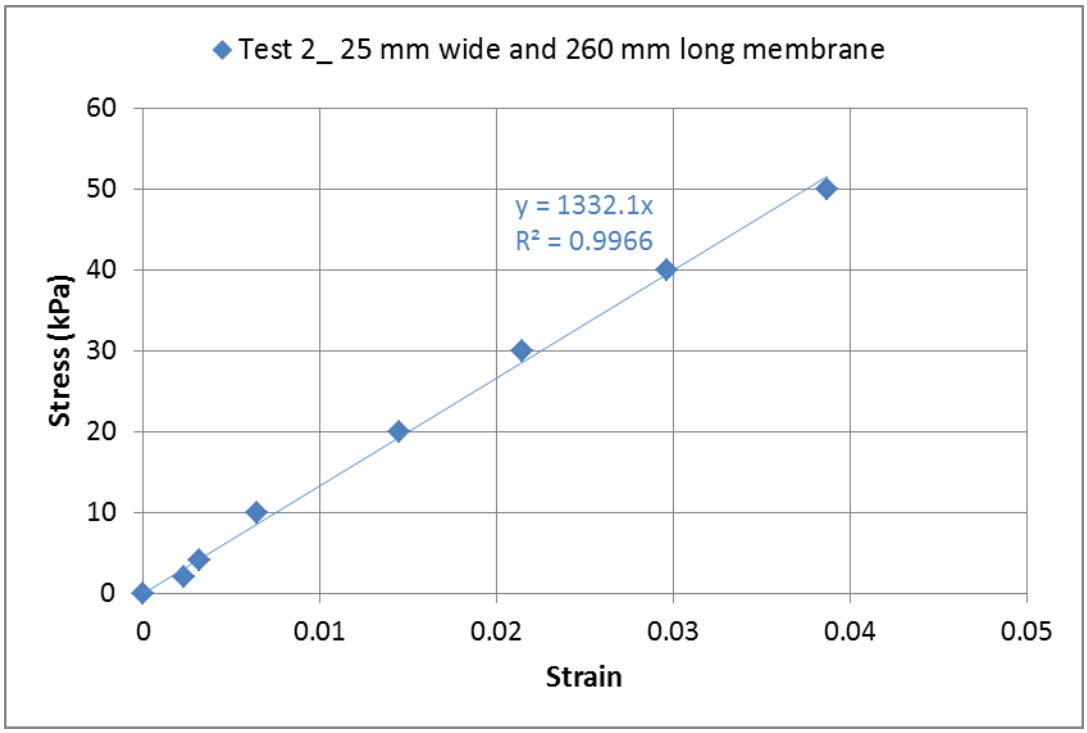

(b) Test 2 : deflection measured by micrometer

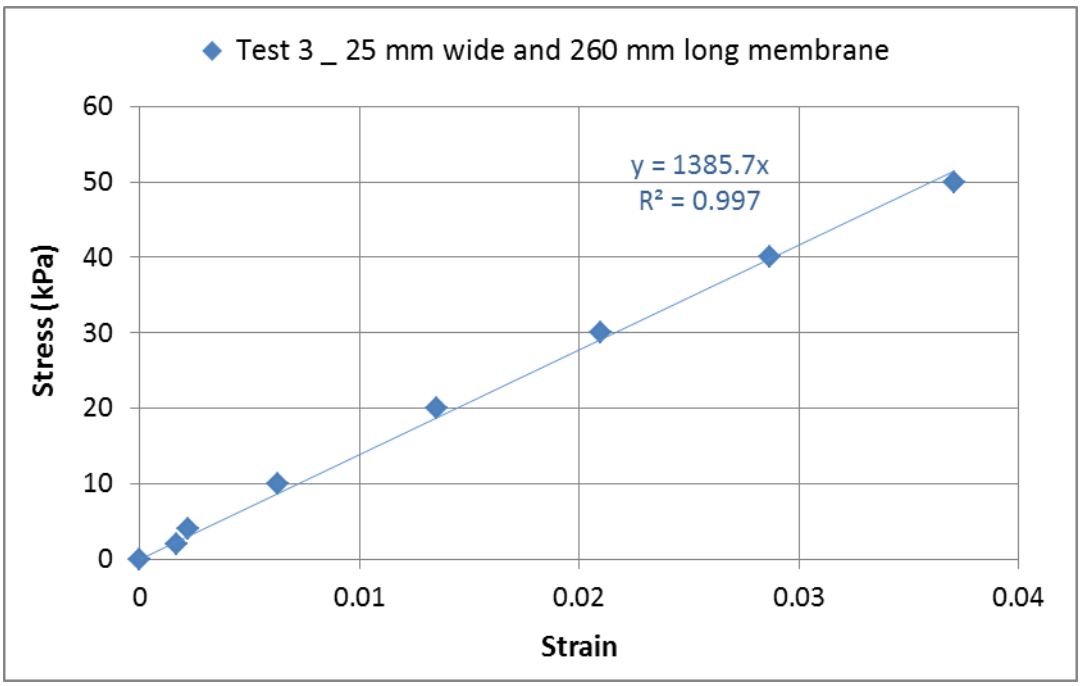

(c) Test 3: deflection measured by height gauge

Figure 4.25: Young modulus determination from the initial loading points

4.6 Triaxial test preparation and test procedure

Through a process of trial and improvement, modifications were made to the specimen preparation procedure.

A metal three split mould dimension of 301 mm height and 150 mm diameter was made in the workshop. This split mould could be joined together using a metal clip and plastic tape for specimen preparation. A metal top cap with apertures to apply suction and insert resin was used. Combinations of thick square and round O-rings were used to hold the membranes and provide a seal. Membranes of 0.4 mm and 1 mm thickness were not sufficient puncture resistant. Thus 2 mm membrane was used for the experiments.

4.6.1 Specimen preparation

A 2 mm thick latex membrane was pulled up and rolled over a split mould and held in place by two O-rings at the top and bottom. A porous disc was placed at the bottom and held in place using flexible metal clips.

A known mass of scaled ballast was taken for specimen preparation. The split mould was then filled with scaled ballast in 3 layers. Each layer was vibrated for 1 minute under self-weight followed by vibration for 1 minute with a 5 kg weight on top of it. The top of the specimen was levelled by hand placement of particles up to the top of the mould followed by further vibration under self-weight. The mass of the specimen was calculated from the remaining test material. Specimens prepared by this vibratory compaction method had initial densities and void ratios in the ranges of 1515-1606 kg/m^3 and 0.73-0.83 respectively. The split mould was then transferred to the triaxial cell base and the flexible metal clips were removed.

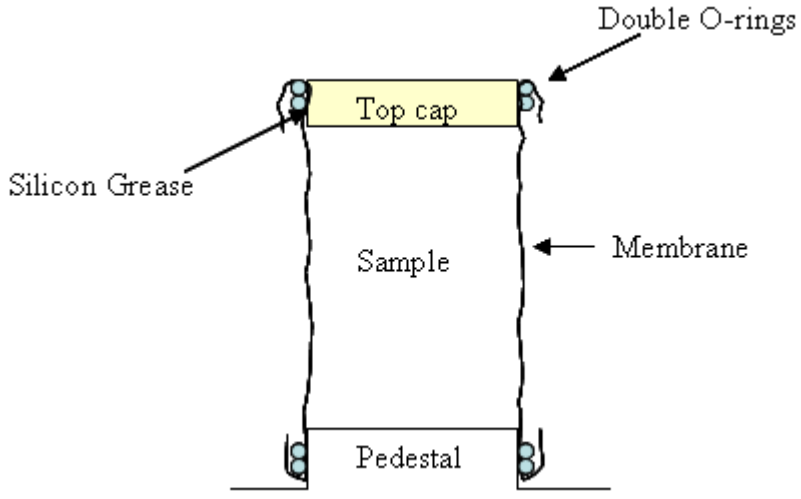

Figure 4.26: Sample seal arrangement

A layer of silicon grease was applied to the rim of the base pedestal and the top cap. The membrane was pulled over and secured using 2 O-rings as shown in Figure 4.26. An internal suction of approximately 20 kPa was then applied to the specimen through the valve at the bottom of the cell base using a vacuum pump. This held the specimen in place and the split mould was removed (Figure 4.27). The triaxial cell was bolted to the cell base. The cell base was then positioned and bolted onto the loading frame. Then the cell was filled with deaired water.

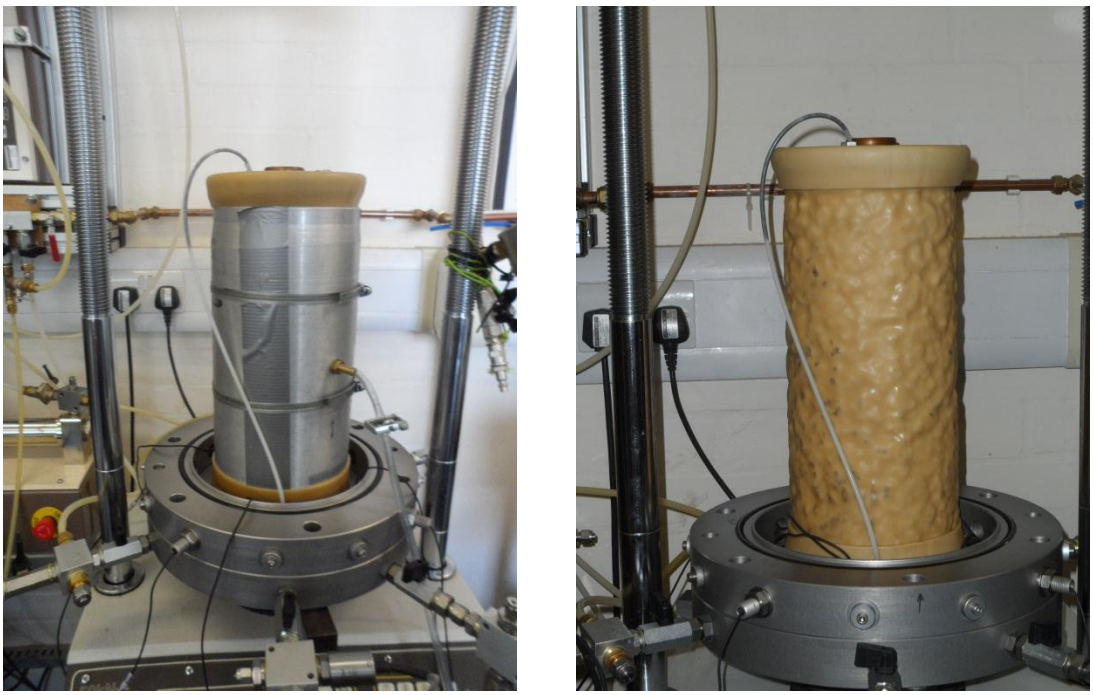

(a) (b)

Figure 4.27: Triaxial test preparation: (a) Scaled ballast specimen within split mould; (b) Specimen under vacuum

4.6.2 Modification for extension test

For extension tests, a ball jointed loading cap was fixed to the existing metal top cap as shown in Figure 4.28. This ball jointed loading cap was directly connected to the load cell. A similar diameter hollow rod was screwed to the loading ram by modifying its top. This hollow rod allows the lowering of triaxial cell to the cell base without disturbing the specimen and it was detached once the cell was in place.

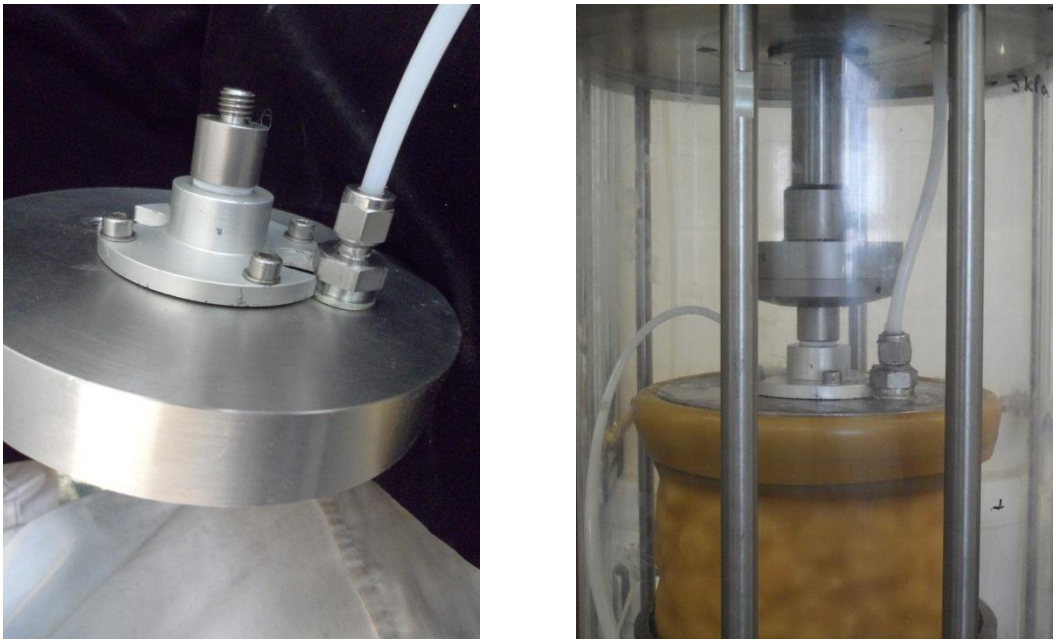

Figure 4.28: Top cap arrangement during extension test

4.6.3 Test Procedures

Monotonic loading tests:

For dry monotonic tests;

- Cell pressure was applied and the internal suction was removed and the specimen was then ready for testing.

For saturated monotonic tests;

- A cell pressure of about 50 kPa was applied.
- The specimen was saturated using suction to speed up the flow of water into the voids of the specimen and to help remove air.
- The cell and back pressure were increased in steps to the target test values. The difference between cell and back pressure was kept around the target effective confining pressure during the incremental increase of cell and back pressure.
- During these pressure increment steps, the degree of saturation was checked by means of a B-value calculation. For example; following the initial saturation stage, specimens had a B value of approximately 95% and 93% at an effective cell pressures of 15 kPa and 200 kPa respectively.
- Saturated specimens were allowed to settle prior to shearing.

Two 1000 cc pressure controllers were used for monotonic loading to provide enough room for water movement during the shearing of specimens. These pressure controllers were incapable of drawing water into and out of the cell at high axial loading rates, resulting in fluctuations in the cell pressure. Thus a loading rate of 0.04 mm/ minute was used.

The experiment was started with a little space between the ram and top cap. The load cell reading was set to zero. Thus when the ram was brought into contact with the top cap, the deviator stress increased from zero. The experiment was usually carried out up to 16% axial strain.

Cyclic loading tests:

For the cyclic tests on a dry specimen, the cell pressure was applied and the suction was removed. The load was slowly brought to median deviator stress.

The amplitude of cyclic loading was selected to obtain the desired q_{min} and q_{max} stress states. A minimum deviator stress q_{min} value of 5 kPa was used to represent the dead weight of the sleeper and rail (see section 4.8).

The maximum deviator stress q_{max} was chosen to be representative of loading by a train. The triaxial apparatus is capable of carrying out cycles at the rate of 5 minutes per cycle. Normally the specimens were loaded at durations of 5 minutes per cycle. The initial 2 cycles were normally carried out over 10 minutes per cycle, with the slower loading rate used to help stabilise the specimens and allow for “bedding in”. Following this, loading was repeated at 5 minutes per cycle until the desired number of cycles had been applied.

Cyclic experiments were carried out using 200 cc advanced and 200 cc dynamic GDS pressure controllers. The 200 cc advanced controller was capable of cycling the deviator stress at 5 minutes/cycle and the cell pressure at 40 minutes/cycle. In comparison, the 200 cc dynamic controller was capable of cycling both deviator stress and cell pressure at 5 minutes/cycle. Thus during the later stages of the project, a 200 cc dynamic controller was procured for testing.

Extension testing:

Extension tests were carried out on some specimens after set numbers of conventional cycles. In these tests, specimens were prepared with an extension top cap. During the

extension stage, the axial stress was kept constant and the cell pressure was applied and removed or cycled. The deviator stress was applied and removed or cycled to maintain the axial stress at a constant value.

For example;

If the cyclic loading stresses were σ_3'=45 kPa and q=5-225 kPa, the extension stage stresses would be σ_3' =45-200 kPa and q=5-(-150) kPa where σ_1' =50 kPa which was the minimum axial stress during the cyclic loading stage.

The extension stage was used to represent in an idealised way the effects of tamping. This is discussed further in section 4.8.

4.7 Description of parameters

Strain parameters:

The axial strain, ϵ_a is calculated as change in height of specimen in the axial direction divided by the initial specimen height. Radial strain, ϵ_r is the change in specimen diameter divided by the initial diameter of the specimen. It was calculated from the pressure controller and the hall effect radial callipers where they were used.

$$Radial\ strain\ from\ controller\ \epsilon_r = (\epsilon_{vol} - \epsilon_a)/2 \tag{4.4}$$

$$Radial\ strain\ from\ calliper\ \epsilon_r = \frac{(\Delta radial\ calliper\ displacement/2)}{initial\ diameter\ of\ specimen} \tag{4.5}$$

The volumetric strain, ϵ_{vol} is the change in volume of specimen divided by initial volume of specimen. It can be calculated from the pressure controller and/or the radial calliper readings. ϵ_{vol} from the radial calliper is calculated as $\epsilon_{vol} = \epsilon_a + 2\epsilon_r$, where ϵ_r is from radial calliper.

Permanent axial and volumetric strain is taken as the strain that occurs at the minimum deviator stress of the cycle.

Stress parameters:

- The deviator stress, q (in kPa) is calculated as

$$q = \frac{Q}{A_{eff}} = \frac{Q}{A_o}\left(\frac{1-\epsilon_{vol}}{1-\epsilon_a}\right)$$

(4.6)

where Q is the ram load (in KN), A_{eff} is the current area of the specimen, A_o is the original area of the specimen, ϵ_a is the axial strain and ϵ_{vol} is the volumetric strain. The effective cross-sectional area of the specimen A_{eff} was calculated assuming the specimen remains a right cylinder during shearing.

- The effective radial stress, σ_3' (in kPa) is calculated as

$$\sigma_3' = (\sigma_c - u) + \delta\sigma_m$$

(4.7)

where σ_c is cell pressure, u is pore pressure and $\delta\sigma_m$ is the additional radial stress due to membrane deformation or membrane correction. The additional radial stress due to membrane deformation $\delta\sigma_m$ can be calculated as (Fukushima and Tatsuoka, 1984).

$$\delta\sigma_m = \frac{2E_m t_m \epsilon_r}{d}$$

(4.8)

where E_m is the young modulus, t_m is the membrane thickness, d is the current specimen diameter and ϵ_r is the specimen radial strain which is $(\epsilon_{vol} - \epsilon_a)/2$.

- The average principal effective stress, p' (in kPa) is calculated as

$$p' = (\sigma_1' + 2\sigma_3')/3$$

(4.9)

where σ_1' and σ_3' are the effective axial and radial stress respectively.

Other parameters:

- The mobilized friction angle, ϕ'_{mob} is calculated as

$$\phi'_{mob} = \sin^{-1}\left(\frac{\sigma_1' - \sigma_3'}{\sigma_1' + \sigma_3'}\right)$$

(4.10)

ϕ'_{mob} is defined by the tangent to the Mohr circle which passes through the origin and is a measure of strength mobilized to enable the specimen to carry the applied stresses.

- The rate of dilation, d is calculated as

$$d = -\frac{d\epsilon_{vol}}{d\epsilon_q} \tag{4.11}$$

where $d\epsilon_{vol}$ is volumetric strain increment and $d\epsilon_q$ is triaxial shear strain increment which is defined as $2(\epsilon_a - \epsilon_r)/3$. The dilation angle is therefore $\psi = \sin^{-1}\left(-\frac{d\epsilon_{vol}}{d\epsilon_q}\right)$

- The resilient modulus (equivalent to Young's modulus ***E***), M_r (in kPa) is calculated as

$$M_r = \frac{\Delta q}{\Delta \epsilon_a} = \frac{q_{max} - q_{min}}{\epsilon_a \, at \, q_{max} - \epsilon_a \, at \, q_{min}} \tag{4.12}$$

Where $\Delta\epsilon_a$ is on the unloading step.

- The shear modulus, G (in kPa) is calculated as

$$G = \frac{\Delta q/2}{\Delta \gamma} \tag{4.13}$$

where γ is shear strain which is $(3\epsilon_a - \epsilon_{vol})/2$.

- The bulk modulus, K (in kPa) is calculated as

$$K = \frac{\Delta p'}{\Delta \epsilon_{vol}} \tag{4.14}$$

where p' is average principal effective stress.

- Poisson's ratio, ν is calculated as

$$\nu = 0.5 - \frac{Resilient\ modulus}{6 Bulk\ modulus} = 0.5 - \frac{M_r}{6K} \tag{4.15}$$

4.8 Justification of loading in the tests

When traffic loading takes place on the rail track, the ballast experiences different vertical stresses during loaded and unloaded states. The confining pressure of the ballast layer also responds to changing vertical stress. In the past, researchers have only considered cycling the deviator stress during the cyclic triaxial experiments on ballast. Cycling the confining pressure is a more realistic way to simulate real track stress conditions. Thus in this research some cyclic tests were carried out where both confining pressure and deviator stress were simultaneously cycled.

As described in section 2.7, some researchers studied the vertical and horizontal stresses experienced by the sub structure components in rail track at different depths below the sleeper (Shenton, 1975, Stewart et al., 1985, Powrie et al., 2007, Le Pen, 2008). The deviator stress and confining pressure for the cyclic loading were selected by considering the literature.

Horizontal stress due to train passage:

Le Pen (2008) measured a confining pressure of around 10 kPa for an applied vertical load of 80 kN (corresponding to an axle load of 160 kN) after 100 cycle applications below the centerline of the crib. Applying the same logic to the vertical load of 200 kN (Shenton's axle load) will result the confining pressure of 12.5 kPa (10 kPa x 200kN / 160 kN = 12.5 kPa).. However, the confining pressure below the rail seat would have been higher. Stewart et al. (1985) reported that the horizontal stress in the ballast at maximum and minimum loads of cyclic loading fluctuated between 20 kPa and 60 kPa and eventually reached approximately 30 kPa.

Vertical stress due to train passage:

The location being modelled was considered to be below the railseat as shown in Figure 4.29. If the vertical load is due to a heavy freight train;

Axle mass of heavy freight train is 22.5 tonnes

Axle load = $(22.5 \times 10^3 \times 9.81)/10^3 = 220.725$ kN

Standard given by Network Rail, RT/CE/C/039 (2003), assumes a 50% of axle load transfers to the sleeper immediately beneath an axle and the other 50 % to the sleepers adjacent to that on both sides.

G44 sleeper length and width are 2.5 m and 0.285 m

Average sleeper base contact pressure = 220.725 / (2 x 2.5 x 0.285)

= 154.38 kPa

This is an average pressure below the sleeper. Shenton's (1975) work shows the uneven distribution of pressure below the sleeper. He reported maximum sleeper base contact pressure varied between 200 kPa and 250 kPa for an axle load of 200 kN and the location of maximum sleeper base contact pressure was beneath the rail. Considering a straight rail line condition, using symmetry it could be concluded that the axel load is distributed equally between two wheels.

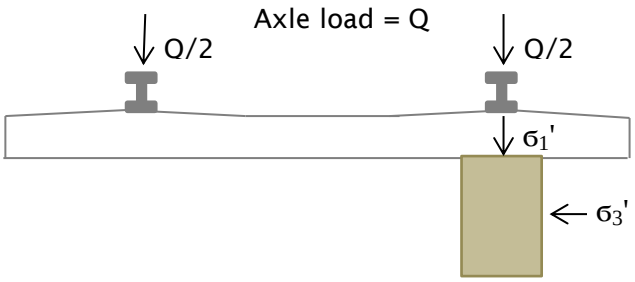

Figure 4.29: Stress state in the ballast directly below rail

Stresses due to tamping:

As discussed in section 2.2, during tamping, the rails and sleepers are raised and tamping tines are lowered into the ballast on either side of sleeper to squeeze the ballast. Crib ballast is pushed into the gap beneath the raised sleeper and support the sleeper at the required profile. In reality, the track soon returns to its pre-tamping profile under train loading. Tamping tines disturb the already densely packed ballast and fill the gap with loose ballast to the required level by vibration. Also these vibrating tines cause ballast damage which produces fine particles (Selig and Waters, 1994).

During tamping, a higher horizontal force is applied compared to the vertical force. Tamping can be simulated in the laboratory by stress reversal. Extension testing can be used to reverse the direction of major (σ_1') and minor (σ_3') principal stresses during the cyclic loading.

Loading chosen for monotonic failure tests:

To determine the strength of the ballast material over a range of stresses appropriate to the in-situ stress on real track, monotonic loading tests were carried out to failure over an appropriate range of confining stresses. These tests also informed the cyclic tests so that the cycles of load would be within the static failure strength of the ballast.

Loading chosen for cyclic tests:

Cyclic tests are carried out in two stages a train loading stage (1) and a tamping stage (2). The loading selected for the triaxial testing is described below.

(1) Train loading

A maximum deviator stress, q_{max} value of 225 kPa was applied to most of the cyclic tests which is close to Shenton's value. A minimum deviator stress, q_{min} value of 5 kPa was applied to represent the dead weight of the sleeper and rail.

For example,

G44 sleeper weight is 310 kg

G44 sleeper length and width are 2.5 m and 0.285 m

Sleeper spacing is 0.65 m

Rail weight per sleeper = (sleeper spacing x rail load per meter x 2)

= (0.65 m x 60 kg/m x 2) = 78 kg

Average pressure below the sleeper due to self-weight of sleeper and rail

= (self-weight of sleeper and rail) / (Area of sleeper)

= (310+78) x 9.8 / (0.285 x 2.5 x 1000) = 5.34 kPa

The magnitude of confining pressure was selected as 45 kPa and 55 kPa for the constant cell pressure cyclic tests. For the cyclic cell pressure tests, the cell pressure was cycled between 15 kPa and 45 kPa (Figure 4.30).

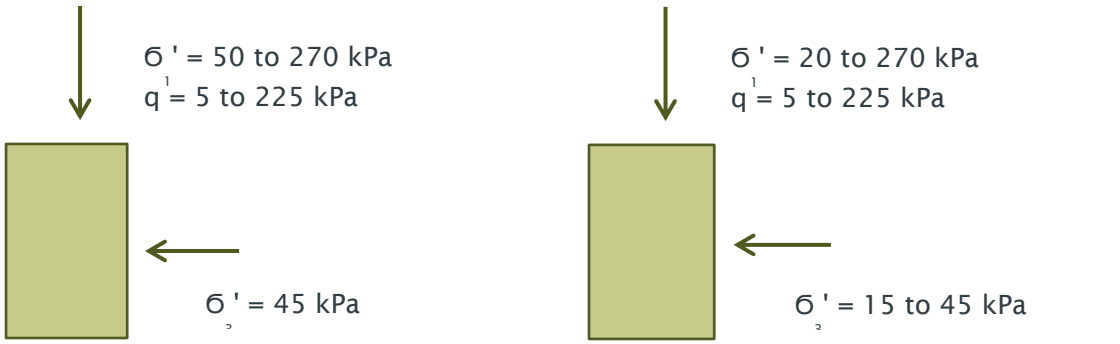

(a) Cyclic loading – constant cell pressure

(b) Cyclic loading – cyclic cell pressure

Figure 4.30: Stress condition during cyclic loading

Figure 4.31 shows the stress path during the constant cell pressure and cyclic cell pressure tests. A more realistic stress path is plotted considering the horizontal pressure to be the major principal stress on unloaded track. The more realistic stress path is plotted for comparison, because during the cyclic test axial stress (σ_1') was the major principal stress even on the unloaded state of cycle. The stress path followed in the cyclic cell pressure tests is not much different from the more realistic stress path. σ_2' is constrained to equal σ_3' in the triaxial test, but it can vary in real track. ϕ_{mob}'=50° is drawn assuming it is as a possible Mohr coulomb failure line.

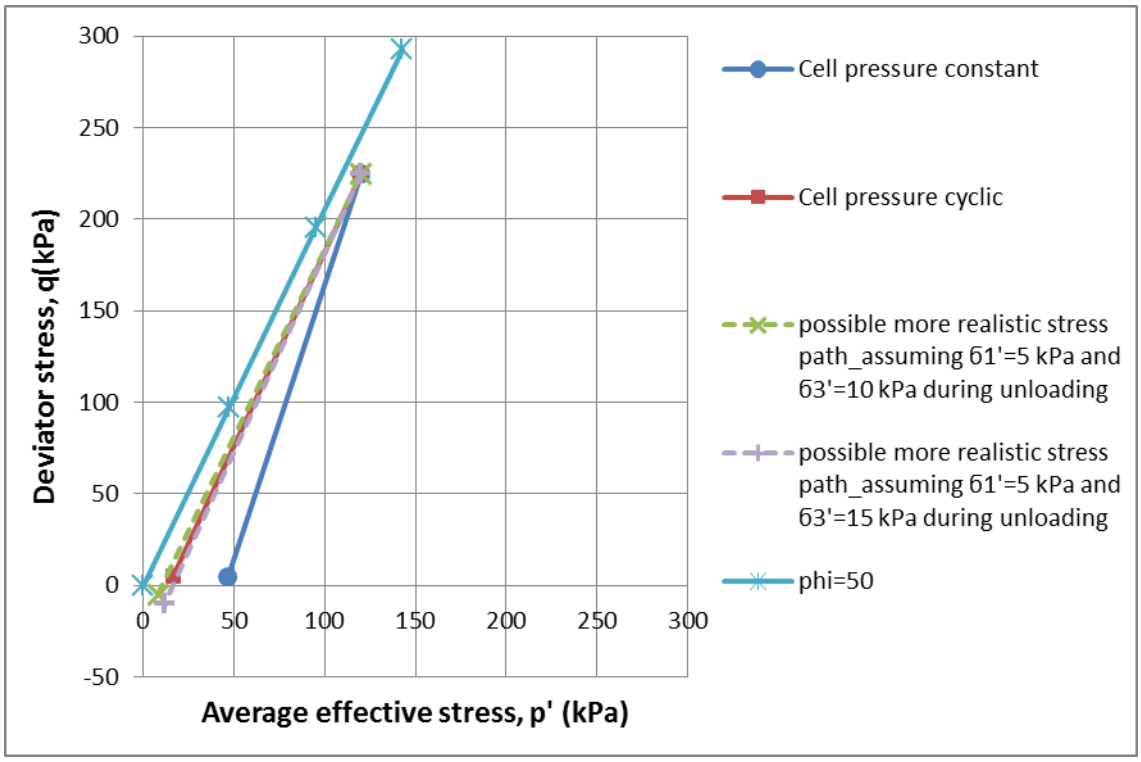

Figure 4.31: Stress path during constant cell pressure and cyclic cell pressure tests

(2) Tamping stage

Figure 4.32 shows how a principal stress reversal was applied to simulate tamping. This may be termed an extension stage.

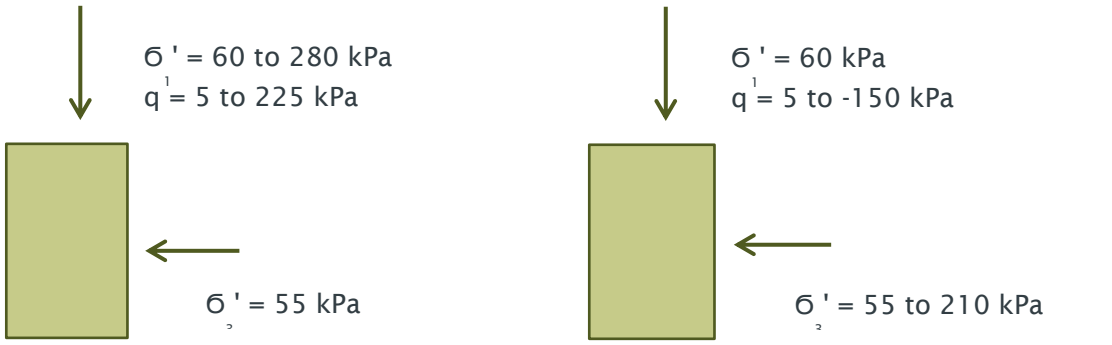

(c) Cyclic loading – major principal stress vertical

(d) Extension loading- major principal stress horizontal

Figure 4.32: Principal stress reversal during extension stage

5. Monotonic triaxial test results

5.1 Monotonic test programme

Monotonic tests were carried out on dry and saturated scaled ballast specimens. Dry monotonic tests were carried out at confining pressures of 15 kPa, 25 kPa, 30 kPa, 37 kPa, 60 kPa, 115 kPa, 200 kPa, and 300 kPa. Saturated monotonic tests were carried out at confining pressures of 15 kPa, 30 kPa, and 200 kPa.

The test parameters are summarised in Table 5.1. The density index was calculated based on a density range of 1424-1636 kg/m^3 and a void ratio range of 0.699-0.952 obtained within a 150 mm diameter mould for scaled ballast. Loose specimens were prepared by pouring the ballast into the mould. Dense specimens were prepared by vibrating the ballast into the mould in layers.

Test	Initial dry density	Void ratio (G_s=2.78)	Density Index $\frac{(e_{max}-e)}{(e_{max}-e_{min})}$	Target σ_3'
15 kPa dry	1555	0.788	0.6497	15
25 kPa dry	1544	0.801	0.5994	25
25 kPa dry (2)	1558	0.784	0.6633	25
30 kPa dry	1549	0.795	0.6224	30
37 kPa dry	1537	0.809	0.5670	37
60 kPa dry	1580	0.759	0.7615	60
115 kPa dry	1570	0.771	0.7172	115
200 kPa dry	1567	0.774	0.7038	200
300 kPa dry	1583	0.756	0.7746	300
15 kPa saturated (cell pressure 215 kPa, Back pressure 200 kPa)	1556	0.787	0.6543	15
30 kPa saturated (cell pressure 230 kPa, Back pressure 200 kPa)	1566	0.775	0.6993	30
200 kPa saturated (cell pressure 400 kPa, Back pressure 200 kPa)	1561	0.781	0.6769	200

Table 5.1: Monotonic test parameters

5.2 Results and discussion

Figure 5.1 shows graphs of deviator stress against axial strain for dry ballast. The deviator stress behaviour for the saturated tests at comparable confining pressures is shown in Figure 5.2. The curves are not particularly smooth; this can be attributed to a stick-slip phenomenon as a relatively small number of particles slide and/or rotate past each other. The deviator stress eventually reaches a peak and starts to drop slightly showing strain softening behaviour. A critical state is not evident even after significant post peak straining. Visual examination of the specimens showed no clear failure plane, with the failure apparent only as bulging. Figure 5.3 shows the bulged specimen after shearing.

Both dry and saturated tests show increasing peak deviator stress with increasing confining pressure. Dry and saturated tests show similar peak deviator stress at 15 kPa and 30 kPa confining pressures (Figure 5.4 and Figure 5.5). At 200 kPa confining pressure, the dry test shows a slightly higher deviator stress than the saturated test (Figure 5.6).

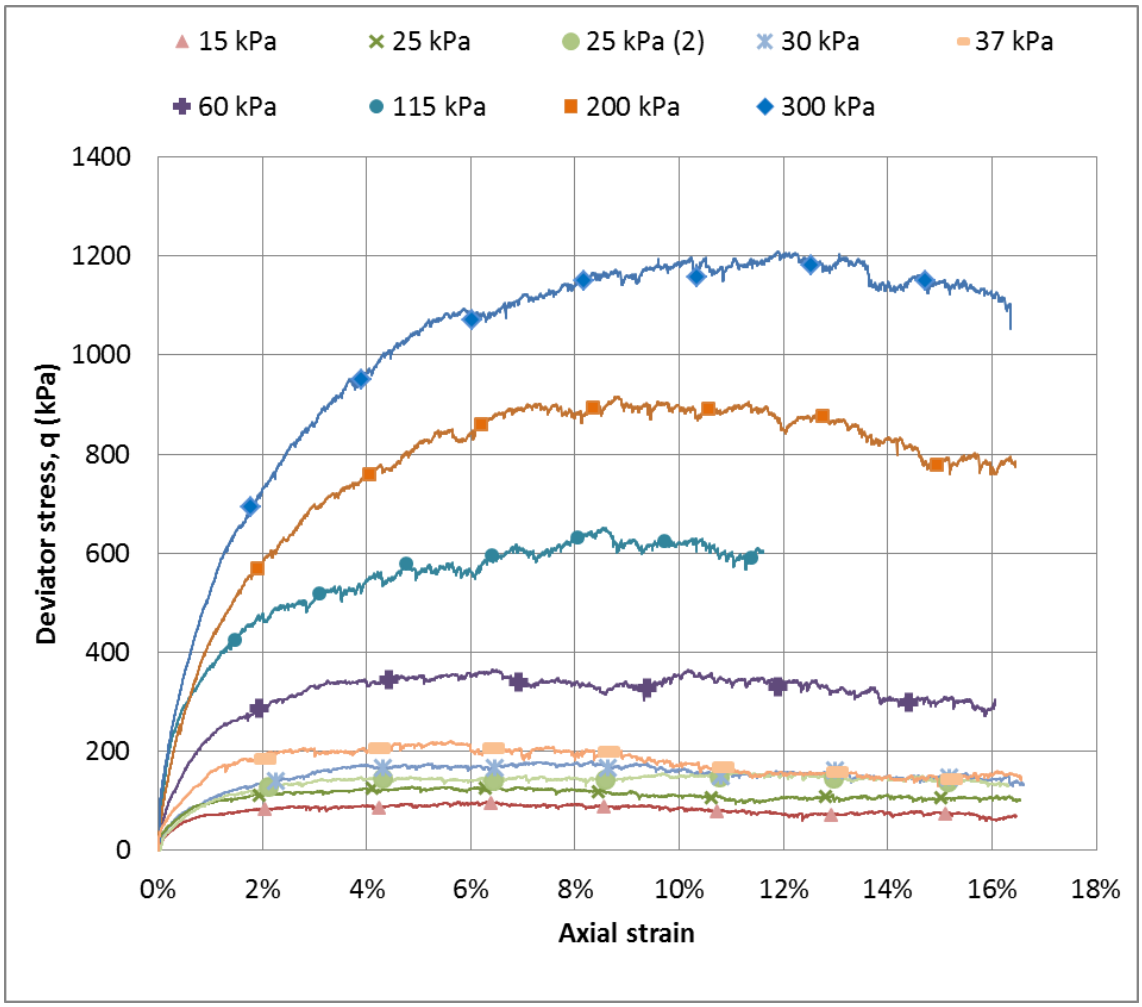

Figure 5.1: Stress-strain behaviour of dry specimens

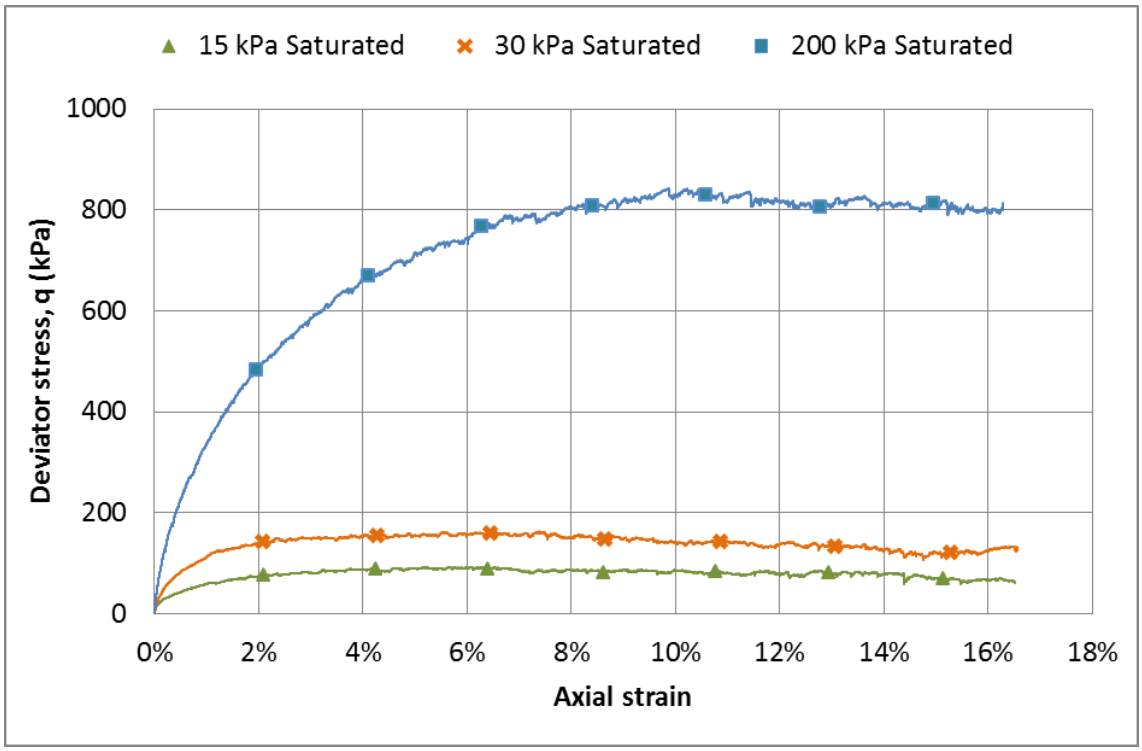

Figure 5.2: Stress-strain behaviour of saturated specimens

Figure 5.3: Specimen after shearing of 15 kPa saturated test

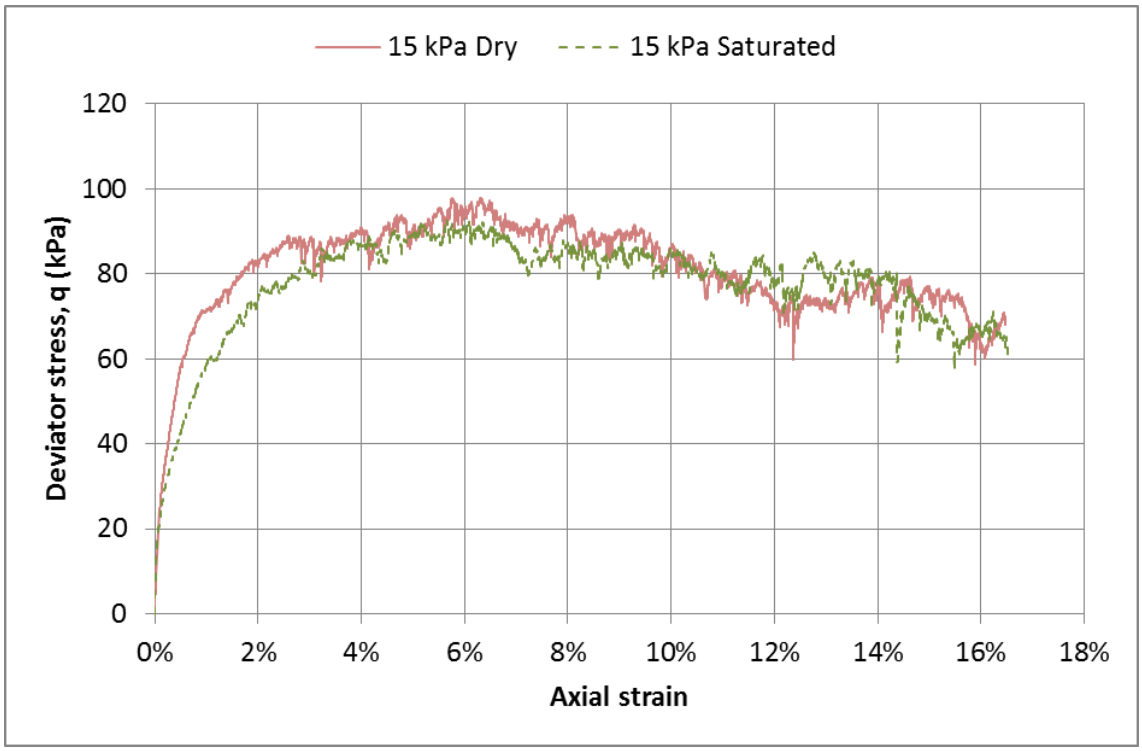

Figure 5.4: Stress-strain behaviour at 15 kPa confining pressure

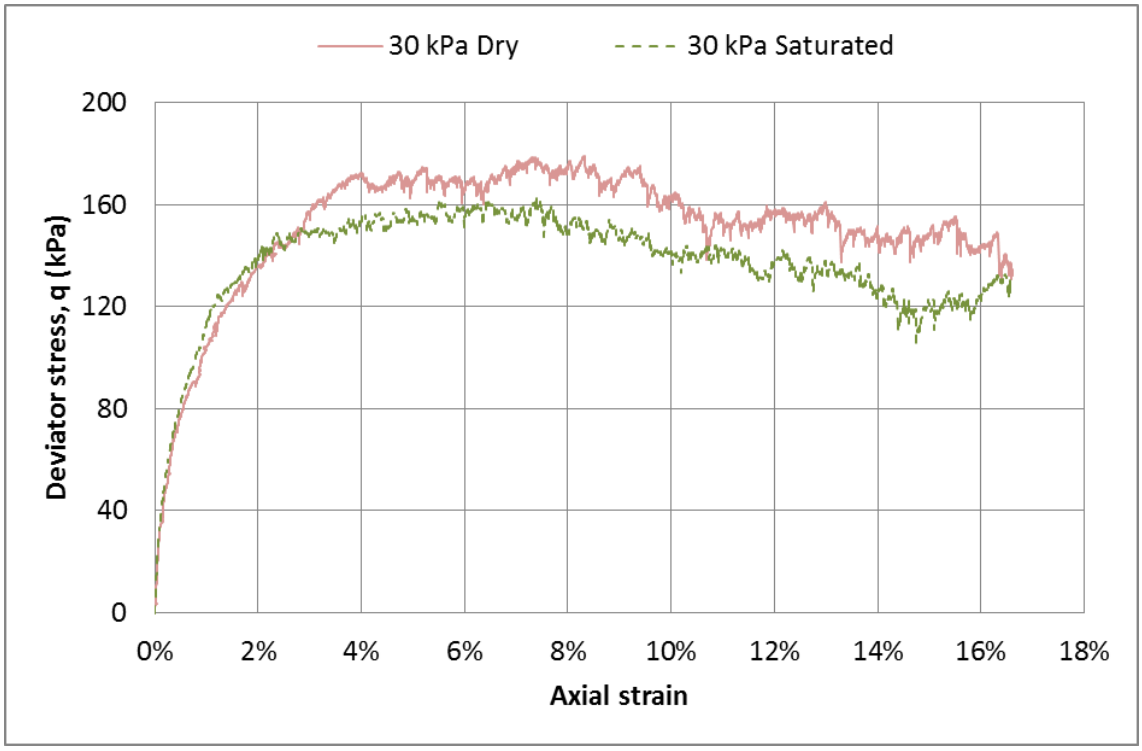

Figure 5.5: Stress-strain behaviour at 30 kPa confining pressure

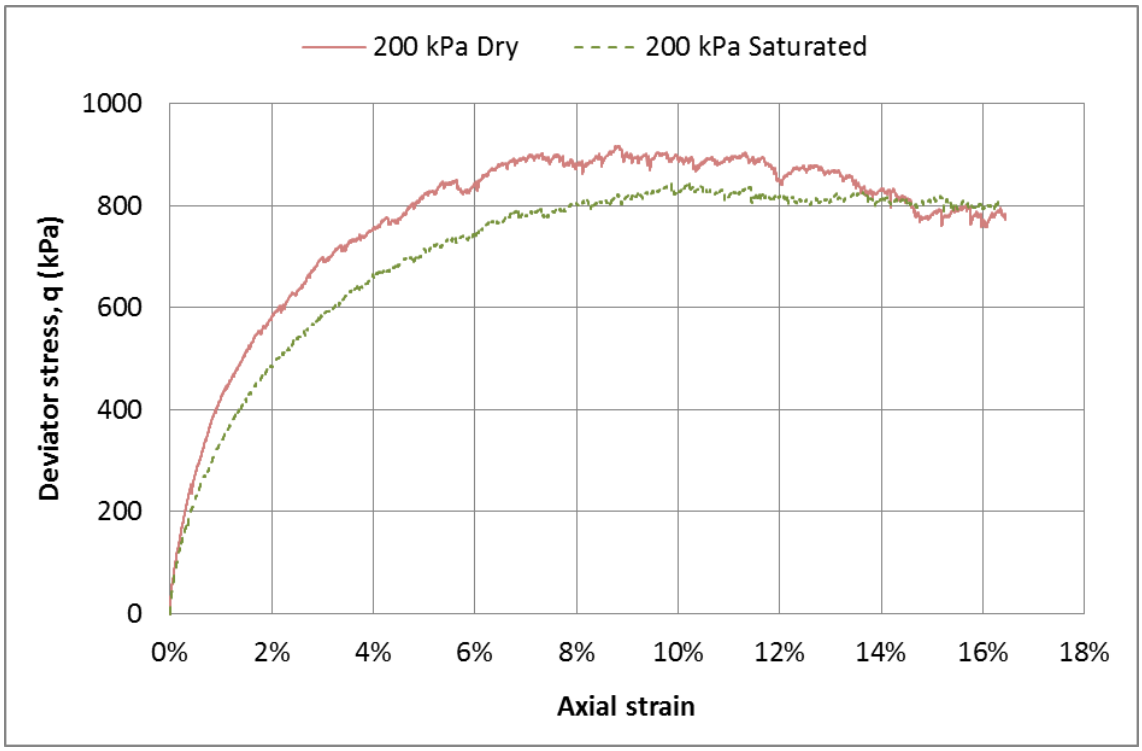

Figure 5.6: Stress-strain behaviour at 200 kPa confining pressure

The stiffness of a material during monotonic loading can be described as either a tangent or a secant modulus. The secant modulus (E_s) is the stress divided by the strain at any given value of stress or strain.

Secant modulus values for the dry specimens are shown in Figure 5.7. The reduction in secant modulus values during the test indicates that the initial stiffness reduces during shearing. With increasing confining pressure the secant modulus increases during the initial axial deformation, toward the end of the test secant modulus values fall within a narrow range. Also, the secant modulus values were plotted only for axial strains larger than 0.1 %, because the use of external axial measurements for determining axial strains less than 0.1 % to calculate secant modulus values is inaccurate.

The saturated specimens show a similar behaviour (Figure 5.8 and Figure 5.9). Other researchers also reported increasing initial stiffness with increasing confining pressure (Raymond and Davies, 1978, Indraratna et al., 1998).

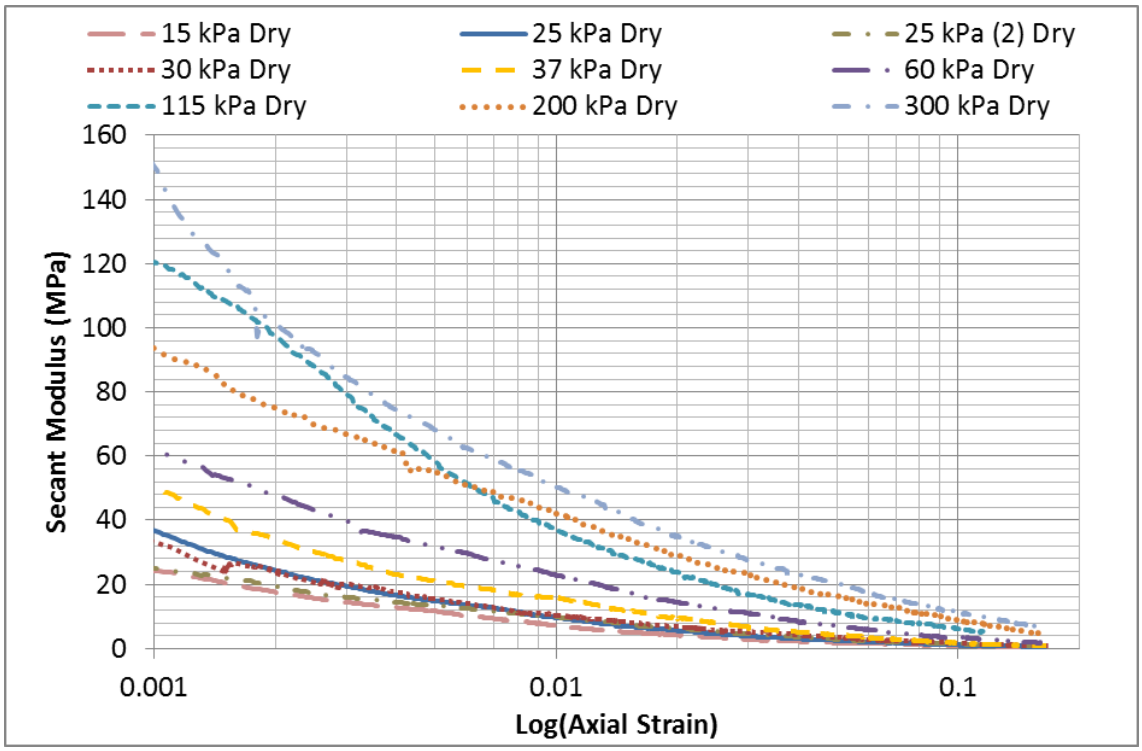

Figure 5.7: Secant modulus against axial strain for dry specimens

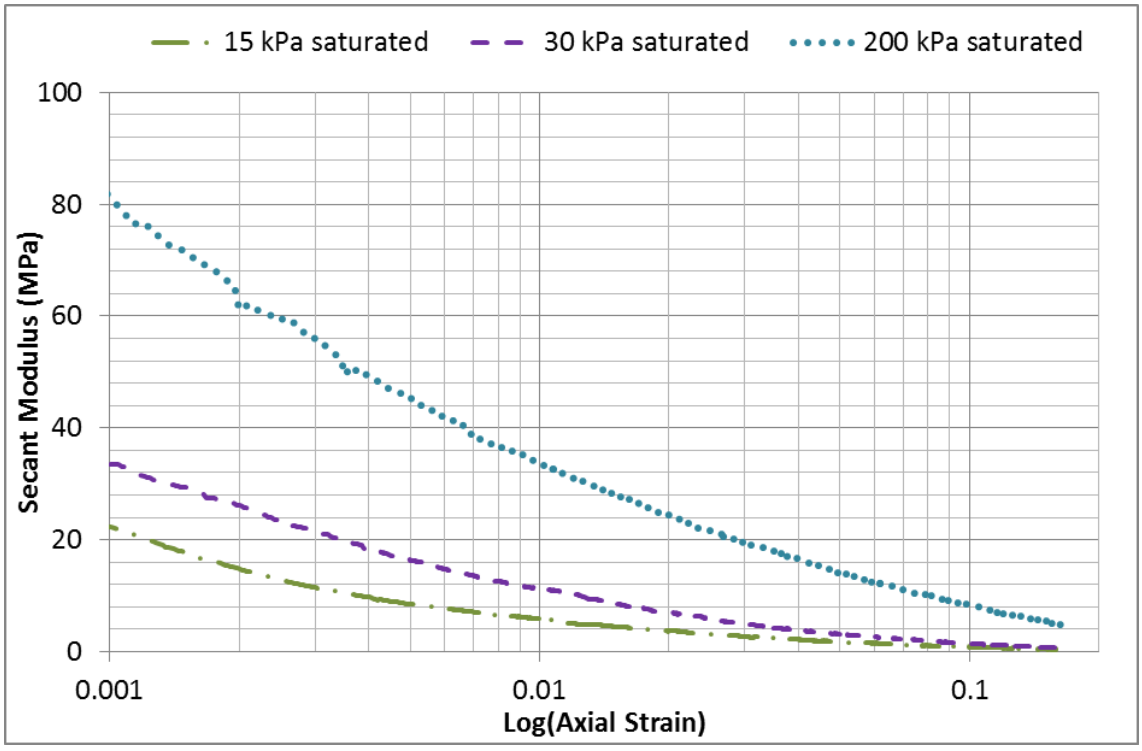

Figure 5.8: Secant modulus against axial strain for saturated specimens

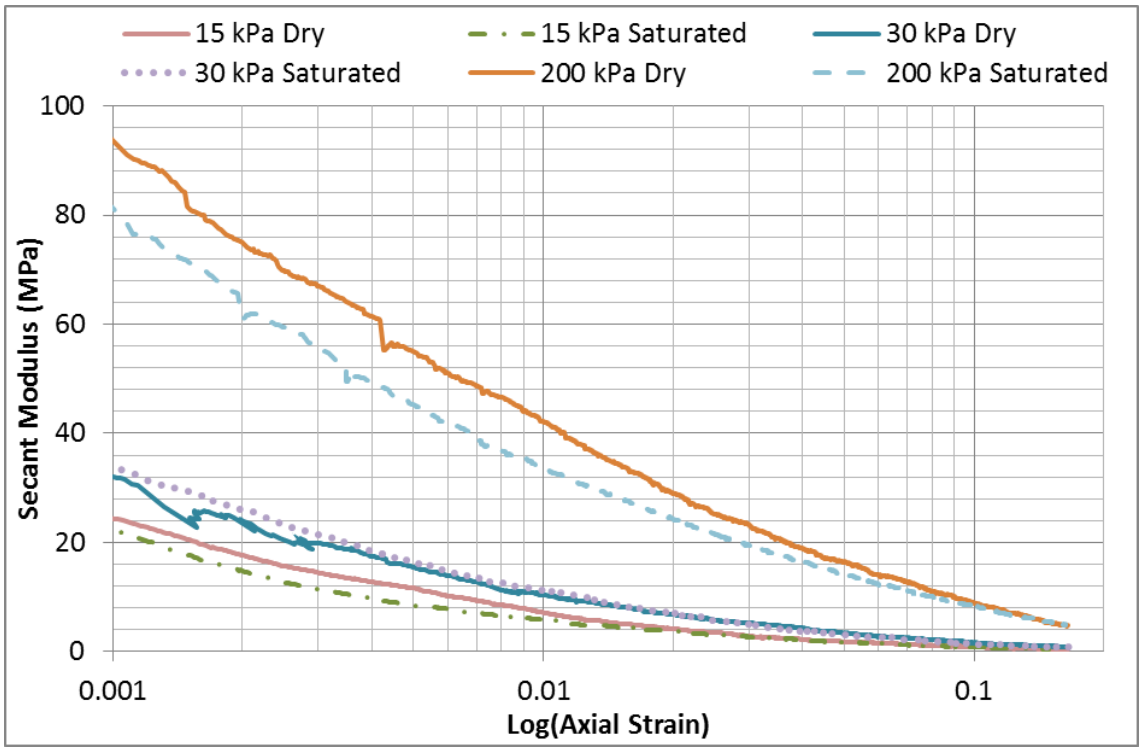

Figure 5.9: Secant modulus values of dry and saturated specimens

The effective stress path under drained monotonic loading is expected to ascend with a gradient of dq/dp'=3 from the starting point ($p'=\sigma_c-u_o$). Figure 5.10 and Figure 5.11 show that tests on scaled ballast follow the expected linear relationship. The fluctuation towards the end of the line is due to fluctuation in cell pressure by +/- 1 kPa.

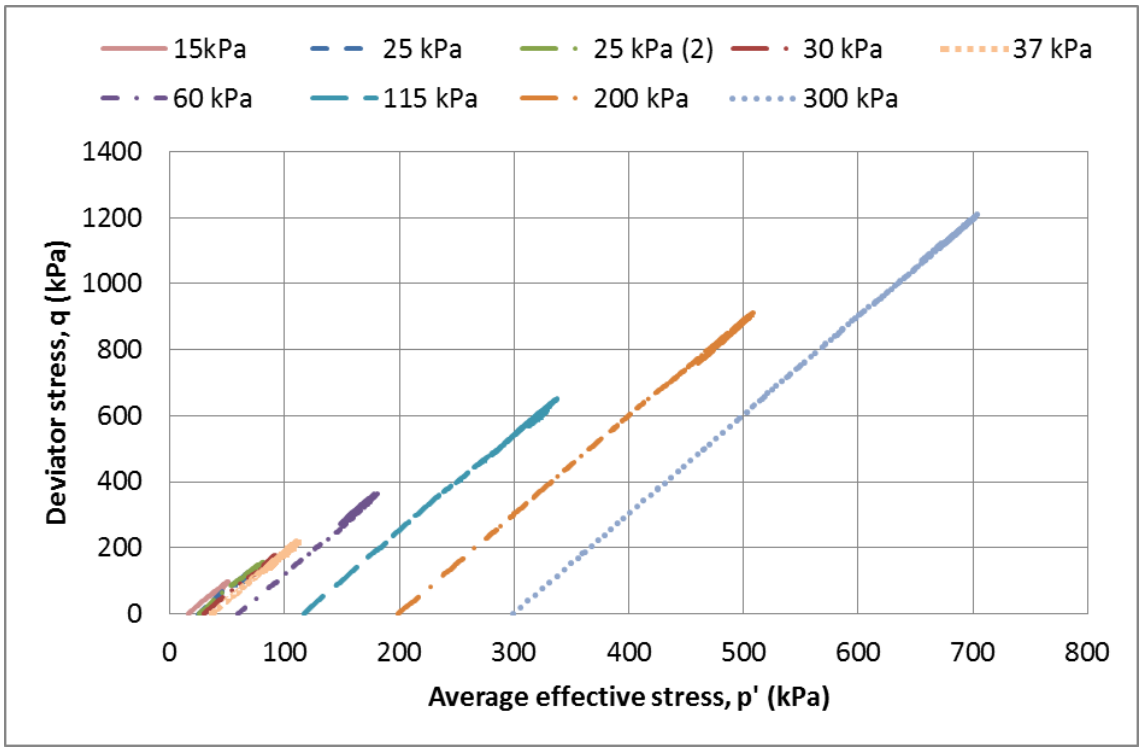

Figure 5.10: Stress paths of dry specimens

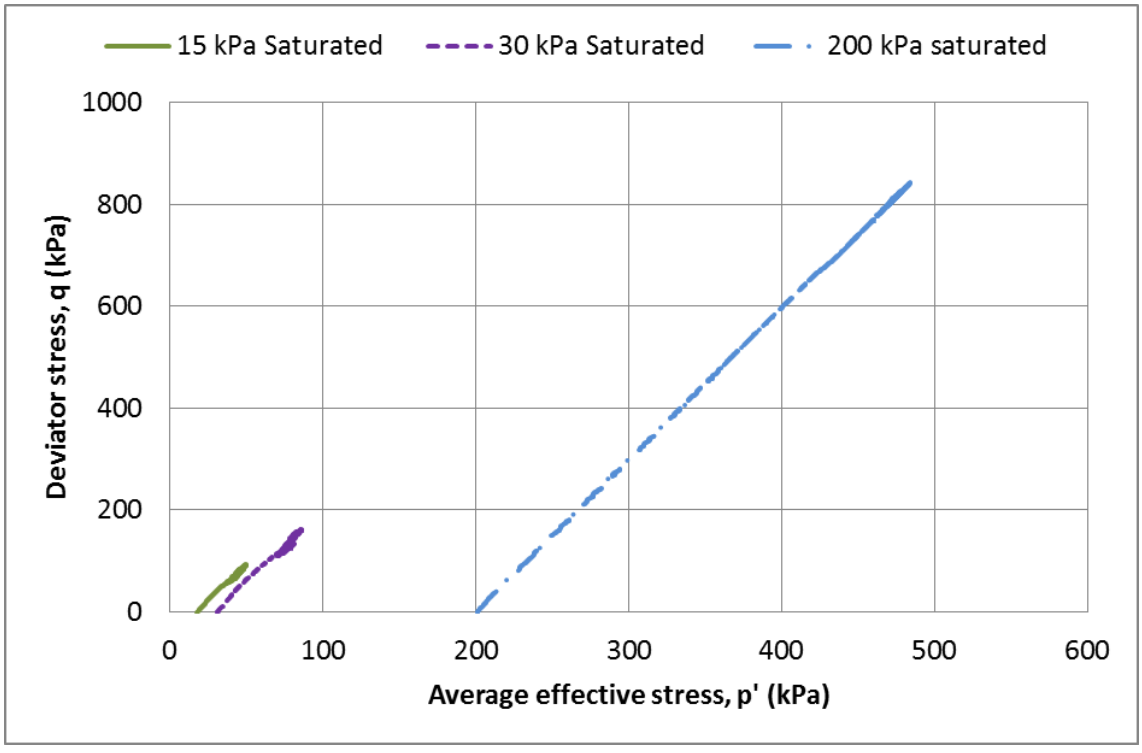

Figure 5.11: Stress paths of saturated specimens

Figure 5.12 shows the volume change behaviour of the dry scaled ballast as volumetric strain against axial strain. In general, with reducing cell pressure there is less compression and more dilation. This trend is not obvious at the cell pressures of 25 kPa, 30 kPa and 37 kPa. This confusion in the overall trend may be due to these values being close to each other and perhaps a slight tilting of the top cap during shearing influencing the volumetric measurements. In comparison, the volume change behaviour for saturated tests shows similar trends (Figure 5.13).

Dry tests at 15 kPa and 200 kPa confining pressure dilate more than the saturated specimens at the same confining pressure (Figure 5.14 and Figure 5.16). The difference between the 30 kPa dry and the 30 kPa saturated specimen is not significant. The 30 kPa dry specimen dilates more towards the end compared to the 30 kPa saturated specimen (Figure 5.15).

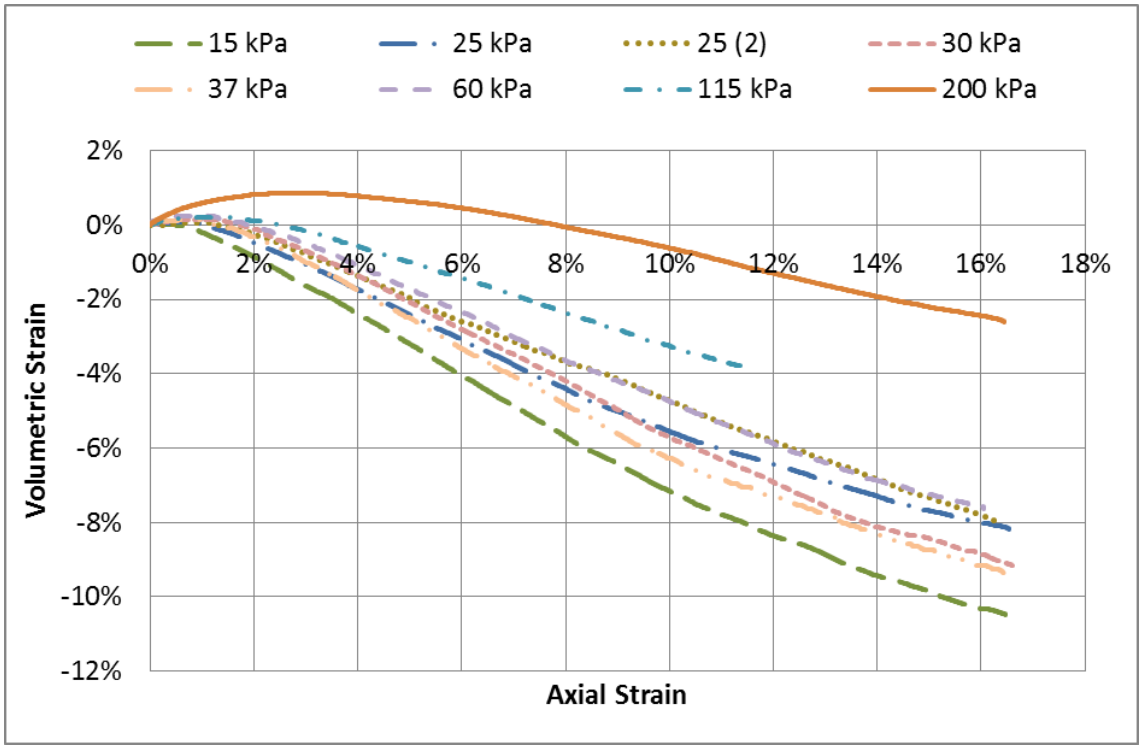

Figure 5.12: Volumetric behaviour of dry specimens

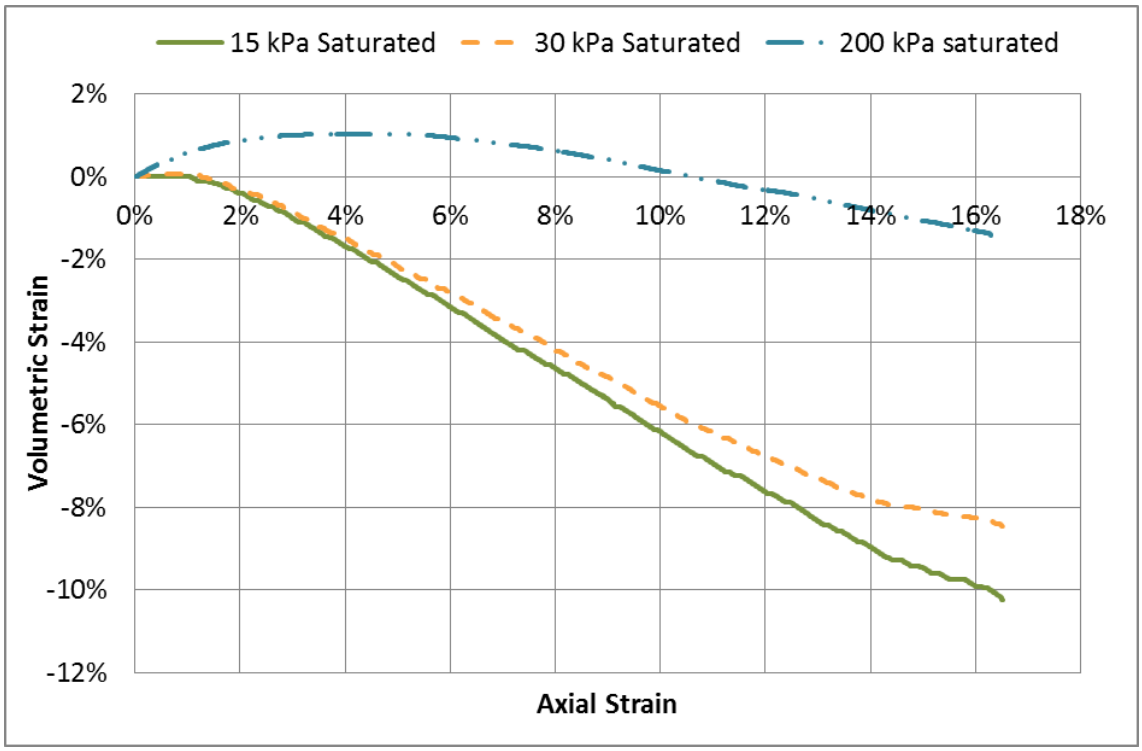

Figure 5.13: Volumetric behaviour of saturated specimens

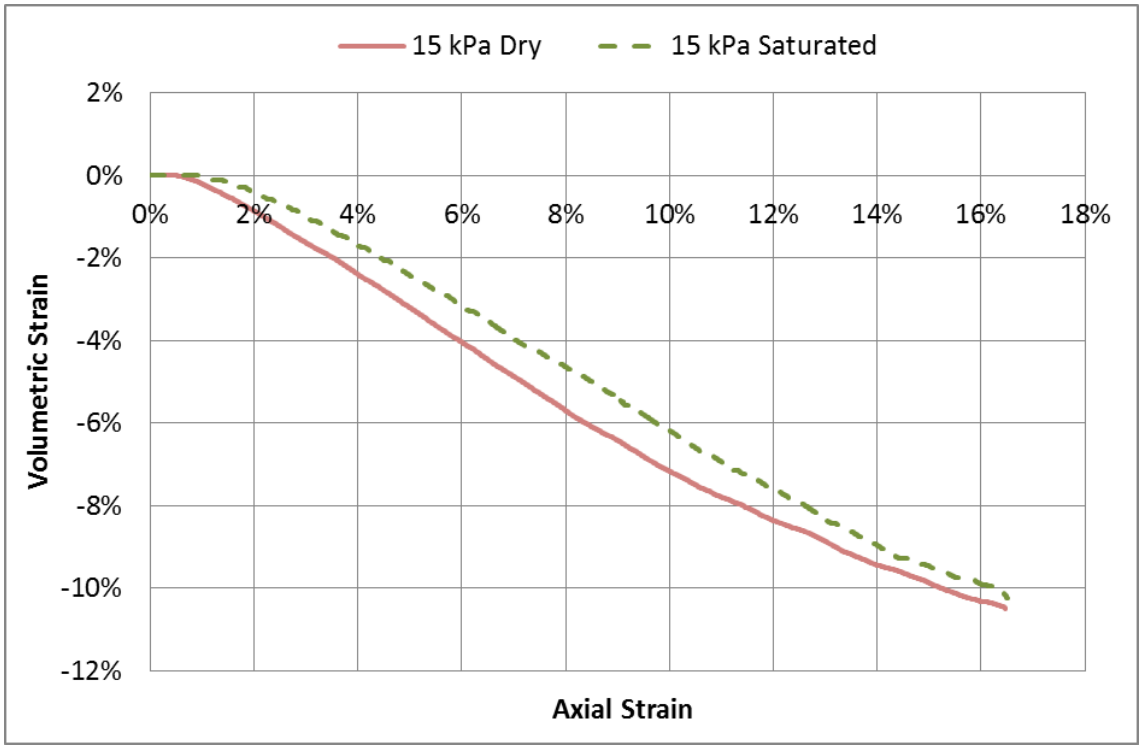

Figure 5.14: Volumetric behaviour at 15 kPa confining pressure

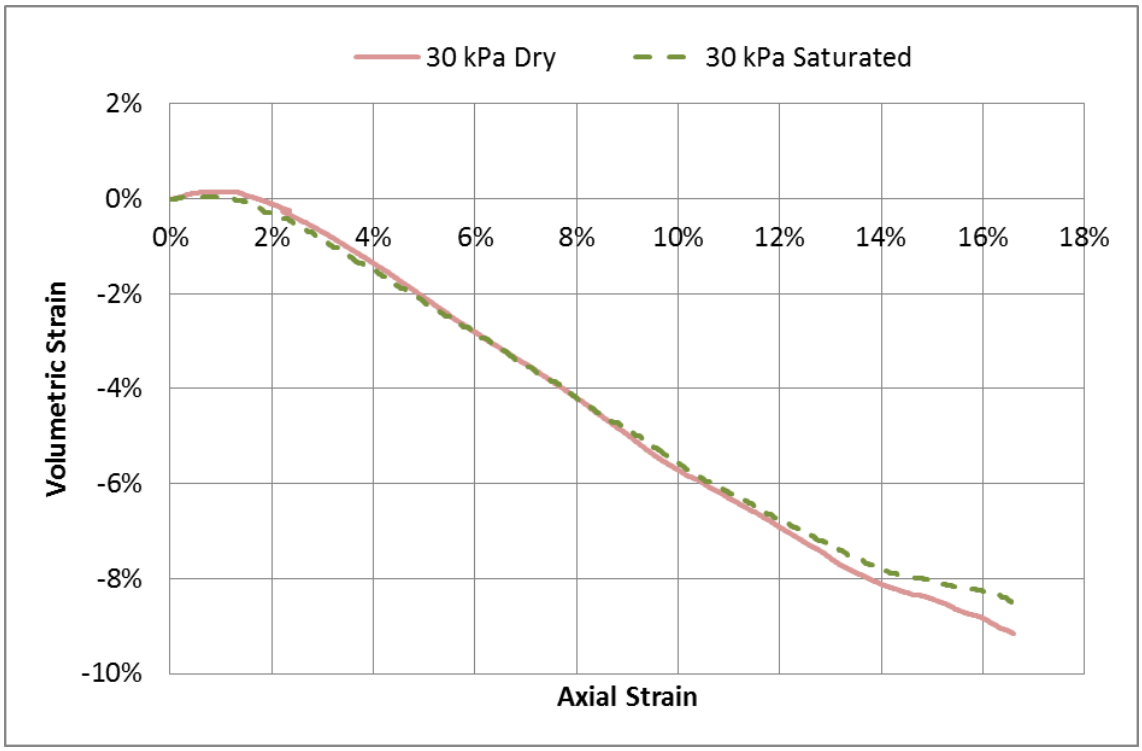

Figure 5.15: Volumetric behaviour at 30 kPa confining pressure

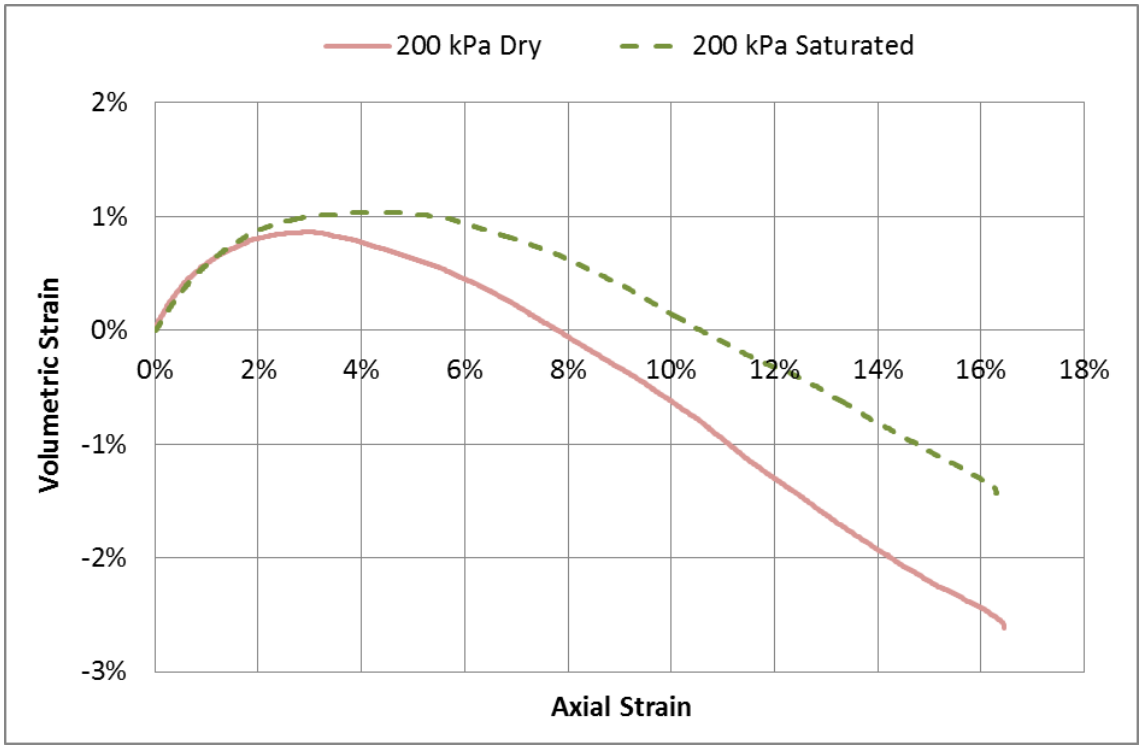

Figure 5.16: Volumetric behaviour at 200 kPa confining pressure

To calculate the rate of dilation, $-d\epsilon_v/d\epsilon_q$, the volumetric strain data were filtered, because cell pressure controller behaved in an off/on manner. This means there were periods of no volume change followed by periods of constant rate of volume change as the controllers tripped on/off at their predefined pressure deviation trigger levels. To smooth the volumetric strain data, the following method was applied. From the 30th data point, a rolling average over 60 data points (30 ahead and 30 behind) was taken for each point up to the 90th data point. From the 90th data point onward, a rolling average over 120 data points was used (60 ahead and 60 behind). For the first 30 data points, rolling averages over reduced ranges were taken. Volumetric strain before and after filtering over a very short period of time is shown in Figure 5.17. It clearly shows the on/off behaviour of the controller. To calculate $d\epsilon_v$ and $d\epsilon_q$, the difference between points 50 ahead and 50 behind was taken from the 50th filtered data point onward. For the first 50 data points, the difference between the reduced filtered data range was taken.

Figure 5.18 and Figure 5.19 show the stress ratio plotted against rate of dilation measured in dry and saturated tests respectively. In general, with increasing confining pressure there is more compression and less dilation. The critical state parameter, M, can be obtained from the following equation (Powrie, 2004),

$$\frac{q}{p'} \cdot \frac{\delta\epsilon_q}{\delta\epsilon_{vol,plastic}} + 1 = M \cdot \frac{\delta\epsilon_q}{\delta\epsilon_{vol,plastic}}$$

where $\delta\epsilon_q$ and $\delta\epsilon_{vol,plastic}$ are changes in triaxial shear strain and irrecoverable volumetric strain.

This equation can be rearranged as,

$$\frac{q}{p'} = \frac{-\delta\epsilon_{vol,plastic}}{\delta\epsilon_q} + M$$

The value of M is equal to q/p', when the rate of dilation is zero. In the stress dilatancy plots, q/p' falls into a narrow range of values when the rate of dilation=0. The range of values is due to experimental uncertainties; for example, volume measurement is not accurate due to the on/ off behaviour of controller.

M is 1.54 as an average. This value was calculated as an average of all the confining pressure dry and saturated test values. The critical angle is calculated as, $\sin\phi_{crit} = 3M/(6+M)$, which is 37.8°.

The Mohr circles of stress for the dry and saturated scaled ballast specimens are shown in Figure 5.20 and Figure 5.21 respectively. Mohr circles were drawn using effective confining pressure (after membrane correction) and axial stress values when the peak angle of effective shearing resistance was mobilized. Tangents are drawn from the origin to 15 kPa, 115 kPa, 200 kPa and 300kPa circles for dry tests and to all circles for saturated tests. Mobilized angle of effective shearing resistance, ϕ'_{mob} is defined by the slope of the tangent to the Mohr circle through origin. It shows that the mobilized angle of effective shearing resistance increases in general with increasing confining pressure.

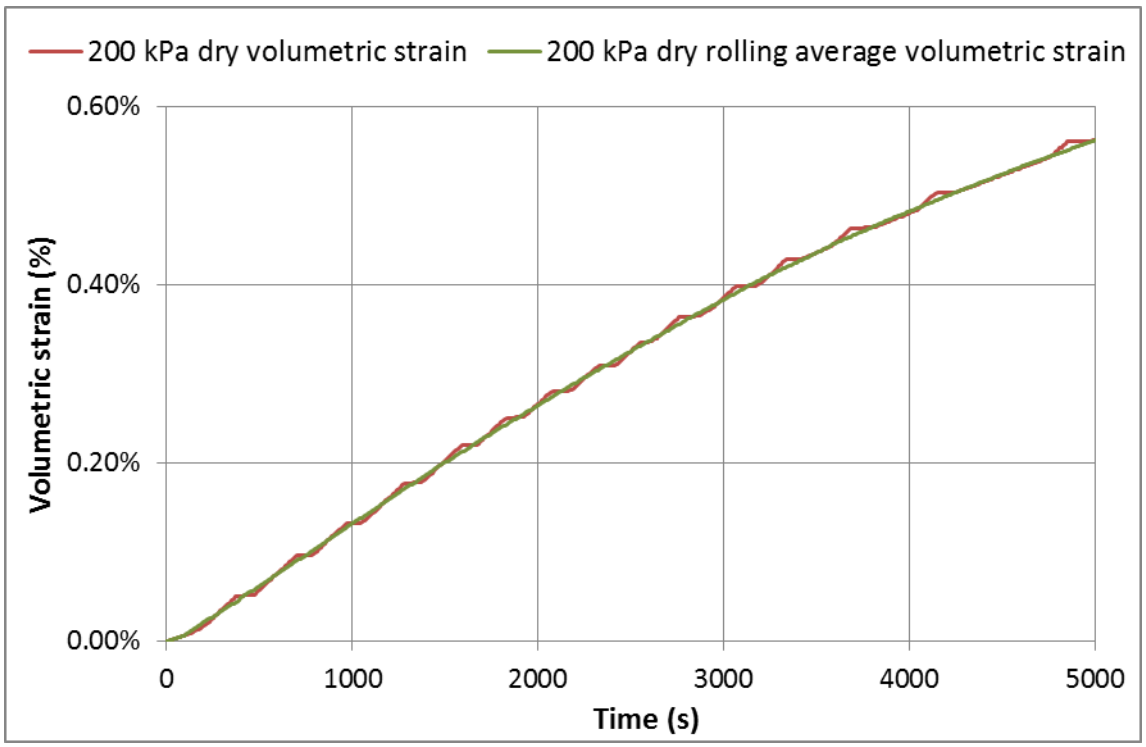

Figure 5.17: On/Off behaviour of controller during 200 kPa dry test and filtered data

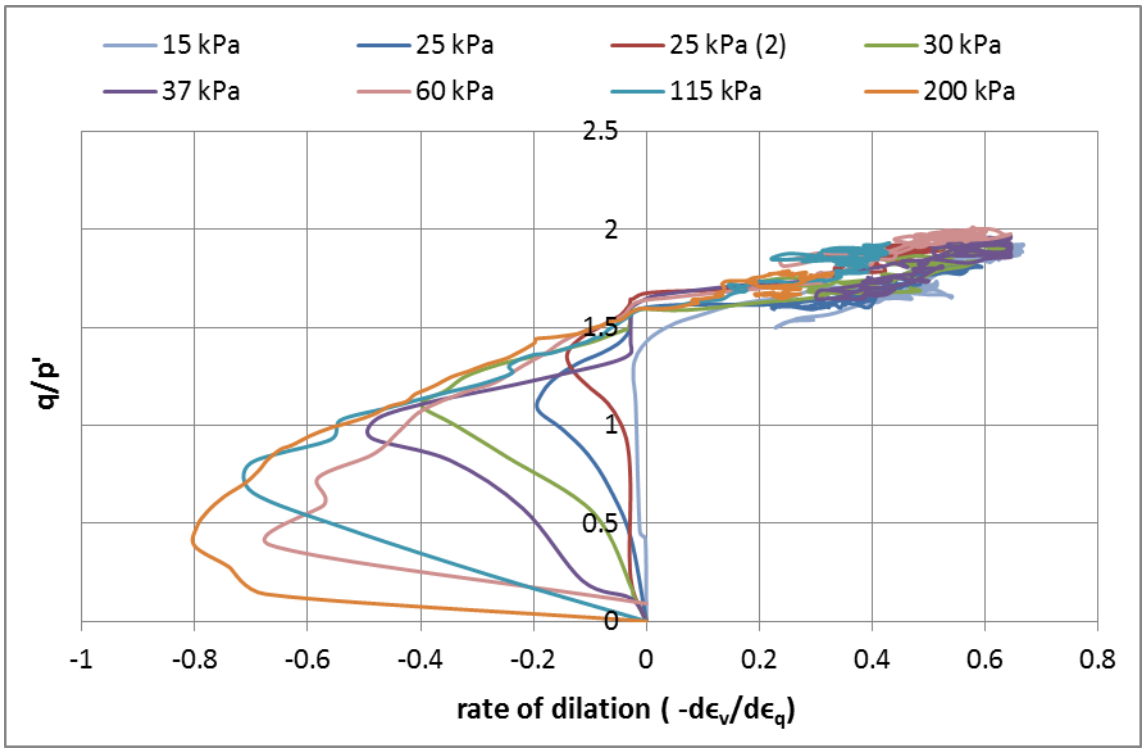

Figure 5.18: Stress dilatancy plot for dry specimen

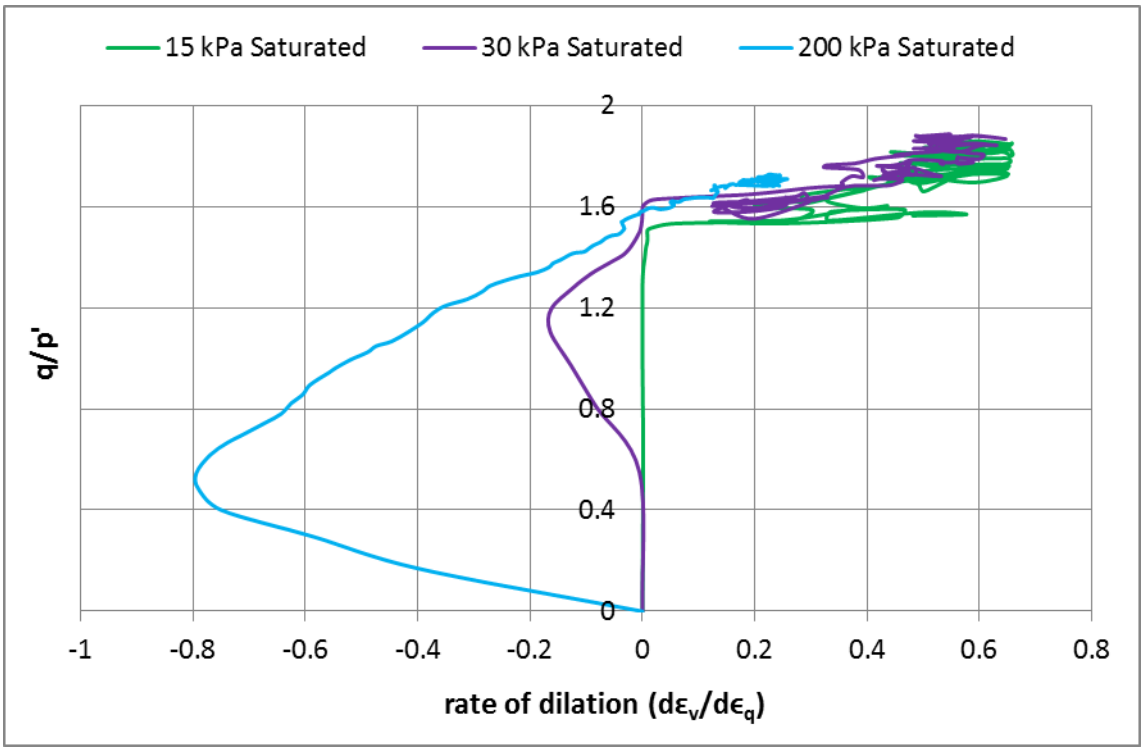

Figure 5.19: Stress dilatancy plot for saturated specimen

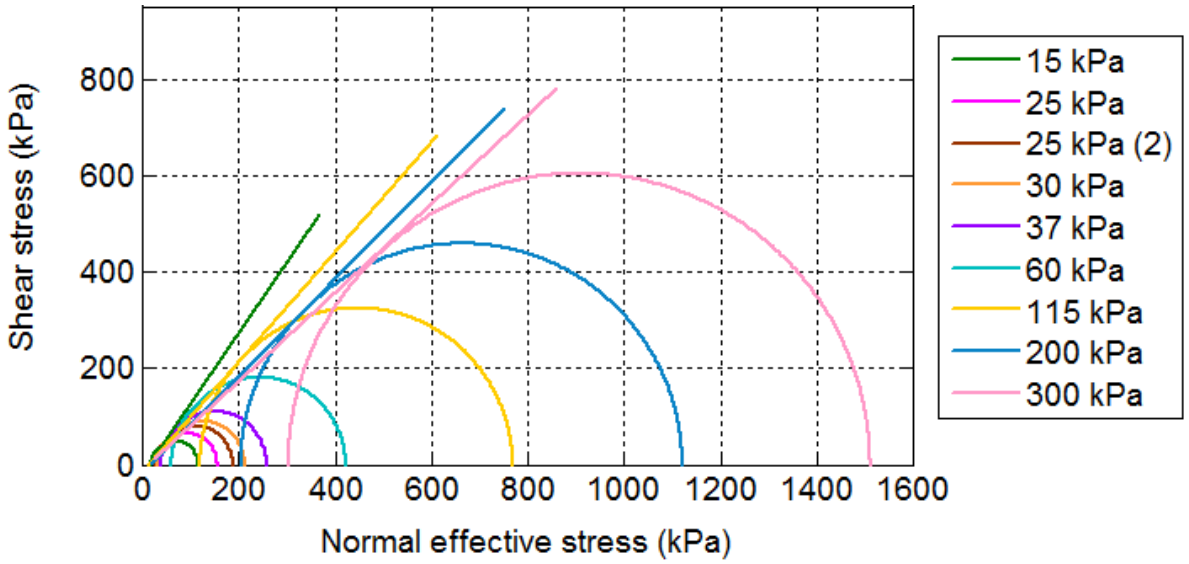

Figure 5.20: Mohr circles for dry specimens

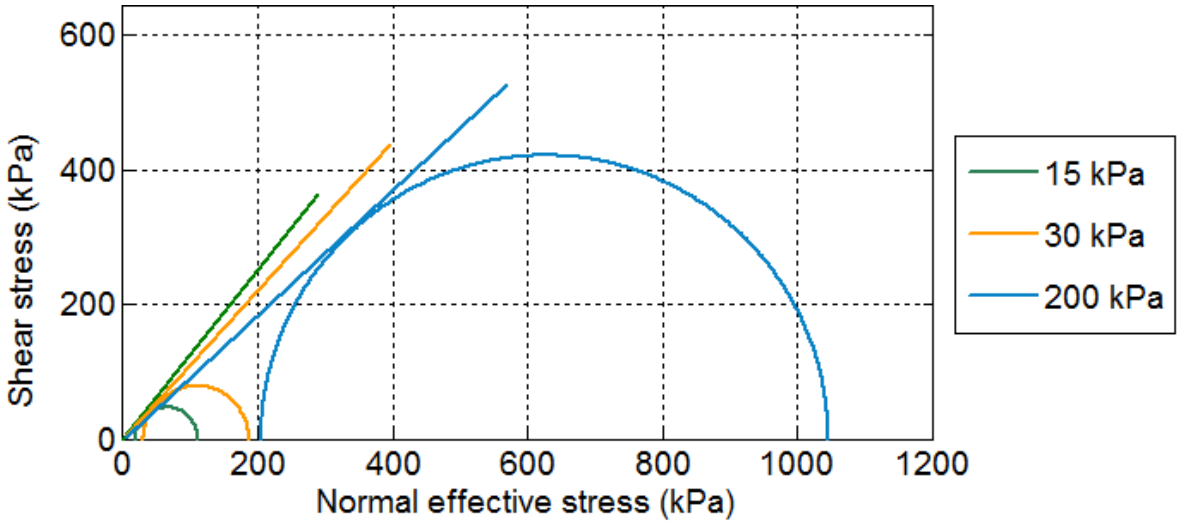

Figure 5.21: Mohr circles for saturated specimens

Figure 5.22 shows the mobilized angle of effective shearing resistance obtained over a range of confining pressures for scaled ballast before membrane correction was applied. Figure 5.23 compares the peak angle of effective shearing resistance before and after membrane correction. Scaled ballast shows a mobilized angle of effective shearing resistance between 40° and 50° during shearing. Saturated specimens show a

slightly lower peak angle of effective shearing resistance compared to dry specimens by 2% to 4%.

The calculated angle of effective shearing resistance reduces when the membrane correction is applied, especially at lower confining pressures. There is a clear reduction in angle of effective shearing resistance with increasing confining pressure. Table 5.2 summarizes the scaled ballast data.

Table 5.3 shows full size ballast test data taken from the literature, with the angle of effective shearing resistance and peak deviator stress determined by scaling from figures and by calculation. Figure 5.24 compares the peak angle of effective shearing resistance of scaled ballast with that of full size ballast from tests in the literature. Scaled ballast falls within the range of data for full size ballast in the literature, but shows a relatively lower angle of effective shearing resistance at lower confining pressure than full size ballast. Interestingly, Raymond and Davies (1978) reported that the peak angle of effective shearing resistance may decrease as particle size decreases at low cell pressures.

Peaks angle of effective shearing resistance obtained for certain confining pressures differ between researchers. For example, Indraratna et al. (1998) obtained higher friction angles than others. Reasons for this variation include variations in:

- Mineralogy
- Preparation methods giving rise to varying initial relative density
- Membrane materials and thicknesses with some very thick membranes used to guard against particles piercing the membranes
- Membrane corrections applied

For many of the tests reported in the literature, researchers have not stated exactly how membrane effects have been allowed for and differing approaches have been applied.

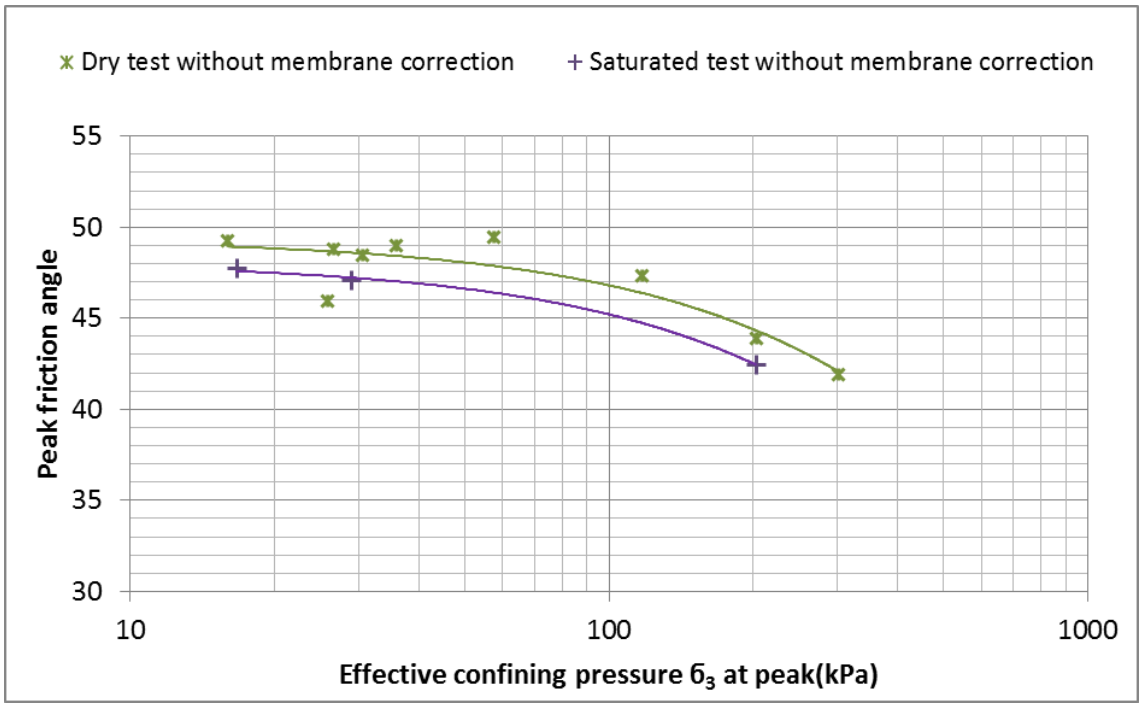

Figure 5.22: Peak angle of effective shearing resistance before membrane correction

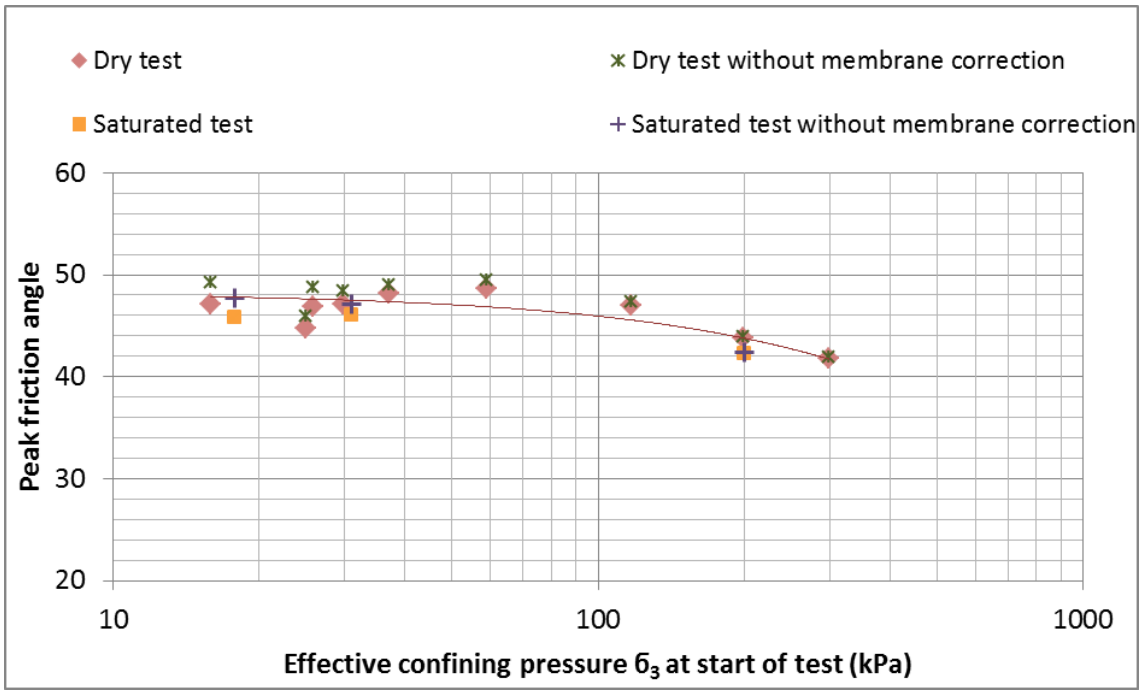

Figure 5.23: Peak angle of effective shearing resistance of scaled ballast

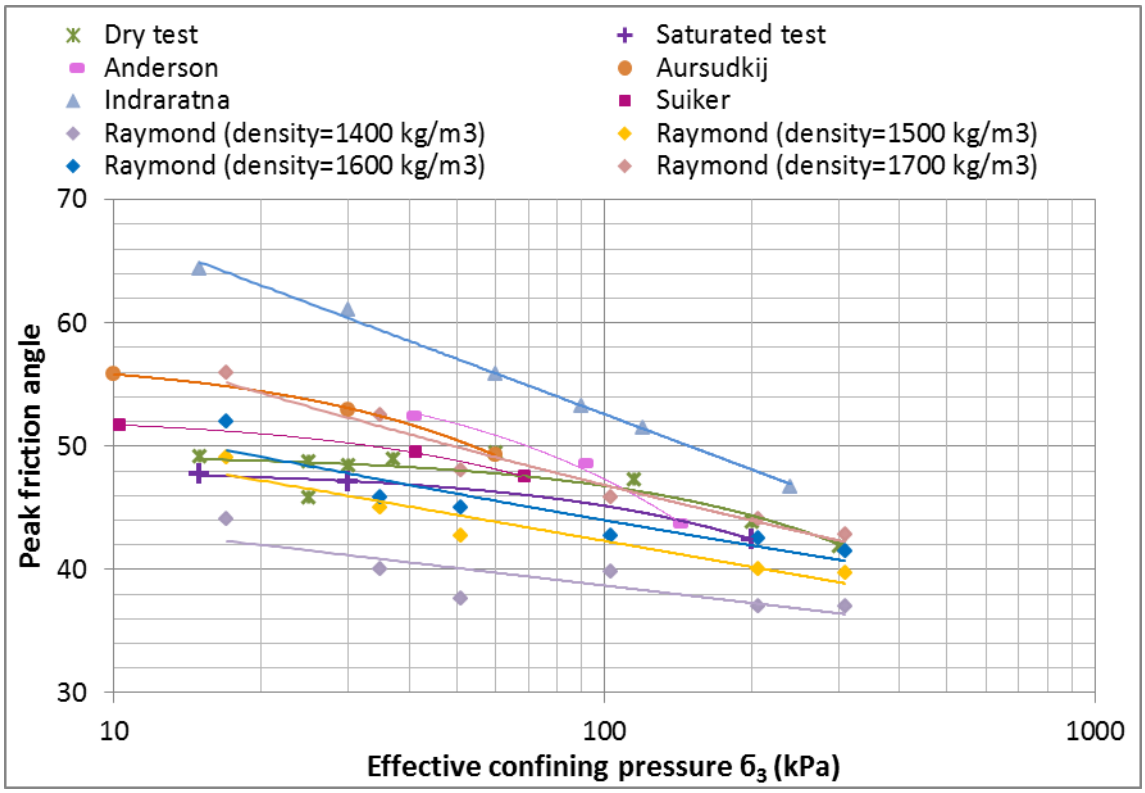

Figure 5.24: Peak angle of effective shearing resistance of scaled and full size ballast

Test	Initial dry density ϒ (kg/ m^3)	σ_3' at start of test (kPa)	σ_3' at ϕ'_{peak} after membrane correction (kPa)	σ_3' at ϕ'_{peak} before membrane correction	q peak at ϕ'_{peak} (kPa)	q/p' at ϕ'_{peak}	ϕ'_{peak} after membrane correction (degrees)	ϕ'_{peak} before membrane correction (degrees)	difference on ϕ'_{peak} with membrane correction
15 kPa dry	1555	15.9	17.9	16.0	98.0	1.94	47.1	49.2	4.3%
25 kPa dry	1544	25.0	27.1	25.8	128.5	1.84	44.7	45.9	2.7%
25 kPa dry (2)	1558	25.9	29.4	26.5	158.3	1.93	46.8	48.8	4.0%
30 kPa dry	1549	29.8	32.7	30.5	179.3	1.94	47.1	48.5	2.8%
37 kPa dry	1537	37.0	37.6	36.0	220.5	1.99	48.2	49.0	1.6%
60 kPa dry	1580	59.0	60.2	57.5	361.8	2.00	48.6	49.5	1.8%
115 kPa dry	1570	116.7	119.5	117.5	649.5	1.93	47.0	47.3	0.7%
200 kPa dry	1567	198.8	204.4	202.8	916.8	1.80	43.8	43.9	0.4%
300 kPa dry	1583	299.0	303.1	301.1	1207.9	1.71	41.7	41.9	0.3%
15 kPa saturated	1556	17.8	18.4	16.7	92.7	1.88	45.8	47.7	4.1%
30 kPa saturated	1566	31.0	30.4	29.0	156.6	1.90	46.1	47.1	2.1%
200 kPa saturated	1561	200.8	204.9	203.2	841.6	1.73	42.3	42.4	0.4%

Table 5.2: Monotonic test data

Source	Rock type	Test type	Cell dimension (diameter *height) (mm)	Membrane detail	Initial dry density (kg/m^3)	Void ratio calculated (G_s=2.78)	Target σ_3' (kPa)	q peak (kPa)	Peak friction angle ϕ'_{peak} (degrees)
Anderson and Fair (2008)	Granite	Dry	236*455	Double 0.75 mm thick rubber membrane	1450	0.917	40	308	52.5
					1470	0.891	90	544	48.7
					1470	0.891	140	631	43.8
Aursudkij et al (2009)	Limestone	Dry	300*450	Two latex membrane 2 mm and 1mm thick	1511	0.840	10	96	55.9
					1539	0.806	30	242	53
					1545	0.799	60	375	49.3
Indraratna et al. (1998)	Latite basalt	Saturated	300*600	4mm thick rubber membrane	1530	0.817	15	320	64.4
					1530	0.817	30	390	61.1
					1530	0.817	60	640	55.9
					1530	0.817	90	730	53.3
					1530	0.817	120	840	51.5
					1530	0.817	240	1275	46.7
Raymond and Davies (1978)	Dolomite	Saturates	225*450	Membrane detail wasn't stated	1400	0.986	17	-	44.1
					1400	0.986	35	-	40
					1400	0.986	51	-	37.6
					1400	0.986	103	-	39.8
					1400	0.986	206	-	37
					1400	0.986	310	-	37
					1500	0.853	17	-	49.1
					1500	0.853	35	-	45
					1500	0.853	51	-	42.8

					1500	0.853	206	-	40
					1500	0.853	310	-	39.7
					1600	0.738	17	-	52
					1600	0.738	35	-	45.9
					1600	0.738	51	-	45
					1600	0.738	103	-	42.8
					1600	0.738	206	-	42.5
					1600	0.738	310	-	41.5
					1700	0.635	17	190	56
					1700	0.635	35	280	52.5
					1700	0.635	51	320	48.1
					1700	0.635	103	570	45.9
					1700	0.635	206	1015	44.1
					1700	0.635	310	1400	42.9
Suiker et al (Suiker et al., 2005)	Basalt	Dry	254*645	0.76 mm thick latex membrane	1610	0.727	10.3	75	51.7
					1700	0.635	41.3	275	49.5
					1620	0.716	68.9	387	47.5

Table 5.3: Full size ballast data taken from literature

5.3 Summary

Increasing peak deviator stress with increasing confining pressure was observed. Dry specimens showed slightly higher deviator stresses than saturated specimens, but the differences were not large. Increasing initial stiffness with increasing confining pressure was observed. The reduction in secant modulus during shearing indicates the loss of stiffness. Dry specimens showed slightly higher initial stiffnesses at 15 kPa and 200 kPa confining pressures, but this was not observed at 30 kPa confining pressure.

Specimens compressed more and dilated less with increasing confining pressure. Dry specimens dilated slightly more than saturated specimens, but this trend was not obvious at 30 kPa confining pressure. The stress dilatancy plot confirmed the trend of more compression and less dilation with increasing confining pressure. The critical angle of shearing resistance was deduced from this plot. Mohr circles were drawn at the peak mobilized strength.

Membrane effects introduce a significant error in the peak angle of shearing resistance at lower confining pressures, unless they are corrected for. A trend of reduction in angle of effective shearing resistance with confining pressure was observed. This trend was weak at confining pressures less than 100 kPa. Scaled ballast falls within the range of angle of effective shearing resistance reported for full size ballast in literature. Indraratna et al. (1998) obtained the greatest angles of effective shearing resistance and Raymond and Davies (1978) obtained the lowest angles of effective shearing resistance. The differences in angle of effective shearing resistance observed by different researchers can be attributed to differences in rock mineralogy, density, specimen preparation, the effect of membrane thickness and whether and how a membrane correction is applied.

6. Cyclic and Extension triaxial test results

6.1 Cyclic test results

Cyclic tests were carried out on dry ballast specimens. Load was typically applied up to approximately 1000 repetitions although some tests varied.

Two types of cyclic experiments were carried out.

i. The cell pressure was held constant and the deviator stress was cycled
ii. The cell pressure and deviator stress were cycled simultaneously.

The test parameters can be found in Table 6.1.

Constant cell pressure cyclic tests were commonly carried out at 55 kPa. One constant cell pressure test was carried out at 45 kPa for comparison with the cyclic cell pressure tests in which the cell pressure was cycled between 15 kPa and 45 kPa.

The stress paths followed during the cyclic tests are shown in Figure 6.1.

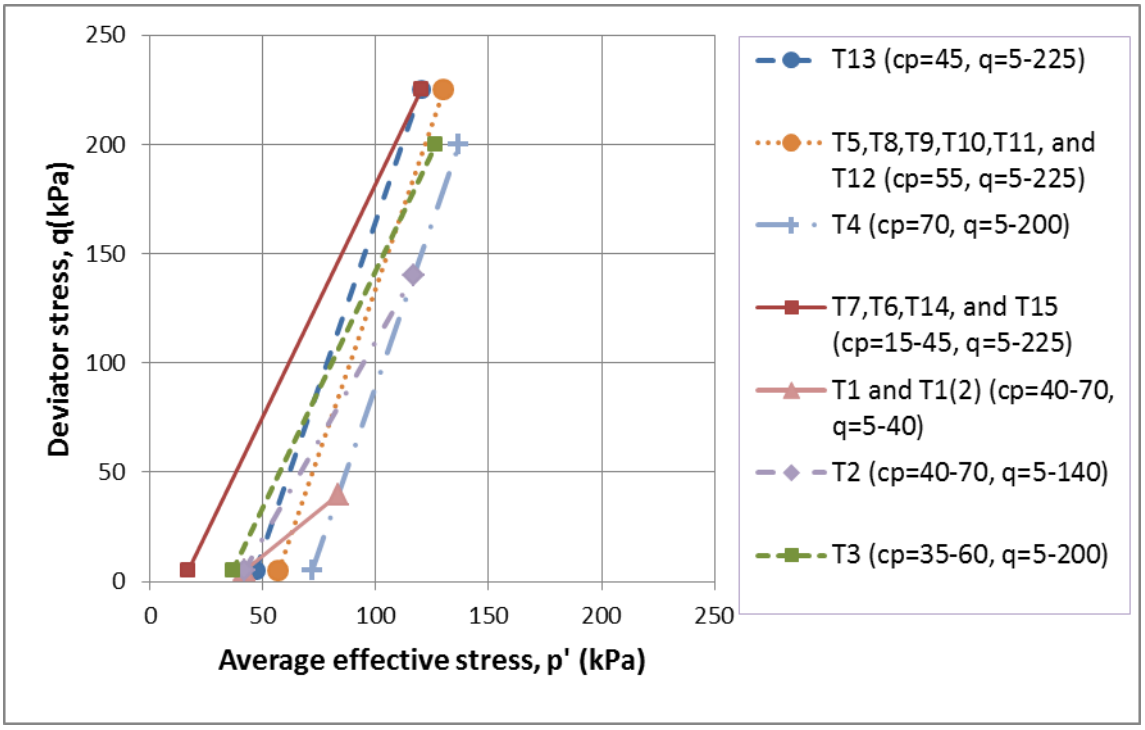

Figure 6.1: Stress paths followed during the cyclic tests

Test	σ_3' - Cell pressure (kPa)	q (kPa)	(σ_1'/ σ_3') at q_{max}	(σ_1'/ σ_3') at q_{min}	(q/p') max	Density (kg/m^3)	Void ratio (G_s=2.78)	Density Index*
T13	45	5-225	6	1.11	1.875	1528	0.819	0.5266
T5	55	5-225	5.09	1.09	1.731	1606	0.731	0.8745
T8	55	5-225	5.09	1.09	1.731	1559	0.783	0.6697
T9	55	5-225	5.09	1.09	1.731	1515	0.835	0.4649
T10	55	5-225	5.09	1.09	1.731	1543	0.802	0.5931
T11	55	5-225	5.09	1.09	1.731	1583	0.756	0.7736
T12	55	5-225	5.09	1.09	1.731	1536	0.810	0.5635
T4	70	5-200	3.85	1.07	1.463	1595	0.742	0.8287
T7	15-45	5-225	6	1.33	1.875	1550	0.793	0.6272
T6	15-45	5-225	6	1.33	1.875	1549	0.795	0.6201
T14	15-45	5-225	6	1.33	1.875	1558	0.785	0.6614
T15	15-45	5-225	6	1.33	1.875	1568	0.773	0.7090
T1	40-70	5-40	1.57	1.13	0.48	1585	0.754	0.7832
T1(2)	40-70	5-40	1.57	1.13	0.48	1602	0.735	0.8580
T2	40-70	5-140	3	1.13	1.2	1568	0.773	0.7089
T3	35-60	5-200	4.33	1.14	1.579	1600	0.737	0.8491

Table 6.1: Cyclic test parameters

*density index was calculated based on γ_{max}=1636 & γ_{min}=1424 kg/m^3)

Figure 6.2 shows the axial strain against number of cycles for the constant cell pressure tests. Test T4 shows lower strains owing to the lower stress ratio than in the other tests (see Table 6.1). The permanent axial strain for similar test conditions falls into a range of values (Figure 6.3). There is no clear pattern to relate the variation in permanent strain to the variation in density. The variation in permanent axial strain is largely caused by random bedding variations during the first few cycles.

According to Fair (2003), the permanent axial strains from cyclic triaxial tests on ballast from similarly prepared tests are not consistent. He noticed the cause of this discrepancy is the bedding errors occurring during the first cycle. Following that, permanent axial strain of the first cycles from all tests were removed by Aursudkij (2007). Even in that case, the permanent axial strain of similarly prepared specimens (σ_3' = 90 kPa, q_{max} = 270 kPa, density= 1506-1579 kg/m^3) varied and fall within the range of 1.3% to 2% after 100,000 cycles, except one test where the permanent axial strain reported to be 0.5%.

Figure 6.4 shows the permanent axial strain against number of cycles between 100 and 1000 cycles, where the permanent axial strain has been zeroed at the 100th cycle. Permanent axial strains follow an approximately linear trend with the logarithm of the number of cycles between 100 and 1000. The gradient of the logarithmic trend falls in the range of 0.0009-0.0019, with an average value of 0.0013 (Table 6.2). The gradient obtained for 45 kPa confining pressure test T13 is higher than the 55 kPa confining pressure tests except for T10. The gradient obtained for the 70 kPa confining pressure test T4 is lower. Therefore the rate of strain reduces with increasing confining pressure with the same deviator stress range. This is similar to the observation by Lackenby et al. (2007), Aursudkij et al. (2009), and Anderson and Fair (2008) where the permanent axial strain reduces with increasing confinement with same deviator stress range.

Figure 6.5 shows the permanent axial strain at the 1000th cycle, re-zeroing after various numbers of initial cycles. The difference in permanent axial strain between tests reduces if the initial cycles are eliminated. The permanent axial strain at the 1000th cycle varies by approximately 0.3% (0.63 % to 0.95%) after neglecting the first 5 cycles. There is not much difference between the 45 kPa and 55 kPa constant cell pressure tests in terms of axial strain.

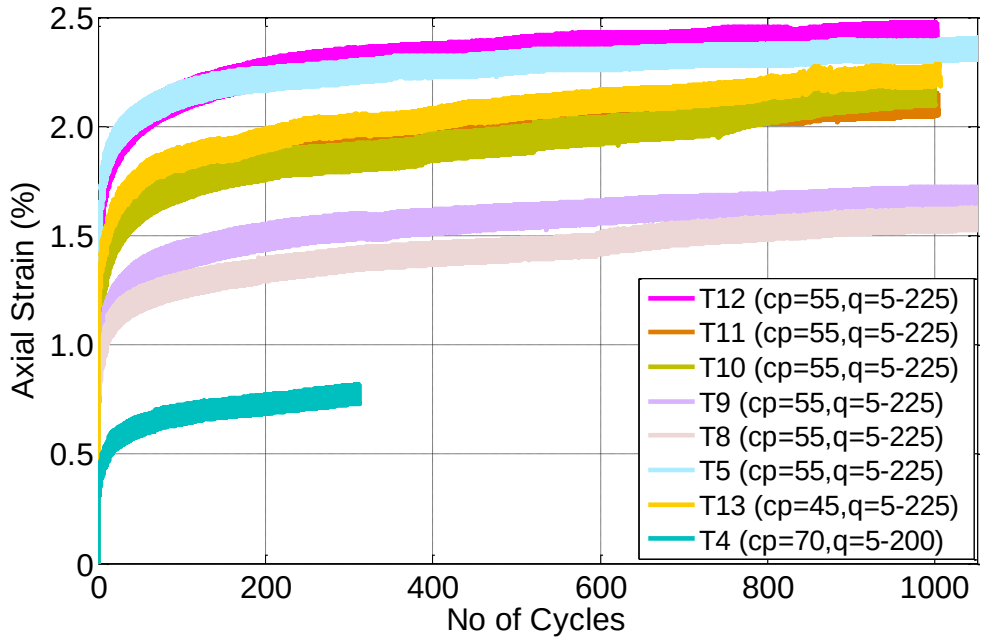

(a) From 1st cycle

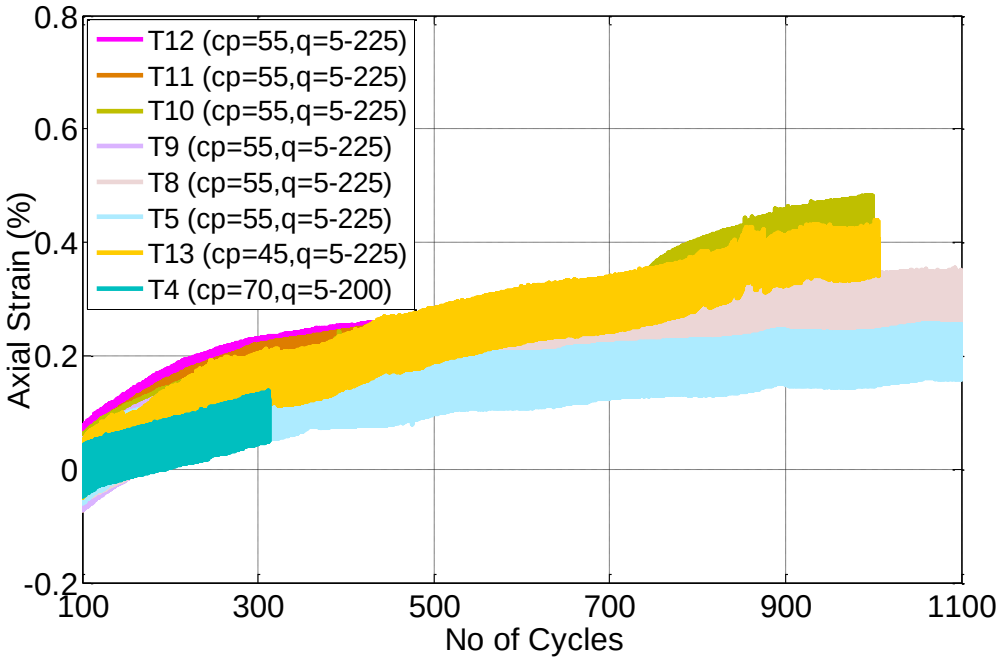

(b) After axial strain is zeroed at 100th cycle

Figure 6.2: Axial strain against number of cycles for constant cell pressure tests

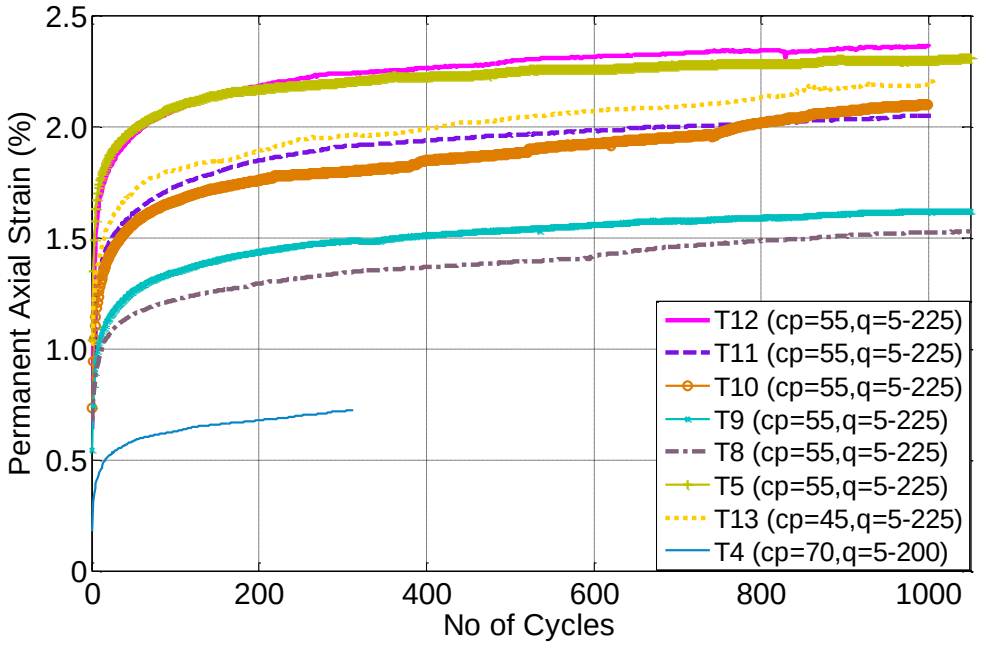

(a) Linear scale

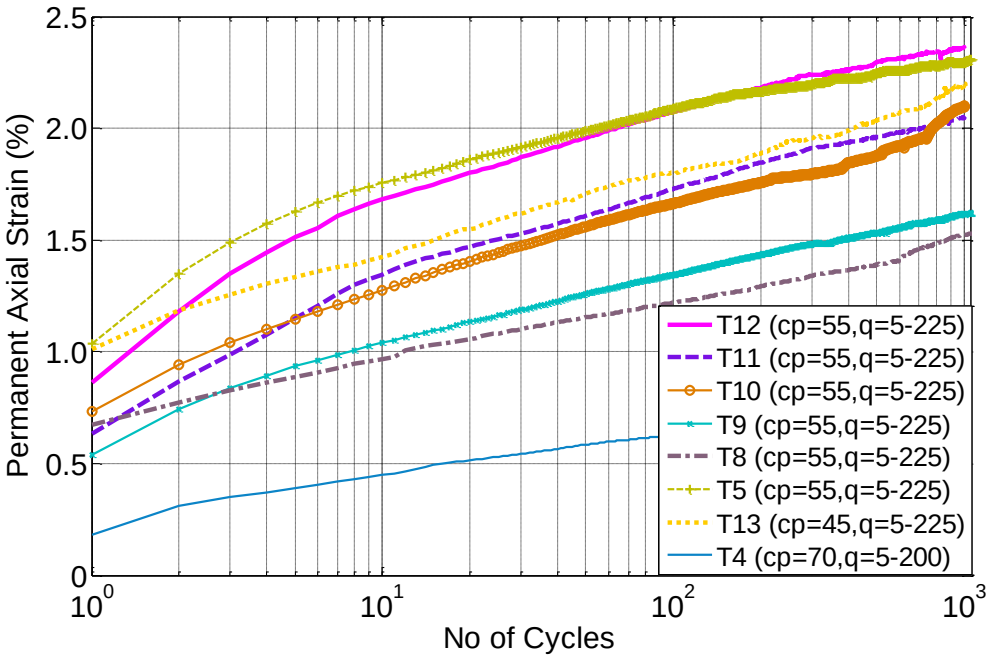

(b) Log scale

Figure 6.3: Permanent axial strain against cycles for constant cell pressure tests

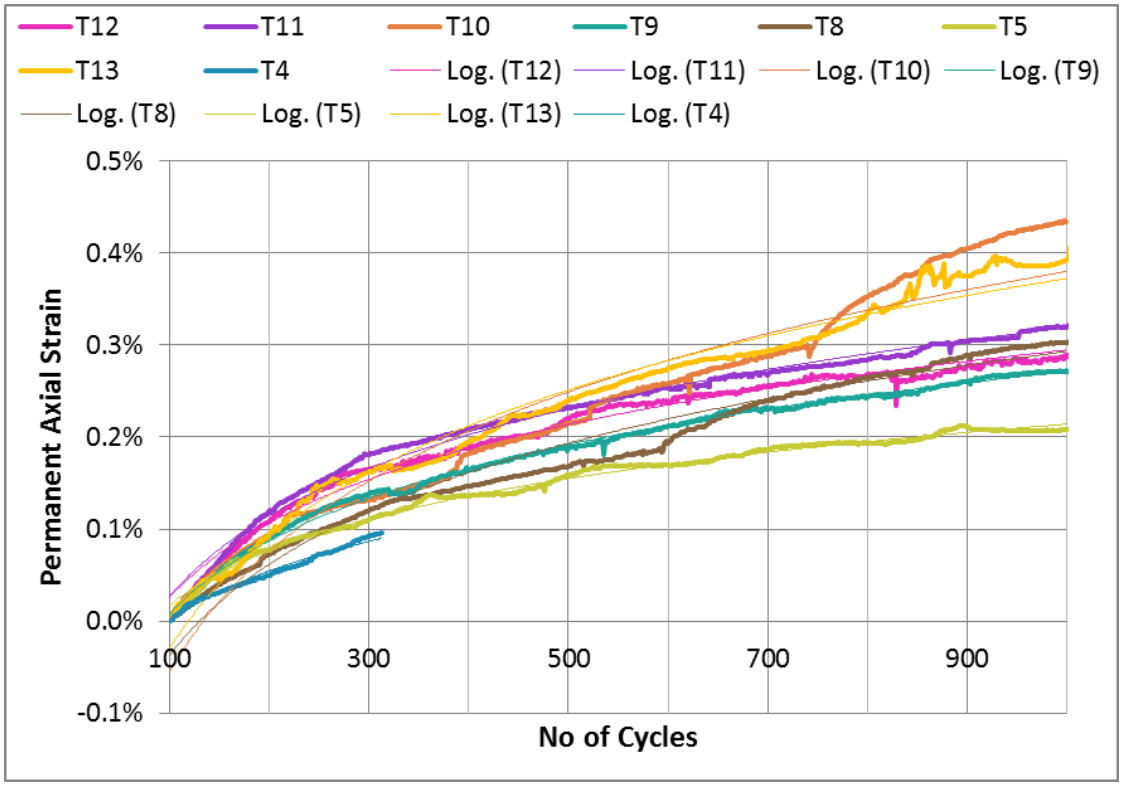

(a) Linear scale

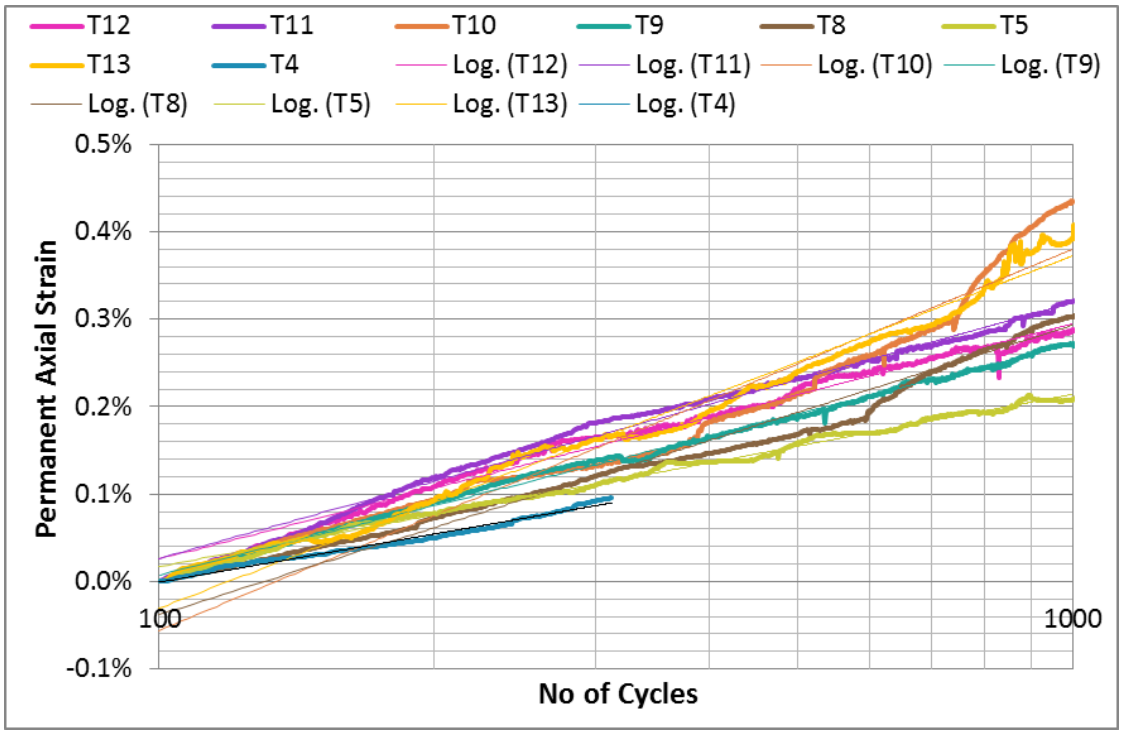

(b) Log scale

Figure 6.4: Logarithmic trend between permanent axial strain and log number of cycles

Test	Equation	Coefficient of correlation, R2	Gradient
T12 (cp=55, q=5-225)	y=0.0012ln(x)-0.0051	0.9878	0.0012
T11 (cp=55, q=5-225)	y=0.0013ln(x)-0.0056	0.9905	0.0013
T10 (cp=55, q=5-225)	y=0.0019ln(x)-0.0093	0.9252	0.0019
T9 (cp=55, q=5-225)	y=0.0011ln(x)-0.0052	0.9979	0.0011
T8 (cp=55, q=5-225)	y=0.0014ln(x)-0.007	0.9808	0.0014
T5 (cp=55, q=5-225)	y=0.0009ln(x)-0.0038	0.9948	0.0009
T13 (cp=45, q=5-225)	y=0.0017ln(x)-0.0084	0.9763	0.0017

Table 6.2: Equations of the logarithmic trend between permanent axial strain and log number of cycles

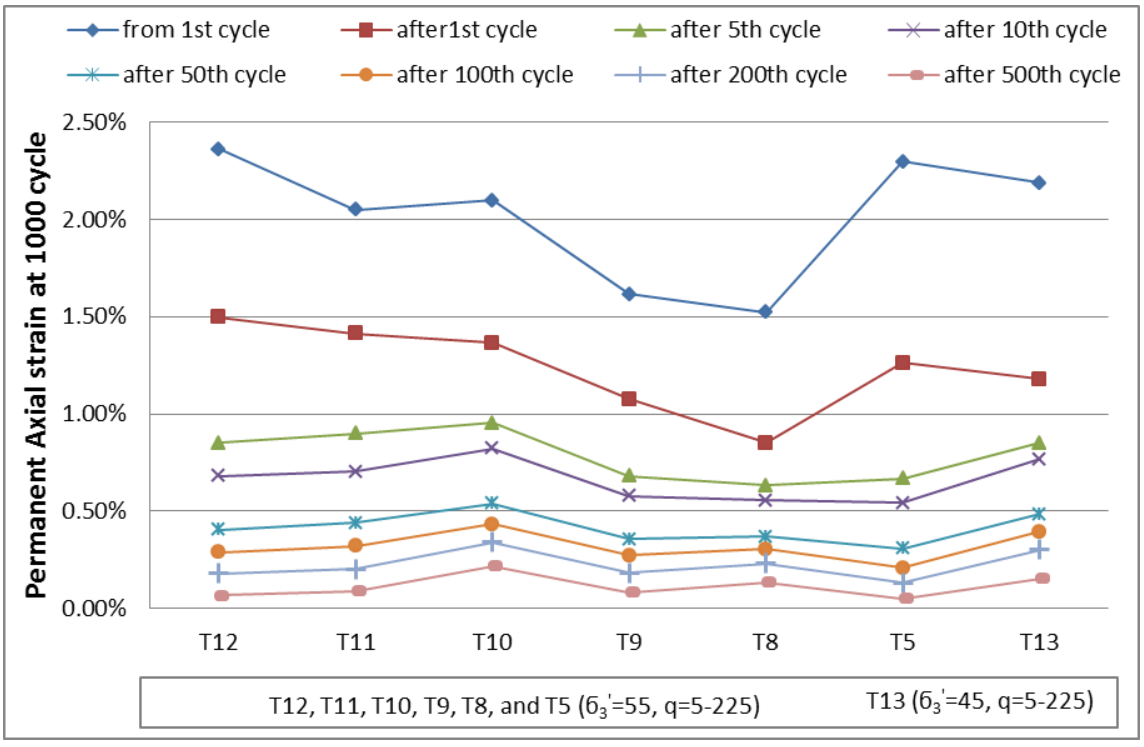

Figure 6.5: Permanent axial strain at 1000 cycles for constant cell pressure tests

Figure 6.6 compares the permanent axial strain in the 15-45 kPa cyclic cell pressure tests with the 45 kPa constant cell pressure cyclic test. The permanent axial strain is higher in the cyclic cell pressure tests. Although the same deviator stress range was

applied in both tests, in the cyclic cell pressure tests the confining pressure was reduced to 15 kPa resulting in higher strain. In other words, during cyclic cell pressure test, the stress ratio q/p′ is higher within a cycle (Figure 6.1), which results in higher strain.

For e.g. the stress ratio at datum deviator stress level;

Cyclic cell pressure test:

q=115 kPa; σ_3'=30; σ_1'=145; p′=68.33..... q/ p′=115/68.33=1.68

Constant cell pressure test:

q=115; σ_3'=45; σ_1'=160; p′= 83.33..... q/ p′=115/83.33= 1.38

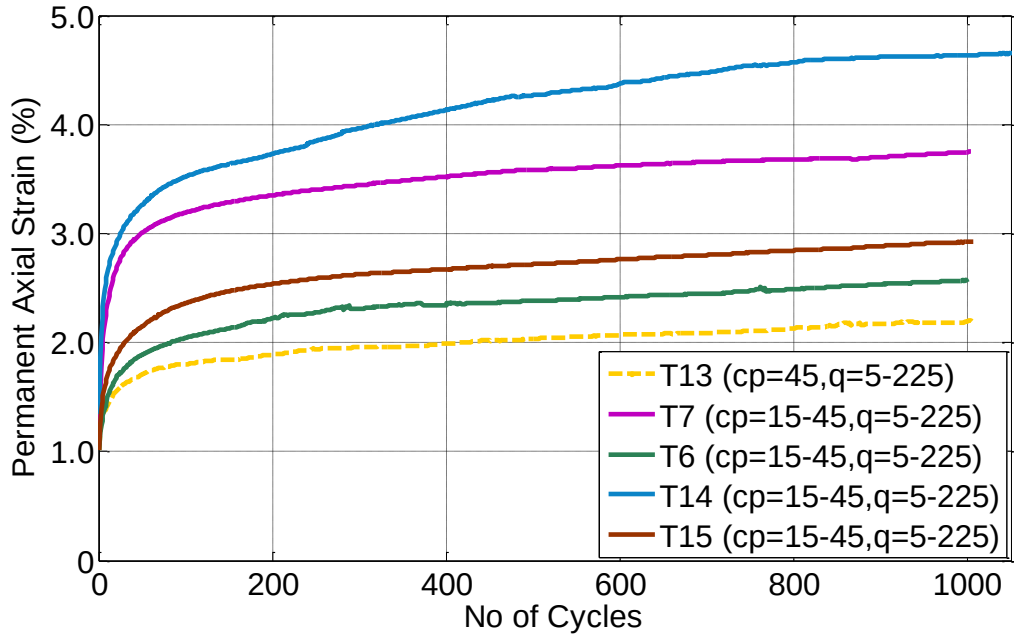

Figure 6.6: Comparison of permanent axial strain for cyclic and constant cell pressure tests

Figure 6.7 compares the permanent axial strain at the 1000th cycles for both constant and cyclic cell pressure tests, re-zeroing after various numbers of initial cycles. Tests T6 and T15 show similar permanent axial strain accumulation after the 5th cycle. The permanent axial strain accumulation for cyclic cell pressure tests is similar after the 50th cycle except for test T14 where permanent axial strain accumulation is higher throughout the cycles. Permanent axial strain rate accumulation is higher for cyclic cell pressure tests all through the cycles.

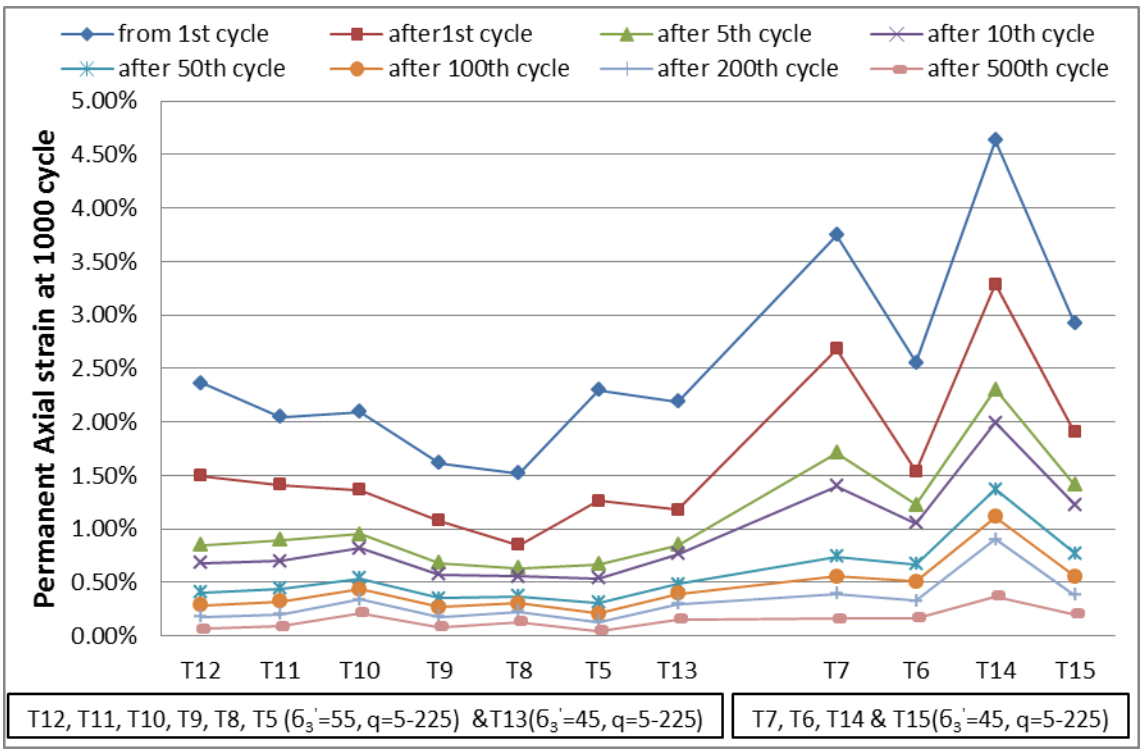

Figure 6.7: Permanent axial strain at 1000 cycles for cyclic and constant cell pressure tests

Figure 6.8 shows that permanent axial strain increases with increasing deviator stress ranges for similar cycled cell pressure ranges. Test T2 shows higher axial strain compared to T1 and T1(2) which were tested at the same cell pressure range but at a lower deviator stress range (Table1). Test T3 shows highest axial strain, which was subjected to a similar cell pressure range but a higher deviator stress range. This is similar to the observation by Lackenby et al. (2007) and Aursudkij et al. (2009) where the permanent axial strain increases with increasing deviator stress for the same constant cell pressure applied.

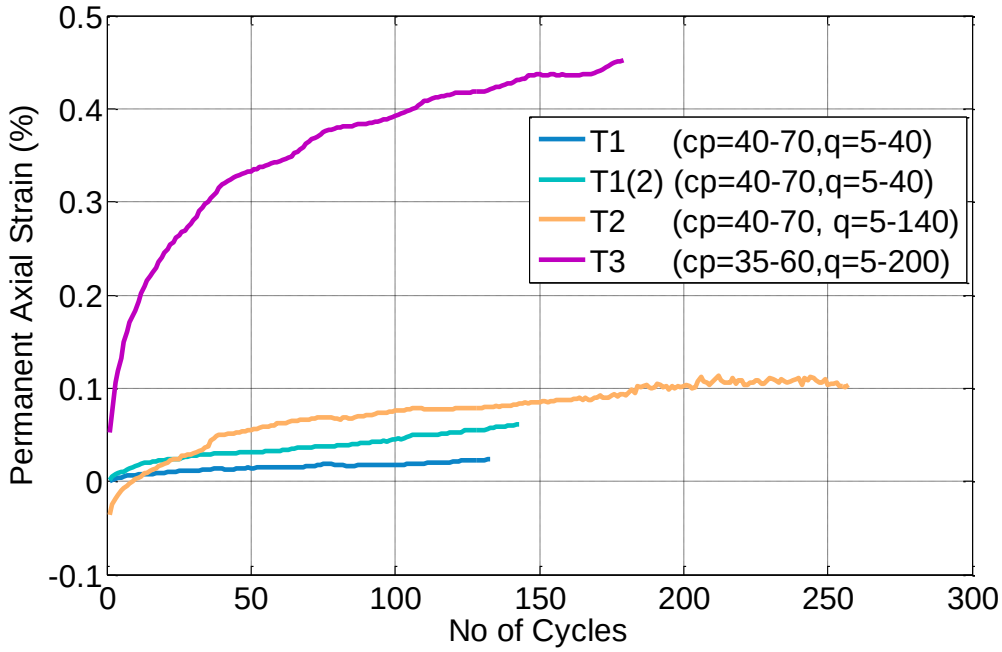

Figure 6.8: Permanent axial strain with increasing deviator stress

Figure 6.9 to Figure 6.13 shows permanent volumetric strain obtained both from controller and calliper readings during each test. Calliper readings are not included for 'T5' and 'T8' tests as callipers were out of limit during the test. In general volumetric deformation from the controller and calliper are different. Specimen volume change from the controller can be influenced by creep, membrane penetration, membrane slippage, temperature changes, and air in the system. The radial callipers were fixed on the membrane and supported by 3 mm x 4 mm aluminium plates glued inside the membrane to provide a stable support. Due to the particle size of ballast irrespective of this arrangement, the callipers rest on very few particles and these can therefore be influenced by local variation in the specimen deformation behaviour.

The volumetric strain from the controller is increasing throughout the test (Figure 6.9 to Figure 6.13). It can be due to creep effects as the test was run over a couple of days. The overall volumetric strain accumulation pattern obtained from the calliper looks closer to the permanent axial strain accumulation pattern. Thus volume change from controller was considered unreliable and the calliper readings were used.

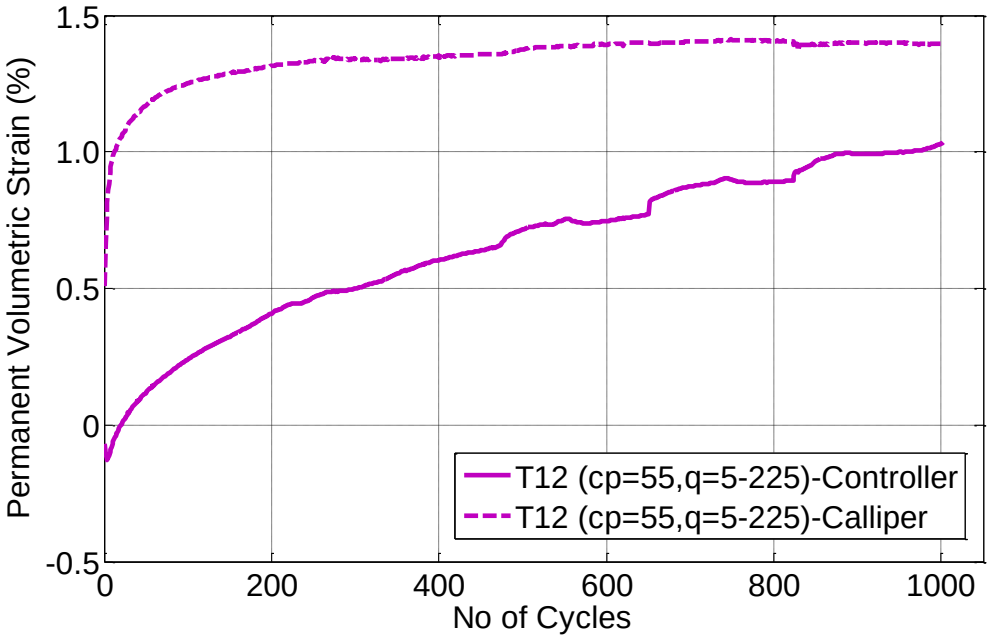

Figure 6.9: Permanent volumetric strain for 'T12' test

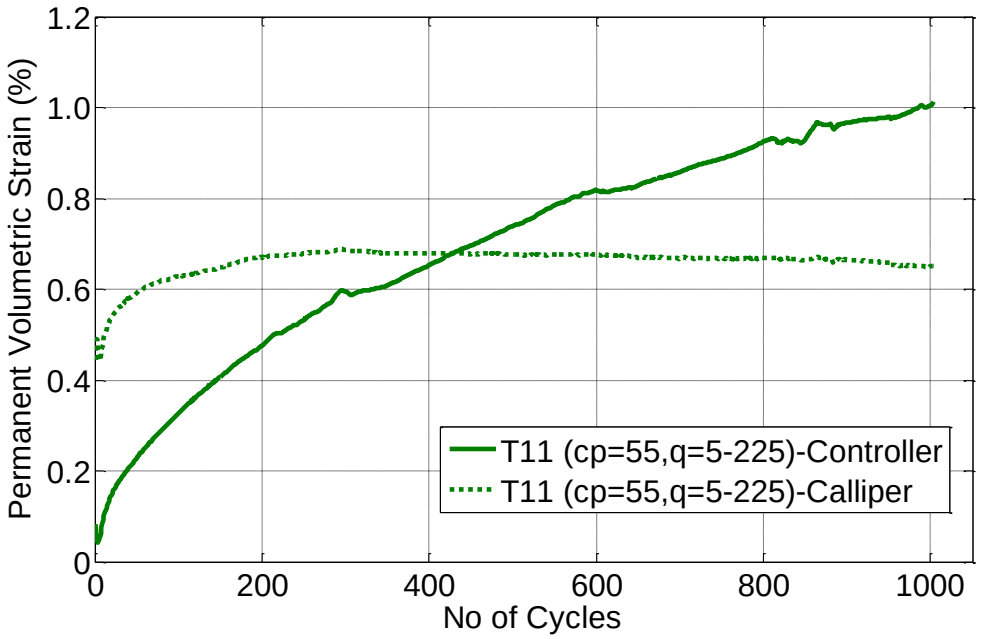

Figure 6.10: Permanent volumetric strain for 'T11' test

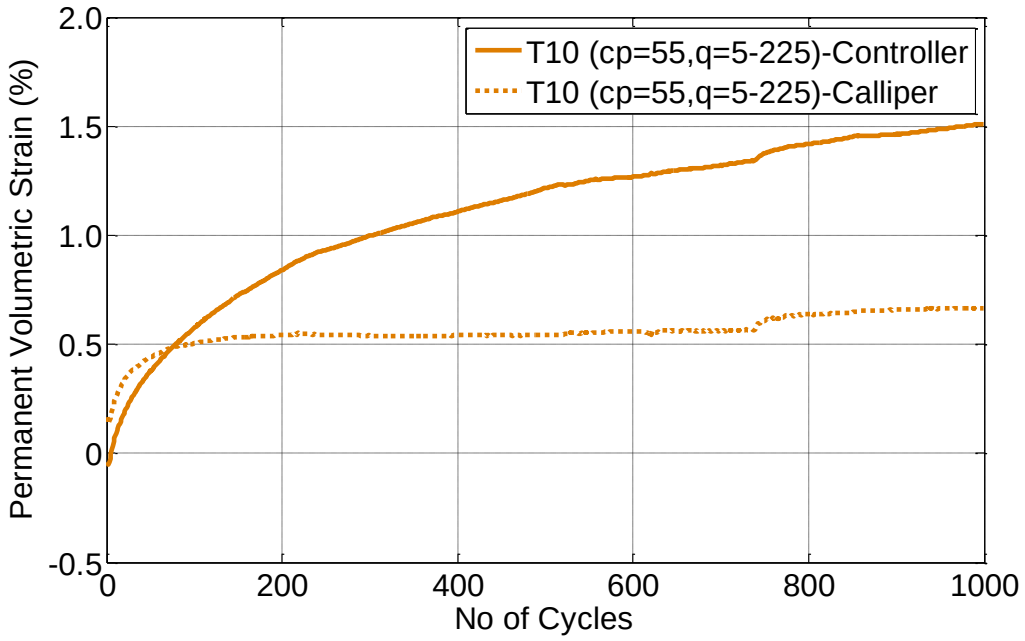

Figure 6.11: Permanent volumetric strain for 'T10' test

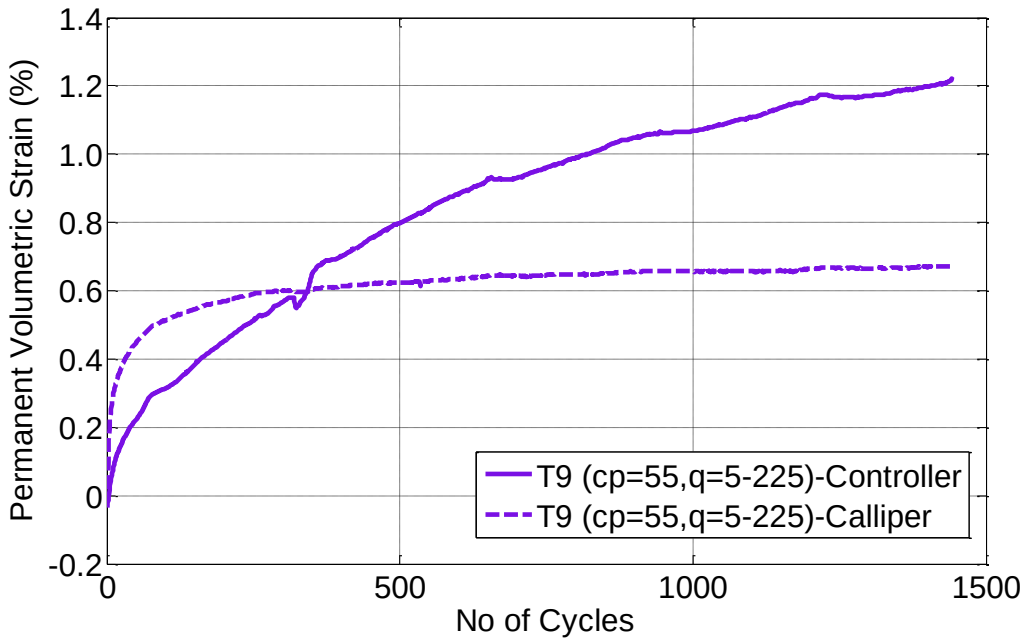

Figure 6.12: Permanent volumetric strain for 'T9' test

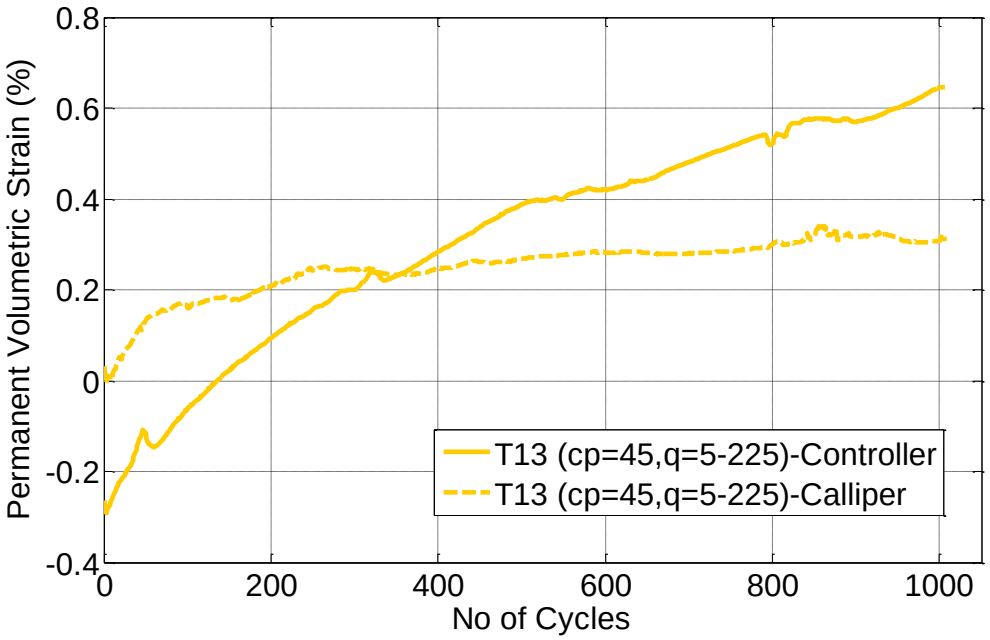

Figure 6.13: Permanent volumetric strain for 'T13' test

Anyhow the permanent volumetric strains calculated from cell pressure controller readings for constant cell pressure tests are shown in Figure 6.15. Constant cell pressure specimens fall into a narrow band except test T10.

Figure 6.16 shows the volumetric deformation of specimens determined using radial calliper readings. In the constant cell pressure tests except for 'T13', only one radial calliper was fixed at the mid height of specimen. These readings are from one radial calliper. This is due to only one radial calliper was available during these test setup. During 'T13' and cyclic cell pressure tests radial measurements were obtained using 3 radial callipers fixed at three equal intervals (75 mm, 150 mm, and 225 mm from the base of the specimen). In this case, the average of the top and bottom calliper readings was used for radial and volumetric strain calculations. In other words, the middle calliper readings were omitted for volumetric strain calculations.

The triaxial tests showed barelling and although deformation is commonly assummed as a right circular cyclinder for triaxial tests which facilitates relatively simple volumetric calculations, for the ballast tested this is further from reality than usual. Interestingly, Indraratna et al. (1998) reported that in contrast to the case of sand or granulated fine media, in the case of ballast specimen no distinct failure plane was

eminent even after significant post peak straining and the mode of failure is considered to be “bulging”. During testing ballast bulges outward in the middle; therefore the middle calliper overestimates the radial strain compared to the average for the whole. The top and bottom callipers are away from the middle being located in the middle of either half of the test height. Thus the average for the top and bottom calliper readings was considered a better estimate of the average radial strain for the calculations based on an idealised barrelling shape as shown in Figure 6.14.

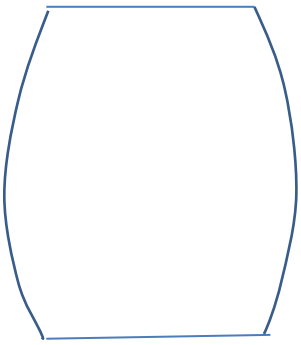

Figure 6.14: Barrelling shape of deformation

The relationship between average readings from the top and bottom callipers and the middle calliper was not consistent. Although the average of the top and bottom callipers was approximately 2/3 of the middle calliper for tests T13, T6 and T15, this wasn’t true in other cases. Although the overall deformation shape is barrelling, the calliper readings were affected by the local variations of the specimen deformation as the callipers were rested on few ballast particles unlike clay or sand. The variation between callipers regarding barrelling could be due to the result of the small contact area and highly localised nature of the radial measurements which may not be representative of the overall average change in radial strain but rather just due to the movements of a very few ballast particles in contact with the calliper. More callipers are needed to increase the data set for averaging the radial measurements and removing local variations. Thus, if more callipers are fixed in the specimen, the true shape of deformation can be caught. An alternate means of radial strain measurement that is less localised such as a direct measurement of the full change in circumference (rather than a localised measure of the diameter from two discrete contact locations) can catch the true shape of deformation more accurately.

The major part of the volumetric deformation occurs during the initial cycles as shown in Figure 6.17. Variation in permanent volumetric strain in the tests from calliper

readings is high during the initial cycles but reduces greatly after the10th cycle. Similary Aursudkij (2007) observed permanent volumetric strain (calculated from the differential pressure transducer) of similarly prepared ballast specimens varied.

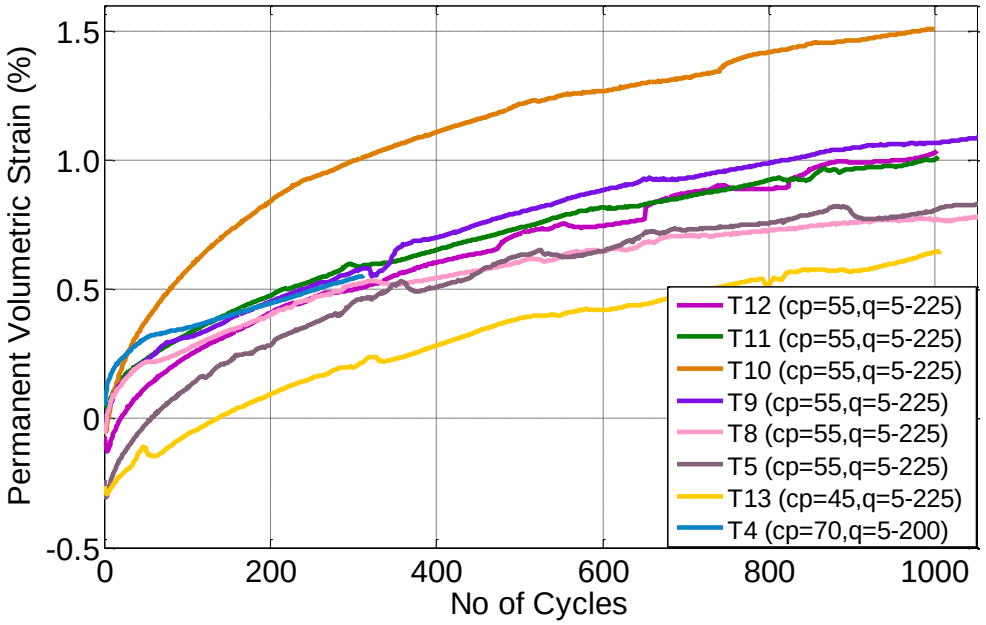

(a) From 1st cycle

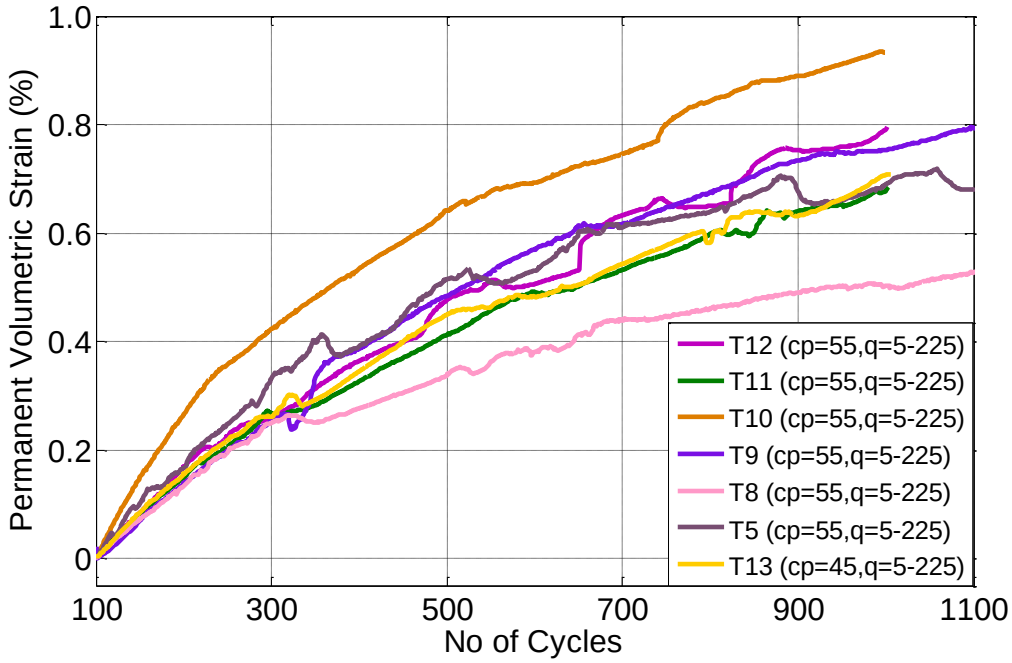

(b) After permanent volumetric strain is zeroed at 100th cycle

Figure 6.15: Permanent volumetric strain from cell pressure controller readings

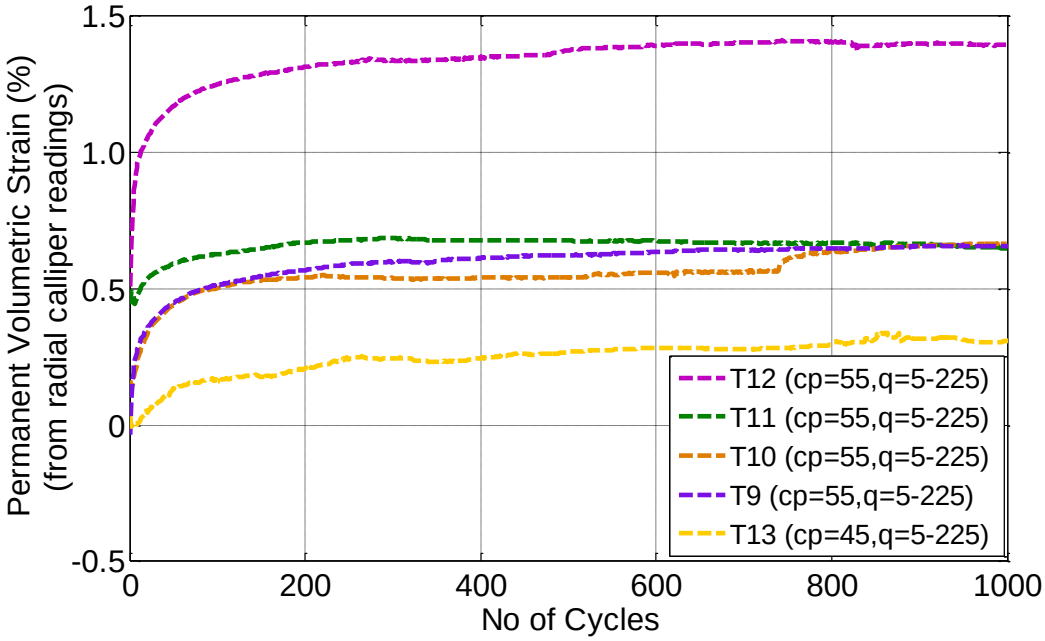

(a) From 1st cycle

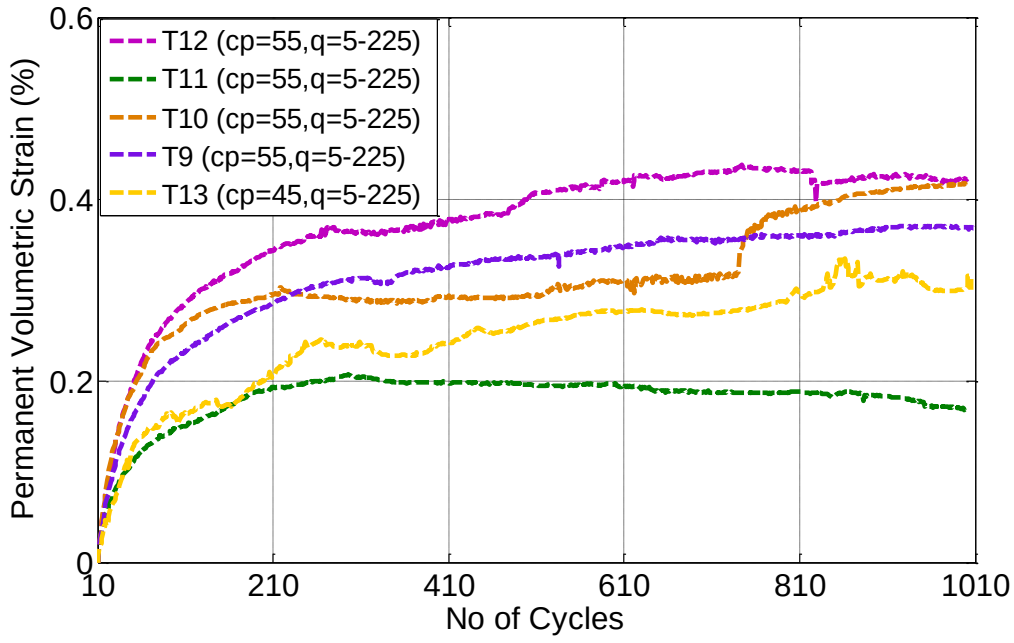

(b) After 10th cycle

Figure 6.16: Permanent volumetric strain from radial calliper readings

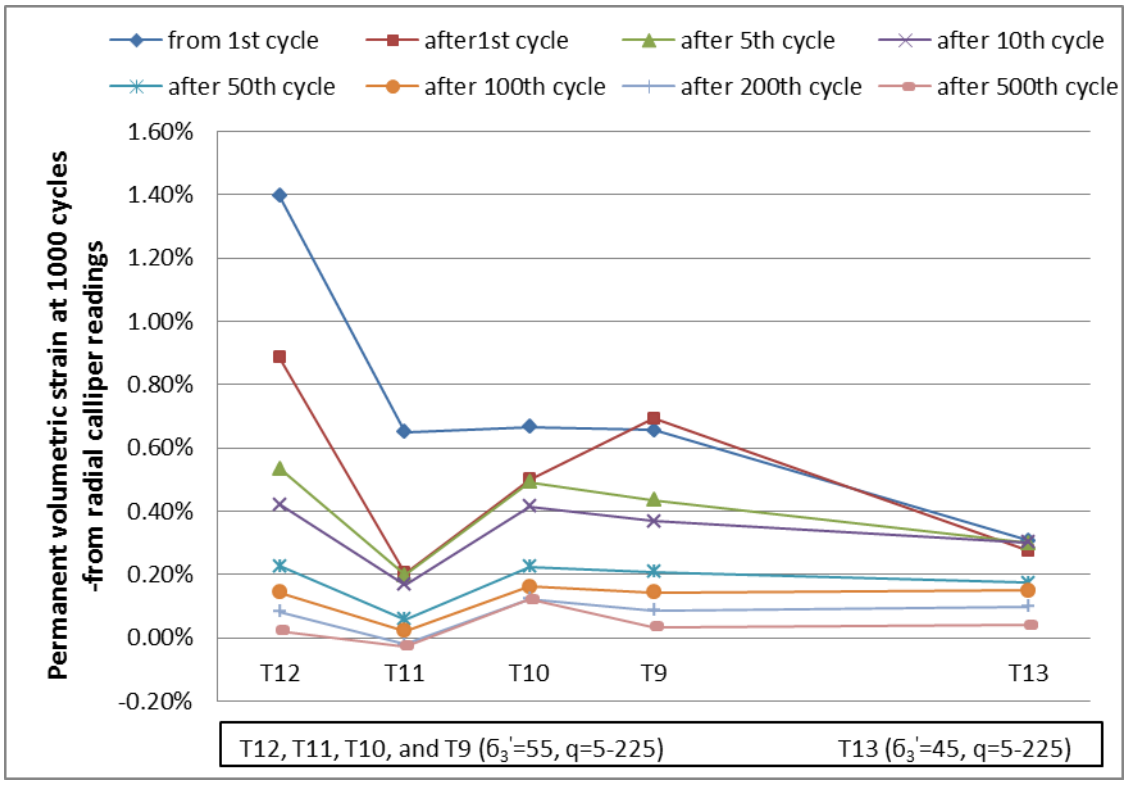

Figure 6.17: Permanent volumetric strain at 1000 cycles

In the cyclic cell pressure tests, volumetric strain was measured using 3 radial callipers. In this case, volume measurement from the controller was severely influenced by membrane penetration as the cell pressure was cycled. For example Figure 6.18 shows the volumetric strain from the controller for the constant cell pressure test 'T13' and cyclic cell pressure test 'T6'. The amplitude of volume change within a cycle is very high for the cyclic cell pressure test due to the significant amount of membrane penetration.

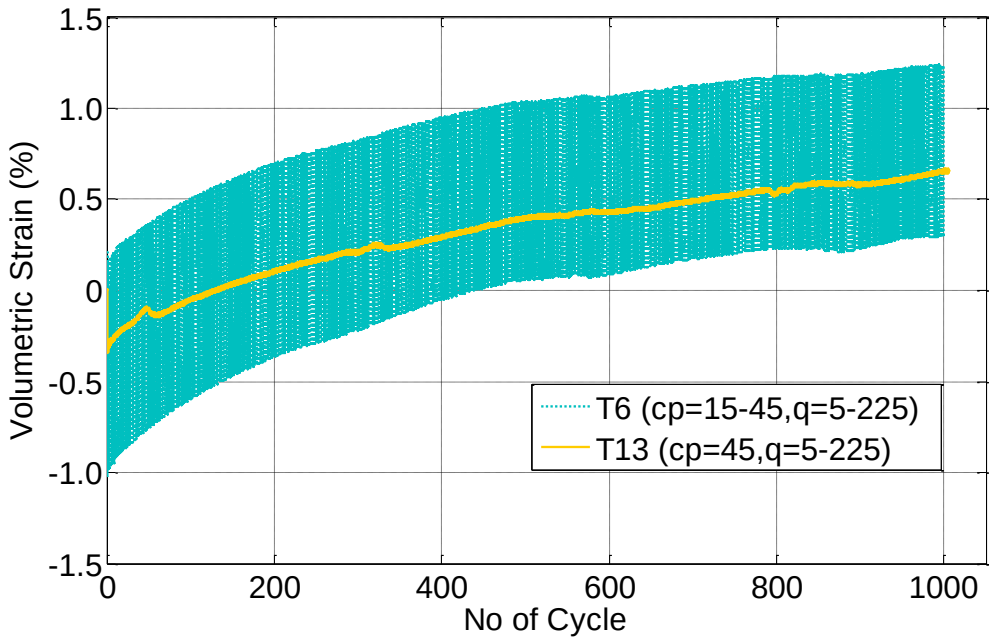

Figure 6.18: Volumetric strain from controller affected by membrane penetration

Figure 6.19 shows the permanent volumetric strain of the cyclic cell pressure tests together with T13, a constant cell pressure test. The permanent volumetric strain calculated from the radial calliper readings depends on both the permanent axial strain and the radial strain.

Variations in permanent volumetric strain , permanent axial strain, and radial strain between tests reduce during later cycles as shown in Figure 6.20 and Figure 6.21. The permanent volumetric strains of constant cell pressure test T13 and cyclic cell pressure tests T6 and T15 are close over different intervals. Comparatively higher axial strain accumulation and radial contraction of tests T7 and T14 lead to higher permanent volumetric strains.

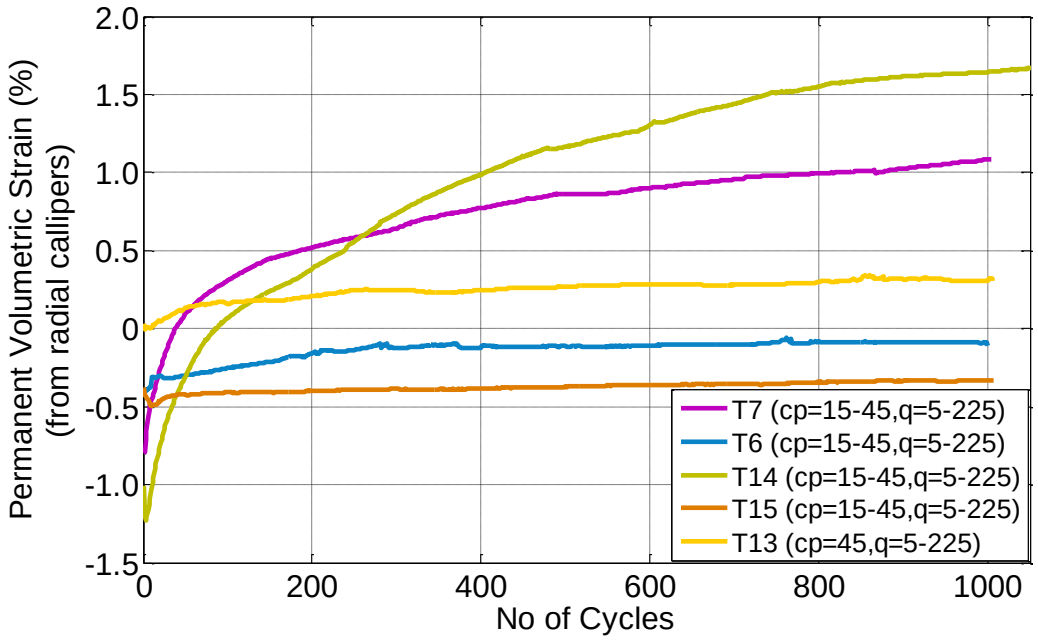

(a) From 1st cycle

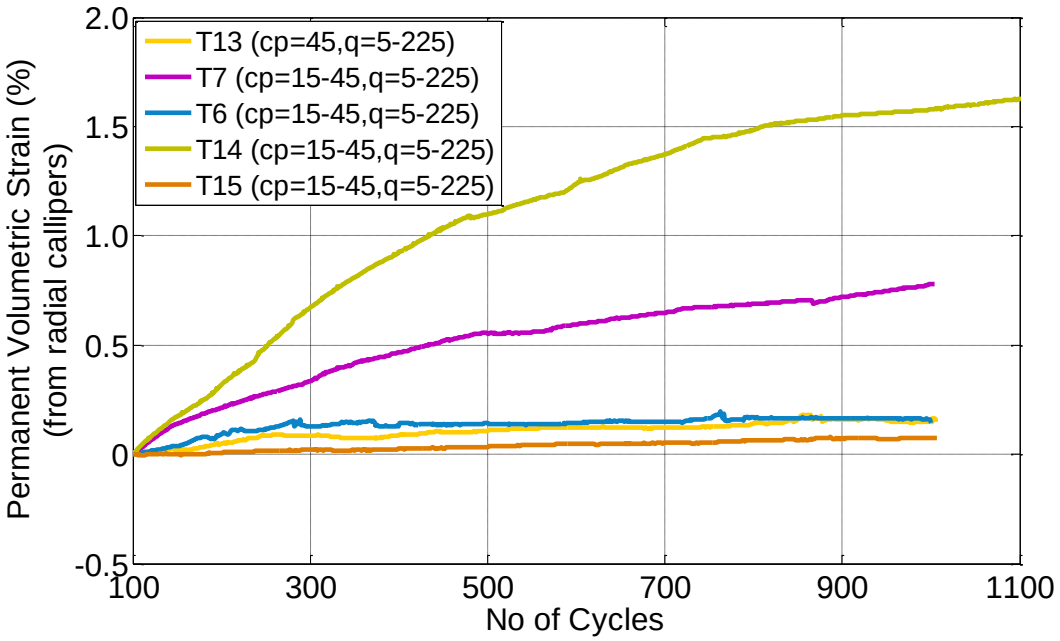

(b) After permanent volumetric strain is zeroed at 100th cycle

Figure 6.19: Permanent volumetric strain for cyclic cell pressure test and 'T13'

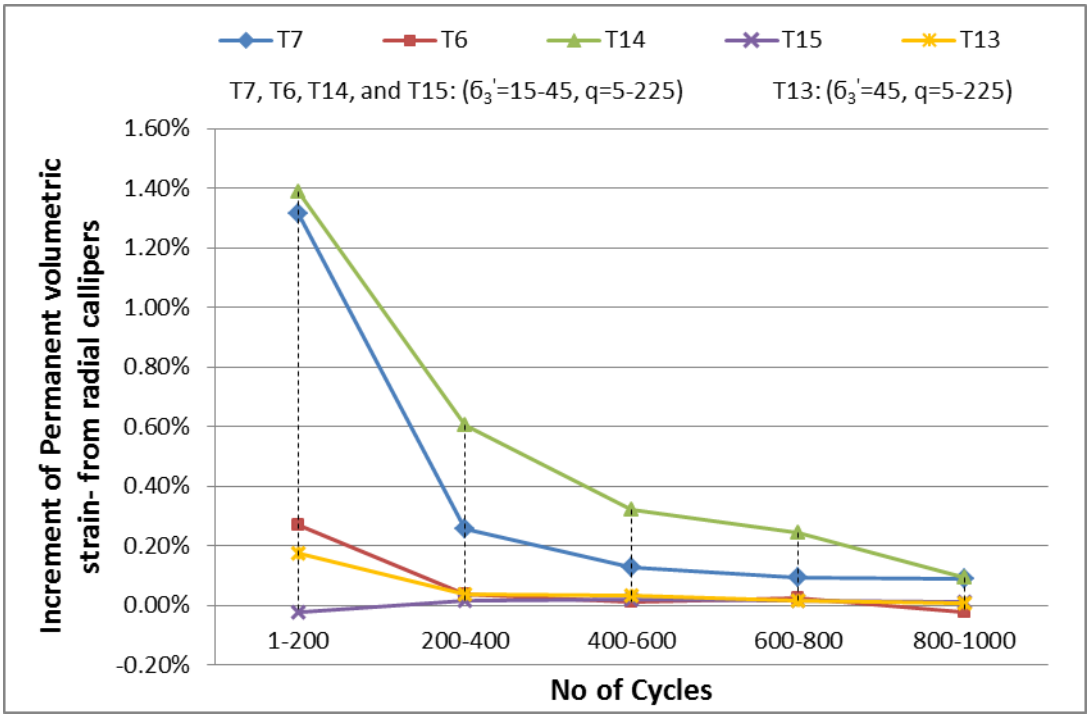

Figure 6.20: Volumetric strain accumulation over different interval no of cycles

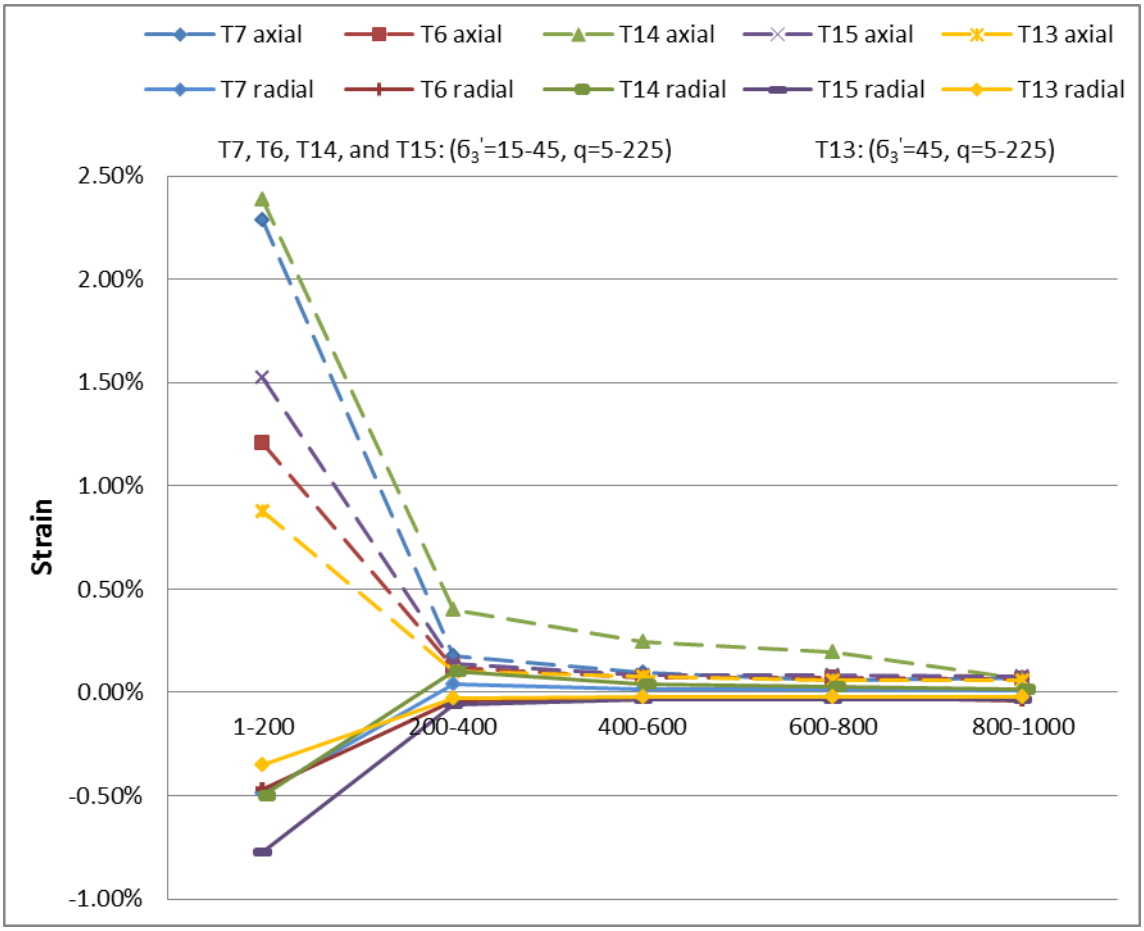

Figure 6.21: Axial and radial strain accumulation over different intervals of cycles

Figure 6.22 shows the radial strain values for constant cell pressure cyclic tests. Except for T13, the other readings are from one radial calliper fixed at the mid height of the specimen. Constant cell pressure test specimens show radial expansion.

Figure 6.23 shows the comparison of radial strain for cyclic cell pressure tests and constant cell pressure test T13. Higher radial strain values for cyclic cell pressure tests can be attributed to the reduction in cell pressure during the cycle. Tests T7 and T14 expanded during initial cycles but then started to contract, whereas the other two tests expanded throughout the tests. This can be attributed to higher volumetric compression of T7 and T14 or local variation from the placement of the callipers being unrepresentative of the overall behaviour.

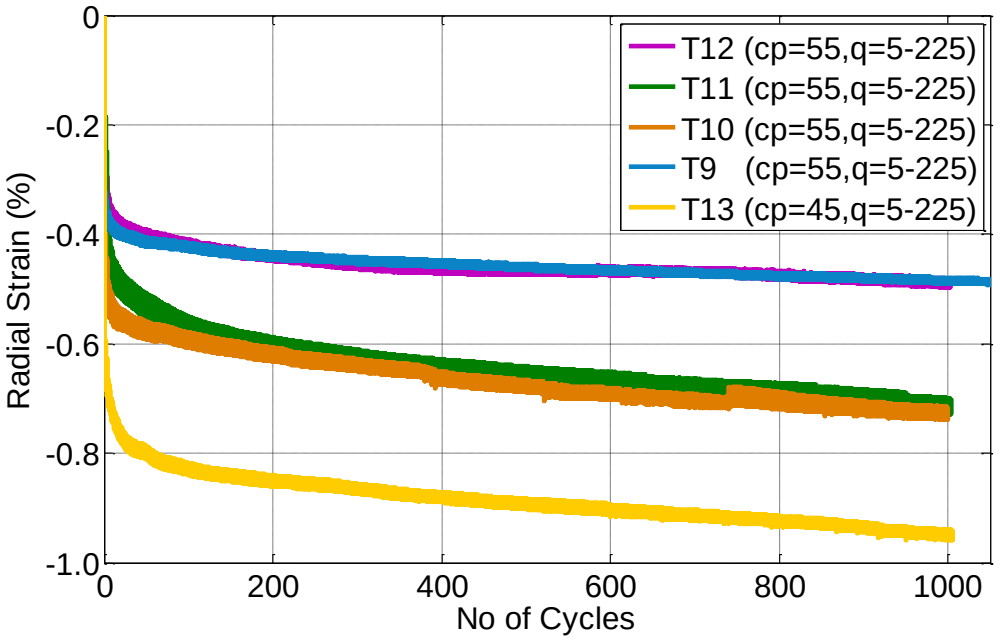

Figure 6.22: Radial strain of constant cell pressure tests

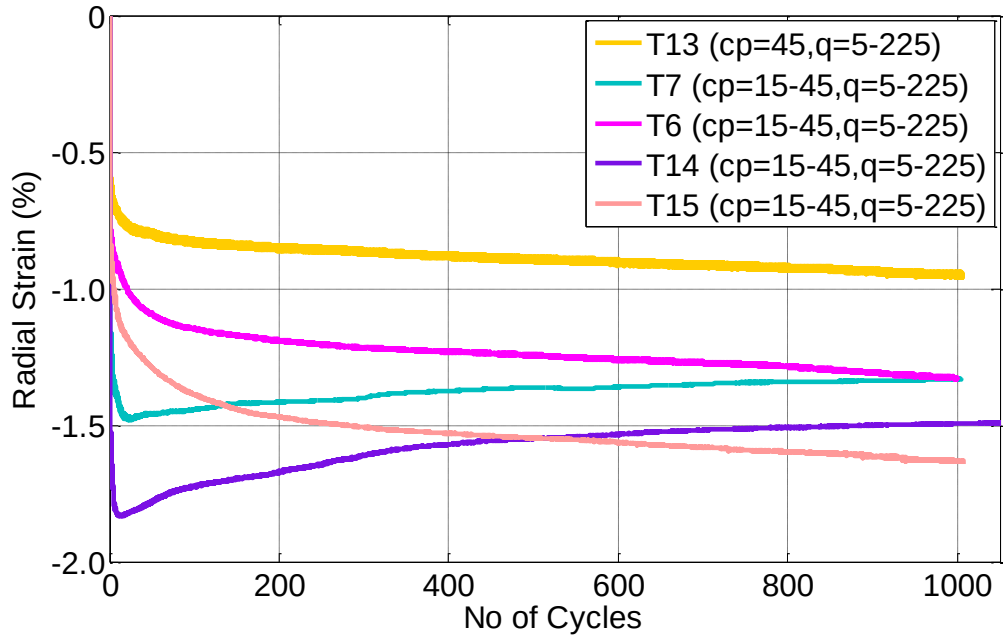

Figure 6.23: Radial strain of cyclic cell pressure tests and 'T13'

Figure 6.24 shows the resilient modulus of constant cell pressure tests evaluated over each cycle. The resilient modulus of 190-250 MPa obtained at 1000th cycle is closer to

the vaues obtained by Lackenby et al. (2007), Anderson and Fair (2008) and Sevi() at 1000th cycle. For example, Sevi (2008) reported the resilient modulus of 150-220 MPa at 1000th cycles for the three ballast gradations tested at different stress ratios. Lackenby et al. (2007) observed the resilient modulus of 175 MPa at 1000th cycle at q=45-230kPa and σ_3'=60kPa. Anderson and Fair (2008) reported the resilient modulus of 244 MPa at q=15-250 kPa and σ_3'=40kPa.

Cyclic cell pressure tests show a lower resilient modulus compared to the constant cell pressure test T13 (Figure 6.25). This indicates that the stiffness reduces when the cell pressure is cycled during loading.

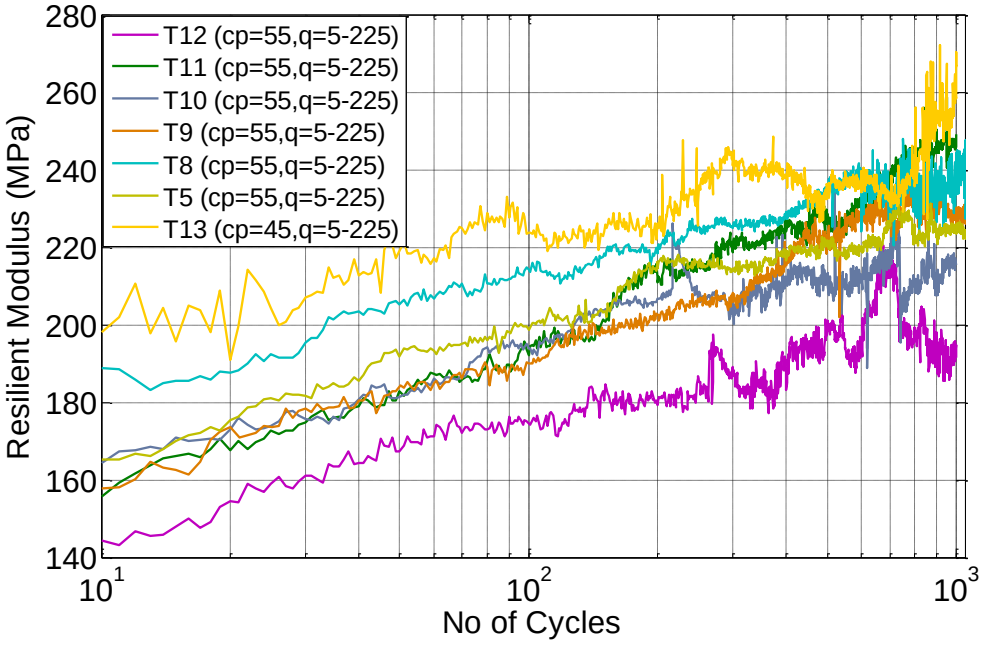

(a) Log scale

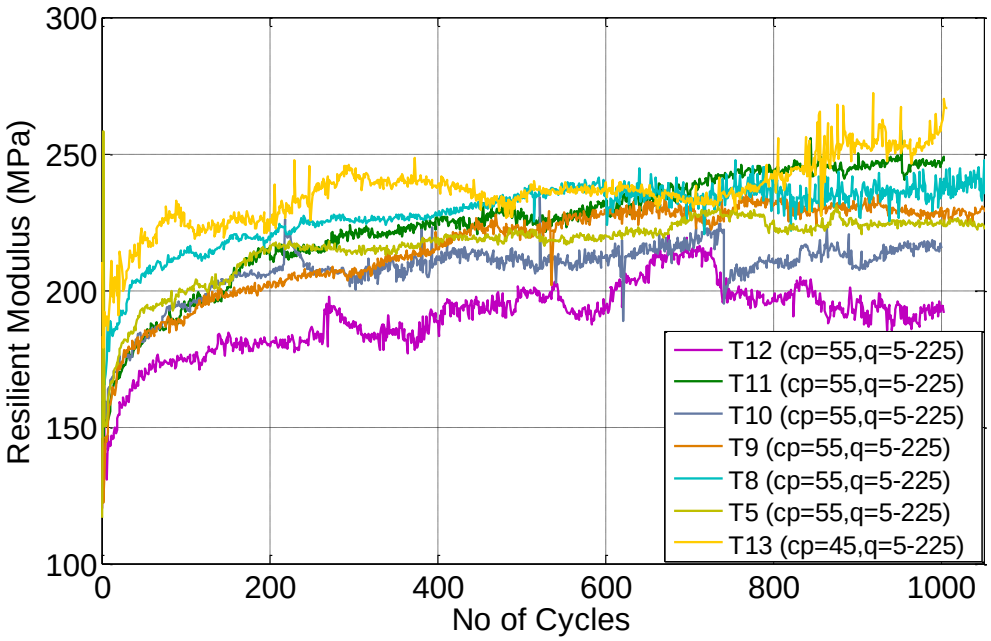

(b) Linear scale

Figure 6.24: Resilient modulus of constant cell pressure tests

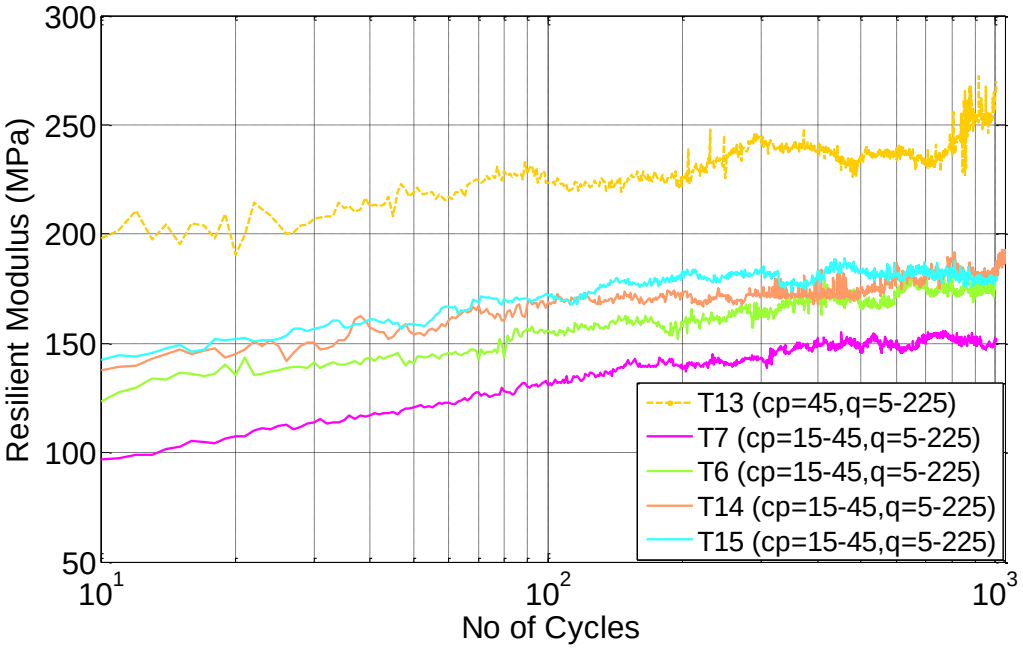

(a) Log scale

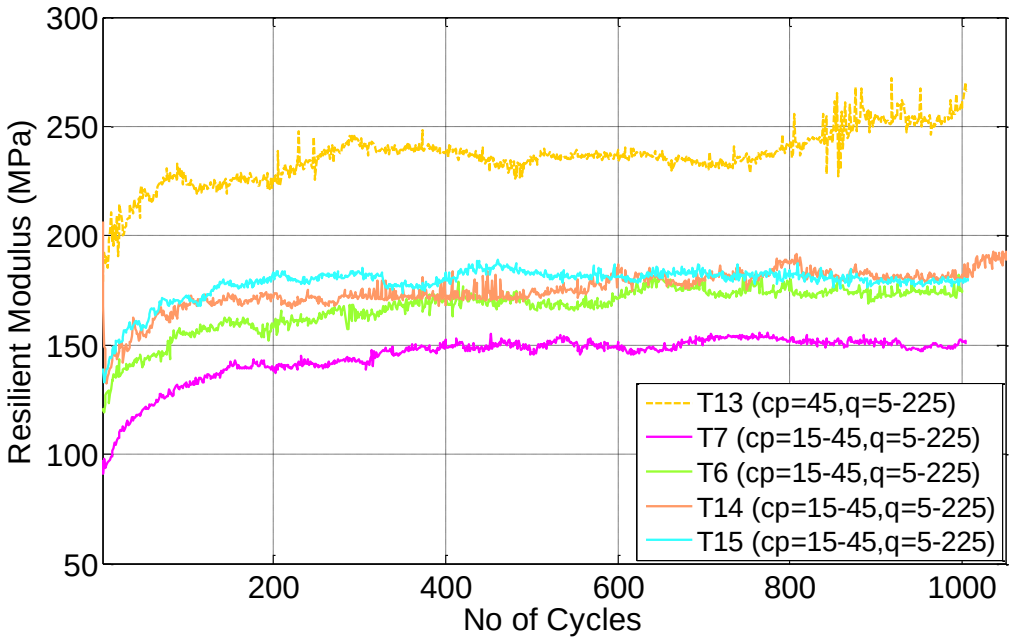

(b) Linear scale– from 2nd cycle

Figure 6.25: Resilient modulus of cyclic cell pressure tests

Figure 6.26 shows the shear modulus for constant cell pressure tests obtained from radial callipers. Shear modulus values are lower for cyclic cell pressure tests than for the constant cell pressure test T13 (Figure 6.27).

In general, resilient and shear modulus values are increasing with number of cycles. Lackenby et al. (2007), Aursudkij et al. (2009), and Sevi (2008) reported increase in the resilient modulus with number of cycles during the constant cell pressure tests on ballast.

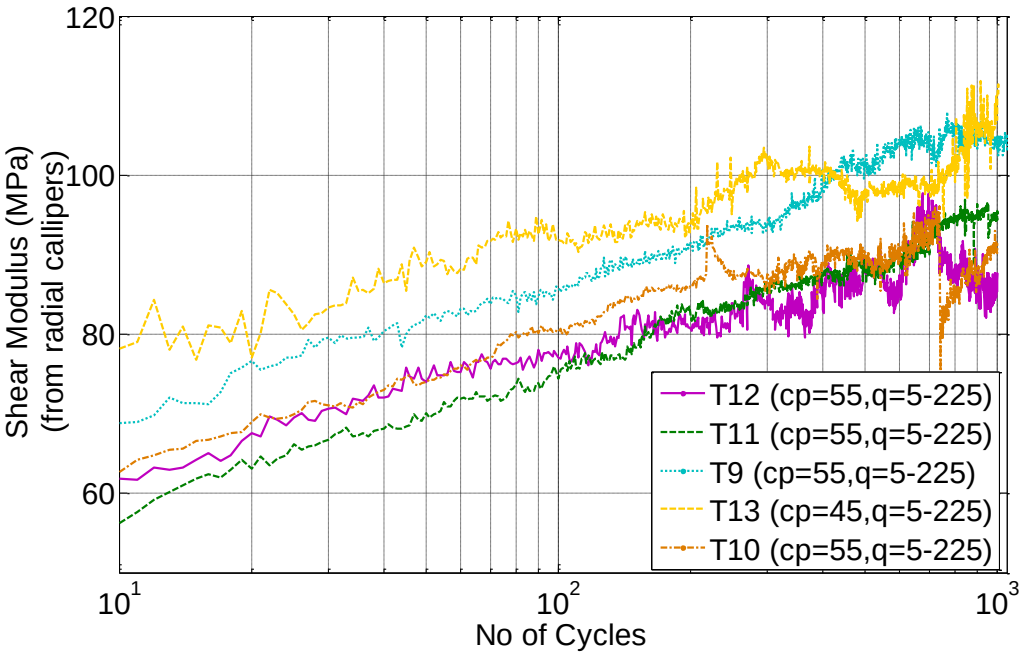

(a) Log scale

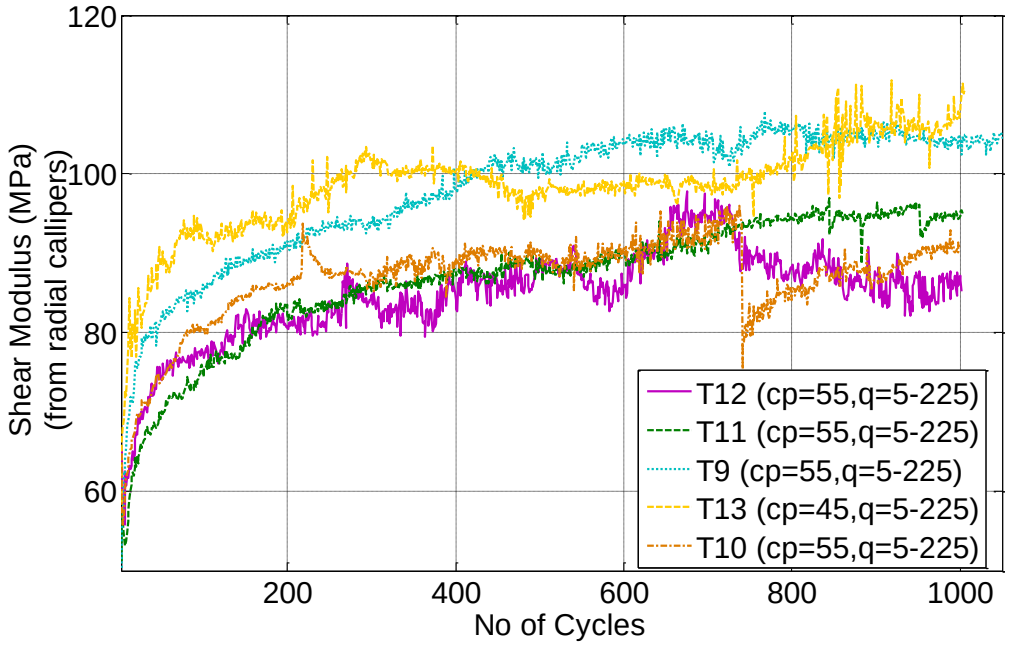

(b) Linear scale- from 2nd cycle

Figure 6.26: Shear modulus of constant cell pressure tests

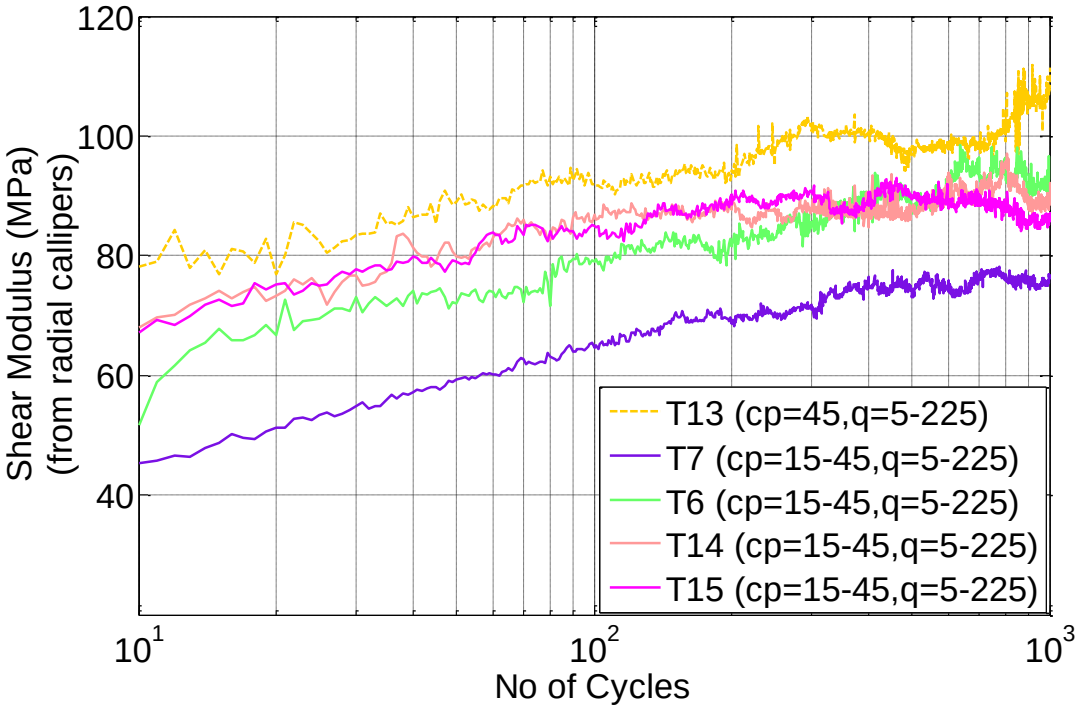

(a) Log scale

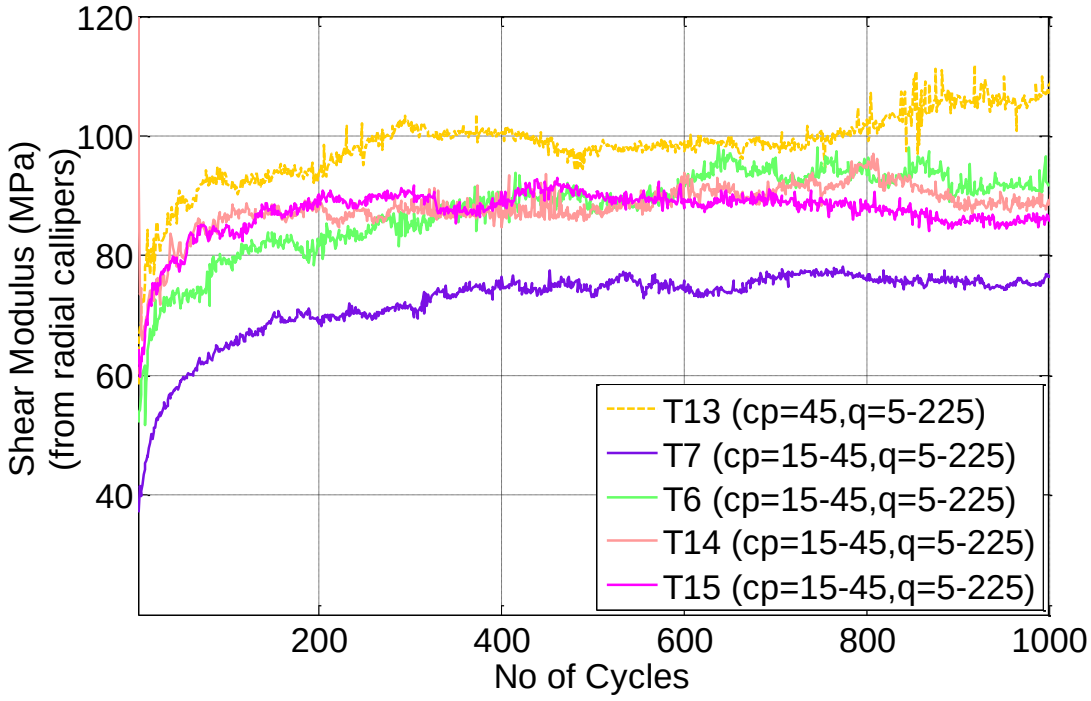

(b) Linear scale- from 2nd cycle

Figure 6.27: Shear modulus of cyclic cell pressure tests

Bulk moduli calculated from radial calliper readings are shown in Figure 6.28. Bulk modulus values are lower for cyclic cell pressure tests than for the constant cell pressure test (Figure 6.29). This is due to the average effective stress, p′ being lower during the cyclic cell pressure tests.

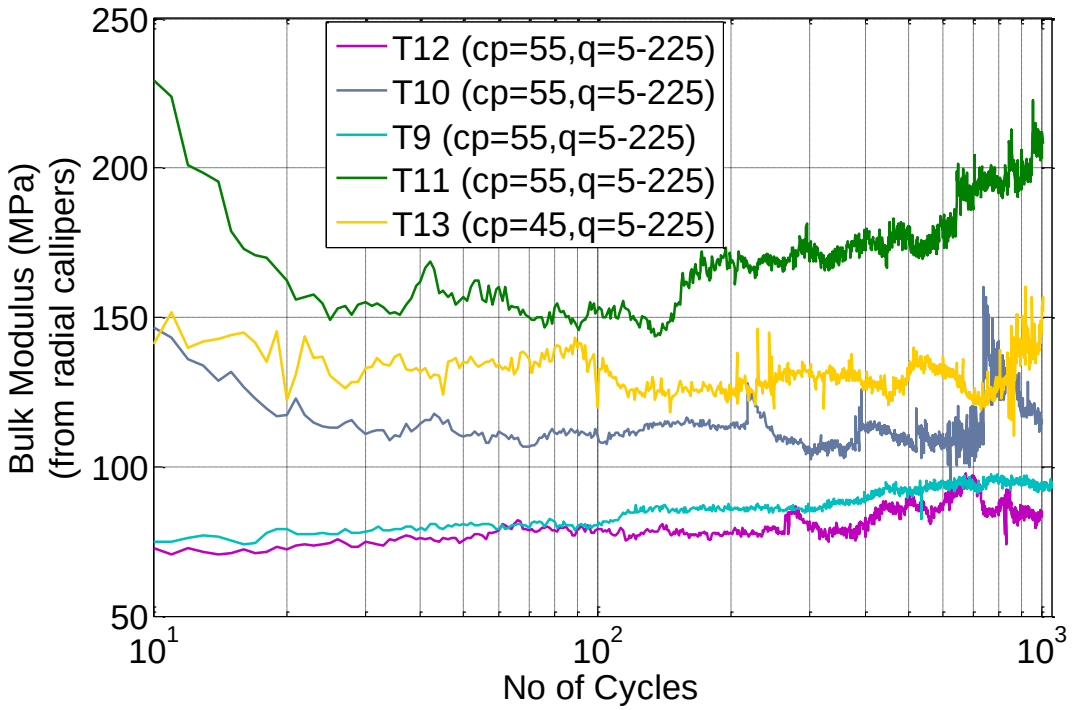

(a) Log scale

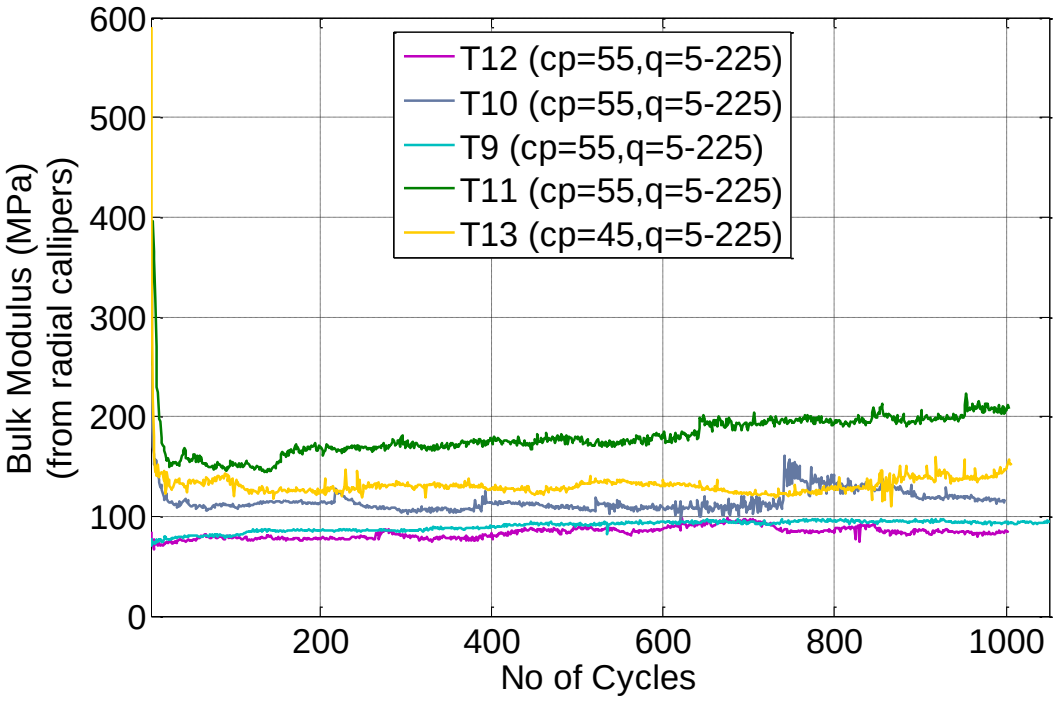

(b) Linear scale- from 3rd cycle

Figure 6.28: Bulk modulus of constant cell pressure tests

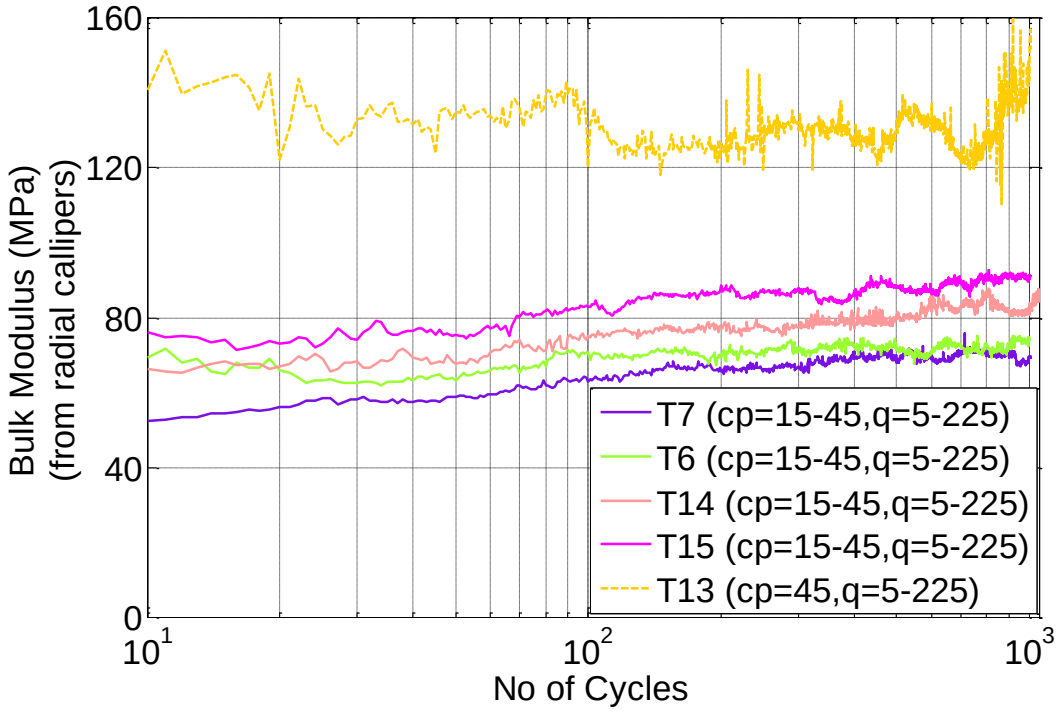

(a) Log scale

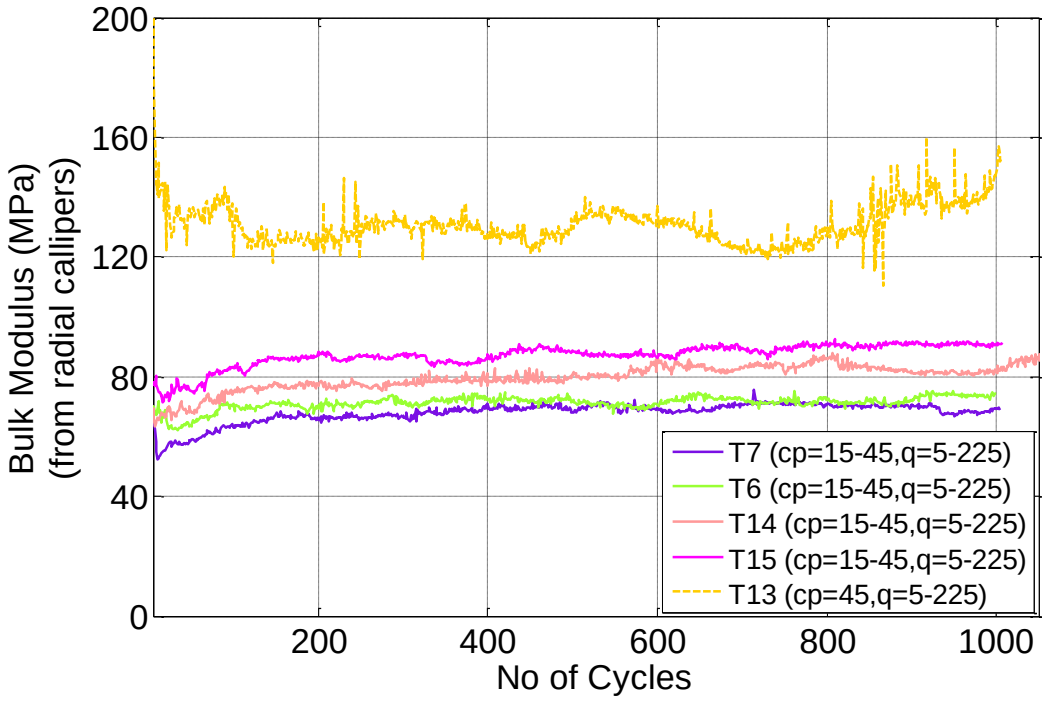

(b) Linear scale- from 5th cycle

Figure 6.29: Bulk modulus of cyclic cell pressure tests

Figure 6.30 shows the Poisson's ratio for constant cell pressure tests. Poisson's ratios from radial callipers fall within the range of 0.1-0.3. Aursudkij et al. (2009) reported Poisson's ratio in the range of 0.25-0.47 from their testing on full size ballast. Cyclic cell pressure tests show lower Poisson's ratios compared to the constant cell pressure test (Figure 6.31).

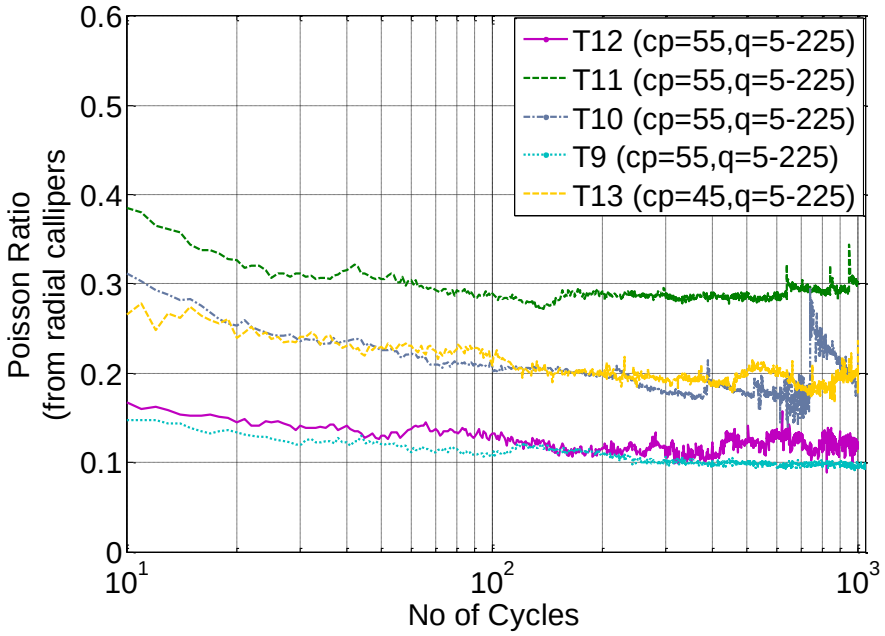

(a) Log scale

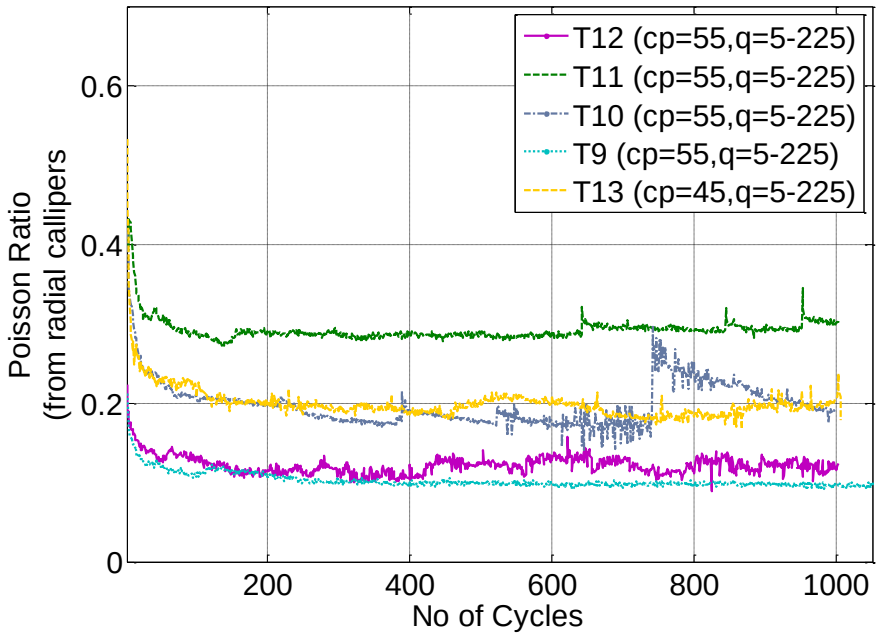

(b) Linear scale- from 2nd cycle

Figure 6.30: Poisson ratio of constant cell pressure tests

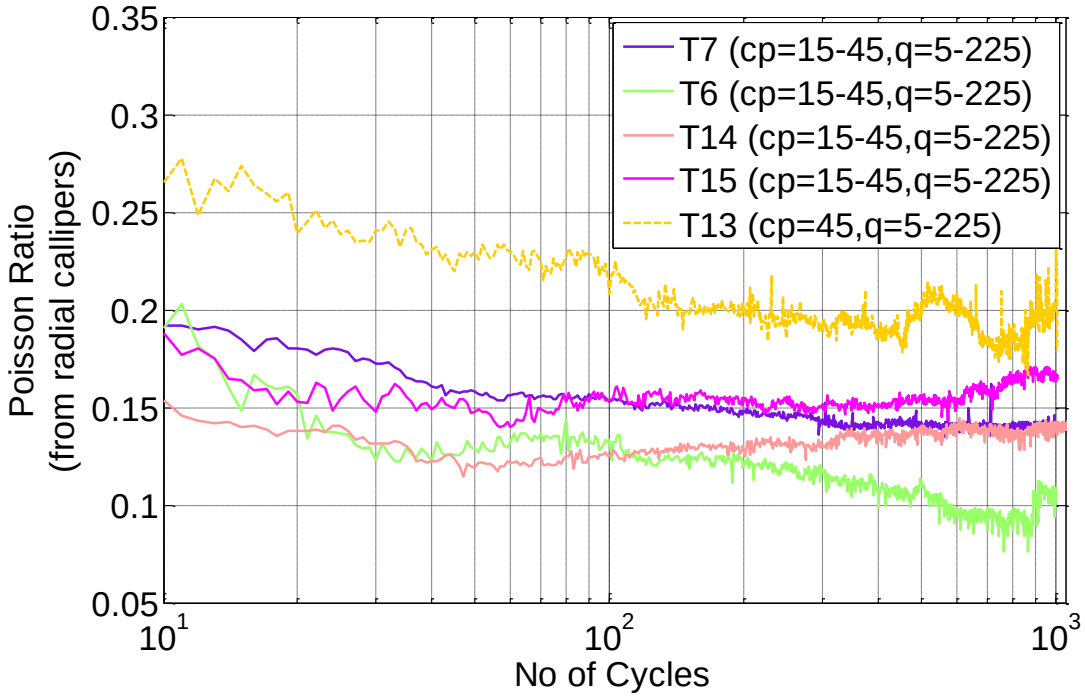

(a) Log scale

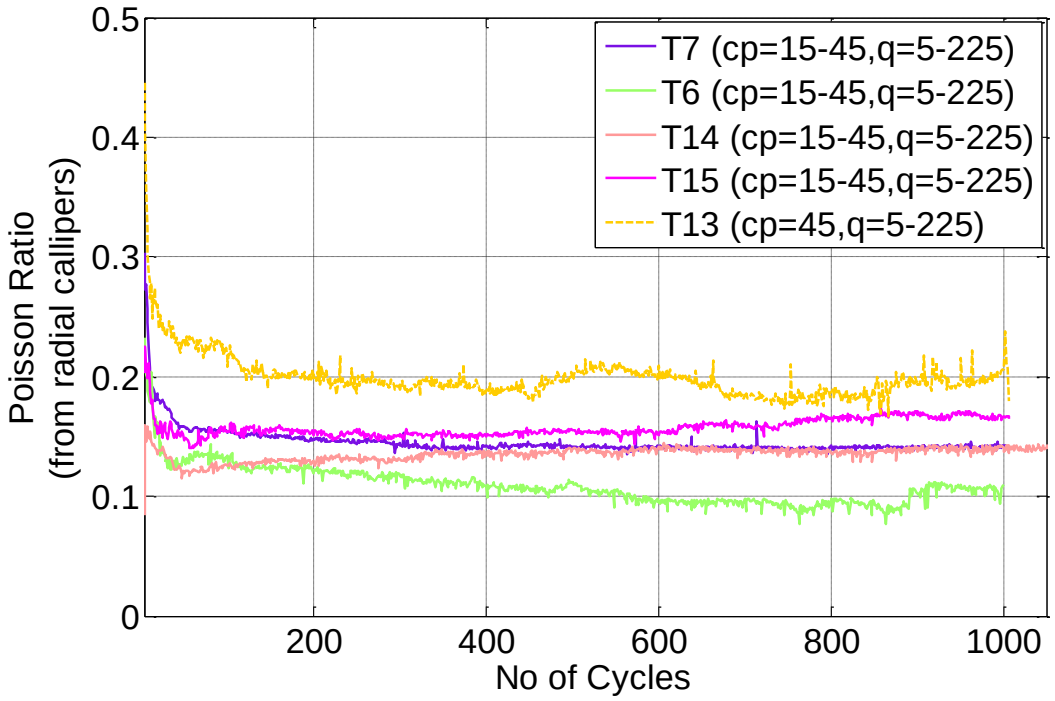

(b) Linear scale- from 3rd cycle

Figure 6.31: Poisson ratio of cyclic cell pressure tests

6.2 Extension test results

Extension loading was carried out following the cyclic loading in certain cases to mimic the process of tamping.

Test conditions are shown in Table 6.3. Cell pressure and deviator stress were cycled 1 time during the extension stage, except for T8 and T12, where they were cycled approximately 10 times.

Test	Extension loading			Cyclic before extension			Cyclic after extension			Density (kg/m^3)
	σ_3' (kPa)	q (kPa)	σ_1' (kPa)	σ_3' (kPa)	q (kPa)	No of cycles	σ_3' (kPa)	q (kPa)	No of cycles	
T8	55-90	5-(-30)	60	55	5-225	1400	55	5-225	180	1559
T10	55-210	5-(-150)	60	55	5-225	1000	55	5-225	1000	1543
T11	55-210	5-(-150)	60	55	5-225	1000	55	5-225	1600	1583
T12*	55-210	5-(-150)	60	55	5-225	1000	55	5-225	1600	1536
T7*	45-200	5-(-150)	50	15-45	5.225	1000	-	-	-	1550
T13*	45-200	5-(-150)	50	45	5-225	1000	-	-	-	1528
*Resin was poured at the end of the test for the test specimens T12, T7, and T13										

Table 6.3: Extension test specimen details

Figure 6.32 to Figure 6.37 show the absolute height during the tests. This is thought to be a suitable plot because the test initial height of 300 mm approximates to the true depth of ballast on real track. For T8 the cell pressure was cycled by a very small amplitude which didn't cause significant height change. Thus for the other tests, to more closely match the expected tamping lifts (at least a particle diameter) cell pressure was cycled by greater amounts. For the cycled extension tests the major change in height occurred during the first cycle and the subsequent cycles caused very little change (Figure 6.35).

The increase in height during the extension stage varied between tests. This could be due to natural variation between the arrangements of particles. When the vertical cyclic loading was reimposed after the extension stage immediately a significant height reduction occurred.

With the continuing cycles, specimen height returns back to the value prior to the extension stage. In comparison with the situation after track tamping, the lifted ballast layer is brought to pre-tamping level with continuing traffic loading. Thus tamping is needed periodically to maintain the track geometry. Disruption/Loosening of a densely packed ballast layer by tamping contributes to higher settlement in track soon after tamping (Selig and Waters, 1994).

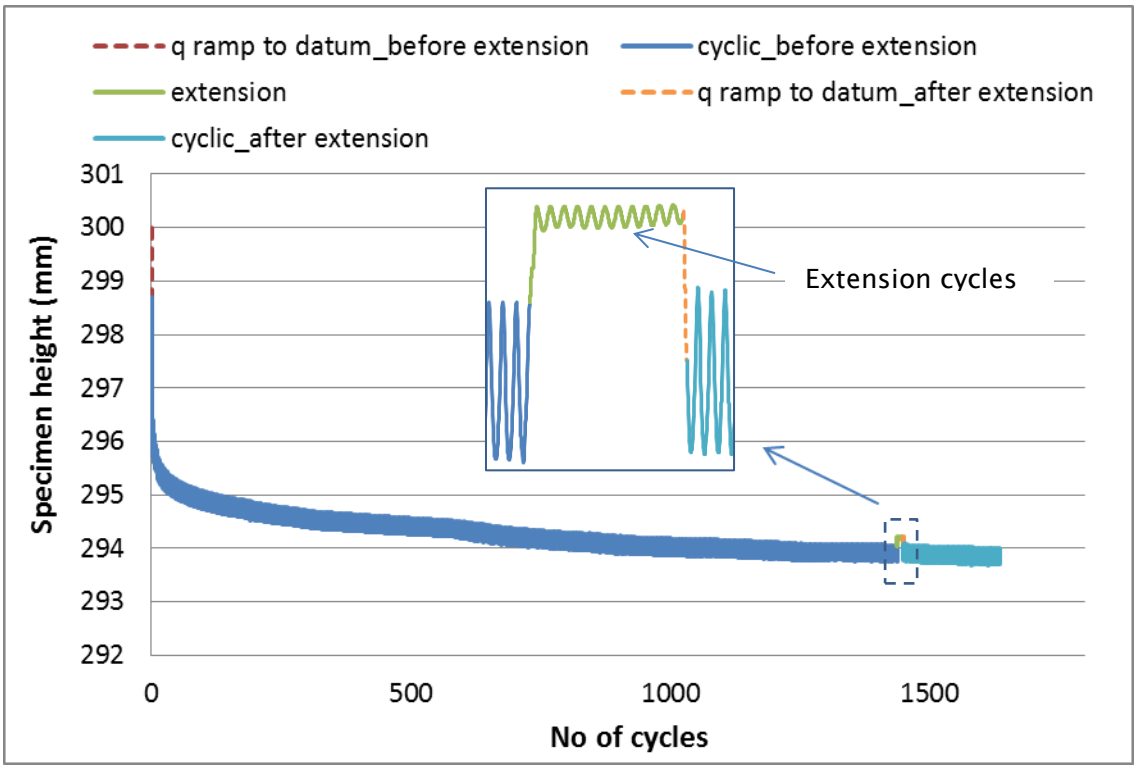

Figure 6.32: Specimen height against cycles for Test 'T8'

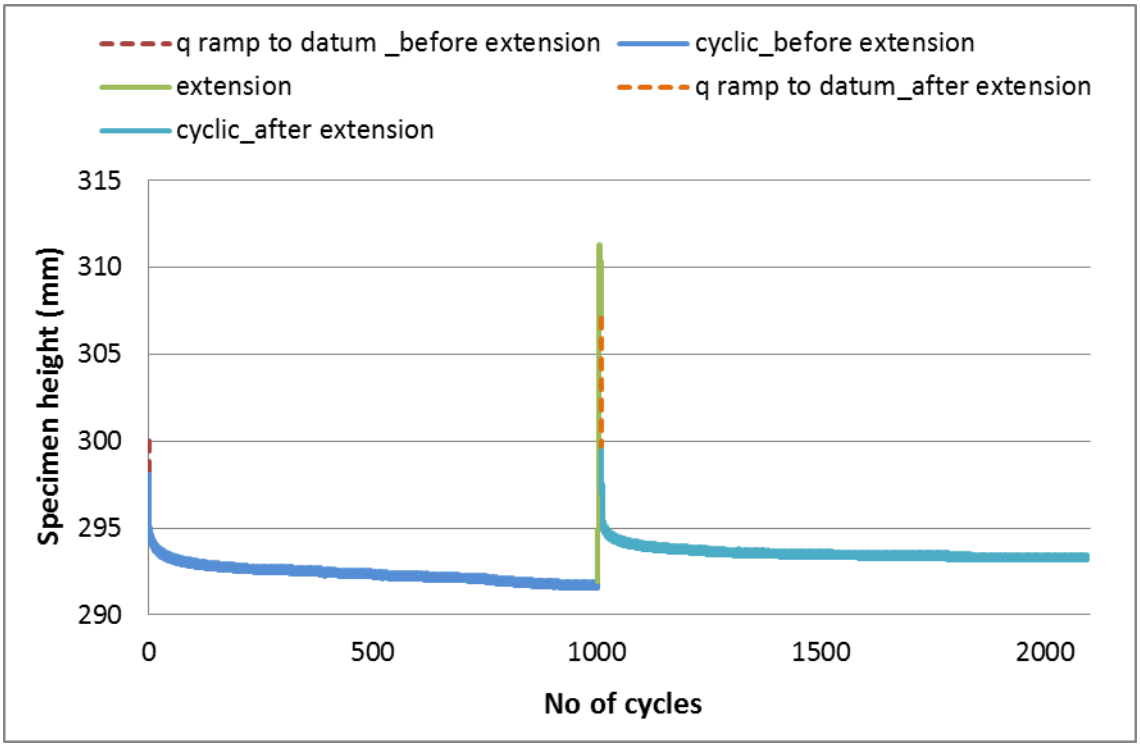

Figure 6.33: Specimen height against cycles for Test 'T10'

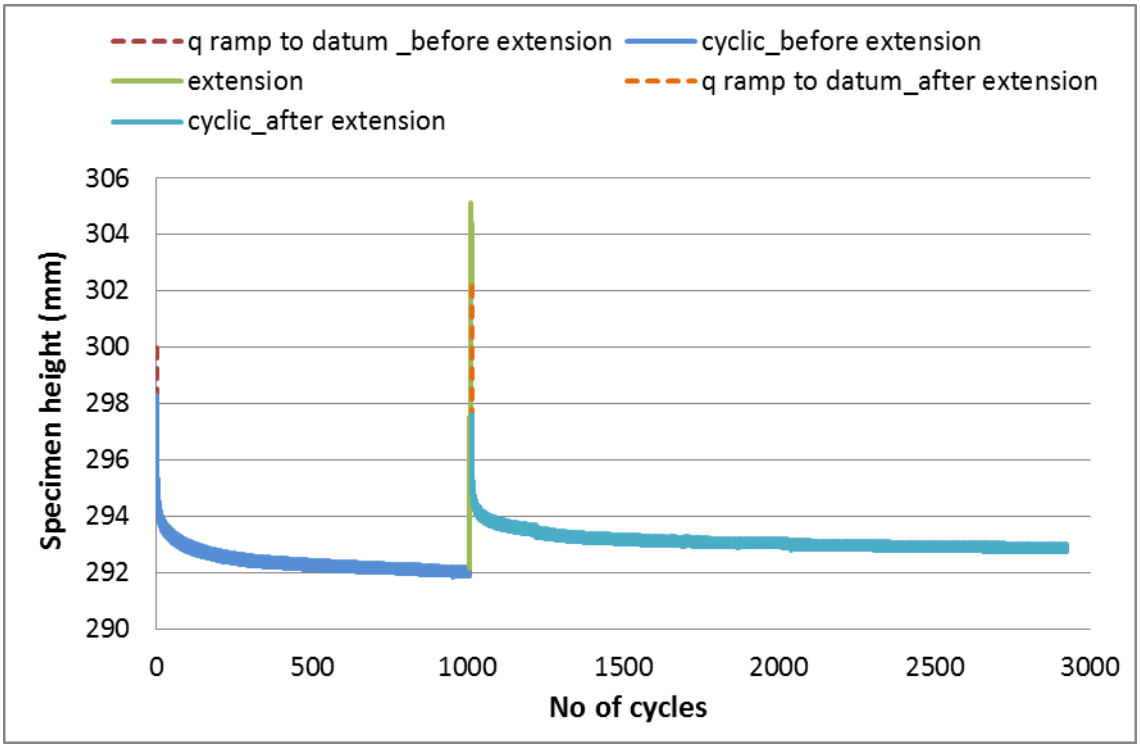

Figure 6.34: Specimen height against cycles for Test 'T11'

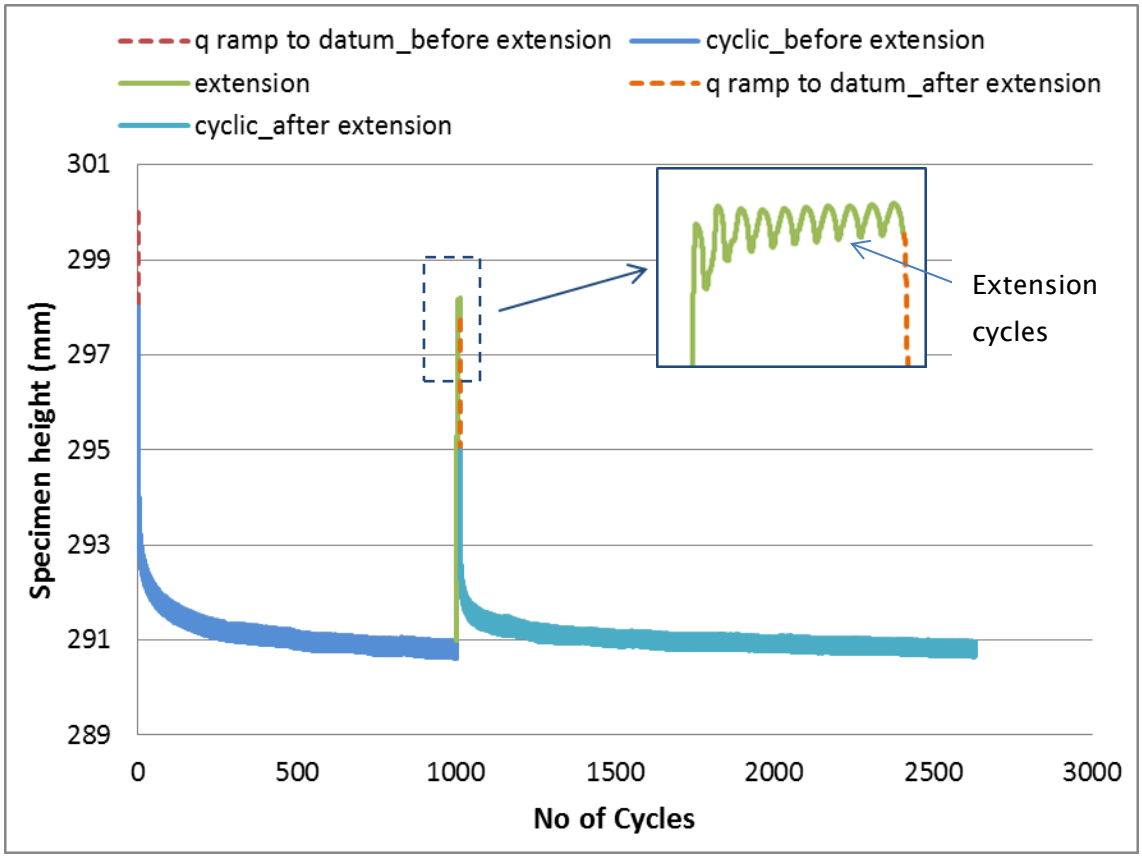

Figure 6.35: Specimen height against cycles for Test 'T12'

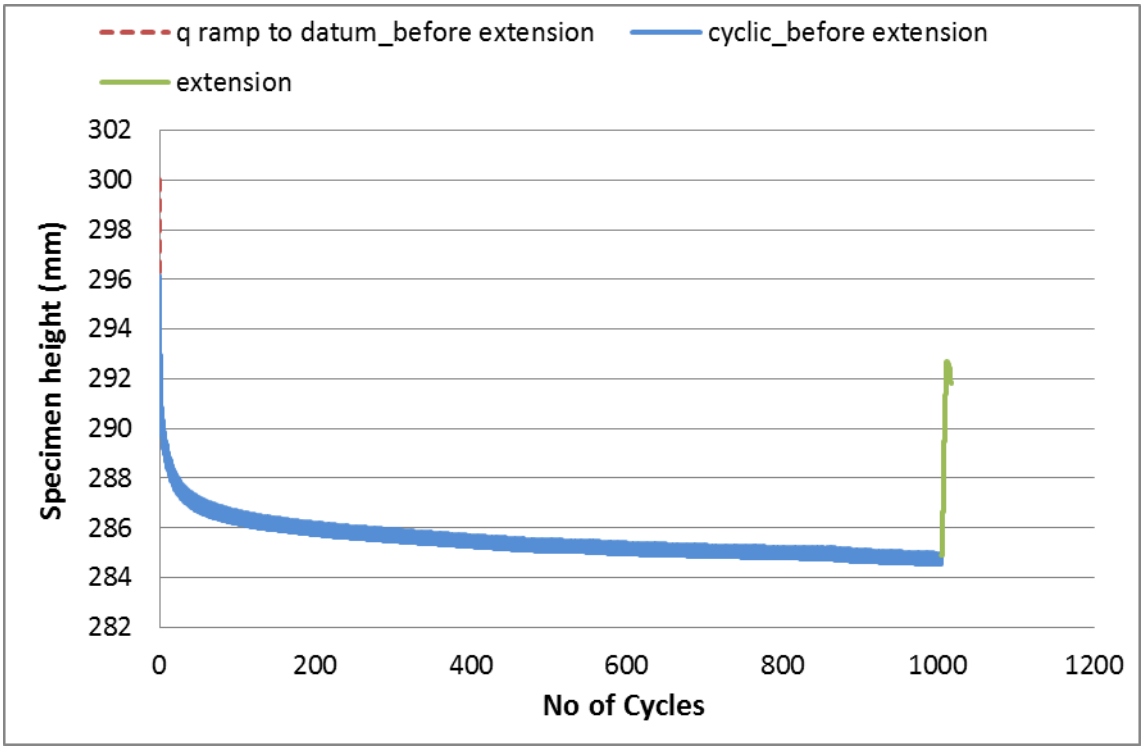

Figure 6.36: Specimen height against cycles for Test 'T7'

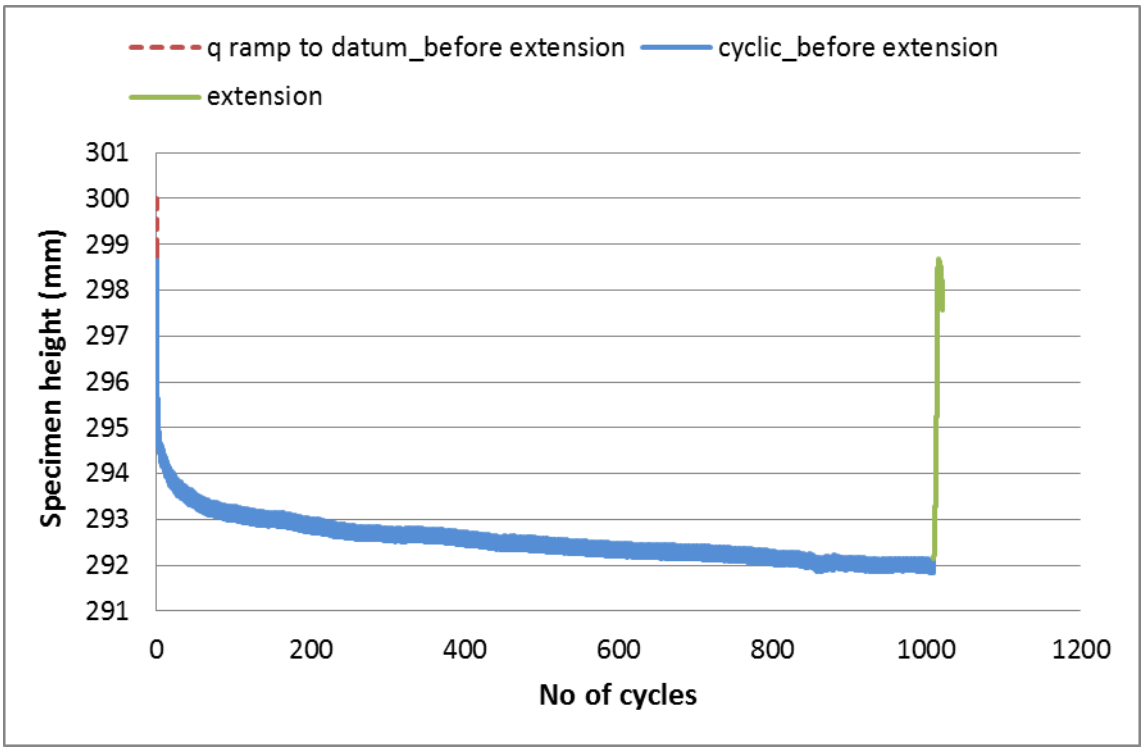

Figure 6.37: Specimen height against cycles for Test 'T13'

Figure 6.38 to Figure 6.42 shows the local radial calliper readings throughout the tests. For tests T10, T11, and T12 one calliper was fixed at the mid height. For the test specimens T7 and T13 three callipers were fixed. For T8 the radial calliper went out of range during the very initial cycles, thus there are no radial calliper readings. Readings toward the negative direction imply expansion and the positive direction implies contraction of the specimen diameter.

Contraction of mid height diameter during the extension supports the height increase during this stage. Also during the cyclic loading after the extension, the mid height diameter expands consistent with the ongoing height reduction.

For T7, the middle calliper showed an expansion during extension, while the top and bottom calliper both showed contraction (Figure 6.41). For T13, all 3 callipers show diameter contraction during the extension stage (Figure 6.42).

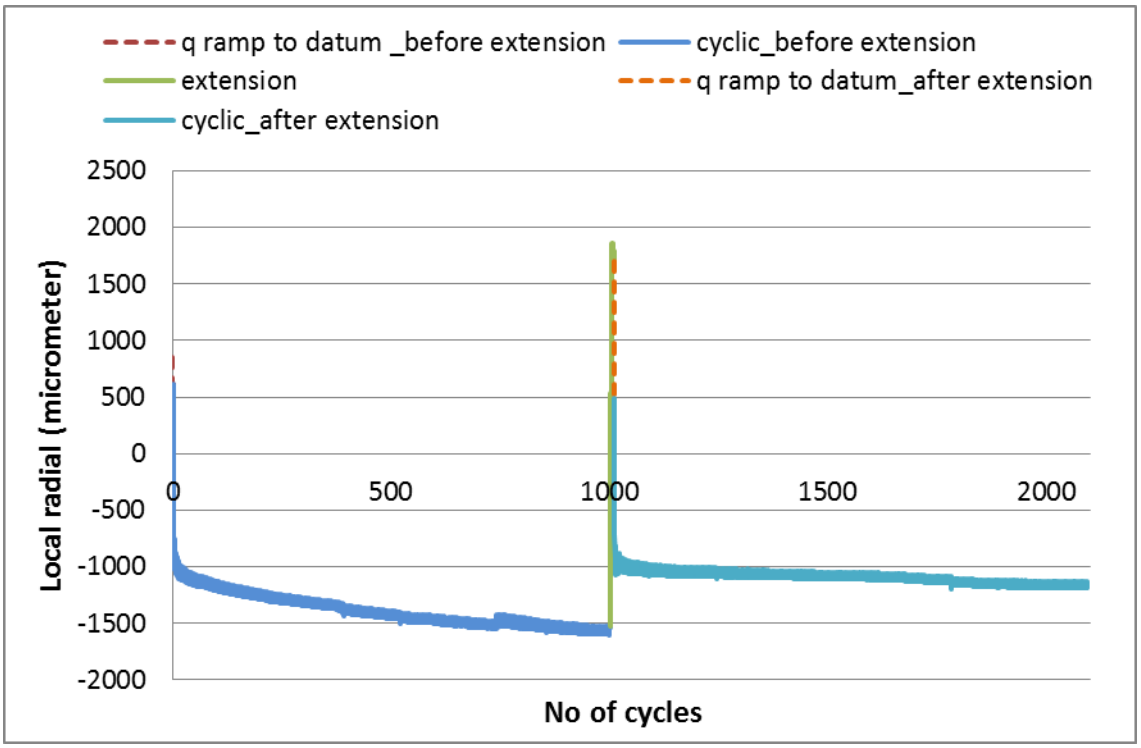

Figure 6.38: Radial calliper readings for Test 'T10'

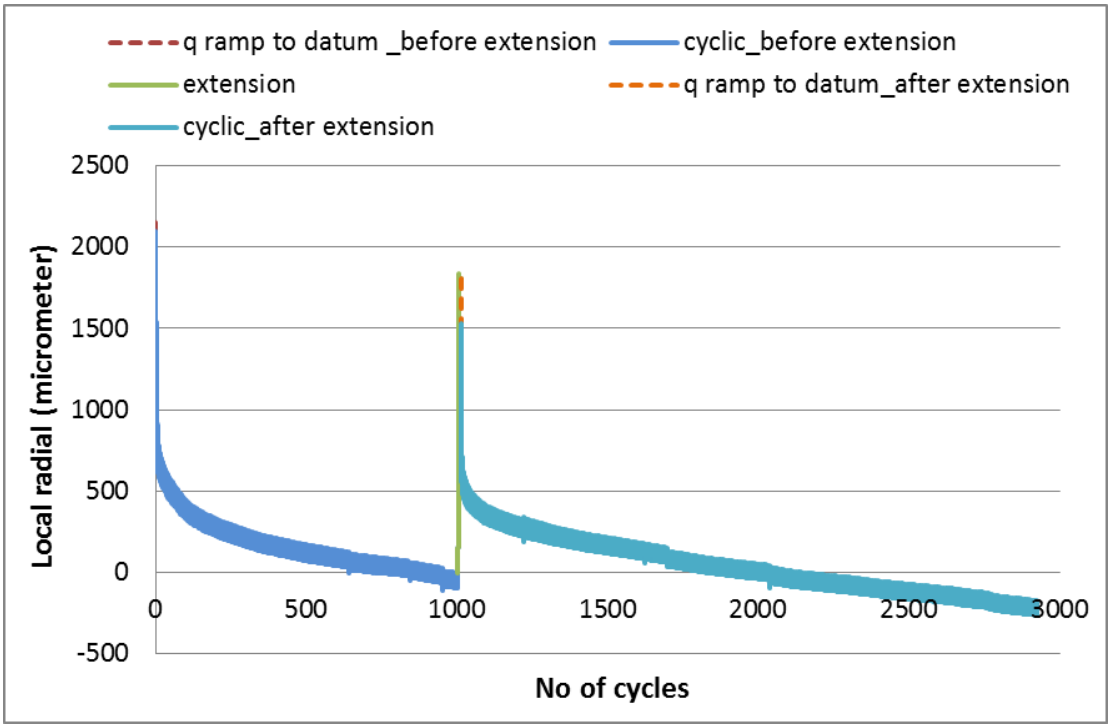

Figure 6.39: Radial calliper readings for Test 'T11'

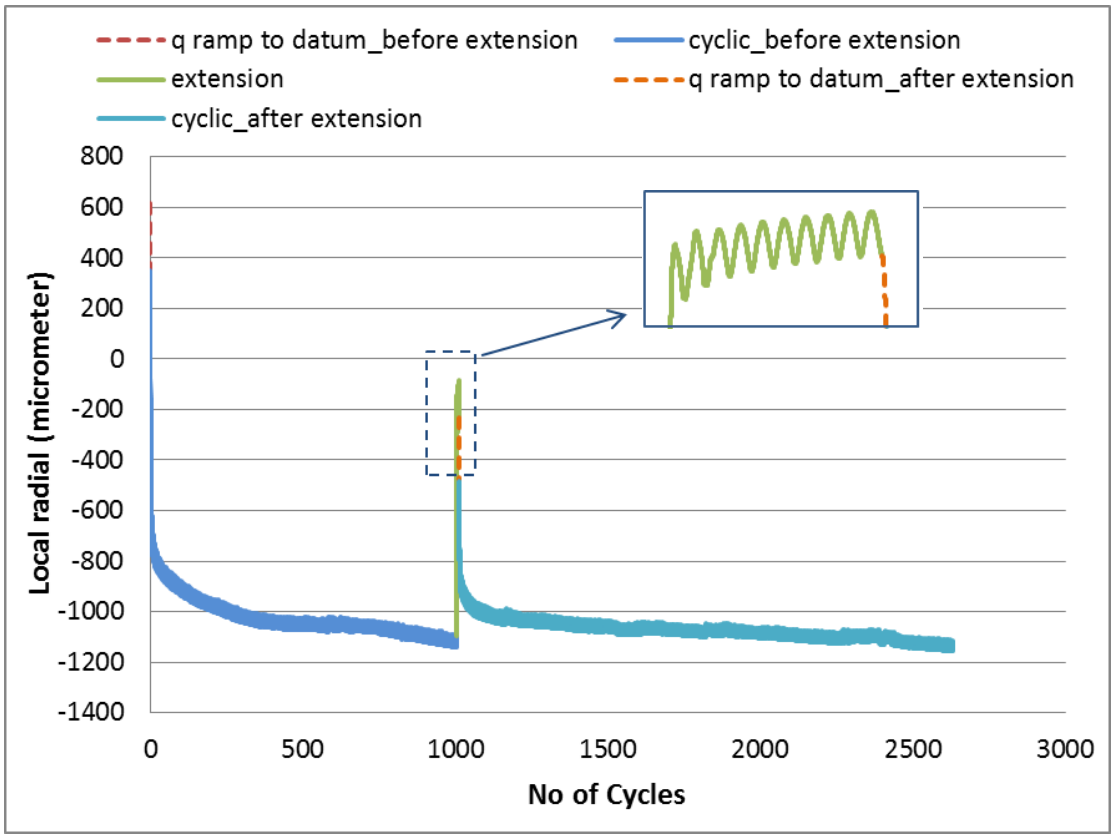

Figure 6.40: Radial calliper readings for Test 'T12'

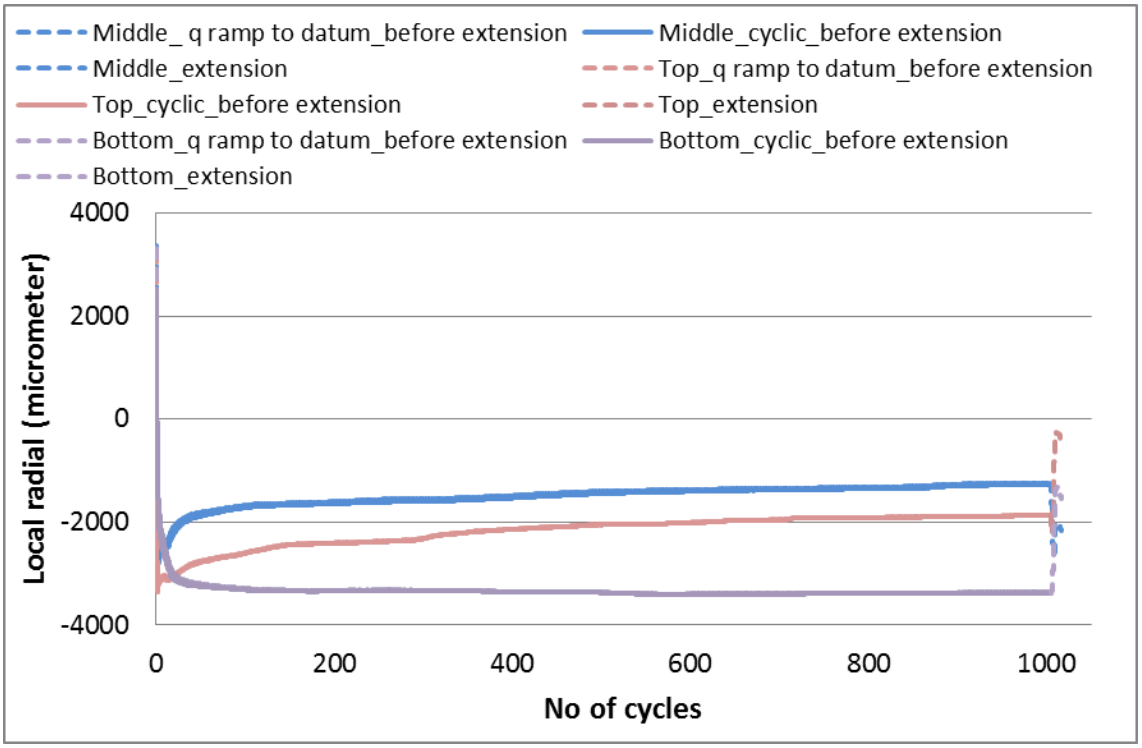

Figure 6.41: Radial calliper readings for Test 'T7'

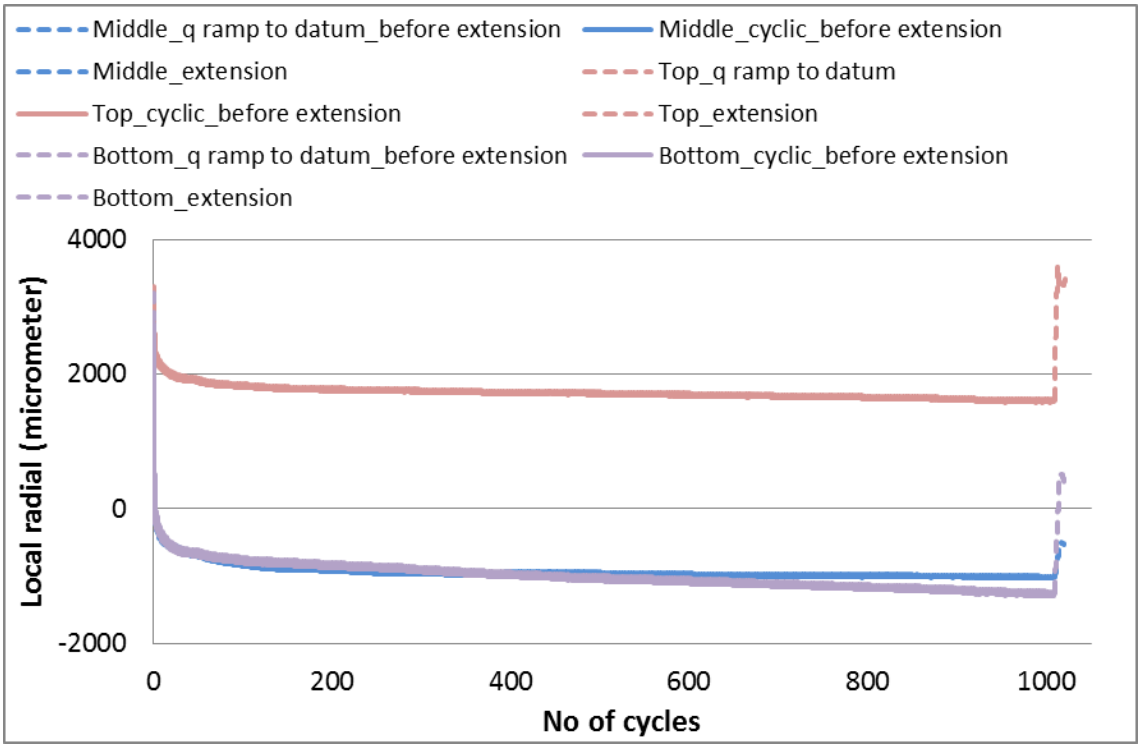

Figure 6.42: Radial calliper readings for Test 'T13'

Figure 6.43 to Figure 6.46 show resilient modulus of ballast before and after the extension stage. These Figures show that resilient modulus drops suddenly after the extension which is consistent with the loosening of the compacted ballast layer during the tamping. During T8 the applied extension load wasn't significant, and the resilient modulus didn't drop much soon after the extension (Figure 6.43). With continuing cycles, resilient modulus values increase and can reach higher than pre-extension stage values. It means vertical resilient deformation of ballast reduces and the ballast gets stiffer.

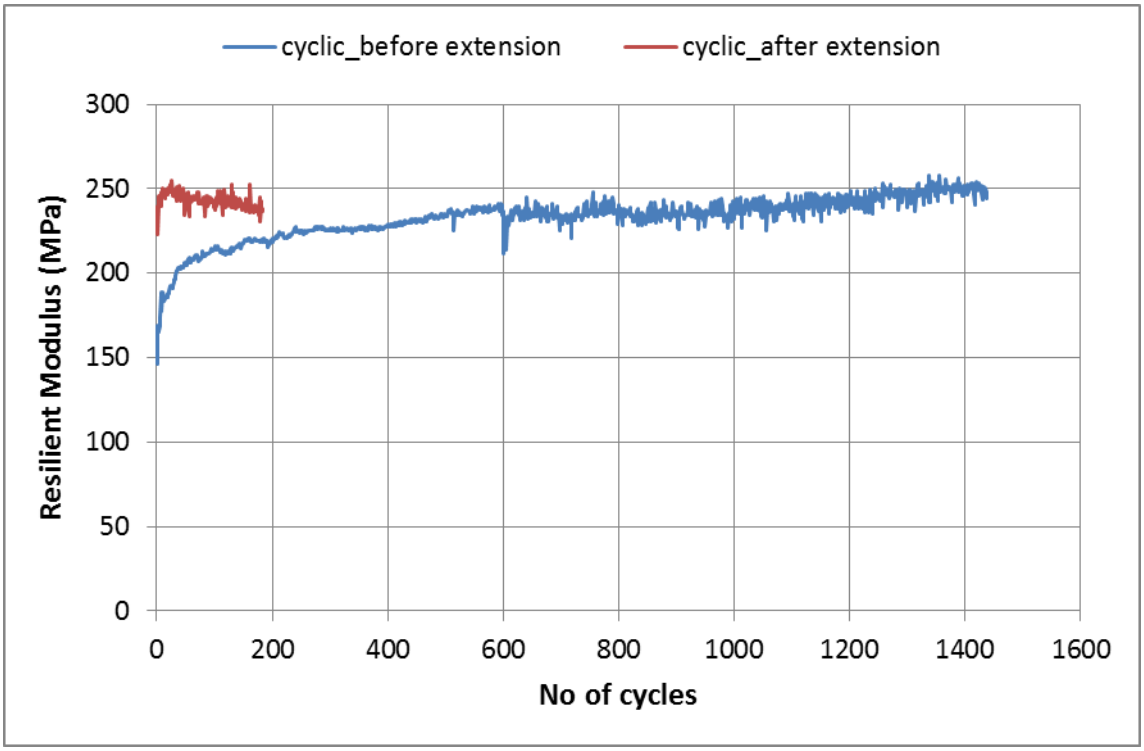

Figure 6.43: Resilient modulus for Test 'T8'

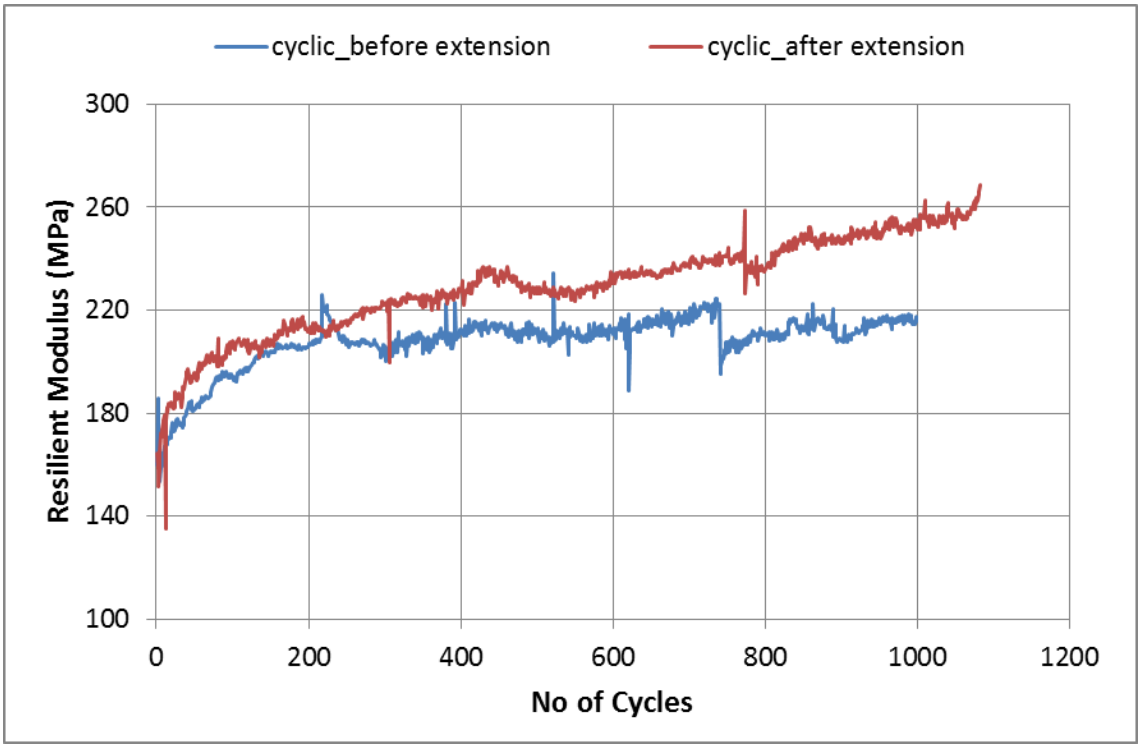

Figure 6.44: Resilient modulus for Test 'T10'

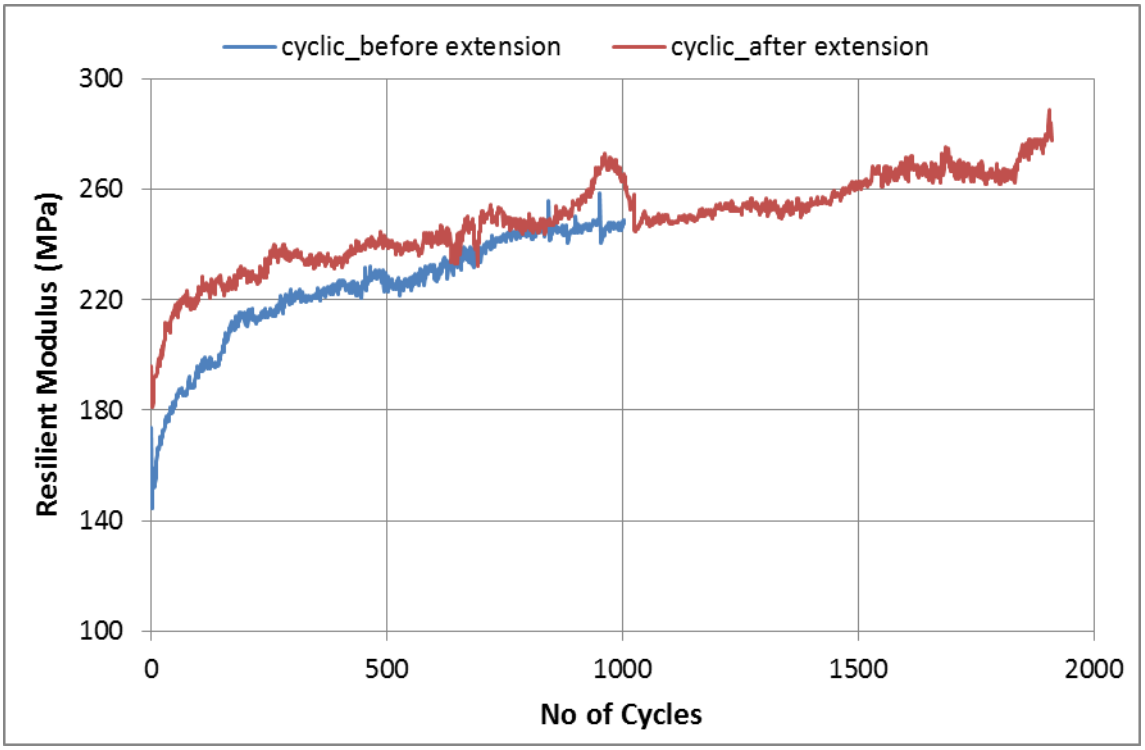

Figure 6.45: Resilient modulus for Test 'T11'

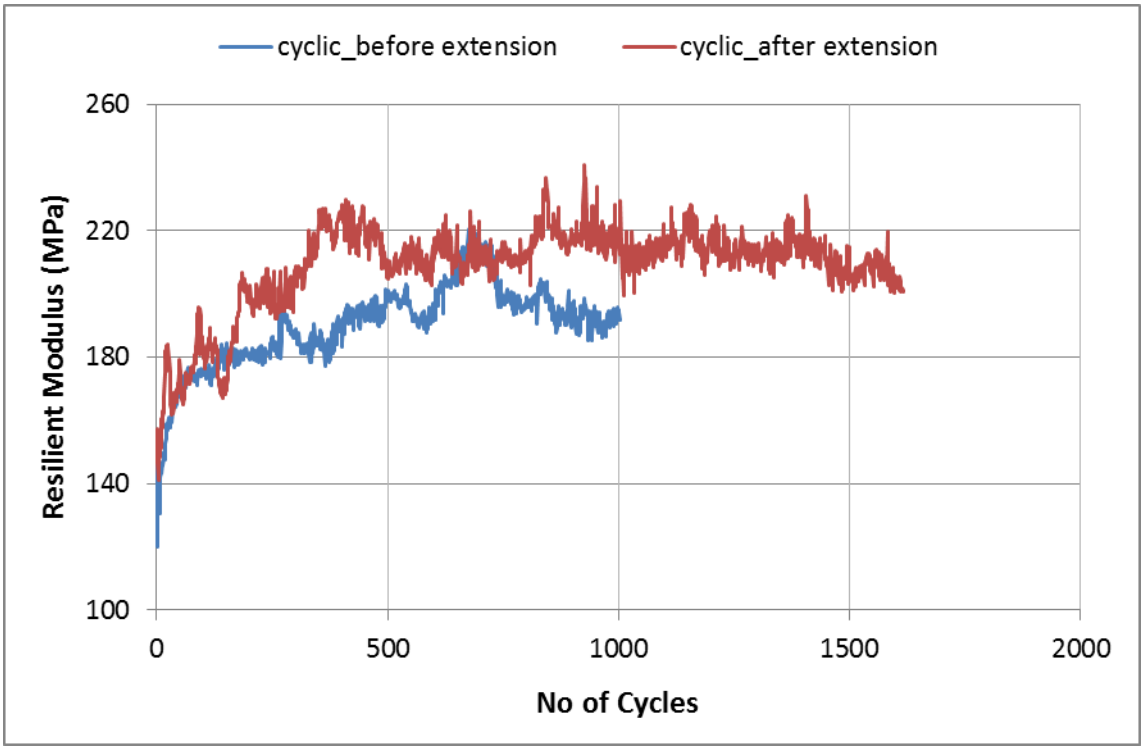

Figure 6.46: Resilient modulus for Test 'T12'

As significant membrane penetration occurred when the cell pressure was cycled by a larger amount, readings and calculations based on the cell pressure controller are not presented.

Extension stage plots are shown in Figure 6.47 to Figure 6.51. T10 and T11 reached -20 kPa more deviator stress when the cell pressure reached maximum than was intended (Figure 6.47). In the plots, axial strain values have been rezeroed at the start of the extension stage.

Axial strain accumulations were varied. This could be because of natural variations between tests. Figure 6.51 shows the volumetric strain calculated from the middle calliper readings for all the tests. For T7 and T13, volumetric strains calculated from the average of top and bottom callipers are also shown. These values could have been slightly affected by membrane penetration, although the aluminium plate was fixed inside the membrane to provide stable support to the callipers. The overall trend shows volumetric expansion/ dilation during the extension stage.

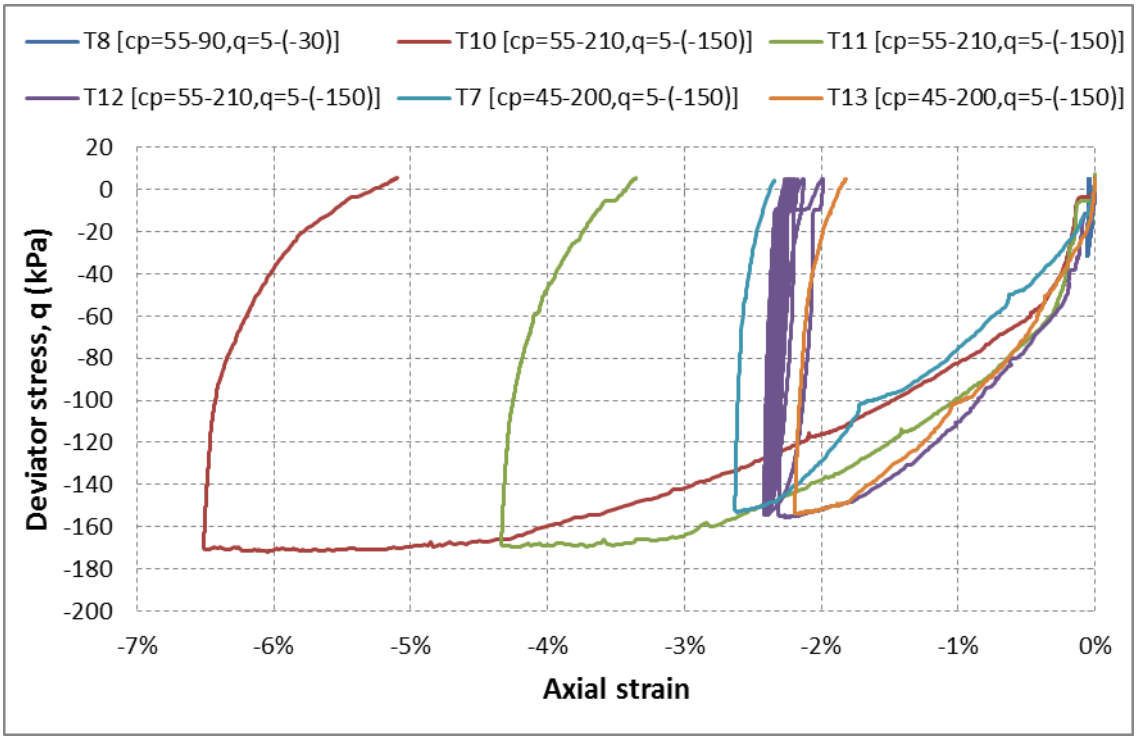

Figure 6.47: q against axial strain during the extension stage

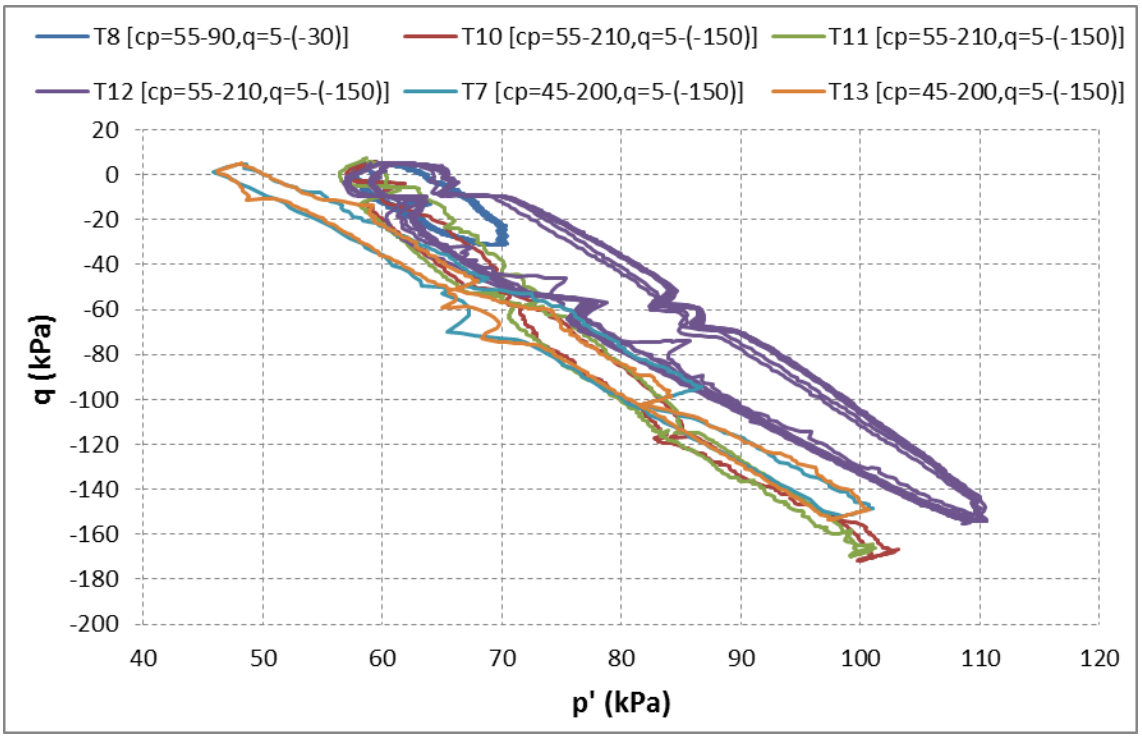

Figure 6.48: Stress path during the extension stage

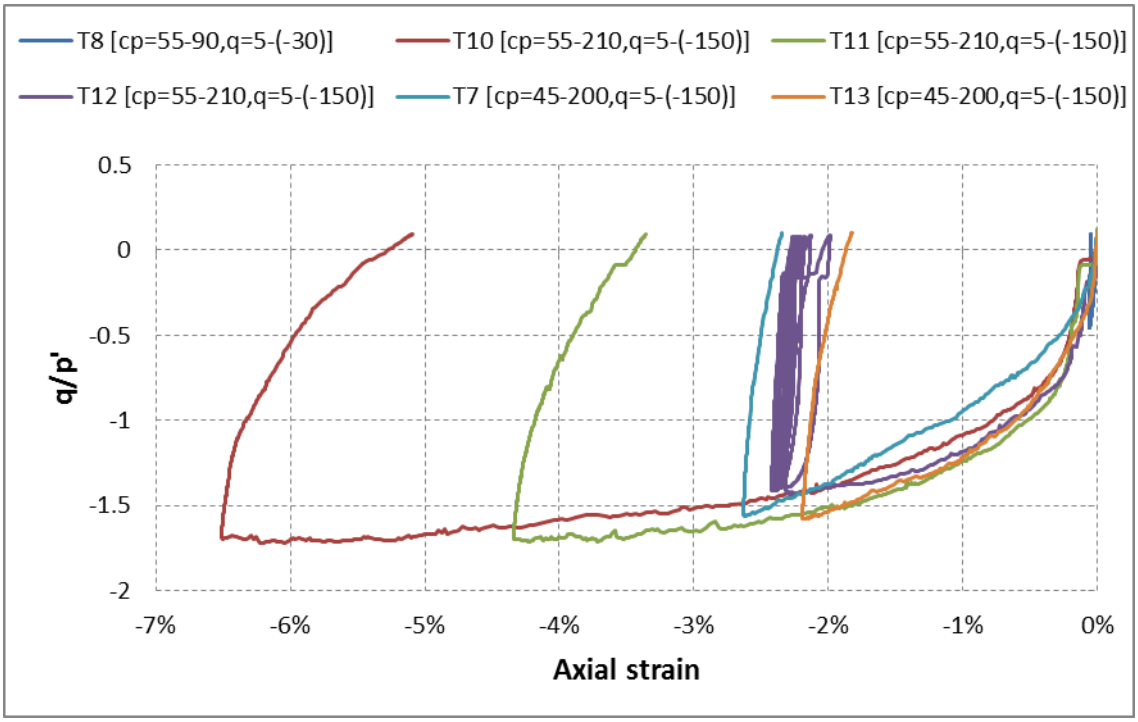

Figure 6.49: q/p' against axial strain during the extension stage

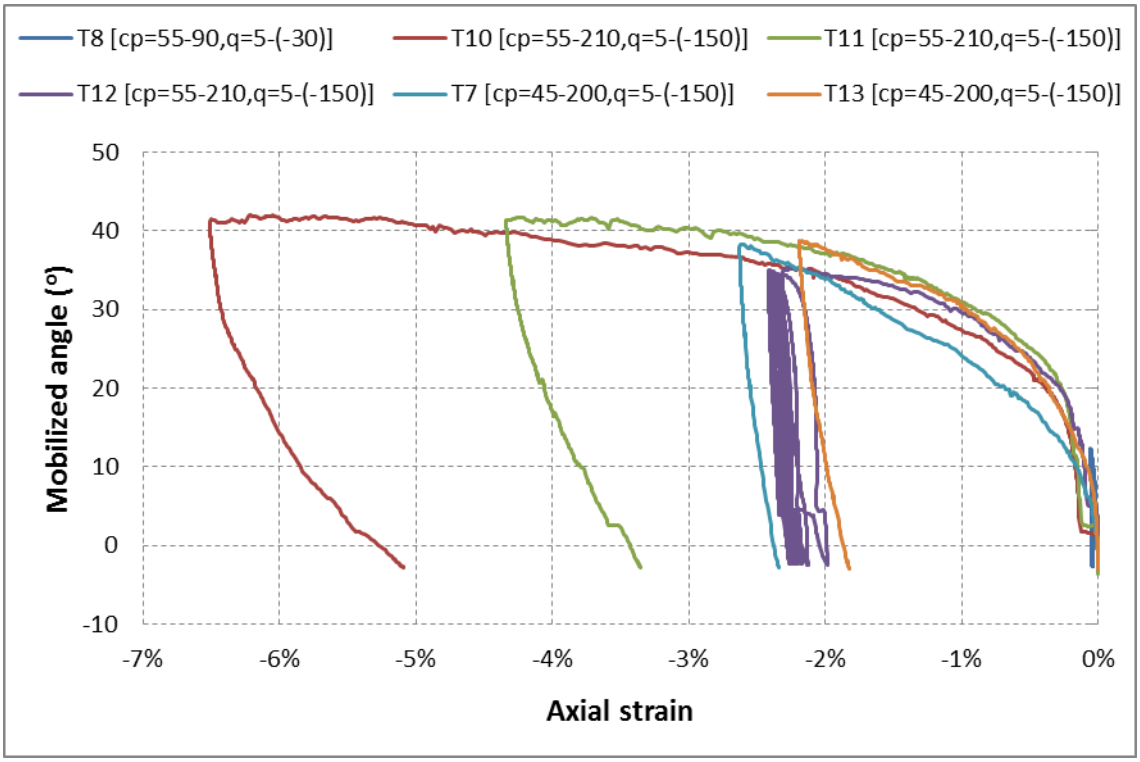

Figure 6.50: Mobilized friction angle against axial strain during the extension stage

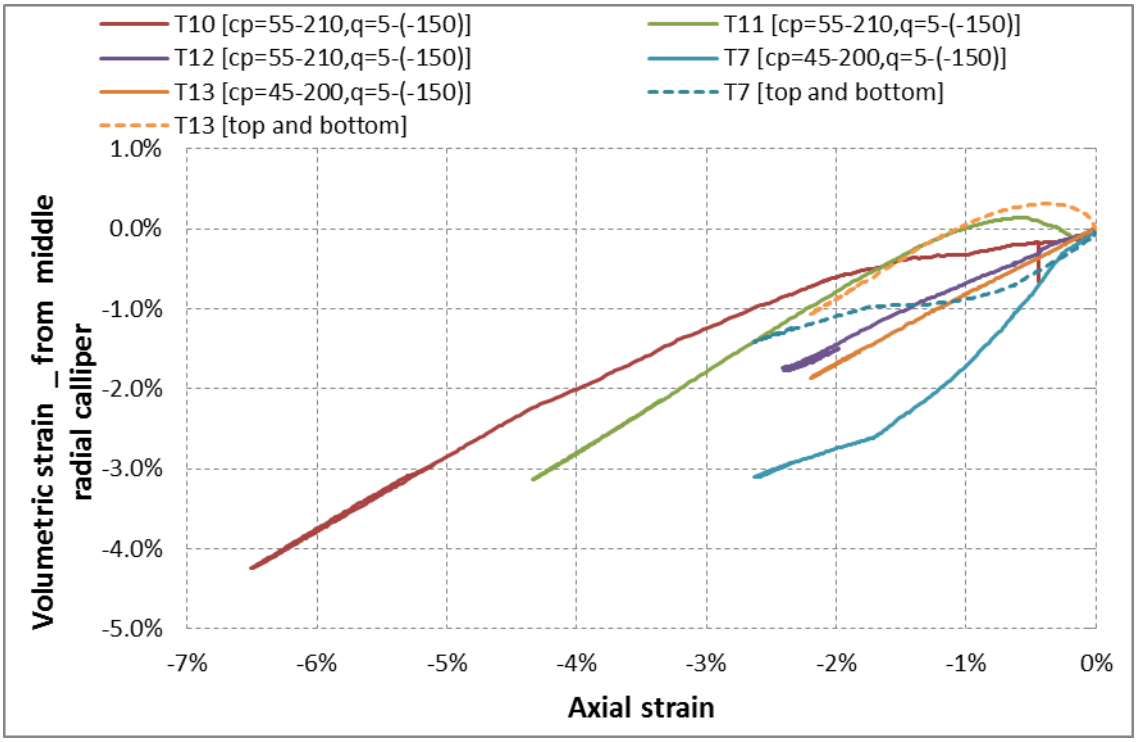

Figure 6.51: Volumetric strain against axial strain during the extension stage

Triaxial specimens T6, T12, T7, and T13 were resin stabilised at the end of the test to preserve the particle arrangement following testing and the details are in Appendix B. A resin stabilisation technique was implemented to stabilise the ballast specimen within the triaxial apparatus after loading. The resin stabilised specimens were CT scanned and analysed. A change in orientation interms of Length Orientation Phi (degrees) between specimens was observed. However, a detailed understanding of effect of stress path on particle structure needs further research.

6.3 Summary

The accumulation of axial strain depends on the stress ratio, confining pressure and deviator stress. Permanent axial strain reduced with increasing confinement for the same deviator stress range. Permanent axial strain increased with increasing deviator stress for the same confining pressure. These findings agrees with the conclusions from the experiments on full size ballast reported by Lackenby et al. (2007), Aursudkij et al. (2009), and Anderson and Fair (2008).

The variation in permanent axial strain for tests at similar stress conditions and constant cell pressure was due to random bedding variation. This is similar to the observations reported by Fair (2003) and Aursudkij (2007). This variation reduces when the first few cycles are eliminated.

The stress path followed in the cyclic cell pressure tests was closer to the expected realistic stress path in rail track rather than the constant cell pressure tests. Permanent axial strain was higher for cyclic cell pressure tests compared to constant cell pressure tests. Permanent axial strain accumulation was similar for cyclic cell pressure tests after the 50^{th} cycle except for T14.

The permanent volumetric strain of constant cell pressure tests calculated from radial calliper falls into a narrow band (0.2 % range) after eliminating first 10 cycles. The volumetric strain calculated for constant cell pressure tests from the cell pressure controller and calliper were varied. As the volumetric strain from controller seemed to be influenced by creep, it was considered unreliable and the radial calliper readings were used for calculations. Anyhow the volume calculations from radial calliper readings have a limitation due to calliper rests on few ballast particles and therefore it can be influenced by local variations in the specimen deformation.

Membrane penetration was significant during cyclic cell pressure tests. Permanent volumetric strain varied between cyclic cell pressure tests. The variations between cyclic cell pressure tests in terms of permanent volumetric strain, axial strain, radial strain were reduced during the later parts of cycles. Volumetric strain was in close approximation for cyclic cell pressure tests T6 and T15 and constant cell pressure test T13 over different cyclic intervals. Cyclic cell pressure tests showed more radial expansion compared to constant cell pressure tests due to the reduction in confinement within each load cycle.

In general, resilient and shear modulus values increased with number of cycles for both constant and cyclic cell pressure tests. An increase in the resilient modulus with number of cycles during the constant cell pressure case was also reported by Lackenby et al. (2007), Aursudkij et al. (2009), and Sevi (2008). Stiffness (Resilient modulus, shear modulus, bulk modulus) and Poisson's ratio reduced when the cell pressure cycled.

The extension loading stage was used to simulate the process of tamping in the triaxial apparatus. The test height was increased by significant amount during the extension stage due to the higher horizontal force. The major part of height increase occurred during the first cycle of the extension. Settlement returned back closer to the pre-extension level with subsequent cyclic loading.

The extension tests show that principal stress reversal during tamping causes a distruption of the ballast structure developed due to compaction and train loading based on the observation of large initial settlement after the extension stage back to the pre-extension height. It gives an insight into the mechanism whereby the ballast layer may returns rapidly to its pre-tamping profile under train loading which is called the "ballast memory" phenomenon by Selig and Waters (1994).

Radial callipers showed that the contraction of diameter during the extension stage concided with the increase in height. A reduction in resilient modulus soon after the extension stage was observed which implies the loosening of compacted ballast layer during tamping. The resilient modulus values gradually increased with continued cycles.

7. Conclusions and future research

7.1 Conclusions

Experiments were carried out on a scaled railway ballast to understand the mechanical behaviour of ballast and study the effect of tamping. Significant conclusions drawn from this project are summarised below.

Particle characterisation:
Particle characterisation was carried out to investigate the validity of the use of scaled ballast. A weak trend for larger particles to have lower S/L and ellipseness was observed. However the trend was not clear between any two sieve size intervals. There were measurable differences in S/L and ellipseness between different sieve size intervals. As the differences were small in magnitude and the scaled ballast material was prepared using parallel gradation technique from same parent rock of full size ballast, the scaled ballast was used for lab testing programme.

Monotonic loading:
Monotonic test results showed general stress-strain behaviour similar to a conventional granular material. Peak deviator stress and initial stiffness was observed to increase with increasing confining pressure. Specimens compressed more and dilated less with increasing confining pressure. Dry specimens showed a trend of slightly higher deviator stress, initial stiffness and slightly more dilation than saturated specimens, but the trend was not very strong. A trend of reduction in angle of effective shearing resistance with confining pressure was observed. Scaled ballast fell within the range of angle of effective shearing resistance reported for full size ballast in the literature.

Cyclic loading:
In cyclic loading, larger settlement was observed during the initial cycles. During constant cell pressure tests, the variation in settlement between specimens tested at similar stress conditions was reduced by eliminating first few cycles, and the variation in volumetric strain reduces after eliminating first 10 cycles. During cyclic cell pressure tests, variation between specimens in terms of settlement, volumetric strain was observed. The variations were reduced during the later parts of cycles. Resilient and shear modulus increased with number of cycles during both constant and cyclic cell pressure tests.

More settlement occurred for cyclic cell pressure tests than for constant cell pressure tests. It is due to stress ratio, q/p′ was higher within a cycle during cyclic cell pressure tests, as the confining pressure was lower on average during cycle. Specimen expanded more in radial direction when the cell pressure cycled. Stiffness and Poisson's ratio reduced when the cell pressure cycled.

Extension loading:
Extension loading was carried out as an idealised way to simulate tamping in the triaxial cell. Massive settlement was observed after the extension cycle. This indicates the disruption of ballast structure during extension, probably due to the principal stress reversal during extension/ tamping disrupting the ballast structure. In rail track, although tamping used to restore track geometry, it causes a faster rate of settlement afterwards.

7.2 Recommendation for future research

In this project scaled ballast was used for testing programme. Characterisation work was carried out to assess the validity of the use of scaled ballast. There is a scope to better examine the suitability of the model material by carrying out direct comparison experiments on full size railway ballast of same parent rock as model material.

In this project, 1/3 scaled material was used. All these experiments can be done using different scale similar shape same parent rock quarry materials. This will help to assess the parallel gradation technique further.

The CT work can be carried out to study the changes in the structure of ballast during tamping. A technique was developed to stabilise the triaxial specimen after a certain stress path. Similarly prepared specimens can be stabilised at different stages of a test. For example, if the testing programme is cyclic loading followed by extension then cyclic loading, the specimens can be stabilised after cyclic stage, after the peak height lift during the extension stage, after the first few cycles after extension, at the end of the programme. This will help to investigate in detail the specimen structure changes during different stages of ballast life cycles using CT analysis and processing technique.

The Hall Effect callipers used in this project had a range of +/- 3 mm. This range is very small compared to the ballast particle size. As a result, the callipers reached the end of their range during the first cycle for few tests and setting up the callipers was quite challenging. However, the callipers were observed to behave better than radial LVDT in initial trials. Design of larger range callipers will assist in carrying out experiments on larger scaled materials like ballast.

More radial callipers can be used to increase the data set for averaging the radial measurements and remove local variation. An alternate means of radial strain measurement that is less localised such as a direct measurement of the full change in circumference rather than a localised measure of the diameter from two discrete contact locations can be used in future research. Such a development is recommended for future experiments in this area.

Appendix A. Published article

Le Pen, L.M., Powrie, W., Zervos, A., Ahmed, S., Aingaran, S. 2013. Dependence of shape on particle size for a crushed rock railway ballast. Granular Matter, Volume15, Issue 6, pp 849-861.

The published article is available online from SpringerLink;
http://www.springerlink.com/openurl.asp?genre=article&id=doi:10.1007/s10035-013-0437-5

DEPENDENCE OF SHAPE ON PARTICLE SIZE FOR A CRUSHED ROCK RAILWAY BALLAST

L.M. Le Pen, W. Powrie, A. Zervos, S. Ahmed, S. Aingaran

University of Southampton, Southampton, Hampshire, United Kingdom

ABSTRACT

Laboratory testing of railway ballast poses practical difficulties because the particle size is often too large for most standard apparatus. There are therefore advantages in developing a scaled material whose behavior is representative of the full size material. A first stage in validating such an approach is to investigate whether the particle shape is affected by the change in scale. This paper sets out methods for evaluating form and roundness (aspects of shape) and proposes a new measure for evaluating roundness, termed ellipseness. These methods are then applied to a crushed rock railway ballast over a range of particle sizes. Statistical analysis demonstrates a measurable variation in the distributions of form and roundness with particle size over a range of sieve intervals, although the differences are slight and do not necessarily rule out the use of a scaled material for investigating the factors influencing macro mechanical behavior.

Keywords: Ballast, shape, form, statistics, weibull, scale, roundness, angularity, ellipseness

Introduction

The application of soil mechanics principles to the mechanical behavior of railway ballast should lead to improved ballast specifications and track sub-structure designs, and reduced maintenance requirements and whole life cost. However, a significant difficulty in carrying out experimental investigations into the behavior of railway ballast is the typical particle size (up to 62.5 mm), which is too large for a representative specimen to be accommodated in most standard laboratory soil element testing apparatus. Large scale apparatus has been developed (e.g.[1], [2], [3]), but is expensive to build and run and tests can be challenging and time-consuming.

An alternative approach is to develop and test a scaled material having the same characteristics as railway ballast but a small enough particle size to be tested in standard laboratory apparatus. A potential concern is the preservation of particle properties with scaling; for example, particle shape has been shown to influence the bulk density, stiffness and strength of natural and crushed sands (e.g. [4]). Historically, research into scaled particulate materials was in the context of rockfill (e.g. [5]) but recent research has been driven by the need to understand the behavior of railway ballast (e.g. [6]). However, despite some notable efforts there have been few systematic attempts to investigate the use of appropriate scaled materials. Such an investigation would require consideration of the shape (form, roundness and roughness), stiffness (contact and material) and strength (fracture toughness and abradability) of particles; how these attributes vary within and over a range of particle sizes; and how any variation affects the macromechanical behavior.

This paper describes an investigation to measure and evaluate how particle shape may change with scale. The same parent rock is used, minimizing the potential for variations in surface roughness does not vary; the focus is therefore on comparing the form and roundness over a range of particle sizes in convenient sieve intervals from full size to reduced scale.

In particular the paper

1. develops appropriate methods for defining and quantifying particle shape,
2. shows that there are measurable and quantifiable, although small, differences in particle shape with size.

The detailed measurements of shape will also facilitate numerical simulation using particles that represent crushed rocks by taking advantage of recent advances that permit particles of arbitrary shape to be used (e.g. [7]).

Background

Two principal approaches have been proposed to create of an analogous or model material at a smaller scale. They are:

- scalping (e.g. [8]), i.e. the removal of all particles from the original material that are greater than a certain size;

- parallel gradation (e.g. [9]), i.e. the formation of a laboratory specimen with a particle size distribution smaller than but parallel to that of the original material.

The feasibility of using either method may depend on the material being tested. For example scalping might be appropriate for a well graded material where relatively few oversize particles need to be removed. However, for a more uniformly sized material such as a railway ballast, scalping might result in the removal of much of the specimen so the parallel gradation technique would be more appropriate.

The validity of the parallel gradation approach relies on the smaller scale particles behaving in the same way as the larger scale particles they are intended to model. [5], [6], and [10] investigated this by means of triaxial tests on rockfills over a range of parallel gradations, in triaxial cells of varying size. In general all three studies demonstrated that the volumetric strain varied with scale for tests under the same stress conditions. However it is not clear if these trends resulted from changes in shape or changes in other characteristics related to scale.

[6] also compared particle shapes for the three parallel gradations of Iron Mountain Trap Rock from Missouri in the USA tested on the basis of plan view images. Although only averages of the data on particle shape were reported, they showed that larger particles tended to have greater aspect ratios (maximum to minimum dimensions, or form) and sharper corners (greater angularity, defined as the average radius of the smallest four corners within a particle).

Scale is known to influence the strength of individual particles, with smaller particles being statistically likely to be stronger owing to their lower probability of containing flaws (see e.g. [11], [12]). Hence assemblages of smaller particles may appear to be less compressible than assemblages of larger particles, if the stress applied is sufficient to fracture some of the larger particles.

The applied boundary stresses should be the same in corresponding tests on full size and scaled material. If it is assumed that the particle shape remains similar and that Hertzian (elastic) contact theory (see [13], [14]) can be applied, then the interparticle contact stresses and hence compressibility of the assembly will remain the same. In practice there may be some differences: Hertzian contact theory assumes that each surface is topographically smooth on both the micro and macro scale, and in reality there is also likely to be some inelastic behavior [15].

Experimental work to establish the importance of changes in shape on the behavior of soils (without varying scale) is still at a relatively early stage. Research findings are generally restricted to changes in behavior resulting from large changes in shape characteristics. For example [16] established that the relative proportions of bulky or platy particles (extremes of shape) had a strong influence on the shear strength and deformation characteristics of sands. [4] explored the impact of particle shape on sandy soils by comparing data from published studies; they too considered relatively large changes in shape to identify a number of trends in soil behavior.

Brief review of Particle Shape characterization approaches and chosen measures

In this section the historical development of ideas related to shape and some of the more established methods are briefly discussed. Full details may be found in the references provided.

Overview

It is widely recognized that there are three **independent** properties of particle shape– form, roundness and surface texture – which have quite different scales as shown in 2D in Figure 1 [17]. These properties are independent because each can vary widely without influencing the others. Accepting these broad definitions, it is then necessary to come up with means of measuring or characterizing each of the three properties. For form and roundness this has usually meant combining measurements into a dimensionless index, but taking measurements is not trivial and it is usually necessary to take measurements from 2D images or 3D data cloud representations of particles rather than the physical objects themselves.
Particle imaging has traditionally been based on 2D projections (e.g. using camera lucida [18]), but contemporary imaging now uses digital cameras for 2D (e.g. [19]) and laser scanning or computer tomography (CT) scanning for 3D (e.g. [20, 21, 22, 23]). However, there are issues with the interpretation of such data both in 2D and 3D, mainly related to the relative particle to pixel or voxel size. Also, while it might be supposed that 3D measures would be superior to 2D ones this largely depends on the reasons for making the measurements. Furthermore laser and CT scanning is not readily available to most researchers or practitioners and

CT scanning in particular is costly in terms of both money and time. Also, with CT analysis there are physical limits on the sizes of samples that can be scanned and the resolution achievable. Therefore the methods adopted for this paper are essentially pseudo 3D measures of 2D digital images with the advantage that these methods are readily available to all researchers and practitioners working in this area and are appropriate for the aims of this work.

Some of the better known measures for form and roundness and the measures chosen for use in this research are discussed below. Also, where appropriate, issues with the use of digital images are highlighted. Roughness is not considered as this is reasoned to be similar for all of the particles evaluated owing to their method of manufacture (crushing). Therefore the pixel size used for imaging has been set to a size larger than that needed to capture this smallest scale aspect of shape.

Form: measures

Form is the largest-scale particle property. Most quantifications of form are based on measuring the longest (***L***), shortest (***S***) and intermediate (***I***) orthogonal dimensions and combining two or all of them into a dimensionless index. ***L***, ***S*** and ***I*** can be obtained or approximated from 2D images as shown in Figure 2.

One of the earliest attempts at quantifying form was by Zingg [24], who as long ago as 1935 used the position of a particle on a plot of ***I/L*** against ***S/I*** to classify it as either flat, columnar, spherical or flat-columnar (Figure 3). ***I/L*** and ***S/I*** are sometimes termed the flatness and elongation ratios respectively. Another commonly used index is the ***S/L*** ratio, termed the degree of equancy [25]. The ***S/L*** ratio is the product of the coordinates in the Zingg plot (***I/L*** and ***S/I***). Lines of equal ***S/L*** are hyperbolae on the Zingg plot and each may pass through up to three of the classification sectors. Measures that include all three of the parameters ***S***, ***I*** and ***L*** have appeared in the literature (e.g. [26]). However there are ambiguities because two of the parameters (and hence the form) can vary and still yield the same result. In this sense they are generally less effective than the simpler ***S/L*** ratio which at least retains some link to a shape type.

Identifying orthogonal axes coincident with ***S***, ***I*** and ***L*** and measuring these dimensions for large numbers of particles presents practical difficulties. It is possible to measure ***S***, ***I*** and ***L*** manually using calipers, although this is time

consuming and any set of measurements may be subject to user variation. There are now various algorithms that may be implemented using 2D digital images or 3D data clouds. However, there are issues with automated methods and in choosing a method consideration should be given to the types of shape being evaluated and how the algorithm might distort the intended measure (e.g. [27]). Pseudo 3D measurements can be generated using orthogonal views and can be just as good as estimates gained from 3D data. For example [23] compared using 3D representations of particles (from CT or laser scanning) to using orthogonal 2D images to determine form and concluded that for 2D and 3D methods ". No one is consistently better than the other ….". A technique that will be adopted for this research was put forward by [28]. This technique relies on allowing the particles to fall onto a flat horizontal surface, on the basis that the particles will tend to come to rest with their shortest dimension (***S***) upward and their longest and intermediate dimensions visible in plan (***I*** and ***L***). Thus digital plan view images could be used to measure ***I*** and ***L***. By assuming that the shape of the particle would correspond approximately to a scalene ellipsoid (i.e., an ellipsoid where the three major axes have different lengths) and measuring the mass (***W***) of the particle, ***S*** can be estimated for single or groups of particles using Equation 1:

$$S = \left({}^{W}/_{\rho_w G_s} \right) \left({}^{6}/_{\pi LI} \right) \quad (1)$$

where G_s is the specific gravity of the particle (for granite typically 2.65) and ρ_w is the density of water (1000 kg/m^3 at 4°C).

This approach to estimating ***S*** from measurements of ***L***, ***I*** and ***W*** is termed the scalene ellipsoid equivalent sphericity, or SEES. [28] validated the approach by taking orthogonal views of a number of particles of varying shapes and comparing the ratio of ***S***/***L*** obtained from each method. Of the materials they tested, Leighton Buzzard sand (fraction B) is geometrically the most similar to railway ballast (albeit at smaller scale) for which the averaged measured ***S***/***L*** of 0.532 compared well with the calculated value (using equation 1) of 0.549 for the six particles individually measured and weighed. A more detailed description and a validation of the SEES approach by comparison to orthogonal views for the ballast material, are given in the section on materials and methods.

Roundness: measures

Roundness is the intermediate scale descriptor of shape, commonly considered the inverse of angularity in that as one increases the other decreases. Unlike form there is no direct physical method of measurement for roundness. Roundness has most usually been quantified using 2D views of particles, but 3D methods have appeared in the literature [29]. Measures can be complex and subjective in application. Probably the most well-known method was put forward by Wadell [18], in which the radius of identifiable corners in the particle outline are measured and averaged and then divided by the radius of the maximum inscribed circle. In effect this is a measure of average angularity. Another well-known method was put forward by Krumbien [30], this uses comparison charts to classify particles by eye. A version of this type of chart can be found in [31] where shapes are shown in a 4 by 5 array with progressively increasing roundness [18] across the horizontal scale and aspect ratio (form) on the vertical scale. It is extremely time consuming to carry out either of these procedures manually, and while some progress has been made in automating Wadell's methods (e.g. [32]) there remain difficulties in defining what constitutes a corner. Furthermore the use of pre-drawn reference charts is more suited to the classification of different materials rather than examining particles from the same source material (as is the case in this research), where differences in shape with scale may be too small to register.
In this research we have chosen to use a relatively simple method easily adapted to automatic digital image analysis, based on quantifying the ratio of the perimeter (P) of the 2D projection of a particle to the perimeter of a reference shape of the same area (A) i.e. $A_o=A_e$ but $P_o \neq P_e$. The subscripts o and e denote respectively the particle (object) and the reference shape, assumed here to be an ellipse.
In the current research, for consistency with the reference shape adopted in the analysis of form, we use a new measure of roundness that we call "ellipseness" E, defined as:

$$E = \frac{Perimeter\ of\ equivalent\ area\ ellipse}{Perimeter\ of\ particle} = \frac{P_e}{P_o} \qquad (2)$$

In this calculation E will always be less than 1, meaning that the perimeter of the actual particle is greater than that of an ellipse of the same area. As the calculated value of E approaches 1, the particle becomes more ellipse like. This has some similarity to the commonly used "equivalent disc method", in which the reference

shape is a circle of the same area. However, using a circle would imply an ***I*** dimension greater than is physically possible. The use of an ellipse having the same major dimension and area provides a better estimate of the smooth shape used to describe the particle. That particles do not all tend to circles when perfectly round was noted by Wadell as long ago as 1932 [18]. Methods of determining ***E*** using digital images are discussed in the section on materials and methods. It is recognized that ellipseness is an average measure of roundness (or inverse angularity) as the same numerical value may be achieved in a variety of ways (e.g. two very sharp projections/corners on a notionally elliptical 2D image may result in the same ellipseness as a number of smaller, less pronounced, projections/corners).

Materials and methods

Materials

Full size and reduced scale crushed granite ballast was obtained from Cliffe Hill Quarry, Leicestershire, England which supplies ballast for Network Rail. Most ballast around the world is formed of particles within the range 22.4 mm to 63.5 mm. For this study the lower limit of the particle range is extended to 9.5 mm so that the scaled and full size particles can be grouped over a sequential range of eight sieve intervals as follows: (1) 9.5 mm to 11.2 mm, (2) 11.2 mm to 13.2 mm, (3) 13.2 mm to, 16.0 mm and (4) 16.0 mm to 22.4 mm (scaled), (5) 22.4 mm to 31.5 mm, (6) 31.5 mm to 40.0 mm, (7) 40.0 mm to 50.0 mm, and (8) 50.0 mm to 62.5 mm (full size). The smaller sieve size in each interval will be referred to as the catching sieve and the larger the passing sieve. For ease of reference, often only the catching sieve size will be stated.

Figure 4 shows example particles from each sieve interval; the images have been resized so that the particle sizes appear to be approximately the same. The Figure is provided as a visual demonstration that differences in shape with scale appear to be slight and could be subjectively described as not visually appreciably different. For example if the comparison chart provided by [31] were applied the particles could easily be placed in the same classification sector.

Imaging system: methods

Groups of particles were placed on a bench top with a digital camera directly above as shown in Figure 5. The camera was positioned approximately 1.2 m above the particles and the particles placed within an approximately 200 mm sided square immediately below the camera. The focal length of the camera was set to 120 mm. The distortion of objects not directly below the camera was measured and found to be insignificant at up to 100 mm lateral offset.

The camera used is a SONY DSC-R1 Cyber shot 10 mega pixels with a 21.5 x 14.4 mm (max image size 3888 x 2592) CMOS sensor having a pixel density of 4593dpi horizontally and 4572dpi vertically. This research looks at particles of relatively large size (diameters mainly between 10 mm to 60 mm) and the properties of the camera used were suitable for this work as would those of many commonly available modern cameras.

The particles were lit by a pair of 200 watt stroboscopic daylight balanced lamps. Parabolic light modifiers were used to focus the light on to the sampling area. The positions of the lights are set so as to minimise/eliminate shadows in the plane being photographed. Additionally, a black background was used.

Off the shelf image analysis software was used to segment and measure the images using consistent histogram based thresholding. The software used was Image Pro Plus [33], but there are many other suitable software packages available and/or bespoke code could be written. Digital measurements are discussed later.

Form: methods

Two different methods of measuring S, I and L to determine form parameters were compared. In the first method, two images of the particle were taken in two different orthogonal projection planes capturing the longest, intermediate and shortest dimensions. The first view captured was of the plane in which the particle was mechanically most stable thus presenting the longest (L) and intermediate (I) particle dimensions to the camera. Each particle was then rotated and the orthogonal view eliciting the shortest dimension identified. From the images thus obtained, image analysis was used to determine the lengths of the longest (D_{max}) and shortest (D_{min}) lines joining two points on the particle perimeter and passing through its centroid of area (Figure 6). If, as is the case here, the shapes analysed

are reasonably regular, these measurements approximate to L, I and S. L and S were taken as the absolute maximum and minimum values of D_{max} and D_{min} respectively, and I as D_{min} from the first most stable projection.

The second method involved determining L and I from the initial plan image of each particle, and inferring the value of S using the SEES approach (Equation 1). Systematic comparison of the results obtained using the two methods showed that in a minority of cases (less than 9% for the scaled material and less than 4% for the full size material), the plan view image gave L and S rather than L and I so that applying SEES gave I rather than S. In these cases the values S, I and L were reassigned accordingly. This problem occurred because while the ballast particles approximate reasonably well to scalene ellipsoids, some particles have $S \approx I$ and the most stable face is not clearly identifiable.

Roundness: methods

The area and perimeter were measured from the digital images (as described and discussed in the next section). With these values known, Equation 2 was used to quantify roundness by means of the Ellipseness measure as follows. The minor radius b of the equivalent area ellipse was calculated from the major radius $a = L/2$ ($D_{max}/2$) and the measured area A_o using Equation 3. The equivalent perimeter P_e was then calculated using Equation 4.

$$b = \frac{A_o}{\pi a} \tag{3}$$

$$P_e \approx \pi(a+b)\left(1 + \frac{3\left(\frac{a-b}{a+b}\right)^2}{10+\sqrt{4-3\left(\frac{a-b}{a+b}\right)^2}}\right) \tag{4}$$

Equation 4 was first presented in 1913 by the mathematician Ramanujan [34] and is an accurate approximation to the perimeter of an ellipse (which can otherwise be calculated using power series). A discussion on approximations to the perimeter of an ellipse can be found in [35].

Influence of digitization on the measured parameters

In image analysis it is important to define precisely the methods used and evaluate the suitability of the pixel density (i.e. the number of pixels per particle) used. In this study the camera set up was such that each pixel represented approximately 1/8 mm. This was selected so as to remove the effects of surface roughness from the measured perimeters while still providing sufficient pixel density, in all particles analysed, not to unduly influence the measured diameters, perimeters and areas used for the calculation of form and ellipseness. The pixel density over the size range of ballast particles imaged was approximately 10,000 to 300,000 pixels per particle.

The diameters D_{max} and D_{min} are defined in Figure 6 and the associated text. Area measurement is by summation of pixels and it has been shown that this method usually converges after only several hundreds of pixels (e.g. [27]). Therefore with 10,000 pixels or more the measured areas can be considered reliable. The method used to measure the perimeter is "eight point connect" (sometimes termed "polygonal"), which for rough objects is known to give digital perimeters that increase with pixel density.

To investigate the influence of the pixel density on the measurements made in this study - and in particular to evaluate whether the measurements of perimeter would have sufficient pixels present to capture particle roundness – smooth irregular objects, (i.e. objects having no measurable surface roughness for the pixel densities applied) including some of similar form and ellipseness to ballast were imaged over the range of pixel densities used (achieved by repositioning the camera). This investigation resulted in the following observations:

- Form is a dimensionless ratio of combinations of L, I and S (D_{max} and D_{min}). It can therefore be calculated using the number of pixels present and the true scale is irrelevant. This has the advantage that calibration of images to true scale is not needed, and this potential small source of error can be discounted. The investigation confirmed that form was substantially insensitive to the range of pixel density used, (i.e. the aspect ratio thus calculated typically varied by less than 1.0%).
- Ellipseness was calculated using the measurements of L (D_{max}) area and perimeter. Again ellipseness is a dimensionless ratio that may be calculated using measurements in pixel units rather than true scale.

Calculations demonstrated that ellipseness was also substantially insensitive for the range of pixel densities used (i.e. for ellipseness, as the pixel density reduced over the full range ellipseness typically increased by not more than 0.5%).

Measurements of particle shape, results, analysis and discussion

Form

Values of the ratios ***S/L***, ***I/L*** and ***S/I*** measured on the basis of two orthogonal views are compared with those estimated from the plan view using the SEES approximation, for particles retained on each sieve size, in Table 1.

Figure 7a shows a Zingg plot for particle form data determined using SEES, while Figure 7b shows data for the same particles determined using two orthogonal views. A comparison of the ***S/L*** ratio obtained from each of the methods is shown in Figure 8. Estimates of ***S*** for an individual particle and hence its position on the Zingg plot can vary greatly. However, taken overall these variations average to a much smaller error, approximately a 2% underestimate in ***S/L*** by SEES compared with using two orthogonal views for most particle sizes, with bigger errors of -7.7% and -10.2% respectively for the 31.5-40.0 and >40.0 mm particle size ranges. Further measurements were then made using the SEES approach, increasing the total number of particles measured to 875 (Table 2). Figure 9(a) shows a Zingg plot for all data sorted by sieve interval and Figure 9(b) shows the average position on the graph for each sieve interval. Figure 9(b) shows that on average the data are all very near to the crossover between the four particle classification sectors (2/3,2/3). The particles on the 11.2 mm, 13.2 mm and 16.0 mm catching sieves classify as "spherical" and those on the 50.0 mm catching sieve just cross into the "flat" region. The particles on the 9.5 mm, 22.4 mm and 31.5 mm catching sieves are in the "columnar" sector and those on the 40.0 mm catching sieve are in the "flat and columnar" region. The nearness to the crossover may tend to over emphasize differences that in reality are slight. Table 3 summarizes key statistics from the ***I/L, S/I*** data shown in the Zingg plots and also the ***S/L*** data for all particles.

Having considered the effect of all three parameters ***S***, ***I*** and ***L*** in the Zingg plots, the ***S/L*** ratio will now be investigated further. Figure 10 plots separately the cumulative distributions of ***S/L*** ratio for the particles in each sieve interval. The

curves for full size ballast group together on the left. All other distributions form a second band to the right, with the exception of the data for the 9.5 mm catching sieve curve which falls between the two bands.

The distributions shown in Figure 10 may be compared statistically by means of a Kruskal Wallis analysis [36]. This uses the rank of a variable to determine the statistical likelihood that separate data sets have the same median. In Figure 11, the rank (i.e. the relative position of each individual S/L value within the full data set of 875 particles) is plotted on the x axis. The groups designated by catching sieve size are indicated on the y axis. For each group, a line showing the 95% confidence interval for the median has been drawn. Where there is no overlap between the confidence intervals, there is at least a 95% confidence that the medians of the two groups are different. In Figure 11, the 95% confidence limits for the 9.5 mm catching sieve group are indicated by vertical lines which helps to illustrate that there are two possible groupings with overlapping 95% confidence intervals denoted by catching sieve groups as:

- 9.5 mm, 22.4 mm, 31.5 mm, 40 mm and 50 mm
- 11.2 mm, 13.2 mm and 16 mm

The Kruskal Wallis analysis supports the groupings observed in the cumulative particle size distributions shown in Figure 10.

As well as comparing the measured data (Figures 9 and 10) it is possible to fit equations to these distributions. Providing mathematical functions that capture the range and relative distribution of shapes within each size allows others to make comparisons with this data. Statistical confidence limits to the distributions can also be determined. However, there is no fundamental reason why any particular function should be used to fit the shape measurements and it is therefore reasonable to use functions of wide versatility (i.e. able to fit a range of distribution types). A Weibull distribution fits this description and has a record of application to particle properties (e.g. particle crushing strength [11]).

The Weibull cumulative distribution function (CDF) is given by:

$$CDF = y = 1 - e^{-\left(\frac{x}{a}\right)^b} \quad (5)$$

The Weibull probability density function (PDF) is given by:

$$PDF = y = ba^{-b}x^{b-1}e^{-\left(\frac{x}{a}\right)^b} \quad (6)$$

Where a is the scale parameter and b is the shape parameter, both found by obtaining a best fit to the sample data [37]. The Weibull distribution is very similar to the symmetrical normal distribution (PDF) when the shape parameter b is between 3 and 4; as b increases above 4 the curve skews to the right. When b=1 the Weibull distribution reduces to the exponential distribution and when $b = 2$ to the Rayleigh distribution. The scale parameter a serves to smear the function along a greater or lesser length on the x-axis, reducing or raising the relative peak. Equation 5 can be used to match the cumulative distribution curves shown in Figure 10. A least squares fit to the S/L data for each sieve interval, performed using the software Matlab [38], gave the values shown in Table 4 for the parameters a and b. Figure 12 shows the Weibull fits for the cumulative distribution functions for the S/L data from each catching sieve size. Comparison of Figure 12 with Figure 10 shows that the Weibull functions are generally close to the measured data. Figure 13 shows the Weibull fit for the probability density function for the S/L data for each catching sieve size which again shows the differences between the catching sieve groupings. The data shows that there is a weak trend for S/L to reduce for larger particles (as found by [6]), but there are exceptions. Some of the data are more spread out, indicated by a greater standard deviation (Table 3) and or flatter looking probability density function (Figure 13) such as the data in the catching sieve intervals 11.2 mm, 13.2 mm and 16 mm. These observations are not necessarily common to the other form indicators (I/L and S/I) which can be seen by comparing the values in Table 3.

Roundness

For the dataset shown in Table 2, Image Pro Plus was used to estimate L (D_{max}), the perimeter P_e and the area A_e of each particle, from which the ellipseness was calculated using Equations 7, 8 and 9. Basic statistics for the ellipseness data is shown in Table 5. Figure 14 shows the cumulative distributions of ellipseness for each sieve interval; as with form, the curves cover a range of ellipseness values. Figure 15 presents a Kruskal Wallis analysis of ellipseness. Vertical lines are shown at the 95% confidence limits for the 22.4 mm data set. Four possible groupings with overlapping 95% confidence intervals are apparent denoted by catching sieve groups as:

- 9.5 mm, 11.2 mm, 13.2 mm

- 16 mm, 22.4 mm, 31.5 mm, 50 mm
- 22.4 mm, 31.5 mm, 40 mm, 50 mm
- 11.2 mm, 22.4 mm (just)

These groupings are different from those identified for form.

Again applying a Weibull fit gives the values of parameters ***a*** and ***b*** shown in Table 6.

Figure 16 shows the CDF calculated using the Weibull functions for ellipesness. Figure 17 shows the Weibull PDFs which are severely skewed by the high shape factor (***b***).

The ellipseness analysis again demonstrates measurable differences in roundness between particles within each sieve range. The data in general suggests that there is a tendency for larger size particles to be more angular – again, consistent with [6]. However, it is still possible for comparisons between particular sieve intervals to counter this trend. The actual and idealized distributions of particle aspect ratio ***S/L*** and ellipseness (angularity) could be used as checks to aid in the creation of numerical specimens for particle level discrete element analysis, for example using the approach proposed by [39] and developed by [7] or other codes capable of generating arbitrary shapes such as [40].

Conclusions

It has been demonstrated that the SEES approach to determining ***S***, ***I*** and ***L*** is reasonably consistent with a two-view approach for the ballast investigated and has the advantage of being less time consuming.

A new measure of roundness (termed ellipseness) has been introduced. This relates the perimeter of the particle to the perimeter of an idealized elliptical particle of the same area, and can be determined automatically using appropriate imaging and analysis software.

The data indicate a weak trend in the ballast investigated for larger particles to have a lower ***S/L*** and greater angularity, although comparison between any two individual sieve intervals may not follow these trends. However, the ranges of variation in ***S/L*** and angularity are relatively small in magnitude, and do not necessarily rule out the use of scaled materials as appropriate substitutes for testing purposes.

Further work is needed to evaluate whether the small changes in shape measured in this research translate into differences in macromechanical behavior that are attributable to shape alone. Such further work might involve the use of particle scale discrete element analysis, in which case the distribution functions presented in this paper could be used as checks to aid in the creation of numerical specimens.

ACKNOWLEDGEMENTS

This research was facilitated by a grant from the Engineering and Physical Sciences Research Council for the project titled "Development and role of structure in railway ballast" (Reference: EP/F062591/1). We also acknowledge the work of Ben Powrie in carrying out particle imaging and Andrew Cresswell for his contributions to the original research proposal.

LIST OF SYMBOLS

L	Longest dimension
I	Intermediate dimension
S	Shortest dimension
G_s	Specific gravity
ρ_w	Density of water
W	Mass of particle
P_o	Perimeter of object
P_e	Equivalent perimeter
A_o	Area of object
A_e	Equivalent area
E	Ellipseness
a	Major radius of ellipse
b	Minor radius of ellipse
PDF	Probability density function
CDF	Cumulative distribution function

REFERENCES

1. Indraratna, B., Ionescu, D. & Christie, H. 1998. Shear behavior of railway ballast based on large-scale triaxial tests. Journal of Geotechnical and Geoenvironmental Engineering, 124, 439-450.

2. Anderson, W. & Fair, P. 2008. Behavior of Railroad Ballast under Monotonic and Cyclic Loading. Journal of Geotechnical and Geoenvironmental Engineering, 134, 316.

3. Aursudkij, B., McDowell, G. R. & Collop, A. C. 2009. Cyclic loading of railway ballast under triaxial conditions and in a railway test facility. Granular Matter, 11, 391 to 401.

4. Cho, G.-C., Dodds, J. & Santamarina, J. C. 2006. Particle Shape Effects on Packing Density, Stiffness and Strength: Natural and Crushed Sands. Journal of Geotechnical and Geoenvironmental Engineering, ASCE, 132, 591 to 602.

5. Marachi, N. D., Chan, C. K. & Seed, H. B. (1972) Evaluation of Properties of Rockfill Materials. Journal of the Soil Mechanics and Foundations Division, Proceedings of the American Society of Civil Engineers, Vol.98, pp.95-114.

6. Sevi, A. F. 2008. Physical Modeling Of Railroad Ballast Using The Parallel Gradation Scaling Technique Within The Cyclical Triaxial Framework. Doctor of Philosophy PhD thesis, Missouri University of Science and Technology.

7. Harkness, J. 2009. Potential particles for the modelling of interlocking media in three dimensions. International Journal For Numerical Methods In Engineering, Volume 80, 1573 to 1594.

8. Zeller, J. & Wullimann, R., 1957. The shear strength of the shell materials for the Go-Schenenalp Dam, Switzerland. In Proc., 4th Inst. J on SMFE. London, p. 399–404.

9. Lowe, John, 1964. Shear Strength of Coarse Embankment Dam Materials. Proceedings, 8th Congress on Large dams, pp. 745-761.

10. Varadarajan, A., Sharma, K. G., Venkatachalam, K. & Gupta, A. K. 2003. Testing and Modeling Two Rockfill Materials. Journal of Geotechnical and Geoenvironmental Engineering, ASCE, 129, 203 to 218.

11. McDowell, G. R. 2001. Statistics of soil particle strength. Geotechnique, 51, 90.

12. Frossard, E., Hu, E., Dano, C. & Hicher, P.-Y. 2012. Rockfill shear strength evaluation: a rational method based on size effects. Geotechnique, 62, 415 to 427.

13. Hertz, H. R. 1896. Miscellaneous Papers, London, MacMillan and Co. Ltd, New York, Macmillan and Co.

14. Johnson, K. L. 1985. Contact mechanics, Cambridge, Cambridge University Press.

15. Cavarretta, I., Coop, M. & O'sullivan, C. 2010. The influence of particle characteristics on the behaviour of coarse grained soils. Geotechnique, 60, 413 to 423.

16. Abbireddy, C. 2008. Particle Form and its Impact on Packing and Shear Behaviour of Particulate Materials. Doctor of Philosophy, University of Southampton.

17. Barrett , P. J. 1980. The shape of rock particles, a critical review. Sedimentology, 27, 291-303.

18. Wadell, H. (1932) Volume, shape and roundness of rock particles. J. Geol., Vol.40, pp.443 to 451.

19. Francus, P. (ed.) 2004. Image Analysis, Sediments and Paleoenvironments, Volume 7, The Netherlands: Springer.

20. Erdogan, S. T., Quiroga, P. N., Fowler, D. W., Saleh, H. A., Livingston, R. A., Garboczi, E. J., Ketcham, P. M., Hagedorn, J. G. & Satterfield, S. G. 2006. Three-dimensional shape analysis of coarse aggregates: New techniques for and preliminary results on several different coarse aggregates and reference rocks. Cement and Concrete Research, Vol. 36, pp 1619 to 1627.

21. Masad, E., Saadeh, S., Al-Rousan, T., Garboczi, E. & Little, D. 2005. Computations of particle surface characteristics using optical and X-ray CT images. Computational Materials Science, 34, 406-424.

22. Taylor, M. A., Garboczi, E. J., Erdogan, S. T. & Fowler, D. W. 2006. Some properties of irregular 3-D particles. Powder Technology, Vol. 162, pp. 1 to15.

23. Quiroga, P. N. & Fowler, D. W. The Effects of Aggregates Characteristics on the Performance of Portland Cement Concrete, Research Report ICAR – 104-1F. International Center for Aggregate Research, ICAR.

24. Zingg, T., 1935. Contribution to the gravel analysis (Beitrag zur Schotteranalyse). Schweizminer. Petrog. Mitt, 15(38-140).

25. Blott, S. J. & Pye, K. (2008) Particle shape: a review and new methods of characterization and classification. Sedimentology, Vol.55, pp.31-63.

26. Sneed, E. D. & Folk, R. L. (1958) Pebbles in the Lower Colorado River, Texas, a study in particle morphogenesis. J. Geol., Vol.66, pp.114 to 150.

27. Pirard, E. (2005). Image Measurements. In: FRANCUS, P. (ed.) Image Analysis, Sediments and Paleoenvironments. Kluwer Academic Publishers, Dordrecht, The Netherlands.

28. Clayton, C. R. I., Abbireddy, C. O. R., & Schiebel, R. 2009. A method of estimating the form of coarse particulates. Geotechnique, 59, Issue 6, 493 to 501.

29. Garboczi, E. J. 2002. Three-dimensional mathematical analysis of particle shape using X-ray tomography and spherical harmonics: Application to aggregates used in concrete. Cement and Concrete Research, Vol. 32(10), pp. 1621 to 1638.

30. Krumbein, W. C. (1941) Measurement and geological significance of shape and roundness of sedimentary particles. J. sedim. Petrol, Vol.11, pp.64 to 72.

31. Krumbein, W. C. & Sloss, L. L. 1963. Stratigraphy and Sedimentation, W. H. Freeman and company, San Francisco and London.

32. Pirard, E. 1994. Shape processing and analysis using the calypter. Journal of Microscopy, Vol. 175, Pt 3, pp. 214 to 221.

33. Mediacy (2011) Image Pro Plus webpage: http://www.mediacy.com/index.aspx?page=IPP accessed March 2011.

34. Ramanujan, S. 1913-1914. Modular Equations and Approximations to π. Quarterly Journal of Pure and Applied Mathematics, Vol. 45 pp. 350 to 372.

35. Almkvist, G. & Berndt, B. 1988. Gauss, Landen, Ramanujan, the arithmeticgeometric mean, ellipses, and the Ladies Diary. The American Mathematical Monthly, Vol. 95, pp. 585 to 608.

36. Corder, Gregory W., and Dale I. Foreman.(2009) Nonparametric Statistics for Non-Statisticians. 1st ed. Hoboken: John Wiley & Sons, Inc pages 99-105

37. Weibull, W. 1951. A Statistical Distribution Function of Wide Applicability. Journal of Applied Mechanics, 18, 293-297.

38. Mathworks. 2012. Matlab [Online]. Available:http://www.mathworks.co.uk/products/matlab/ [Accessed May 2012].

39. Houlsby, G. T. 2009. Potential particles: a method for modelling non-circular particles in DEM. Computers and Geotechnics, Volume 36, Issue 6, Pages 953-959.

40. Radjaï, F. & Dubois, F. (eds.) March 2011. Discrete Numerical Modeling of granular materials: Hardcover, Wiley-Iste, ISBN 978-1-84821-260-2.

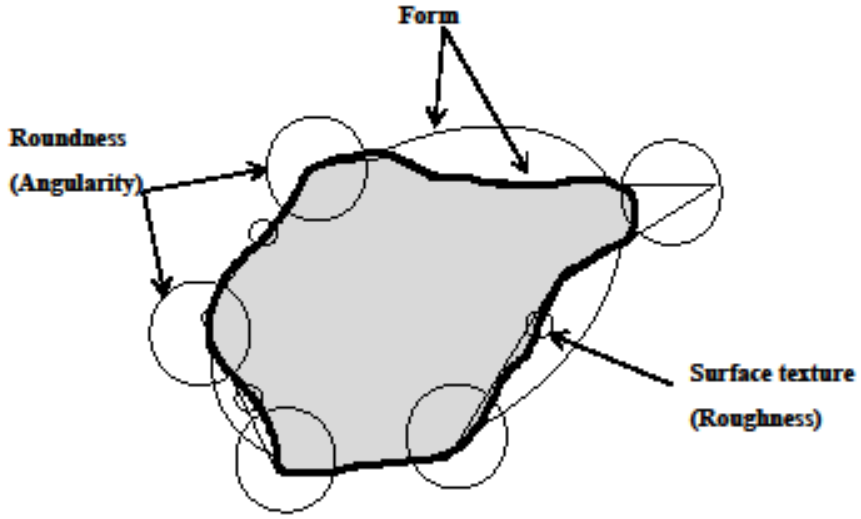

Figure 1: Properties of particle shape (after Barrett, 1980)

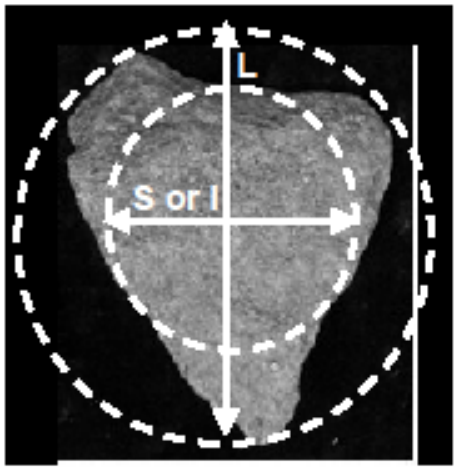

Figure 2: Form indicators

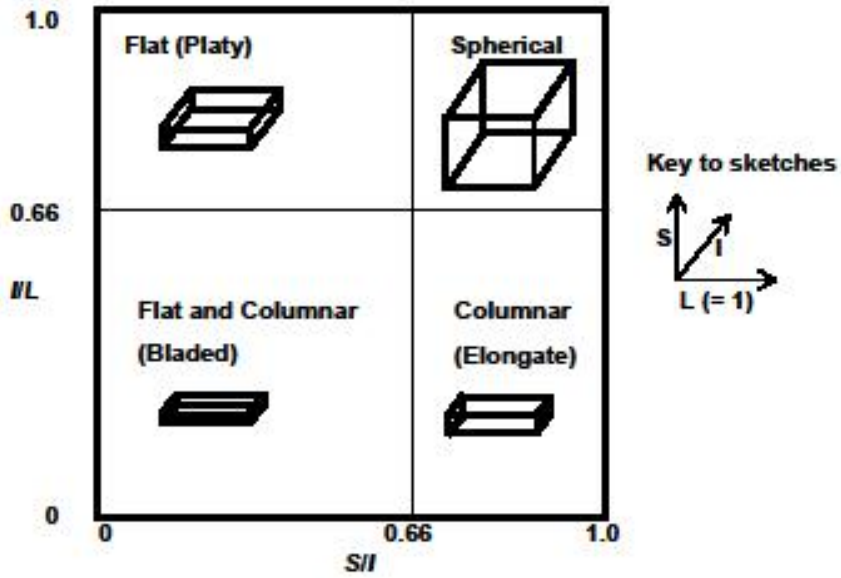

Figure 3: Zingg plot to characterize particle form (redrawn from Zingg, 1935, alternative descriptors in brackets selected from Blott and Pye, 2008)

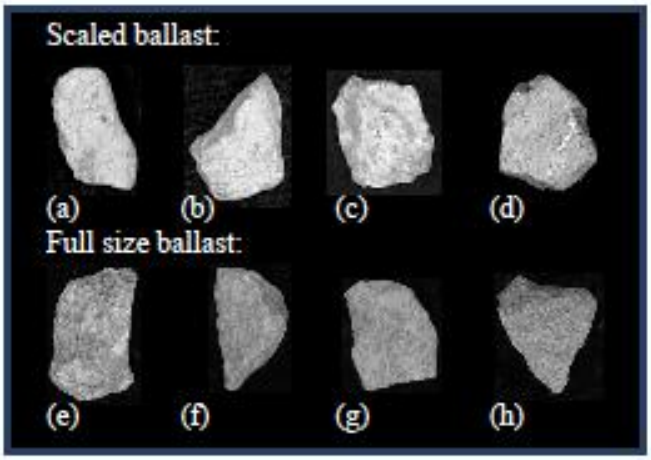

Figure 4: Example particles in sieve intervals (mm): (a) 9.5 to 11.2 (b) 11.2 to 13.2 (c) 13.2 to 16.0, (d) 16.0 to 22.4 (e) 22.4 to 31.5 (f) 31.5 to 40.0 (g) 40.0 to 50.0 (h) 50.0 to 62.5

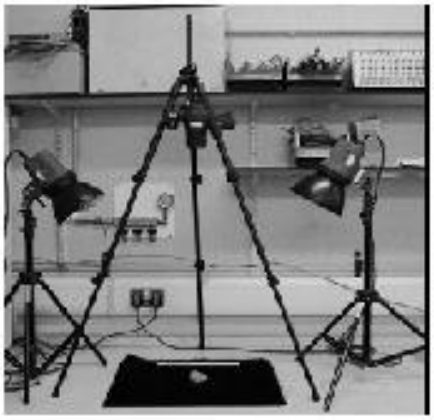

Figure 5: Image capture setup

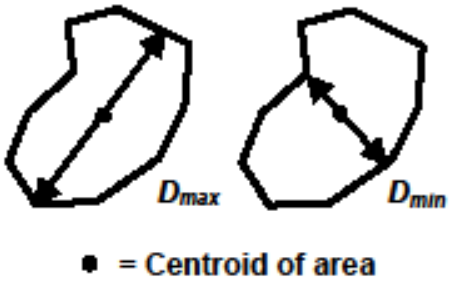

Figure 6: Definitions of D_{max} and D_{min}

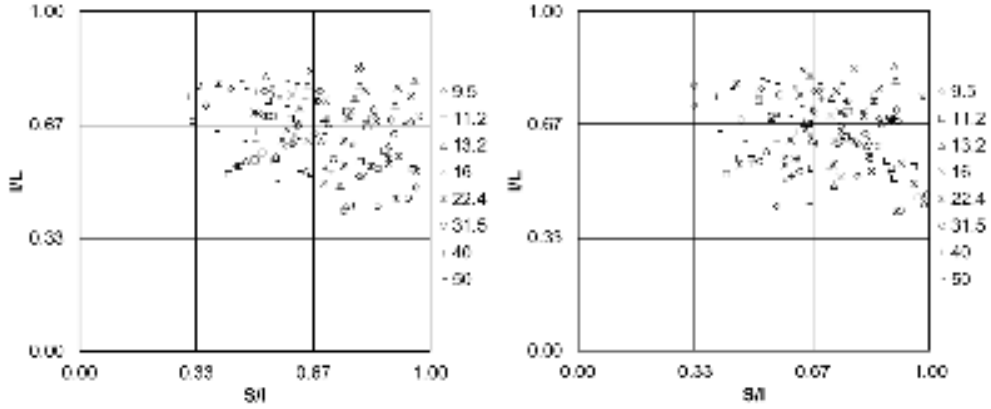

Figure 7: The legend shows the catching sieve in mm (a) Zingg plot for SEES data (b) Zingg plot for data obtained using two orthogonal views

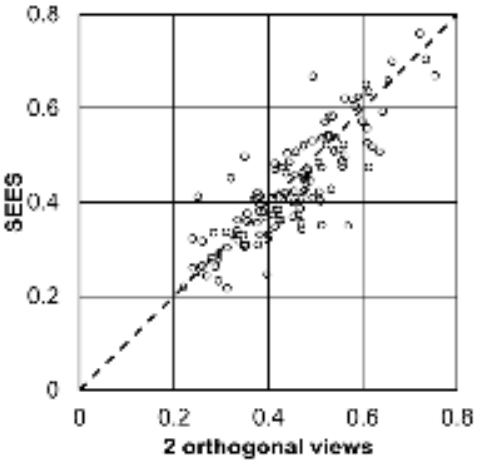

Figure 8: Comparison of S/L ratio obtained from the two different methods (total number of particles evaluated = 120)

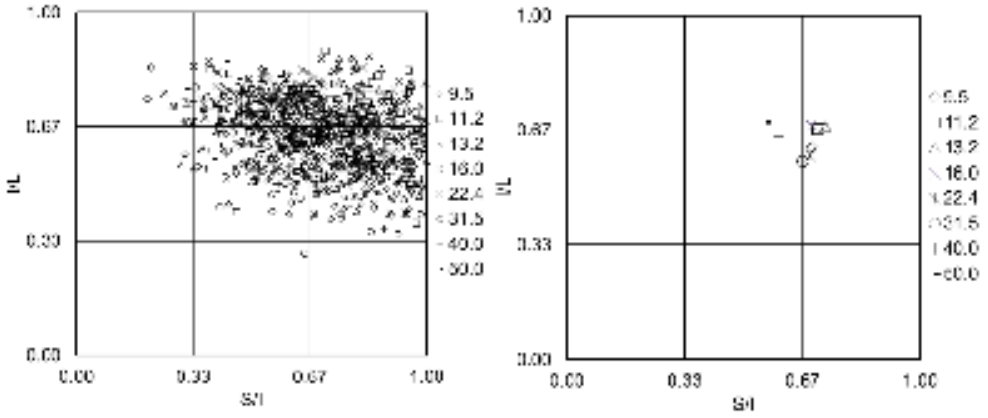

Figure 9 The legend shows the catching sieve in mm, Zingg plots all SEES data for: (a) individual particles (b) averages

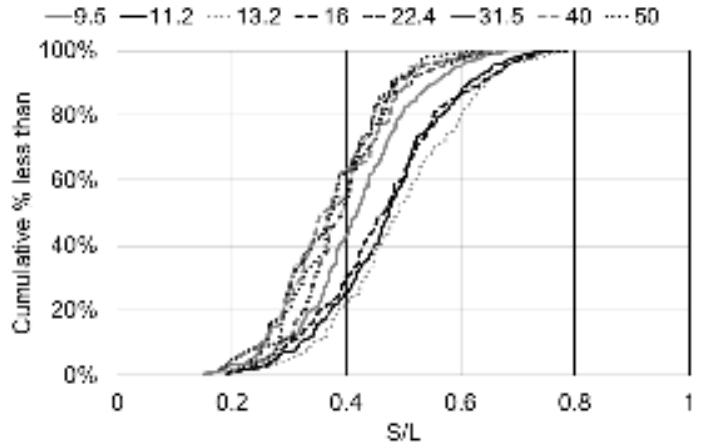

Figure 10: Cumulative distribution curves for *S/L*, the legend shows the catching sieve in mm

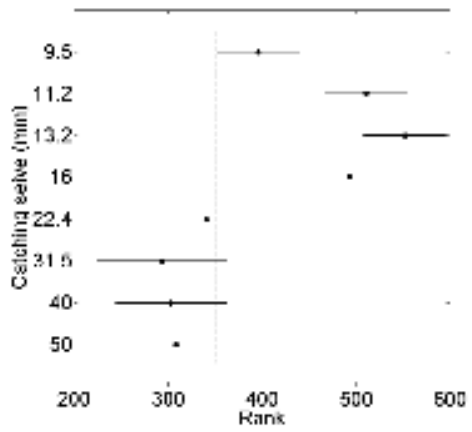

Figure 11: Kruskal Wallis evaluation of form

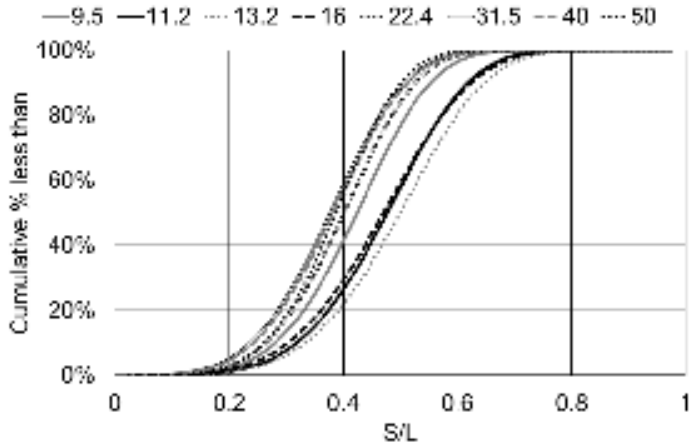

Figure 12: Weibull CDF for S/L, the legend shows the catching sieve in mm

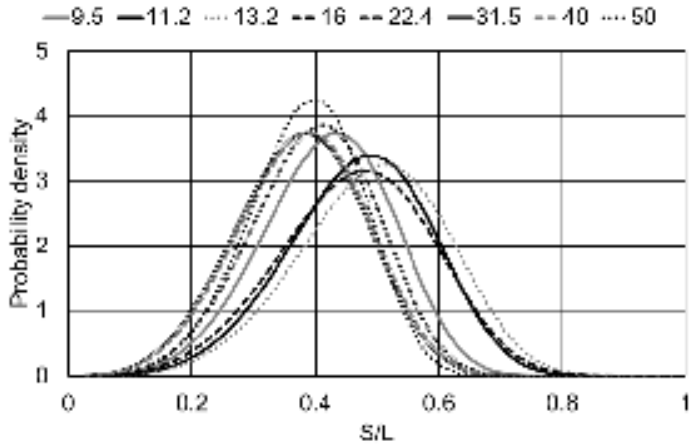

Figure 13: Weibull PDF for S/L, the legend shows the catching sieve in mm

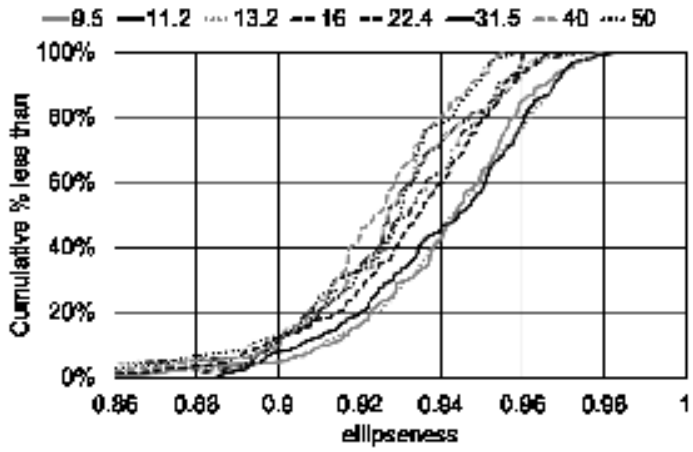

Figure 14: Cumulative distributions, Ellipseness, the legend shows the catching sieve in mm

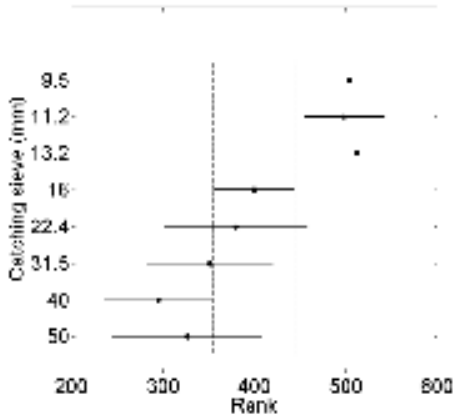

Figure 15: Kruskal Wallis evaluation of ellipseness

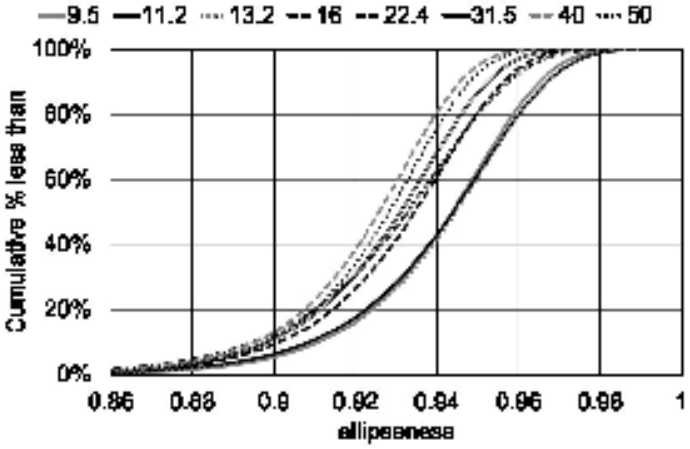

Figure 16: Weibull cumulative distribution functions for ellipseness, the legend shows the catching sieve in mm

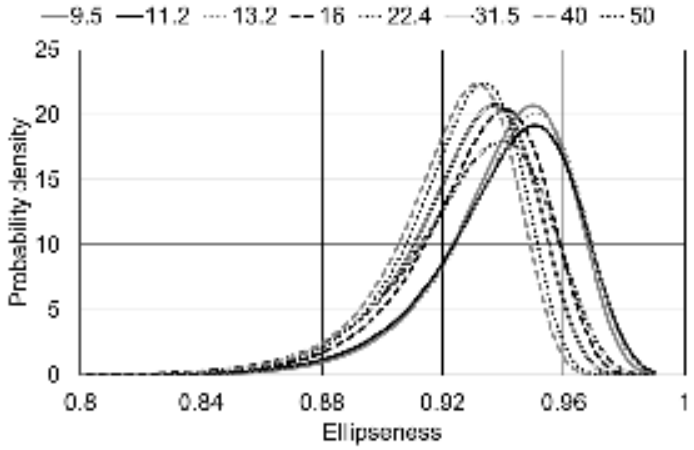

Figure 17: Weibull PDF for ellipseness, the legend shows the catching sieve in mm

Table 1: Basic particle data and comparison between S/L values obtained using two orthogonal views and SEES

	Catching Sieve (mm)							
	9.5	11.2	13.2	16	22.4	31.5	40	50
Number of particles	15	15	15	15	15	15	15	15
Average particle mass (*W*)	2.43	3.76	4.56	8.67	42.04	99.46	165.95	199.17
Average SEES *S/L*	0.46	0.44	0.53	0.53	0.41	0.36	0.36	0.39
Average 2 View *S/L*	0.47	0.45	0.54	0.54	0.42	0.39	0.40	0.40
% difference *S/L*	-2.2%	-1.6%	-1.7%	-1.7%	-1.5%	-7.7%	-10.2%	-2.0%

Table 2: Particles for image analysis using the plan view of the most stable face (SEES)

	Catching Sieve (mm)							
	9.5	11.2	13.2	16	22.4	31.5	40	50
No. of particles	158	158	158	158	50	63	83	47
Average mass (g)	2.31	3.31	3.38	8.78	42.02	100.96	136.64	192.79
Average *S* (mm)	7.8	9.2	9.5	12.5	19.9	25.9	27.9	30.7
Average *I* (mm)	11.4	13.1	13.1	18.4	29.4	39.5	47.5	55.3
Average *L* (mm)	18.9	20.0	19.6	27.5	50.5	71.0	74.9	81.7

Table 3: Summary data for *I/L*, *S/I* and *S/L*

	Measure	Catching Sieve (mm)							
		9.5	11.2	13.2	16	22.4	31.5	40	50
I/L	Maximum	0.838	0.888	0.864	0.869	0.822	0.781	0.818	0.857
	Upper quartile	0.683	0.739	0.737	0.748	0.670	0.658	0.719	0.768
	Mean	0.616	0.668	0.676	0.680	0.592	0.575	0.645	0.688
	Lower quartile	0.550	0.594	0.618	0.636	0.529	0.500	0.579	0.627
	Minimum	0.395	0.386	0.420	0.407	0.411	0.296	0.370	0.481
	Standard Dev.	0.096	0.094	0.090	0.100	0.095	0.114	0.095	0.096
S/I	Maximum	0.996	0.991	0.998	0.989	0.973	0.982	0.983	0.906
	Upper quartile	0.818	0.839	0.848	0.830	0.809	0.804	0.699	0.619
	Mean	0.692	0.712	0.733	0.693	0.688	0.667	0.599	0.563
	Lower quartile	0.573	0.598	0.627	0.585	0.543	0.553	0.483	0.480
	Minimum	0.203	0.315	0.298	0.252	0.337	0.275	0.310	0.373
	Standard Dev.	0.168	0.158	0.156	0.168	0.175	0.173	0.161	0.120
S/L	Maximum	0.679	0.786	0.788	0.758	0.669	0.652	0.675	0.628
	Upper quartile	0.482	0.539	0.586	0.543	0.456	0.445	0.457	0.445
	Mean	0.420	0.472	0.494	0.466	0.399	0.375	0.380	0.385
	Lower quartile	0.360	0.399	0.422	0.390	0.340	0.300	0.308	0.318
	Minimum	0.152	0.191	0.166	0.192	0.212	0.176	0.202	0.223
	Standard Dev.	0.102	0.113	0.119	0.120	0.094	0.100	0.099	0.086

Table 4: Weibull parameters for *S/L*

Catching sieve (mm)	95% confidence intervals				Best fit	
	lower		Upper			
	a	***b***	***a***	***b***	***a***	***b***
9.5	0.4431	4.0420	0.4764	5.1166	0.4594	4.5477
11.2	0.4979	4.1261	0.5345	5.2298	0.5159	4.6453
13.2	0.5213	4.1258	0.5595	5.2450	0.5401	4.6519
16	0.4930	3.7872	0.5326	4.8047	0.5124	4.2657
22.4	0.4080	3.6368	0.4656	5.4363	0.4358	4.4464
31.5	0.3874	3.3777	0.4406	4.8778	0.4131	4.0591
40	0.3956	3.5155	0.4418	4.8426	0.4180	4.1260
50	0.3932	3.8556	0.4467	5.8656	0.4191	4.7555

Table 5: Summary statistics for ellipseness data

Measure	Catching Sieve (mm)							
	9.5	11.2	13.2	16	22.4	31.5	40	50
Maximum	0.980	0.983	0.979	0.967	0.976	0.960	0.955	0.959
Upper quartile	0.955	0.959	0.958	0.948	0.755	0.945	0.754	0.942
Mean	0.940	0.940	0.941	0.931	0.929	0.928	0.923	0.925
Lower quartile	0.928	0.924	0.929	0.919	0.913	0.916	0.913	0.914
Minimum	0.860	0.885	0.858	0.836	0.855	0.882	0.854	0.854
Standard Dev.	0.022	0.023	0.023	0.023	0.025	0.020	0.020	0.022

Table 6: Weibull parameters for ellipseness

Catching sieve (mm)	95% confidence limits				Best fit	
	Lower		Upper			
	a	*b*	*a*	*b*	*a*	*b*
9.5	0.9473	47.3840	0.9531	60.4145	0.9502	53.504
11.2	0.9477	43.9051	0.9540	56.1763	0.9509	49.6631
13.2	0.9484	46.0117	0.9544	58.8745	0.9514	52.0473
16	0.9382	46.1520	0.9441	59.2014	0.9411	52.2711
22.4	0.9342	37.0975	0.9462	56.9157	0.9402	45.9503
31.5	0.9329	43.7752	0.9422	64.0007	0.9375	52.9305
40	0.9281	48.0098	0.9355	67.1111	0.9318	56.7626
50	0.9293	45.4772	0.9391	71.6689	0.9342	57.0903

Appendix B. Resin stabilisation of specimens and CT scanning

B.1 Introduction

In real track, when the ballast particles undergo train loading, they will rearrange and form a structure. In the laboratory also, scaled ballast is expected to rearrange its structure during the test. To investigate the development of structure at a given stage of a test, it is essential to be able to preserve the structure of the scaled ballast at that stage. One way of achieving this is to impregnate the triaxial specimen with resin. Resin has the ability to penetrate through the voids in the specimen and become solid within a particular curing time.

Once the triaxial specimen undergoes CT scanning, it can be looked at in detail in thin cross sections. These thin cross-section CT images can be used to identify the particle interlocking and particle contact points. CT software (For example; VG studio, Osirix, Image J, Avizo Fire) can be used to process these images. This CT software may be able to provide some useful measurements to study the structure of the ballast in detail, such as coordination number, type of contact, orientation of particles, and void ratio.

This chapter includes sections on: 1. Resin stabilization of unloaded specimen; 2. Resin stabilization of triaxial specimens; 3. CT images; 4. CT image processing and Analysis.

B.2 Resin stabilisation of unloaded specimen

A resin specimen was prepared outdoors in a well-ventilated area. As described in section 4.6.1, a scaled ballast specimen was prepared in the split mould with a plastic bung in the bottom. The plastic bung was used to seal the system and prevent resin from leaking out of the mould.

The PX672C/NC resin was prepared by mixing the epoxy resin (RX672C/NC) and hardener (HX672C/NC) components. The epoxy resin and hardener were provided in separate containers to the correct ratio (2:1 by volume) by Robnor Resins Ltd (Robnor, 2009). The resin was poured into the bucket followed by hardener. Then they were stirred well until the material became homogeneous.

The resin was poured into the specimen using a funnel to fill the voids (Figure B.1). The resin was allowed to set over 24 hours. Then the split mould was removed and the specimen was taken for CT scanning.

(a) (b)

Figure B.1: Specimen preparation outdoor: (a) Resin is poured through funnel (b) Resin impregnated specimen

B.3 Resin stabilisation of triaxial specimens

Resin was poured into the triaxial test specimens T6, T12, T7, and T13 at the end of the test to preserve the particle arrangement following testing. Test details of these resin stabilised specimens are given in Table B.1.

The specimen was prepared in the normal way with a plastic bung at the bottom. A hole was drilled in the porous disk. A tube was passed through the top cap and porous disk into the top of the specimen. The bottom end of the tube was cut at an angle to facilitate the resin flow. If the tube end is flat, particles may block the tube and prevent the resin flow. The top cap was sealed to prevent water getting into the specimen. The other end of the tube was sealed using the rubber bung and silicone grease.

Figure B.2 shows specimens standing under suction while resin pouring took place. After the test, the top end of the tube was cut and the funnel was attached. Resin was poured through the funnel (Figure B.3). To facilitate resin flow, suction was applied through the valve in the cell base. The resin was allowed to set over 2 days. Figure B.4

shows the resin impregnated specimens. Specimen T7 shows necking near to the top porous disk.

Resin impregnated specimens were CT scanned to study the structure and the effect of testing on the specimens. All of the CT scanned results were stored for further research. CT scanned results of triaxial loaded specimen ‘T12’, ‘T6’, ‘T7’ and an unloaded specimen (which was prepared outdoors) were analysed.

Test	Cyclic before extension			Extension loading			Cyclic after extension			Initial Density (kg/m^3)
	σ_3' (kPa)	q (kPa)	No of cycles	σ_3' (kPa)	q (kPa)	σ_1' (kPa)	σ_3' (kPa)	q (kPa)	No of cycles	
T12	55	5-225	1000	55-210	5-(-150)	60	55	5-225	1600	1536
T7	15-45	5-225	1000	45-200	5-(-150)	50	-	-	-	1550
T6	15-45	5-225	1000	-	-	-	-	-	-	1549
T13	45	5-225	1000	45-200	5-(-150)	50	-	-	-	1528

Table B.1: Test details of the Resin stabilised specimens

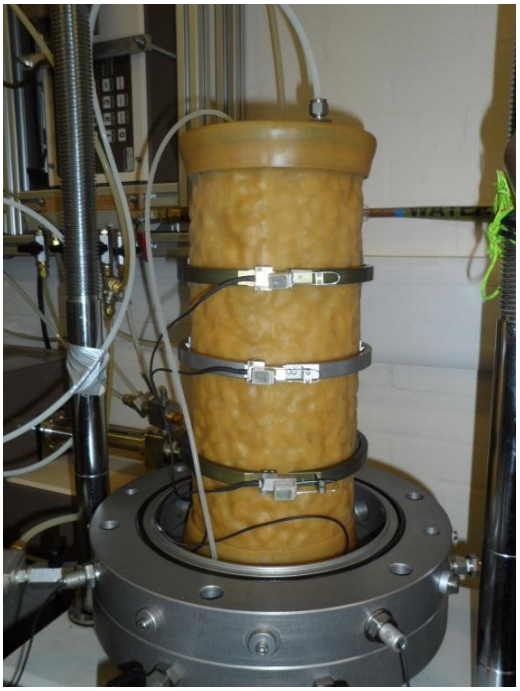

(a)

(b)

Figure B.2: Specimen held by suction with resin pouring arrangement: (a) cyclic test specimen ‘T6’ (b) cyclic and extension test specimen ‘T7’

Figure B.3: Resin being poured into the specimen ‘T7’

(a) T6

(b) T13

(c) T7

Figure B.4: Resin stabilization of triaxial specimens

B.4 CT images

X-ray Computed Tomography (CT) is a radiological scanning technique that enables a series of 2D cross-sections (slices) to be reconstructed into a 3D representation of the whole or part of the object scanned. The slices are produced from multiple x-ray radiographs taken through the specimen at the plane that slice represents. By stacking and comparing adjacent CT slices of a test specimen, a three dimensional image of the interior can be constructed.

When the specimen is scanned, the results will be obtained as sinograms. CT Pro 2D can be used to reconstruct the sinograms as slice stacks.

Figure B.5 shows 2D slices from the unloaded specimen image stack. Figure B.6 shows the two slices in the cross-section of the specimen. These two slices were randomly taken from a top down image stack. Figure B.6(a) shows a higher porosity (more voids) particle arrangement than Figure B.6(b). Figure B.7 shows the two slices in the longitudinal-section of the specimen which were taken from side image stack. The specimen shows less porosity (dense packing) in Figure B.7(b) than in Figure B.7(a).

The types of contacts have an influence on the porosity of the material (Dusseault and Morgenstern, 1979). Different types of contacts are clearly seen in these two dimensional images. These figures show tangential, straight, and concavo-convex contacts. In Figure B.6, examples of particle contacts are shown by ‘A’, ‘B’, and ‘C’. ‘A’ indicates tangential contacts, which result in low contact area and high porosity. ‘B’ shows straight contacts, which give low to medium contact area and a medium to high porosity. ‘C’ shows concavo-convex (or interpenetrative) contacts, which provide medium contact area and medium porosity.

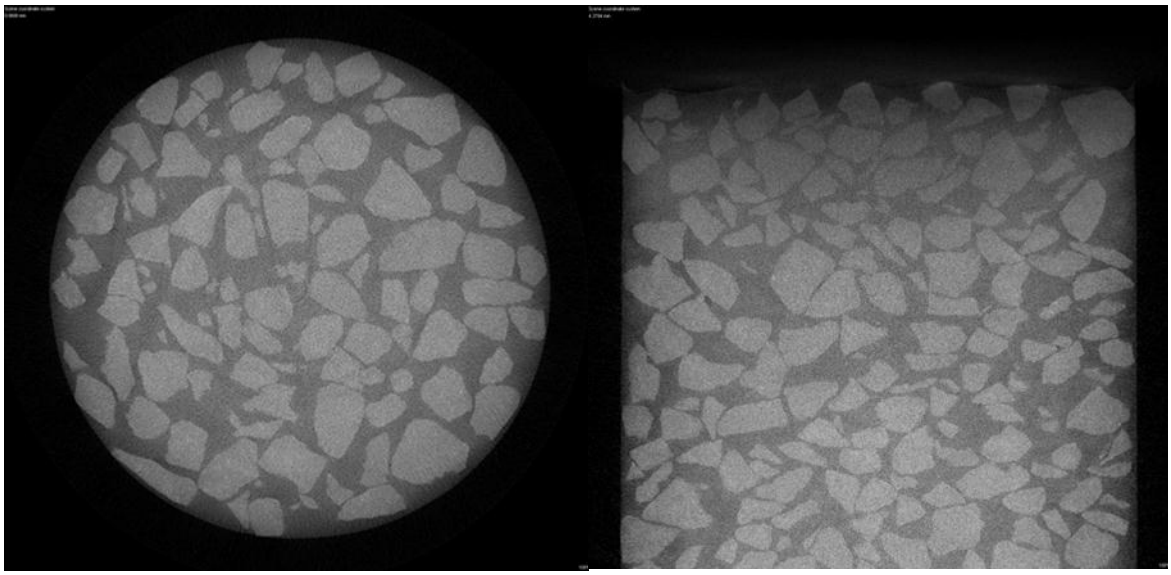

(a) (b)

Figure B.5: CT scanned specimen slices: (a) cross-sectional direction of specimen; (b) longitudinal-section direction of specimen

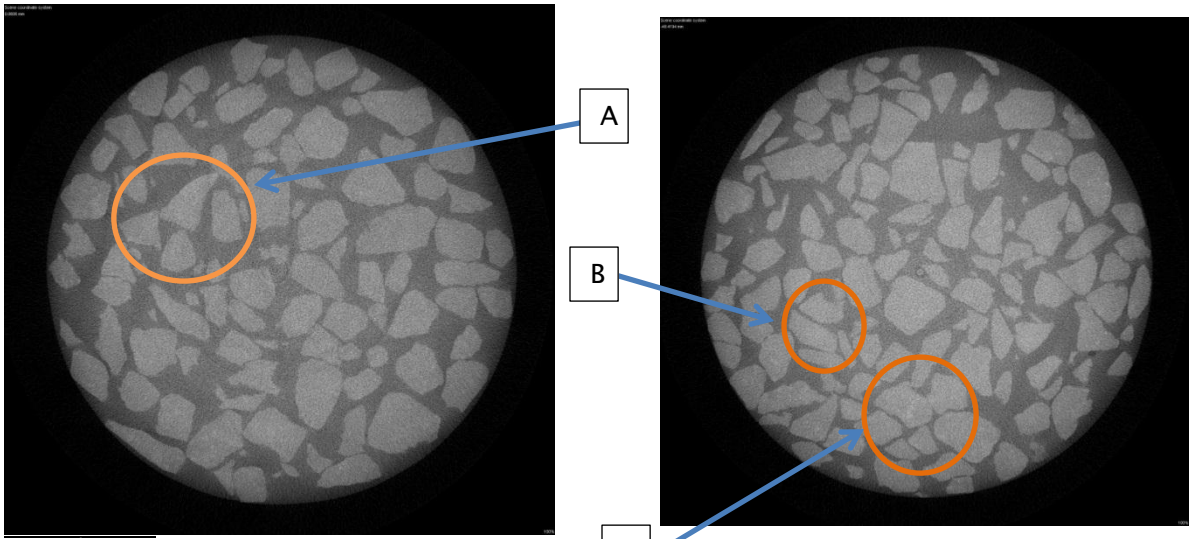

(a) (b)

Figure B.6: Cross-sectional slices of specimen

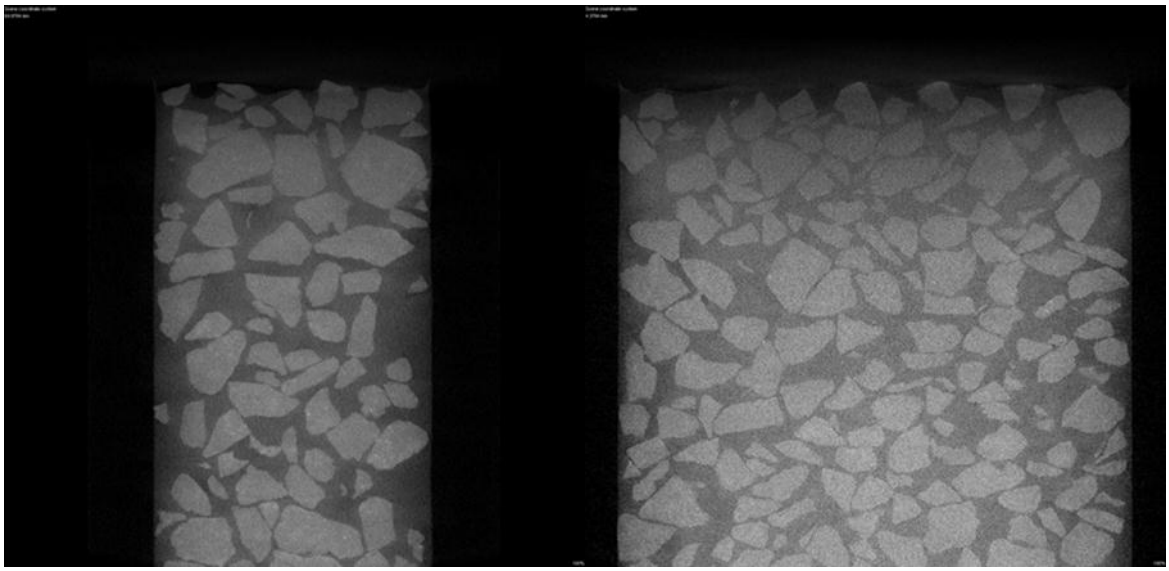

(a) (b)

Figure B.7: Longitudinal-section slices of specimen

B.5 CT image processing, segmentation and analysis

The Avizofire software was used to analyze the slice stack images (Avizo7.1, 2012). Specimen data (slice stack images) were opened in the Avizo Pool view. Orthoslices can be created to visualize the slices in different orientations xy, yz, and xz.

Specimen volume visualization: Specimen volume can be visualized from the slice stack images using the VoltexHighQuality module (Figure B.8). A default volume is created by the module using a limited number of slices to ensure higher performance. The number of slices can be reduced to get a better volume render. Specimen volume colours, transparency, and outlines can be controlled using 'Edit Colormap' option.

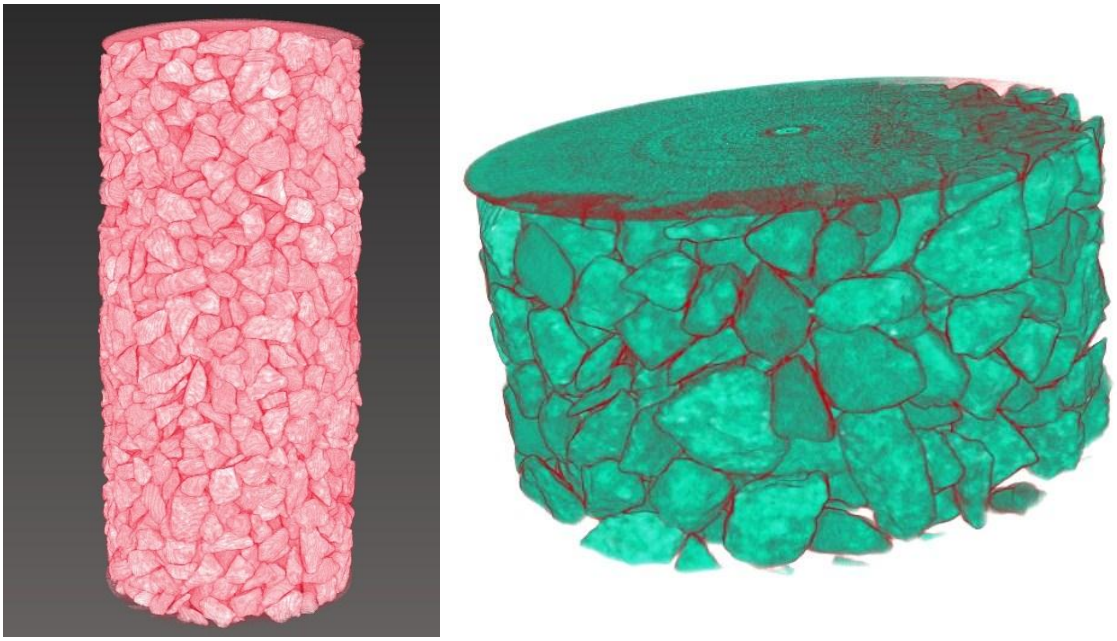

(a) Default volume

(b) Visualization using 300 slices

Figure B.8: Specimen volume visualization

Figure B.9 shows the CT image processing and segmentation steps to analyze the data as described below.

The specimen raw data were filtered to smooth out some of the extreme matrix and make the data less noisy. The data were filtered using Image filters/ Noise reduction median. Filters are image processing operations that use a number of pixels from the source image to compute new pixel value in the filtered data while preserving its geometry. A median filter replaces every pixel value by the median of the pixels in the corresponding neighbourhood, which can be used to reduce noise in the reconstructed data while usually preserving the features of interest (µ-VIS, 2011, Nixon and Aguado, 2008).

Once the dataset had been filtered, the binary image was created using the thresholding module. Particles were isolated from the resin by this operation. The filtered data were thresholded using Quantification/Thresholding/Binarisation/ I-threshold. I_ threshold is an interactive command and the minimum and maximum threshold values were adjusted to get the area of interest visible. Binarization transforms a grey level image into a binary image. This method is used when the relevant information in the grey level image corresponds to specific grey level interval. In the binary image the pixels of interest are set to 1, and to 0 for all other pixels. In

the output binary image, all pixels with an initial grey level value lying between the two bounds are set to 1, all the other pixels are set to 0 (Visilog7, 2012).

Once the thresholding had been performed, the morphological operators were used to separate the particle boundaries. The thresholded data were separated using Quantification/Fast morphology/Separate/Binseperate. Binseperate command only works with binary images. The seperate command is based on the fastwatershed algorithm to extract the watershed lines from either a binary or greyscale input image. These lines are used as boundary lines between overlapping particles (Visilog7, 2012). The principle of the separate command is to compute watershed lines on the grey-level image for black objects or on the inverted image for white objects.

Label operation was performed on the separated data to numerate each separated particle as the returned value. This Label operator assigned unique label to the separated particles.

Specimen data were analyzed using the binary separated labeled data as a mask. This was done by right clicking on the binary separated labeled data and selecting Quantification and then Analysis/Individual/I-analyze. Analysis command extracts data values from an image. The results of the analysis were obtained in a spreadsheet.

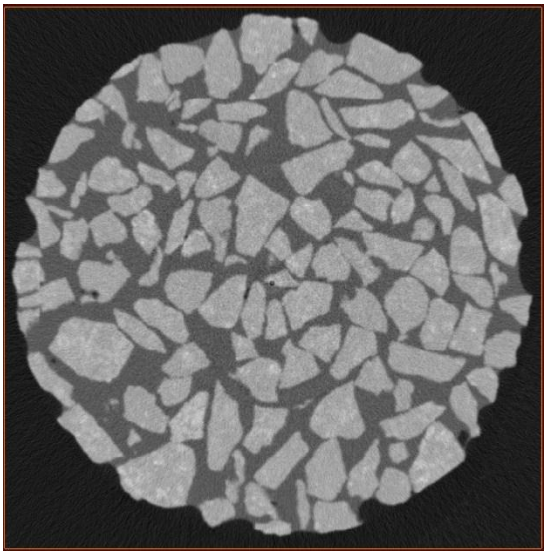

(a) Plain slice

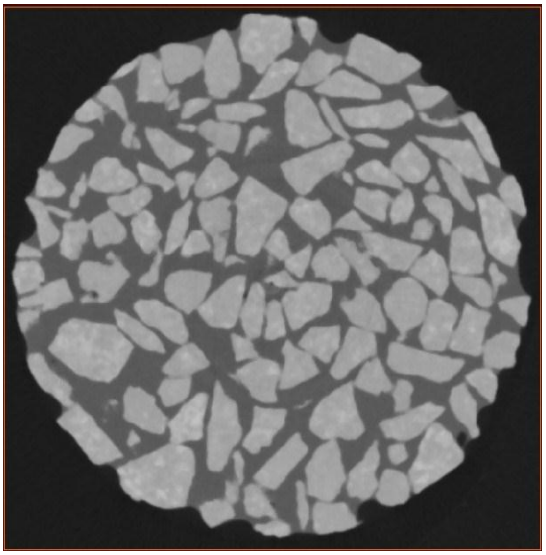

(b) Filtered slice

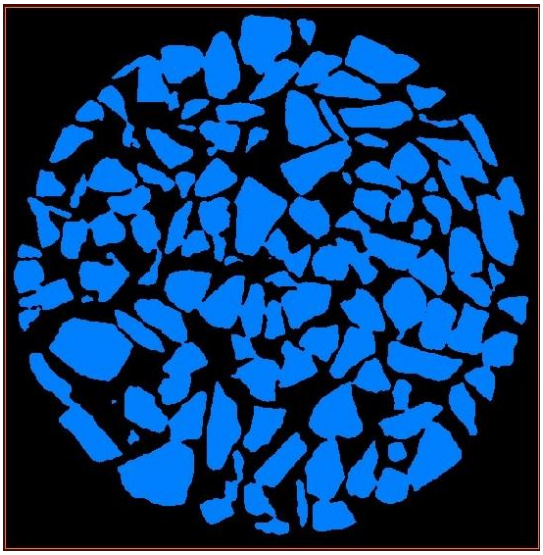

(c) Thresholded slice

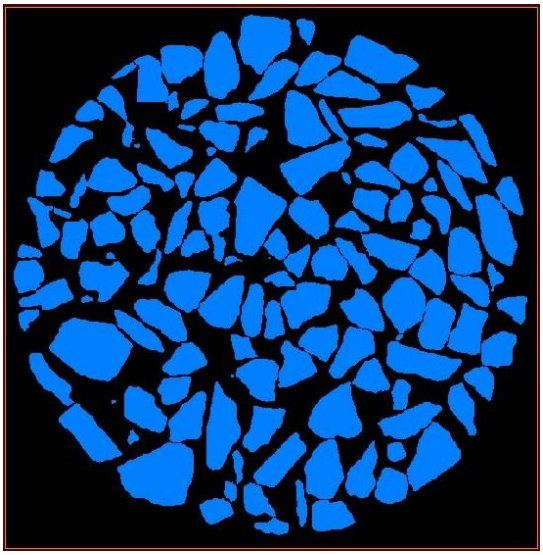

(d) Seperated slice

(e) Seperated Labelled slice

Figure B.9: CT image processing and segmentation for analyzing the dataset

Figure B.11 shows the length to width ratio of particles from the analysis. Length to width ratio for each particle was determined from Length3D and Width3D measurements. Length3D is the maximum of the feret diameters over a range of angles and Width3D is the minimum of the feret diameters over a range of angles. Feret diameter is the width of the bounding box distribution and the list of angles can be modified (Visilog7, 2012). Feret diameter measurements were taken over 1 degree Phi angle and 3 degree theta angle intervals (Figure B.10). The mean length to width

ratio of unloaded, loaded specimens 'T12', 'T6', and 'T7' are 2.18, 2.28, 2.36, and 2.18 respectively. Length/ width ratio is another version of measuring particle dimensions and the Figure B.11 shows the natural variation of particles between each specimen.

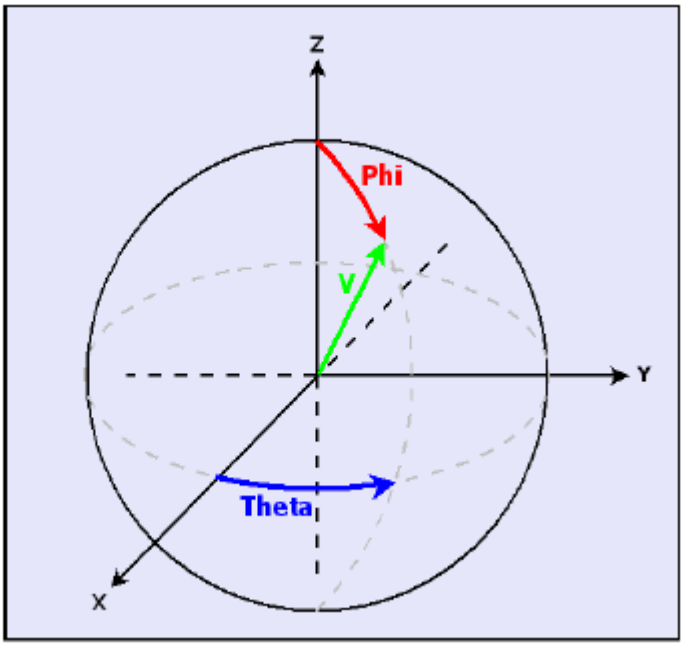

Figure B.10: Coordinate description for 3D images

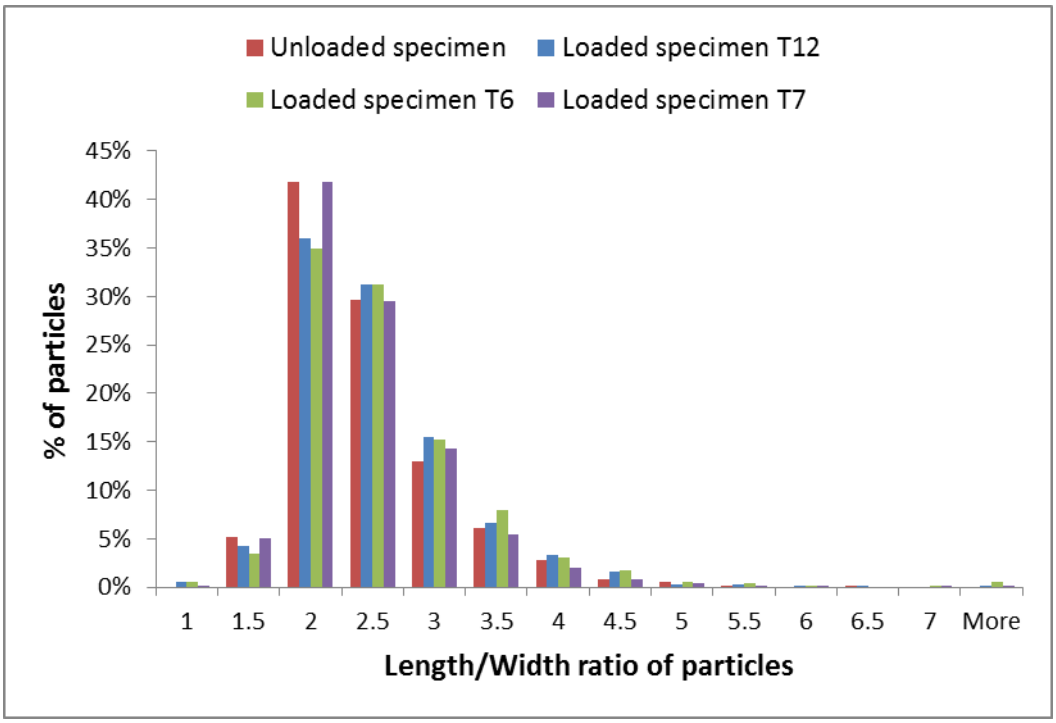

(a) Histogram

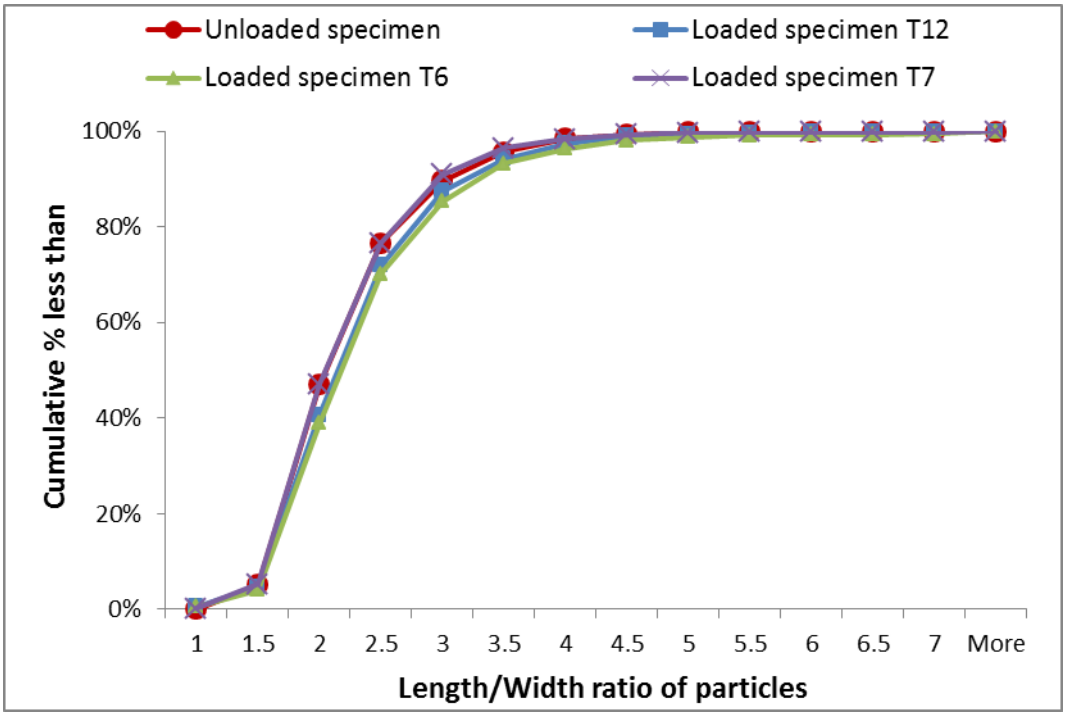

(b) Cumulative plot

Figure B.11: Length to width ratio of particles

Figure B.12 shows the absolute values of Length Orientation Phi angles. Length Orientation Phi (degrees) is the angle Phi of the maximum of the Feret diameters over a range of angles between [-90,+90] (Visilog7, 2012). Angle Phi is the rotation about the z-axis (which is vertical). There is a change in orientation between the specimens. Detail understanding of effect of stress path on particle structure needs further research.

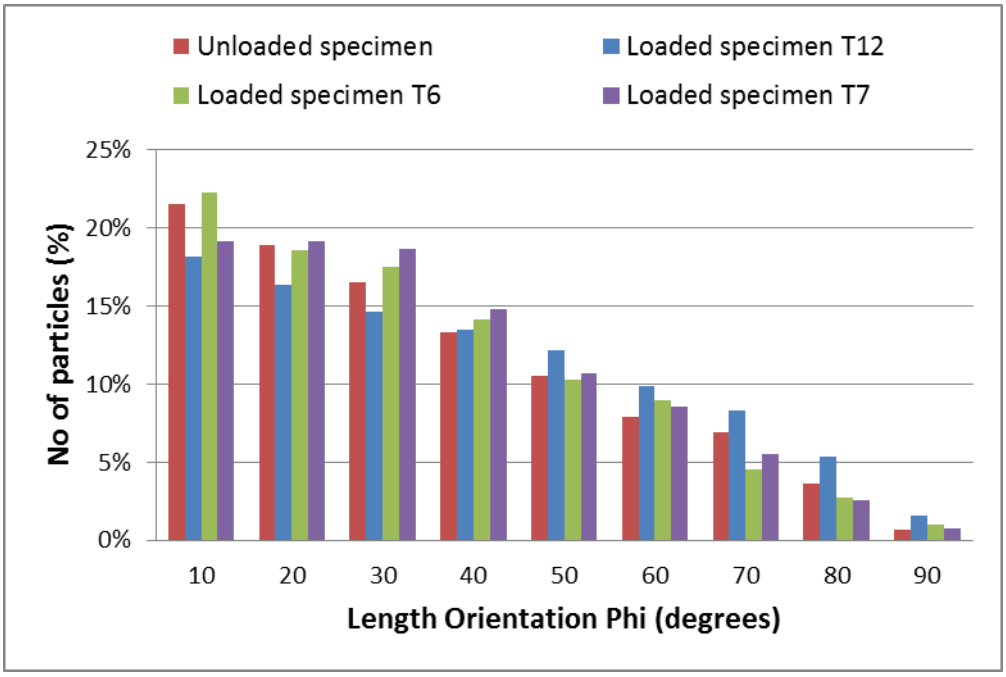

(a) Histogram

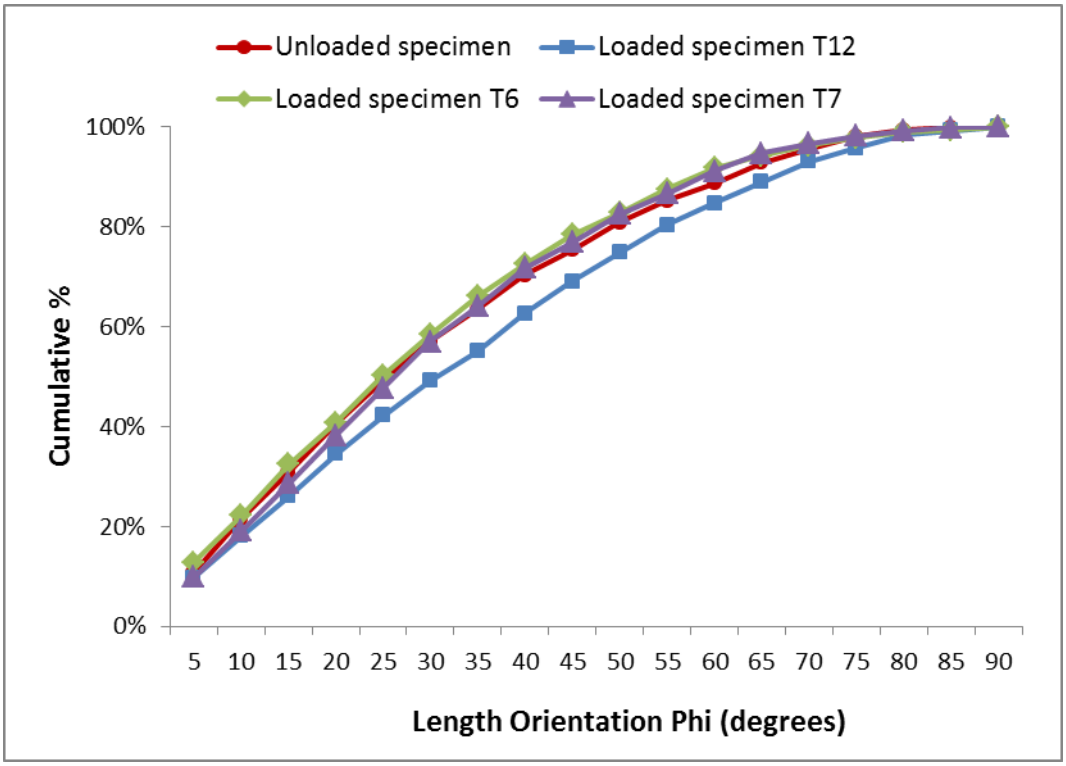

(b) Cumulative plot

Figure B.12: Length Orientation Phi of specimens

Figure B.13 shows the Length Orientation Phi values on rose diagrams (Angle histogram plot). The length of the bins represents the frequency of occurrence of Length Orientation Phi angles that fall in each bin. The frequencies are counted in '15 degree' bins. These diagrams show anisotropy orientation which means frequency changes differently in different directions.

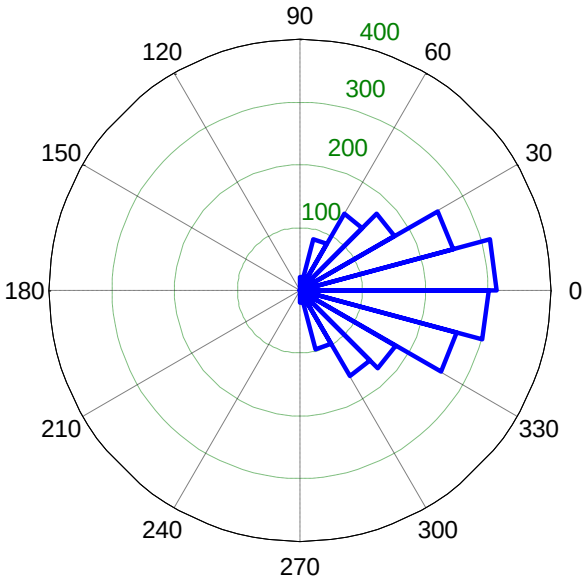

(a) Unloaded specimen

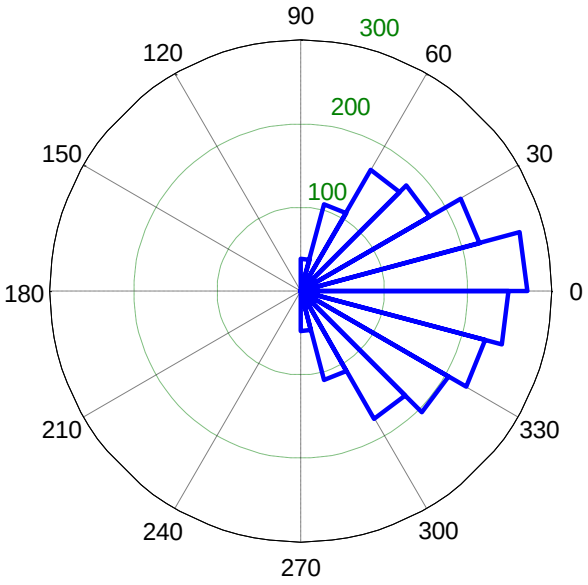

(b) Loaded specimen T12

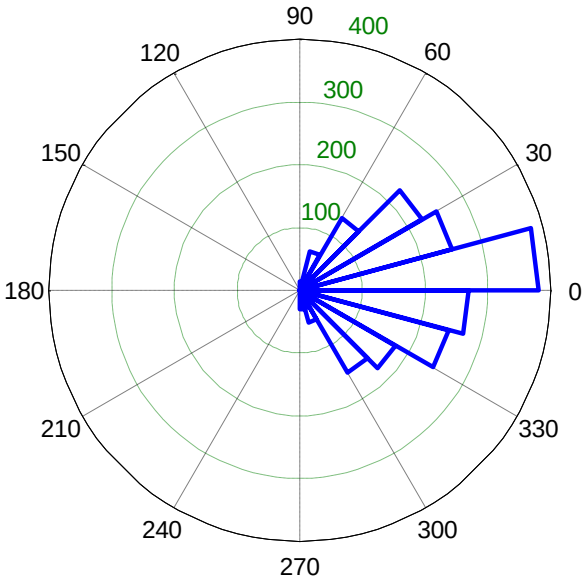

(c) Loaded specimen T6

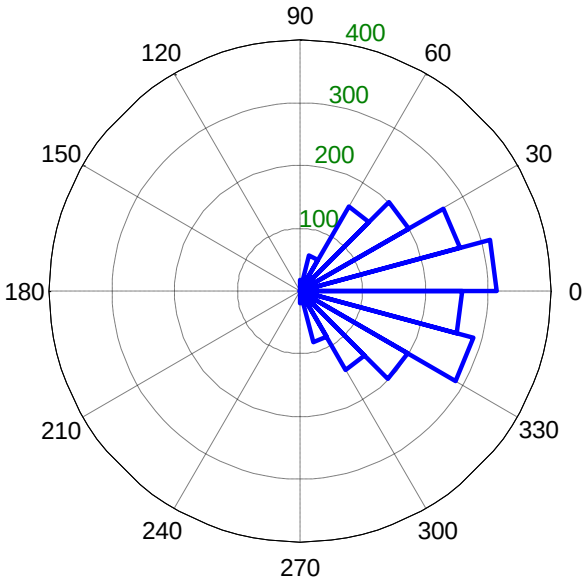

(d) Loaded specimen T7

Figure B.13: Particle orientation diagram

B.6 Summary

A technique was implemented to stabilise the ballast specimen in the outdoors and triaxial apparatus. It made possible the analysis of the structure of specimen even after loading.

CT scanning produces large numbers of 2D images around a single axis of rotation which enable the visualisation of the interior of the specimen. Avizo fire software was used to visualise qualitative and quantitative information on specimen structure. CT images were processed and segmented to quantitatively measure the specimen in detail.

Some initial results were obtained for the unloaded and loaded specimens ‘T12’, ‘T6’ and ‘T7’. A change in orientation between specimens observed. Understanding of the effect of stress paths on specimens needs further research.

References

ALLEN, J. 1973. *The Effects of non-constant lateral pressures of the resilient response of granular materials.* PhD thesis, University of Illinois at Urbana-Champaign, Urbana.

ALLEN, J. J. & THOMPSON, M. R. 1974. Resilient response of granular materials subjected to time-dependent lateral stresses. *transportation Research Record. 510,.* Transportation Research Board, Washington,D.C, 1-13.

ANDERSON, W. & FAIR, P. 2008. Behavior of Railroad Ballast under Monotonic and Cyclic Loading. *Journal of Geotechnical and Geoenvironmental Engineering,* 134**,** 316.

ASTM D4767-02 Standard Test Method for Consolidated Undrained Triaxial Compression Test for Cohesive Soils.

AURSUDKIJ, B. 2007. *A laboratory study of railway ballast behaviour under traffic loading and tamping maintenance.* PhD thesis, University of Nottingham.

AURSUDKIJ, B., MCDOWELL, G. & COLLOP, A. 2009. Cyclic loading of railway ballast under triaxial conditions and in a railway test facility. *Granular Matter,* 11**,** 391-401.

AVIZO7.1 2012. *Avizo user's guide*, Visualization science group.

BARKSDALE, R. D. 1972. Laboratory evaluation of rutting in base course materials. *Proc., 3rd Int. Conf. on Struct. Des. of Asphalt Pavements.* 161-174.

BARKSDALE, R. D. & ITANI, S. Y. 1989. Influence of aggregate shape on base behaviour. *Transportation research record. 1227,.* Transportation Research Board, Washington, D.C., 173-182.

BARRETT, P. J. 1980. The shape of rock particles, a critical review. *Sedimentology,* 27**,** 291-303.

BARTON, M. 1993. Cohesive sands: the natural transition from sands to sandstones. *Geotechnical engineering of hard soils–soft rocks. Edited by A. Anagnostopoulos, F. Schlosser, N. Kalteziotis, and R. Frank. AA Balkema, Rotterdam***,** 367–374.

BISHOP, A. W. & GREEN, G. E. 1965. The influence of end restraint on the compression strength of a cohesionless soil. *Geotechnique,* 15**,** pp.243-266.

BLOTT, S. J. & PYE, K. 2008. Particle shape: a review and new methods of characterization and classification. *Sedimentology,* 55**,** 31-63.

BOYCE, J. R., BROWN, S. F. & PELL, P. S. 1976. The resilient behaviour of a granular material under repeated loading. *Proc., 8th ARRB Conf. Mat. Constr. and Maintenance.* Vol. 8, Part 3, 1-12.

BROWN, S. F. & HYDE, A. F. L. 1975. Significance of cyclic confining stress in repeated-load triaxial testing of granular material. *Transportation Research Record 537.* Transportation Research Board, Washington, D.C., 49-58.

BROWN, S. F. & SELIG, E. T. 1991. The design of pavement and rail track foundations. *Cyclic loading of soils: from theory to design,* M. P. O'Reilly and S. F. Brown, eds., Blackie and Son Ltd., Glasgow, Scotland**,** 249-305.

BSI: BS EN 13450:2002. Aggregates for railway ballast. BSI.

BURKS, M. E., ROBSON, J.D., & SHENTON, M.J. 1975. Comparison of robel supermat and plasser 07-16 track maintenance machines. *Tech.note TN SM 139, British Railways Board R & D Division, December.*

CHRISMER, S. M. 1989. Track surfacing with conventional tamping and stone injection. *Association of American Railroads Research Report No. R-719.* Chicago, Illinois.

CLAYTON, C., ABBIREDDY, C. & SCHIEBEL, R. 2007. A Method of estimating the form of coarse particulates. *Geotechnique***,** 9.

COLLINS, I. F. & BOULBIBANE, M. 2000. Geomechanical analysis of unbound pavements based on shakedown theory. *Journal of Geotechnical and Geoenvironmental Engineering,* 126(1)**,** 50-59.

COX, E. 1927. A method of assigning numerical and percentage values to the degree of roundness of sand grains. *Journal of Paleontology,* 1**,** 179-183.

CRESSWELL, A. & BARTON, M. 2003. Direct shear tests on an uncemented, and a very slightly cemented, locked sand. *Quarterly Journal of Engineering Geology & Hydrogeology,* 36**,** 119.
CRESSWELL, A. & POWRIE, W. 2004. Triaxial tests on an unbonded locked sand. *Geotechnique,* 54**,** 107-115.
CUCCOVILLO, T. & COOP, M. R. 1999. On the mechanics of structured sands. *Geotechnique,* 49**,** No. 6, 741-760.
DAWSON, A. R., THOM, N. H. & PAUTE, J. L. 1996. Mechanical characteristics of unbound granular materials as a function of condition. *Flexible Pavements, Proc., Eur. Symp. Euroflex 1993.* A.G. Correia,ed., Balkema, Rotterdam, The Netherlands, 35-44.
DEHLEN, G. L. 1969. *The effect of non-linear material response on the behaviour of pavements subjected to traffic loads.* PhD thesis, University of California, Berkeley, Calif.
DIYALJEE, V. A. 1987. Effects of stress history on ballast deformation. *Journal of Geotechnical Engineering,* 113**,** pp. 909-914.
DOBKINS, J. & FOLK, R. 1970. Shape development on Tahiti-nui. *Journal of Sedimentary Petrology,* 40**,** 1167–1203.
DUSSEAULT, M. & MORGENSTERN, N. 1979. Locked sands. *Quarterly Journal of Engineering Geology & Hydrogeology,* 12**,** 117.
DUSSEAULT, M. B. 1977. *The geotechnical characteristics of the Athabasca oil sands.* Thesis. Alberta Research Council, University of Alberta.
EN13848-5 2008. Track geometry quality – Part 5: Geometric quality levels.
EN14363 2005. Railway applications – Testing for the acceptance of running characteristics of railway vehicles –
Testing of running behaviour and stationary tests.
ETSC 2003. TRANSPORT SAFETY PERFORMANCE IN THE EU A STATISTICAL OVERVIEW. Brussels: European Transport Safety Council.
FAIR, P. 2003. *The geotechnical behaviour of ballast materials for railway track maintenance.* Thesis. Department of Civil and Structural Engineering, University of Sheffield.
FUKUSHIMA, S. & TATSUOKA, F. 1984. Strength and deformation characteristics of saturated sand at extremely low pressures. *Soils and Foundations,* 24**,** 30-48.
HAYNES, J. H. & YODER, E. J. 1963. Effects of repeated loading on gravel and crushed stone base course materials used in the AASHO Road Test. *Highway Research Record.39.*
HEYDINGER, A. G., XIE, Q. L., RANDOLPH, B. W. & GUPTA, J. D. 1996. Analysis of Resilient Modulus of Dense-and Open-Graded Aggregates. *Transportation Research Record 1547.* Transportation Research Board, Washington, D.C, 1-6.
HICKS, R. G. 1970. *Factors influencing the resilient properties of granular materials.* Thesis, PhD thesis, University of California, Berkeley.
HICKS, R. G. & MONISMITH, C. L. 1971. Factors influencing the resilient response of granular materials. *Highway research record***,** No.345, pp.15-31.
INDRARATNA, B., IONESCU, D. & CHRISTIE, H. 1998. Shear behavior of railway ballast based on large-scale triaxial tests. *Journal of Geotechnical and Geoenvironmental Engineering,* 124**,** 439-450.
INDRARATNA, B., IONESCU, D., CHRISTIE, H. D. & CHOWDHURY, R. N. 1997. Compression and degradation of railway ballast under one-dimensional loading. *Australian Geomechanics***,** pp. 48-61.
INDRARATNA, B. & SALIM, W. 2001. Shear strength and degradation characteristics of railway ballast. *Proceeding of 14th Southeast Asian Geotechnical Conference.* Hong Kong: Vol.1. pp. 521-526.
INDRARATNA, B. & SALIM, W. 2003. Deformation and degradation mechanics of recycled ballast stabilised with geosynthetics. *Soils and foundations,* Vol.43, No.4**,** pp.35-46.
INDRARATNA, B. & SALIM, W. 2005. *Mechanics of ballasted rail tracks: a geotechnical perspective*, Taylor & Francis Group.

INDRARATNA, B., WIJEWARDENA, L. S. S. & BALASUBRAMANIAM, A. S. 1993. Large-scale triaxial testing of greywacke rockfill. *Geotechnique,* 43**,** 37-51.
IONESCU, D., INDRARATNA, B. & CHRISTIE, H. D. 1998. Behaviour of railway ballast under dynamic loads. *Proc. 13 th Southeast Asian Geotechnical Conference.* Taipei. pp. 69-74.
JANARDHANAM, R. & DESAI, C. S. 1983. Three Dimensional Testing and Modeling of Ballast. *Journal of Geotechnical Engineering,* 109**,** No.6, pp.783-796.
JEFFS, T. 1989. Towards ballast life cycle costing. *Proc. 4th International Heavy Haul Railway Conference.* Institution of Engineers, Australia. 439-445.
JEFFS, T. & MARICH, S. 1987. Ballast characteristics in the laboratory. Institution of Engineers, Australia. pp. 141-147.
JEFFS, T. & TEW, G. P. 1991. A review of track design procedures - sleepers and ballast. *Vol 2 of Railways of Australia.* Melbourne, Australia.
JORENBY, B. N. & HICKS, R. G. 1986. Base course contamination limits. *Transportation Research Record, 1095***,** Transportation Research Board, Washington, D.C., 86-101.
KATZENBACH, R. & FESTAG, G. 2004. Material behaviour of dry sand under cyclic loading. *Cyclic Behaviour of Soils and Liquefaction Phenomena***,** 153-158.
KNUTSON, R. M. 1976. *Factors influencing the repeated load behavior of railway ballast.* Ph.D. Thesis, University of Illinois Urbana-Champaign.
KOLISOJA, P. 1997. *Resilient deformation characteristics of granular materials.* PhD thesis, Tampere University of Technology, Publ. No. 223, Tampere, Finland.
LACKENBY, J., INDRARATNA, B., MCDOWELL, G. & CHRISTIE, D. 2007. Effect of confining pressure on ballast degradation and deformation under cyclic triaxial loading. *Geotechnique,* 57**,** 527-536.
LADE, P. V., YAMAMURO, J. A. & BOPP, P. A. 1996. Significance of particle crushing in granular materials. *Journal of Geotechnical Engineering,* Vol.122, No.4**,** pp.309-316.
LASHINE, A. K., BROWN, S. F. & PELL, P. S. 1971. Dynamic properties of soils. *Rep. No. 2, Submitted to Koninklijke/Shell Laboratorium, Department of Civil Engineering, University of Nottingham ,Nottingham, England.*
LE PEN, L. 2008. *Track behaviour: The importance of the sleeper to ballast interface.* Doctor of Philosophy, University of Southampton.
LEKARP, F., ISACSSON, U. & DAWSON, A. 2000a. State of the art. I: Resilient response of unbound aggregates. *Journal of Transportation Engineering,* 126**,** 66-75.
LEKARP, F., ISACSSON, U. & DAWSON, A. 2000b. State of the art. II: Permanent strain response of unbound aggregates. *Journal of Transportation Engineering,* 126**,** 76-83.
LIM, W. L. 2004. *Mechanics of railway ballast behaviour.* PhD thesis, University of Nottingham.
LUBER, B., HAIGERMOSER, A. & GRABNER, G. 2010. Track geometry evaluation method based on vehicle response prediction. *Vehicle System Dynamics,* 48**,** 157-173.
MACKIE, W. 1897. On the laws that govern the rounding of particles of sand. *Trans. Edinburgh Geol. Soc,* 7**,** 298–311.
MARACHI, N. D., CHAN, C. K. & SEED, H. B. 1972. Evaluation of properties of rockfill materials. *Journal of the Soil Mechanics and Foundations Division,* 98**,** 95-114.
MEDIACYBERNETICS 2006. Image Pro Plus 6.1 software update- Technical support for Media Cybernetics products.Available from: URL: http://support.mediacy.com/ipp61.update.asp.
MESRI, G., FENG, T.W. & BENAK, J.M. 1990. Postdensification penetration resistance of clean sands. *Journal of Geotechnical Engineering,* A.S.C.E. 116**,** 1095-1115.
MONISMITH, C. L., SEED, H. B., MITRY, F. G. & CHAN, C. K. 1967. Prediction of pavement deflections from laboratory tests. *Proc., 2nd Int. Conf. Struct. Des. of Asphalt Pavements.* 109-140.
MORGAN, J. 1966. The response of granular materials to repeated loading. *Proc., 3rd Conf.* ARRB, 1178-1192.

NETWORKRAIL 2003. Company Code of Practice: Formation Treatments,. *Issue 2, Dec 2003.* 40 Melton Street, London, W1 2EE.
NIXON, M. & AGUADO, A. S. 2008. *Feature extraction & image processing*, Access Online via Elsevier.
POWRIE, W. 2004. *Soil mechanics: concepts and applications*, Spon Press.
POWRIE, W. 2013. James Forrest Lecture 2013- On track the future.: Available from: http://www.ice.org.uk/Events-conferences/Recorded-lectures/Lectures/James-Forrest-Lecture-2013-On-track--the-future [Accessed 24/04/2014].
POWRIE, W., YANG, L. A. & CLAYTON, C. R. I. 2007. Stress changes in the ground below ballasted railway track during train passage. *Proceedings of the Institution of Mechanical Engineers, Part F: Journal of Rail and Rapid Transit,* Volume 221**,** 247-262.
RAYMOND, G. & BATHURST, R. 1987. Performance of large-scale model single tie-ballast systems. *Transportation Research Record 1131***,** pp. 7-14.
RAYMOND, G. P. & DAVIES, J. R. 1978. Triaxial tests on dolomite railroad ballast. *Journal of Geotechnical and Geoenvironmental Engineering,* 104(6)**,** p 737-751.
RAYMOND, G. P. & DIYALJEE, V. A. 1979. Railroad ballast sizing and grading. *Journal of the Geotechnical Engineering Division,* 105**,** pp. 676-681.
REDFERN, B. 2011. Infrastructure in 2011. A special report on prospects for the year ahead. *New Civil Engineer***,** pp 26 - 28.
REGULATION RT/CE/S/006 Issue 3, 2000. Railtrack line specification : Track ballast and Stone blower aggregate. Safety and Standards Directorate Railtrack PLC, Railtrack House, Euston Square, London, NW1 2EE.
RITTER, N. & COOPER, J. 2009. New Resolution Independent Measures of Circularity. *Journal of Mathematical Imaging and Vision,* 35**,** 117-127.
ROBNOR 2009. Robnor resins- Epoxy safety sheets: Available from : URL: http://www.robnor.co.uk/index.php/products/epoxy/epoxy-safety-sheets.html.
SALIM, M. W. 2004. *Deformation and degradation aspects of ballast and constitutive modelling under cyclic loading.* PhD Thesis, Faculty of Engineering, University of Wollongong, Australia.
SAUSSINE, G., AZÉMA, E., GAUTIER, P., PEYROUX, R. & RADJAI, F. Numerical modeling of the tamping operation by Discrete Element Approach. World Congress Rail Research, 2008. 1-9.
SCHMERTMANN, J. H. 1991. The mechanical aging of soils. *Journal of Geotechnical Engineering,* A.S.C.E. 117**,** 1288-1330.
SEED, H., CHAN, C., LEE, C., TRANSPORTATION, I. O. & ENGINEERING, T. 1962. *Resilience characteristics of subgrade soils and their relation to fatigue failures in asphalt pavements*, Institute of Transportation and Traffic Engineering, University of California.
SEED, H. B., MITRY, F. G., MONISMITH, C. L. & CHAN, C. K. 1965. Predictions of pavement deflections from laboratory repeated load tests. *Rep. No. TE-65-6.* Soil Mech. and Bituminous Mat. Res. Lab.: University of California, Berkeley, Calif.
SELIG, E. & WATERS, J. 1994. *Track geotechnology and substructure management*, Thomas Telford.
SELIG, E. T. & ALVA-HURTADO, J. E. 1982. Predicting effects of repeated wheel loading on track settlement. *Proceeding of the 2nd International Heavy Haul Conference.* Colorado Springs, pp. 476-487.
SEVI, A. F. 2008. *Physical modeling of railroad ballast using the parallel gradation scaling technique within the cyclical triaxial framework.* PhD thesis, Missouri University of Science and Technology.
SHENTON, M. J. 1975. Deformation of railway ballast under repeated loading conditions. *Railroad track mechanics and technology.* British railways, reasearch and development division, The railway technical centre, Derby, England, pp. 387-404.

SHENTON, M. J. 1984. Ballast deformation and track deterioration. *Track Technology. Proceeding of a conference organized by the Institution of Civil Engineers.* University of Nottingham.pp.242- 252.

SIEVER, R. 1959. Petrology and geochemistry of silica cementation in some Pennsylvania sandstones. *Silica in Sediments, Society of Economic Palaeontologists & Mineralogists Special Publication .* Tulsa,No.7**,** 56-79.

SMITH, W. S. & NAIR, K. 1973. Development of procedures for characterization of untreated granular base coarse and asphalt-treated base course materials. *Rep. No. FHWA-RD-74-61,* Federal Highway Administration, Washington, DC.

STEWART, H. E., SELIG, E. T. & NORMAN, G. M. 1985. Failure criteria and lateral stresses in track foundations. *Transportation Research Record,* 1022**,** pp. 59-64.

SUIKER, A. S. J. 2002. *The mechanical behaviour of ballasted railway tracks.* PhD Thesis, Delft university of technology, Netherlands.

SUIKER, A. S. J., SELIG, E. T. & FRENKEL, R. 2005. Static and cyclic triaxial testing of ballast and subballast. *Journal of Geotechnical and Geoenvironmental Engineering,* Vol.131, No.6**,** pp.771-782.

TAYLOR, J. M. 1950. Pore space reduction in sandstones. Bulletin American Ass'n. Petroleum Geologist 34, 701-716.

THOM, N. 1988. *Design of road foundations.* PhD thesis, Dept. of Civ.Eng, University of Nottingham, Nottingham, England.

THOM, N. & BROWN, S. 1989. The mechanical properties of unbound aggregates from various sources. 11-13.

THOM, N. H. & BROWN, S. F. 1987. Effect of moisture on the structural performance of a crushed-limestone road base. *Transp. Res. Rec.112.* Transportation Research Board, Washington, D.C., 50-56.

THOM, N. H. & BROWN, S. F. 1988. The effect of grading and density on the mechanical properties of a crushed dolomitic limestone. *Proc., 14th ARRB Conf., Vol.14, Part 7, 94-100*.

UZAN, J. 1985. Characterization of granular material. *Transportation research record. 1022, Transportation Research Board, Washington, D.C., 52-59.*

VAN NIEKERK, A. A., HOUBEN, L. J. M. & MOLENAAR, A. A. A. 1998. Estimation of mechanical behaviour of unbound road building materials from physical material properties. *Proc., 5th Int. Conf. on the Bearing Capacity of Roads and Airfields***,** R. S. Nordal and G. Rafsdal, eds., Vol. 3, 1221-1233.

VARADARAJAN, A., SHARMA, K. G., VENKATACHALAM, K. & GUPTA, A. K. 2003. Testing and modeling two rockfill materials. *Journal of Geotechnical and Geoenvironmental Engineering,* 129**,** 206-218.

VISILOG7 2012. *Reference guide*, Noesis S.A, France.

WENTWORTH, C. 1919. A laboratory and field study of cobble abrasion. *The Journal of Geology,* 27**,** 507-521.

WRIGHT, S. E. 1983. Damage caused to ballast by mechanical maintenance techniques. *British Rail Research Technical Memorandum* TM TD 15, May.

ZAMAN, M., CHEN, D. & LAGUROS, J. 1994. Resilient moduli of granular materials. *Journal of Transportation Engineering,* 120 (6)**,** 967-988.

ZINGG, T. 1935. Contribution to the gravel analysis (Beitrag zur Schotteranalyse). *Schweizer. Mineralog. u. Petrog. Mitt. 15***,** 39-140.

M-VIS 2011. Filters and morphological operations, accessed 27January2014,,http://sprawl.ses.soton.ac.uk/wiki/index.php5/Filters_and_morphological_operations.